**Dissertation**
**submitted to the**
**Combined Faculties for the Natural Sciences and for Mathematics**
**of the Ruperto-Carola University of Heidelberg, Germany**
**for the degree of**
**Doctor of Natural Sciences**

presented by

Stefan Ulmer

born in Tübingen

Day of oral exam: $4^{\text{th}}$ of July 2011

# First Observation of Spin Flips with a Single Proton Stored in a Cryogenic Penning Trap

First referee: Priv. Doz. Dr. Wolfgang Quint

Second referee: Prof. Dr. Klaus Blaum

**Zusammenfassung**

In dieser Arbeit wird die erstmalige direkte Beobachtung von Spin-Übergängen eines einzelnen, in einer kryogenen Doppel-Penningfalle gespeicherten Protons präsentiert. Der experimentelle Nachweis solcher Spin-Übergänge basiert auf der Anwendung des kontinuierlichen Stern-Gerlach Effekts. Hierbei wird der Spin-Freiheitsgrad über ein inhomogenes Magnetfeld an die nicht-destruktiv messbare axiale Eigenfrequenz des in der Penningfalle gespeicherten Protons gekoppelt. Eine Änderung der Spin-Quantenzahl macht sich so in einer Verschiebung der axialen Frequenz bemerkbar. Die besondere experimentelle Herausforderung beim Proton besteht in seinem winzigen magnetischen Moment. Um eine durch einen Spin-Übergang verursachte Verschiebung der axialen Frequenz beobachten zu können, wurde das Proton in der stärksten, jemals einer Penningfalle überlagerten Magnetfeldinhomogenität gespeichert, und nicht-destruktiv nachgewiesen. Dazu wurden ultrahochempfindliche supraleitende Nachweissysteme entwickelt, welche die direkte Beobachtung des Protons, und die hochpräzise Messung seiner Eigenfrequenzen ermöglichen.
Basierend auf neuartigen experimentellen Methoden, die im Rahmen dieser Arbeit entwickelt wurden, konnte die axiale Frequenz des Protons unter diesen extremen Magnetfeldbedingungen auf ein Niveau stabilisiert werden, das in Kombination mit der entwickelten Hochfrequenzelektronik die Beobachtung von Spin-Übergängen ermöglicht.
Dieser experimentelle Erfolg stellt einen der wichtigsten Schritte zur direkten Messung des magnetischen Moments des freien Protons dar. Mit der Demonstration der erstmaligen nicht-destruktiven Beobachtung von Spin-Übergängen eines einzelnen Protons eröffnet sich darüberhinaus eine reizvolle Perspektive. Die im Rahmen dieser Arbeit entwickelten experimentellen Techniken können auf das Antiproton angewandt werden. So rückt die erstmalige Hochpräzisionsmessung des magnetischen Moments des Antiprotons in greifbare Nähe, was einen neuen hochpräzisen Test der Materie-Antimaterie-Symmetrie ermöglicht.

**Abstract**

In this thesis the very first observation of spin transitions of a single proton stored in a cryogenic double-Penning trap is presented. The experimental observation of spin transitions is based on the continuous Stern-Gerlach effect, which couples the spin of the single trapped proton to its axial eigenfrequency, by means of an inhomogeneous magnetic field. A spin transition causes a change of the axial frequency, which can be measured non-destructively. Due to the tiny magnetic moment of the proton, the direct detection of proton spin-flips is an exceeding challenge. To achieve spin-flip resolution, the proton was stored in the largest magnetic field inhomogeneity, which has ever been superimposed to a Penning trap, and its axial frequency was detected non-destructively. Therefore, superconducting detection systems with ultrahigh-sensitivity were developed, allowing the direct observation of the single trapped proton, as well as the high-precision determination of its eigenfrequencies. Based on novel experimental methods, which were developed in the framework of this thesis, the axial frequency of the particle was stabilized to a level, where the observation of single-proton spin-flips is possible, which was demonstrated.

This experimental success is one of the most important steps towards the high-precision determination of the magnetic moment of the free proton. With the very first observation of spin transitions with a single trapped proton, a highly exciting perspective opens. All experimental techniques which were developed in this thesis can be directly applied to the antiproton. Thus, the first high-precision measurement of the magnetic moment of the antiproton becomes possible. This will provide a new high-precision test of the matter-antimatter symmetry.

**To Eva, Frida, and Yara**
**with all my love**

# TABLE OF CONTENTS

# LIST OF FIGURES

# LIST OF TABLES

Chapter 1

# INTRODUCTION

The understanding of the structure of the proton and the measurement of its properties is an inspiring challenge. Especially since the proton is not one out of hundreds of particles in the zoo of high energy physics. Considered from many different perspectives, the proton is absolutely unique!

Together with the neutron, it is one out of two stable baryons in our universe, and even the only stable free baryon. Thus, it is the only continuously observable "simple system", which is sensitive to the fields and interactions of quantum chromodynamics.

From the perspective of atomic physics, besides the photon, the electron, the neutrino, and the neutron, the proton is one of five fundamental building blocks of matter, and thus, a detailed understanding of its structure will lead to a deeper insight into the riddles of nature. Some important precision experiments are plagued by a lack of knowledge about proton structure. The precision with which quantum electrodynamics can be tested by ultrahigh-resolution laser spectroscopy of hydrogen used to be limited by the precision by which the proton radius is known [1]. The argument can be reversed, of course, and precision atomic physics can be used to establish constraints on proton structure [2]. Spectacular progress has been made very recently in an experiment which used laser spectroscopy of muonic hydrogen to determine the radius of the proton [3].

Historically, experiments dedicated to the precise observation of the proton's properties opened windows towards novel fields of physics. Particularly the study of the magnetic moment of the proton $\mu_\mathrm{p} = (g_\mathrm{p}/2) \cdot (e\hbar)/(2m_\mathrm{p})$, where $g_\mathrm{p}$ is the Landé $g$-factor and $e/m_\mathrm{p}$ the charge-to-mass ratio, played a major role. In 1933, Otto Stern applied his "molecular ray method" to a beam of molecular hydrogen [4]. From the splitting of the beam, sensationally, the magnetic moment of the proton was found to be $\mu_p = 2.5(3) \cdot \mu_N$, where $\mu_N = (e\hbar)/(2m_\mathrm{p})$ is the nuclear magneton. Thus, the measured value differs by a factor

of 2.5 from the value expected from Dirac-theory [5], and was the first indication for the substructure of the proton. For this trailblazing discovery, Stern received the Nobel Prize in 1943.

This spectacular result inspired numerous experimentalists to perpetually increase the resolution of their techniques to measure the magnetic moment $\mu_p$ to even higher precision. Between the 1930s and the 1970s, Rabi [6] (molecular beam method), Bloch [7, 8] (nuclear magnetic resonance method), and Collington [9] (omegatron method) continuously improved the value to a relative precision of $\Delta\mu_p/\mu_p = 1.4 \cdot 10^{-5}$. Presently the most precise value for $\mu_p$ is extracted from an experiment conducted about forty years ago at Massachusetts Institute of Technology [10]. In this high-precision experiment, the ground-state hyperfine splitting in hydrogen was measured by means of a maser in a magnetic field, yielding the ratio of the magnetic moment of the proton and the electron bound in atomic hydrogen $\mu_\mathrm{p}(\mathrm{H})/\mu_\mathrm{e}(\mathrm{H})$ at a level of 10 ppb. From this experiment the $g$-value of the free proton

$$g_\mathrm{p} = g_\mathrm{e} \cdot \frac{\mu_\mathrm{p}(\mathrm{H})}{\mu_\mathrm{e}(\mathrm{H})} \cdot \frac{g_\mathrm{p}}{g_\mathrm{p}(\mathrm{H})} \cdot \frac{g_\mathrm{e}(\mathrm{H})}{g_\mathrm{e}} \cdot \frac{m_\mathrm{p}}{m_\mathrm{e}} \tag{1.1}$$

is calculated, where the $g$-factor of the electron $g_\mathrm{e}$, and the proton-to-electron mass ratio $m_\mathrm{p}/m_\mathrm{e}$ are known at a level of $< 0.001$ ppb [11] and $< 1$ ppb [12], respectively. The theoretical correction terms $g_\mathrm{p}/g_\mathrm{p}(\mathrm{H})$ and $g_\mathrm{e}(\mathrm{H})/g_\mathrm{e}$ are reviewed in [13, 14] and are also known at the sub-ppb level, resulting in [15]

$$g_\mathrm{p} = 5.585\,694\,706(56) \ , \tag{1.2}$$

which is limited by the experimental precision achieved in the hydrogen-maser experiment [10].

All experiments mentioned above are performed with many particles, mostly at "high" energy. The precision achieved by the molecular beam experiments is limited by the magnetic field homogeneity of the apparatus [6], thermal line broadening and velocity broadening. Nuclear magnetic resonance experiments [7, 8] are performed with solids and liquids, and are thus limited by the knowledge of Van der Vaals interaction-shifts and -broadening caused by the specific matrix. In case of the maser experiments, the well-known "wall shift", which is due to the interaction of the atoms with the maser-cavity, limits the precision [16].

The experiment presented in this thesis is based on the "double-Penning trap" method [17]. It aims at measuring the $g$-factor of one single, isolated proton stored in a cryogenic Penning trap [18, 19, 20]. In such a system, one individual particle can be trapped and observed for arbitrarily long time. Furthermore, the motional energy $E_k$ of the trapped charged particle can be cooled below $100\,\mu$eV or, expressed in temperature $T = E_k/k_B$, where $k_B$ is the Boltzmann constant, below 1 K. Unlike in the experiments described above, there are no additional particles involved. By means of "perfectly homogeneous" static electric- and magnetic fields, the proton's motion is constrained to a tiny volume of typically $< 100\,\mu\text{m}^3$. Thus, the experiment is exceptionally "clean" in the sense that corrections due to many-particle interaction, thermal line-broadening, corrections due to interactions with the apparatus, or proton size and proton structure do not enter. In the long term, and with the techniques presented in this thesis, it should be possible to improve the accuracy of the proton $g$-factor by one order of magnitude, at least.

The experiment is based on the continuous Stern-Gerlach effect, which was introduced in 1973 by H. G. Dehmelt and Ekström [21]. This elegant scheme for the non-destructive determination of the spin direction of a trapped charged particle has been used with great success in measurements of the $g$-factor of the electron [11], the positron [22], and the electron bound to the hydrogen-like ions $C^{5+}$ [23, 24] and $O^{7+}$ [25], respectively. Currently, another experiment is set up at the University of Mainz [20, 26], aiming at a $g$-factor measurement of the electron bound to hydrogen-like silicon, which recently allowed to perform the most stringent test of bound-state quantum electrodynamics [27]. All these experiments dealt with magnetic moments on the level of the *Bohr magneton*. A measurement of the magnetic moment of the proton is much more challenging, because it is on the level of the *nuclear magneton*, which is 659 times smaller. Actually, the continuous Stern-Gerlach effect is sensitive to $\Upsilon_i = \mu_i/(m_i\omega_{z,i})$, where $\omega_z$ is the axial eigenfrequency of the trapped charged particle. Comparing this figure of merit $\Upsilon$ for the electron and the proton, the ratio $\Upsilon_p/\Upsilon_e$ is approximately $10^{-4}$, illustrating the outstanding experimental challenge of the "proton experiment".

Since this technique is "clean" and requires only one single trapped particle, another promising perspective opens up - a new ultra high-precision test of the matter-antimatter sym-

metry, also known as $CPT$-symmetry [28]. $C$ stands for charge conjugation, $P$ for parity transformation and $T$ for time-reversal. The unique features of a cryogenic Penning trap apparatus allow for stable storage of a single antiproton as well [29]. Thus, applying the techniques developed for the proton to the antiproton $\bar{p}$, a direct comparison of the $g$-factors of both particles would be possible. This is one of the major motivations of our experiment. Besides our group, a competing group located at Harvard University aims at the same measurement [30]. Presently, the $g$-factor $g_{\bar{\mathrm{p}}}$ of the antiproton is known at a level of $10^{-3}$ only [31, 32]. Achieving the aimed precision of $10^{-9}$ and transferring the techniques to the antiproton, an improvement by six orders of magnitude in $g_{\bar{\mathrm{p}}}$ is possible.

For the high-precision $g$-factor measurement of the proton and the antiproton, the non-destructive detection of spin flips by means of the continuous Stern-Gerlach effect is most important. In this thesis, the very first observation of spin flips with a single trapped proton is accomplished [33], being the major breakthrough towards the challenge of the new high-precision $CPT$-test.

This thesis is organized as follows:

In chapter 2 the theoretical basics of the experiment are described, including a detailed description of the Penning trap, the continuous Stern-Gerlach effect and the lineshape of the $g$-factor resonance curve. Chapter 3 describes the cryogenic Penning trap apparatus. Furthermore useful technical hints for the setup of such a double Penning trap experiment are given. Besides the Penning traps, superconducting high-performance detection systems with single particle sensitivity built the heart of the experiment. In chapter 4 the design and setup of these detection systems are depicted. Having assembled all the required experimental ingredients, in chapter 5, the preparation and detection of one single proton is demonstrated.

In chapter 6, results of experiments with one single proton stored in the homogeneous "precision trap" are presented. Frequency measurements with a resolution of $\Delta\nu/\nu = 3{\cdot}10^{-9}$ are demonstrated and current experimental limitations are discussed. Besides these fundamental techniques, systematic experimental studies are described, including a new characterization scheme for Penning trap imperfections, the observation of "classical Rabi oscillations",

a novel detection scheme for the simultaneous measurement of *all* eigenfrequencies of a trapped proton stored in a Penning trap, and phase-sensitive detection of the axial motion of the proton. The resolution of a frequency change of 200 mHz out of 680 kHz in 1 s is achieved.

In order to achieve non-destructive spin flip resolution with one single trapped proton by means of the continuous Stern-Gerlach effect, a very large magnetic field inhomogeneity of $3 \cdot 10^5\,\mathrm{T/m^2}$ is superimposed to one of our Penning traps - the "analysis trap". This is the largest magnetic field inhomogeneity which has ever been superimposed to a Penning trap. In chapter 7, the experimentally challenging optimization of that trap is described and finally, single particle resolution in that large magnetic field inhomogeneity is demonstrated. Chapter 8 is the highlight of this thesis. There, the very first spin flips ever observed with a single trapped proton are presented. Finally, the thesis is closed with a conclusion (chapter 9).

To any reader of this thesis I wish at least half the pleasure we[1] have had in the laboratory producing these results!

[1] including my colleagues C. C. Rodegheri, H. Kracke and A. Mooser

# Chapter 2

# THEORETICAL BASICS

## *2.1 The Ideal Penning Trap*

The Earnshaw-theorem [34] describes the impossibility of stable storage of charged particles in purely static electric or magnetic fields $\vec{E}$ and $\vec{B}$, respectively. Nowadays, it can be understood as a direct consequence of Maxwell's equations [35] which state, that in divergence-free space only saddle-points exist. Nevertheless, superpositions of electric and magnetic fields were found, which are suitable for stable storage of charged particles. In 1949 Pierce described an *electron trap* consisting of a homogeneous magnetic field in the axial direction $\vec{B} = B_0\vec{e}_z$ and a superimposed quadrupolar electrostatic potential [36]. Hans G. Dehmelt who received the Nobel Prize "for the development of the ion trap technique" in 1989 named this special superposition of electrostatic and magnetostatic fields "the Penning trap". It is the central tool used in our experiment. The Lorentz-force

$$\vec{F} = q\left(\vec{E} + \vec{v} \times \vec{B}\right) \tag{2.1}$$

acting on a charged particle with charge $q$ and velocity $\vec{v}$ due to a homogeneous magnetic field $\vec{B} = B_0\vec{e}_z$ constrains the particle to a circular orbit perpendicular to the magnetic field lines, leading to the periodic cyclotron motion with the so-called "free cyclotron frequency"

$$\omega_c = \frac{q}{m}B \ . \tag{2.2}$$

Superimposing $\vec{B}$ with an electrostatic quadrupolar potential

$$V(\rho, z) = V_0 C_2 \left(z^2 - \frac{\rho^2}{2}\right) \Leftrightarrow \vec{E}(\rho, z) = 2V_0 C_2 \left(z\vec{e}_z - \frac{\rho}{2}\vec{e}_\rho\right) \ , \tag{2.3}$$

provides stable storage of the particle in the axial direction $\vec{e}_z$. The corresponding eigenfrequency, the *axial frequency* $\omega_z$ is given by

$$\omega_z = \sqrt{\frac{2qC_2V_0}{m}} \ . \tag{2.4}$$

$V_0$ is the strength of the trapping voltage and $C_2$ a specific coefficient characterizing the typical geometrical length scale of the quadrupolar potential. Solving the full equations of

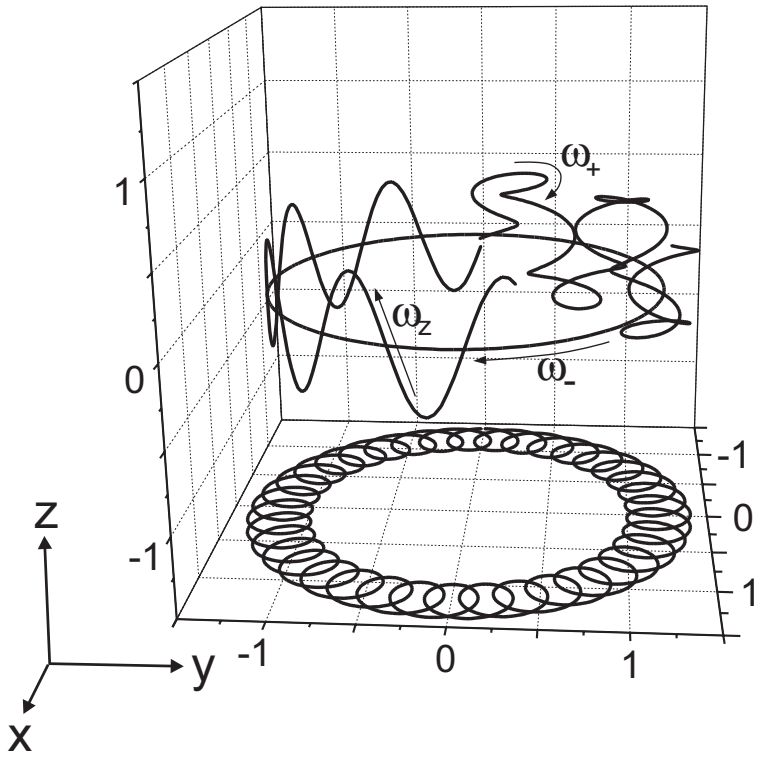


Figure 2.1: Particle trajectories in a Penning trap. The fast cyclotron motion with $\omega_+$ is indicated by the small circles. The large circle represents the magnetron motion with frequency $\omega_-$. Both motions are superimposed by the axial oscillation with $\omega_z$.

motion of such a field configuration [37] leads to a modification of the free cyclotron motion, which is caused by the radial field component of the electrostatic quadrupolar potential. The eigenfrequency $\omega_+$ of this *modified cyclotron motion* is [1]

$$\omega_+ = \frac{1}{2}\left(\omega_c + \sqrt{\omega_c^2 - 2\omega_z^2}\right) \ . \tag{2.5}$$

Furthermore, a third eigenmotion, termed *magnetron motion*, occurs at a frequency

$$\omega_- = \frac{1}{2}\left(\omega_c - \sqrt{\omega_c^2 - 2\omega_z^2}\right) \ . \tag{2.6}$$

[1] In the following the modified cyclotron frequency will be called cyclotron frequency. If we talk about $\omega_c$ we will explicitly write "free cyclotron frequency".

This motion is equivalent to the $\vec{E} \times \vec{B}$-drift in a circular Wien filter

$$v = \frac{E}{B} = \frac{2V_0 C_2 \rho}{2B} \Leftrightarrow \omega_- = \frac{V_0 C_2}{B} \ . \tag{2.7}$$

In first order approximation, the magnetron frequency only depends on the electromagnetic fields, and not on the properties of the charged particle. Penning traps are typically operated in a regime, where the frequency hierarchy $\omega_+ \gg \omega_z \gg \omega_-$ is given.

The three eigenfrequencies are linked via the relation

$$\omega_- = \frac{\omega_z^2}{2\omega_+} \ . \tag{2.8}$$

To get an idea of what the trajectories in the trap look like, an example is shown in Fig. 2.1. The fast cyclotron motion with the frequency $\omega_+$ is indicated by the small circles. The large circle represents the magnetron motion with the frequency $\omega_-$. Both motions are superimposed by the axial oscillation with the frequency $\omega_z$.

The Penning trap provides stable particle storage over a wide range of experimental conditions. Nevertheless, if the radially pulling force due to the electrostatic quadrupole field exceeds the capability of the magnetic field to hold the particle on its circular orbit, the particle's motion becomes unstable. This means mathematically that the discriminant of Eq. (2.5) becomes negative leading to the stability criterion $\omega_c > \sqrt{2}\omega_z$ or, expressed in field strength and particle properties,

$$\frac{q}{m} B > \sqrt{2} \sqrt{\frac{2qC_2V_0}{m}} \Leftrightarrow \sqrt{\frac{q}{m}} > 2\sqrt{\frac{C_2V_0}{B^2}} \ . \tag{2.9}$$

The most interesting properties of the Penning trap are relations between the free cyclotron frequency $\omega_c$ and the eigenfrequencies of the trapped particle $\omega_+, \omega_-$ and $\omega_z$

$$\omega_c = \omega_+ + \omega_- \tag{2.10}$$

$$\omega_c = \sqrt{\omega_+^2 + \omega_-^2 + \omega_z^2} \ . \tag{2.11}$$

The first relation only holds for ideal Penning traps, where the second relation is more robust and is also valid in presence of specific trap errors [38][2]. These relations combine

[2] L. S. Brown and G. Gabrielse discovered this relation. Nowadays in Penning trap physics it is known as "invariance theorem".

the experimentally accessible quantities $\omega_+, \omega_-$ and $\omega_z$ with the fundamental properties charge $q$ and mass $m$ of the trapped particles, making the Penning trap a strong tool for fundamental research!

Since in the ideal Penning trap each eigenmotion is completely decoupled from the other

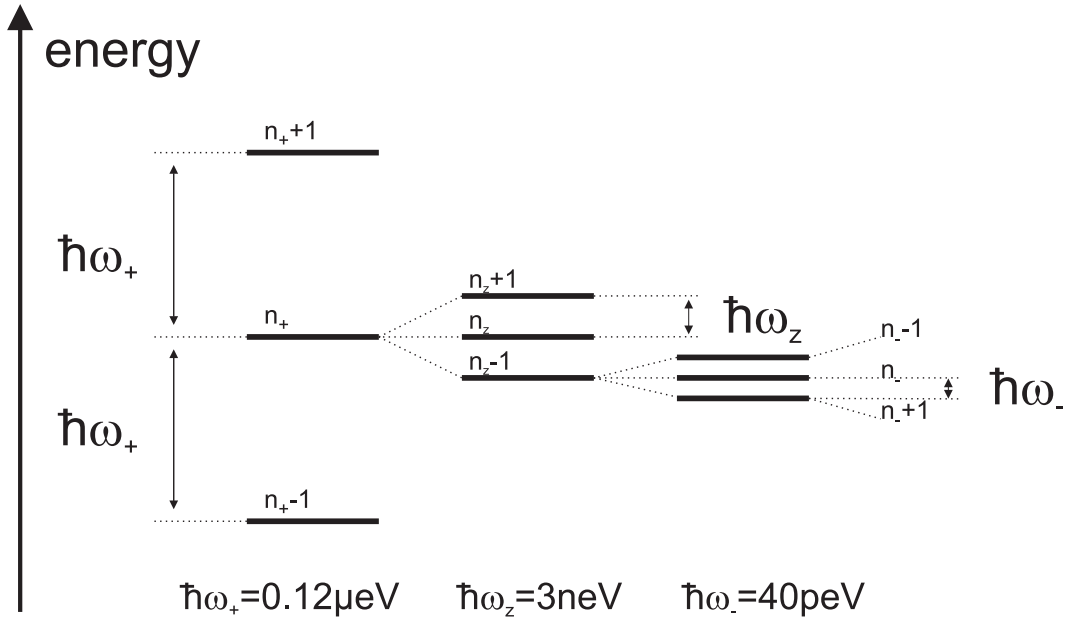


Figure 2.2: Schematic of the energy levels of a charged particle stored in a Penning trap. The distances between the levels of the different modes are not to scale.

modes, the Hamiltonian describing a single spinless particle in the trap can be expressed as a sum [39]

$$H = \hbar\omega_+ \left(n_+ + \frac{1}{2}\right) + \hbar\omega_z \left(n_z + \frac{1}{2}\right) - \hbar\omega_- \left(n_- + \frac{1}{2}\right) \ , \tag{2.12}$$

where $n_+, n_-$ and $n_z$ describe the number of quanta in the respective mode. In Fig. 2.2 an energy-level scheme of the Penning trap is shown and the typical energies, which correspond to a quantum jump in the respective mode, are displayed for the parameters of our precision trap which is operated at a magnetic field of $\approx 1.90\,\mathrm{T}$. Note that an increase of the magnetron quantum number lowers the energy of the particle. This can be understood if the total

energy $E_-$ in the magnetron mode is considered

$$E_- = \frac{1}{2}m\omega_-^2\rho_-^2 - \frac{1}{4}m\omega_z^2\rho_-^2 \ . \tag{2.13}$$

The first term on the right hand side is the kinetic, and the last term the potential energy in the quadrupolar electrostatic potential. Since $\omega_-^2/\omega_z^2 \ll 1$, the magnetron energy is approximately of purely potential nature with respect to the negatively biased ring electrode. Thus, an increase of magnetron radius (increase of the quantum number $n_-$) leads to a decrease of the total energy. Therefore, the magnetron mode is "metastable".
If the mode is decoupled from loss-sources, the only energy loss mechanism is radiation cooling, leading to a typical cooling time constant of [37]

$$\gamma_- = \frac{2q^2}{3mc^3}\omega_-^2 \Leftrightarrow \tau_- = 2 \cdot 10^9\,\mathrm{yr} \tag{2.14}$$

and is thus negligible. To be clear in the following discussions, the magnetron energy is denoted as $-|E_-|$.

### *2.2 Determination of the* g*-Factor*

Besides the charge $q$ and the mass $m$, the $g$-factor is the dimensionless proportionality constant which links the spin $\vec{S}$ of a particle to its magnetic moment $\vec{\mu}_s$

$$\vec{\mu}_s = g\frac{q}{2m}\vec{S} \ . \tag{2.15}$$

In the presence of a magnetic field $B_z$ the spin energy is $E_s = -\vec{\mu_s}\cdot B_z$. Since the proton with its mass $m_p$ is a spin-$\frac{1}{2}$ system, two energy levels occur $E_z = \pm g\frac{q}{2m_p}\frac{\hbar}{2}B_z$ with the energy difference $\Delta E_s = g\frac{e\hbar}{2m_p}B_z$. This difference can be associated with the precession frequency of the spin in a magnetic field, the Larmor frequency $\omega_L = g\frac{q}{2m_p}B_z$. The $g$-factor can thus be determined by a measurement of the Larmor frequency $\omega_L$ and the magnetic field $B_z$. As described above, knowing the charge-to-mass ratio $q/m_p$, a magnetic field measurement is equivalent to the determination of the free cyclotron frequency $\omega_c$. Therefore, the $g$-factor determination simply reduces to the measurement of two frequencies

$$g = 2\frac{\omega_L}{\omega_c} \ . \tag{2.16}$$

The measurement of the cyclotron frequency is straight forward by measuring the eigenfrequencies $\omega_{+,z,-}$ and applying the "invariance theorem" given in Eq. (2.11). For the Larmor frequency measurement the continuous Stern-Gerlach effect [21] is applied, which will be described in detail in section 2.4.

### *2.3 The Real Penning Trap*

Up to now we talked about abstract field configurations and potentials. Experimentally the Penning trap is a stack of gold-plated copper electrodes mounted in the field of a superconducting magnet. A five-pole Penning trap with cylindrical geometry is shown in Fig. 2.3, the direction of the magnetic field is indicated by the black arrow. The electrodes are electrically separated with insulating sapphire rings. The aim for the experimental

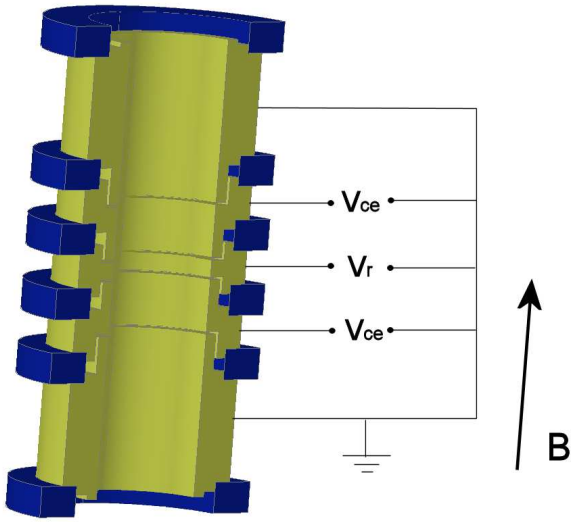


Figure 2.3: Cylindrical Penning trap. Typically, the copper-made electrodes are electrically separated with insulating material as alumina or sapphire. The magnetic field direction is indicated by the black arrow. It is oriented in direction of the symmetry-axis of the cylindrical electrodes.

setup is to fit the theoretical requirements described in section 2.1 as perfectly as possible. Compared to the ideal theoretical formulas presented in section 2.1, a real experimental Penning trap setup shows deviations from the theoretical optimum. In case of the Penning

trap the following errors typically occur:

1. Misalignment between trap axis and magnetic field axis,

2. elliptical corrections of the electrostatic potentials,

3. imperfect quadrupolar potential due to higher order multipolar corrections, and

4. inhomogeneities of the magnetic field.

It is shown in [38], that Eq. (2.11) is not sensitive on the first two points mentioned in the upper list. The effects 3. and 4. will be discussed in the next sections.

### *2.3.1 Trapping Potential*

The electrostatic quadrupolar potential produced by the electrodes should be as ideal as possible, and a magnet with high field-homogeneity should be used. For the production of the quadrupolar potential, in most Penning trap experiments hyperbolic or cylindrical Penning traps are used. The surface of the hyperbolic Penning trap "reproduces" the shape of the quadrupolar potential. It has been shown [40] that for certain ratios of the inner lengths an electrode geometry consisting of stacked cylindrical rings is also suited to produce a nearly perfect quadrupolar potential near the center of the trap. The resulting geometry consists of a stack of five cylindrical rings, the central *ring electrode* with length $l_r$ two neighboring *correction electrodes* with length $l_{ce}$, and two *endcaps* with length $l_{\mathrm{ec}}$. The radius of the trap is $a$. Choosing adequate lengths and length-to-radius ratios, the Penning trap can be designed in "compensated", "orthogonal" design.

1. "Compensation" means that the first higher order corrections $C_4$ and $C_6$ of the multipolar potential expansion can be tuned to zero simultaneously.

2. "Orthogonality" means that the resonance frequency of the particle is independent of the voltage applied to the correction electrodes.

The calculation of the trapping potential of such an electrode geometry is straight forward potential theory. The trapping potential is given by the solution of the cylindrical Laplace equation

$$\nabla^2\Phi\left(\rho,z\right)=\frac{1}{\rho}\frac{\partial}{\partial\rho}\left(\rho\frac{\partial}{\partial\rho}\Phi\left(\rho,z\right)\right)+\frac{\partial^2}{\partial z^2}\Phi\left(\rho,z\right)=0\ , \tag{2.17}$$

which has to be found for Dirichlet boundary conditions $\Phi\left(a,z\right)=V$. $V$ is the voltage applied to the respective electrode. Since the Laplace equation does not show terms of mixed derivatives it is uncoupled and a separation-ansatz $\Phi\left(\rho,z\right)=R(\rho)Z(z)$ can be chosen to solve the linear partial differential equation, leading to two independent ordinary differential equations

$$\frac{1}{\rho}\frac{d}{d\rho}\left(\rho\frac{d}{d\rho}R\left(\rho\right)\right)-k^2R\left(\rho\right)=0 \tag{2.18}$$

and

$$\frac{d^2}{dz^2}Z\left(z\right)+k^2Z\left(z\right)=0\ , \tag{2.19}$$

where $k$ is a separation constant. Both equations are discussed in the mathematical literature [41]. The solution of Eq. (2.18) are modified Bessel-functions $I_k(\rho)$, while Eq. (2.19) is solved by trigonometric functions, leading to the solution

$$\Phi\left(\rho,z\right)=\sum_{n=-\infty}^{\infty}I_0(k_n\rho)\left(A\left(k_n\right)\sin\left(k_nz\right)\right)\ , \tag{2.20}$$

where $k_n=\frac{n\pi}{\Lambda}$, $n\in\mathrm{IN}$. $\Lambda$ is the total length of the trap. The coefficients $A\left(k_n\right)$ are defined by the Dirichlet boundary conditions and can be calculated by simple integration giving the total potential of $p$ stacked electrodes:

$$\begin{aligned}\Phi\left(\rho,z\right) &= \frac{2}{\Lambda}\sum_{n=1}^{\infty}\left[\frac{V_1\cos(k_nz_0)-V_p\cos(k_n\Lambda)}{k_n}+\sum_{i=2}^{p}\frac{V_i-V_{i-1}}{k_n^2d}\left(\sin(k_nz_{2i})-\sin(k_nz_{2i-1})\right)\right]\\ &\times\ \frac{I_0(k_n\rho)}{I_0(k_na)}\sin(k_nz)\end{aligned} \tag{2.21}$$

where $d$ is the spacing between two adjacent electrodes, $z_{2i}$ the axial start coordinate of electrode $i$ and $z_{2i-1}$ the stop coordinate of electrode $i-1$. For the five pole Penning trap

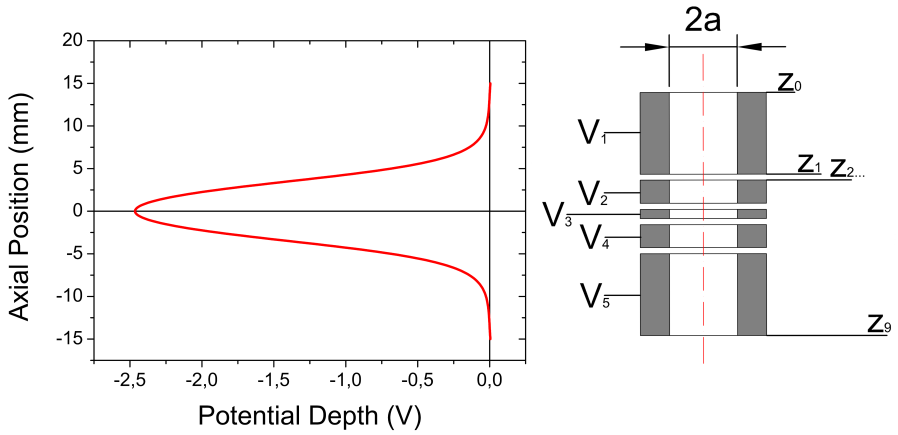


Figure 2.4: Trap potential in the axial direction together with a schematic of the cylindrical electrodes of a five-pole Penning trap. The figure defines the variables used in Eq. (2.22) graphically.

this expression can be simplified to

$$\begin{aligned}\Phi(\rho,z,V_i) &= \frac{2}{\Lambda}\sum_{n=1}^{\infty}\left[\frac{V_1\cos(k_n z_0)-V_5\cos(k_n\Lambda)}{k_n}+\sum_{i=2}^{5}\frac{V_i-V_{i-1}}{k_n^2 d}\left(\sin(k_n z_{2i})-\sin(k_n z_{2i-1})\right)\right] \\ &\times \frac{I_0(k_n\rho)}{I_0(k_n a)}\sin\left(k_n\left(z+\frac{\Lambda}{2}\right)\right)\ . \end{aligned} \tag{2.22}$$

For the definition of the variables used in the formula, see Fig. 2.4. Note, that due to the product structure of the solution $I_0(k_n\rho)\sin\left(k_n\left(z+\frac{\Lambda}{2}\right)\right)$, the radial behavior of the potential is already defined by the knowledge of the potential along the $z$-axis. The result of the electrostatic potential on the z-axis of the trap, which is obtained by Eq. (2.22), is shown in Fig. 2.4, together with the stacked electrodes of a five-pole cylindrical Penning trap.

In [42] a very similar ansatz for the solution of the electrostatic potential of a cylindrical Penning trap is presented, which accounts for the point mirror symmetry of the trap with respect to $(0,0,0)$. There, using symmetry arguments, a much simpler expression as Eq. (2.22) is derived, which is mathematically elegant and easy to handle. But due to the reduction by using symmetry arguments, the discussion of trap asymmetries caused by the real experimental constraints, is not possible anymore. It will be shown in chapter 6, that a detailed understanding of trap asymmetries based on potential theory is an important

experimental tool.

To obtain a clearer picture of the meaning of Eq. (2.22), it is convenient to expand this solution in powers of the coordinates $z^j$

$$\Phi(0,z) = V_0 \sum_{j=0}^{n} C_j z^j \tag{2.23}$$

where the potential coefficients $C_j$ are defined by

$$\begin{aligned} C_j &= \frac{1}{j!\Lambda V_0} \sum_{n=1}^{\infty} \left[ \frac{V_1 \cos(k_n z_0) - V_5 \cos(k_n \Lambda)}{k_n} + \sum_{i=2}^{5} \frac{V_i - V_{i-1}}{k_n^2 d} \left(\sin(k_n z_{2i}) - \sin(k_n z_{2i-1})\right) \right] \\ &\times \frac{(n\pi/\Lambda)^j}{I_0(k_n a)} \sin(\frac{\pi}{2}(n+j)) \ . \end{aligned} \tag{2.24}$$

To obtain this result, Eq. (2.22) was normalized to the voltage $V_0$ which is applied to the ring electrode.

For the further discussion, the ***tuning ratio*** $\mathrm{TR} = V_{ce}/V_0$ is defined, being the ratio of the voltages $V_2 = V_4 = V_{ce}$ which are applied to the correction electrodes, and the voltage $V_0$ which is applied to the ring electrode of the trap. To summarize the properties of Eq. (2.24) briefly:

1. If $V_1 = V_5 = 0$, which is the standard experimental trap operation mode, and symmetric voltages are applied to the correction electrodes $V_2 = V_4 = V_{ce}$, all coefficients $C_j$ can be expressed in the form $C_j = E_j + D_j \cdot \mathrm{TR}$.

2. The coefficients $E_j$ and $D_j$ are defined by the dimensions of the trap electrodes.

3. Important enough to be mentioned again and obvious from the explicit form of the potential: For the design of the electrostatic properties of the trap, the diameter $a$, the length of the central ring electrode $l_r$, and the length of the correction electrodes $l_{ce}$ are three degrees of freedom. These degrees of freedom can be defined in a way, that $D_2$ vanishes (called *orthogonality* and means experimentally that $d\omega_z/d\mathrm{TR} = 0$), and that $C_4$ and $C_6$ simultaneously vanish for a certain tuning ratio (called *compensation*).

The properties described in this enumeration are shown in Fig. 2.5. In plot a.) the axial frequency $\nu_z = \omega_z/2\pi$ is shown as a function of the tuning ratio. With the design value of

the "orthogonality parameter" $D_2$, the slope $d\nu_z/d\mathrm{TR} \approx 12\,\mathrm{mHz{\cdot}mUnit}^{-1}$ is found. Here the new measurement unit "mUnit" was defined, which simply describes a change of the dimensionless tuning ratio by 0.001. For the trap geometries used in our laboratory, this is a typical scale of tuning ratio variation to tune the trap to high harmonicity. Plot b.) shows the simultaneous compensation of the fourth order and sixth order term of the multipolar potential expansion. For a tuning ratio of TR = 0.877 both coefficients simultaneously vanish.

Comparing the expansion Eq.(2.23) to the Legendre-polynomial expansion of the trapping

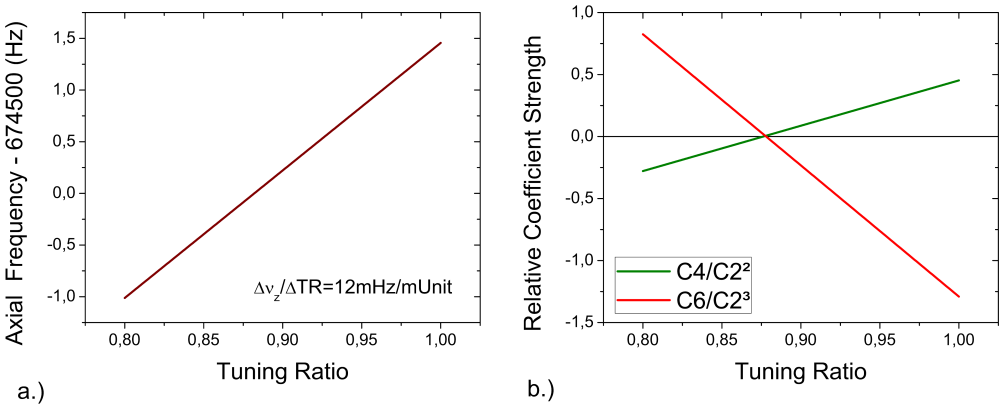


Figure 2.5: a.) Axial frequency $\nu_z$ as a function of the tuning ratio TR, which is defined as the voltage ratio of correction electrode voltage and ring voltage $\mathrm{TR} = V_{ce}/V_0$. b.) Octupolar and hexadecupolar potential coefficent as a function of the tuning ratio $TR$. For compensated trap design both coefficients can be tuned to zero simultaneously.

potential

$$\Phi(r,z) = \frac{V_0}{2}\sum_j \tilde{C}_j \frac{\left(\rho^2+z^2\right)^{j/2}}{d_0^j} P_j\left(\frac{z}{\sqrt{\rho^2+z^2}}\right) \tag{2.25}$$

which is used in the U.S.-literature [37], the coefficient relation

$$C_j = \frac{\tilde{C}_j}{2d_0^j} \tag{2.26}$$

is found, where $d_0$ is defined by the condition $C_2 = 1$. It is important to mention this correspondence, since historically in many papers the effects of potential anharmonicities

are discussed for hyperbolic traps where $d_0$ is an important parameter, and the potential is represented by Eq.(2.25). Combining the potential theory presented in this section and Eq.(2.26), all anharmonic correction effects derived f. e. in [37] can be applied directly to the cylindrical trap.

### *2.3.2 Effects of Electrostatic Anharmonicities*

In this section the physical meaning of the relatively abstract numbers given in the last section are discussed. In other words the question: *Which experimentally observable effects are caused by anharmonicities of the electrostatic potential ?*
should be answered. Therefore the anharmonic electrostatic potential terms are added to the axial equation of motion

$$\ddot{z} = -\frac{e}{m} V_0 \vec{\nabla} \sum_{k=0}^{6} C_k z^k = -\frac{2eC_2}{m} V_0 \left( z + \frac{2C_4}{C_2} z^3 + \frac{3C_6}{C_2} z^5 + \ldots \right) . \tag{2.27}$$

Such nonlinear differential equations are called *Duffing Equations* [43]. Since they are the white mice of nonlinear dynamics and classical perturbation theory, and their treatment can be found in every second chapter of textbooks on chaos and theoretical mechanics [44], only their basic properties should be discussed. For a very detailed discussion of the relevance in Penning traps see [45]. The resonance line shape of a Duffing oscillator is shown in Fig. 2.6 a.). In the presence of nonlinearities $C_4$ and $C_6$ the lineshape is asymmetric. This behavior is due to the scaling of the eigenfrequency with particle energy $E$ and can be derived from Eq. (2.27) replacing the coordinate $z^2$ by the energy $E$. A full calculation for the first two perturbation orders gives the axial frequency dependence as a function of the axial energy $E_z$.

$$\frac{\Delta\omega_z}{\omega_z} = \frac{3}{4} \left( \frac{C_4}{C_2^2} + \frac{5}{4} \frac{C_6}{C_2^3} \left( \frac{E_z}{qV_0} \right) \right) \frac{E_z}{qV_0} . \tag{2.28}$$

For negative $C_4$ the derivative $d\nu_z/dE_z$ is negative and the axial resonance lineshape is tilted towards smaller frequencies, for positive $C_4$ the behavior is the same but with opposite sign. Furthermore, the particle's oscillation amplitude achieved by an rf-excitation is maximal, if the anharmonicities are tuned to zero. Translating this behavior to experimental reality this means, that the trap can be optimized by

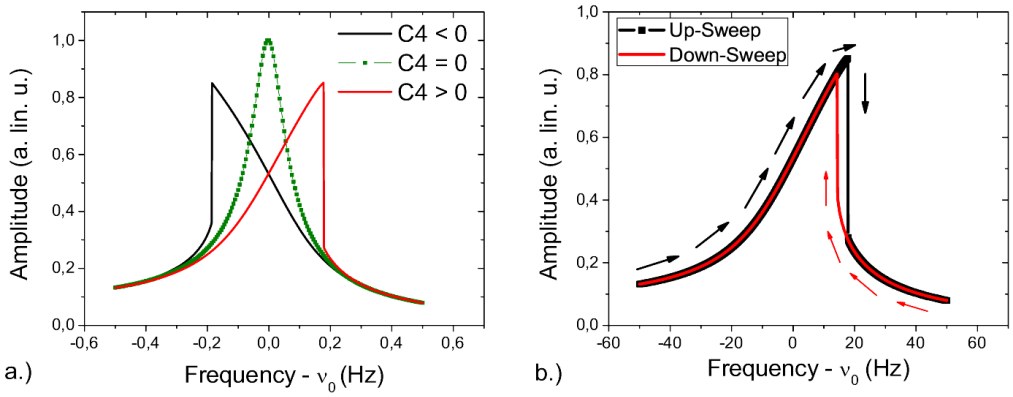


Figure 2.6: a.) Resonance line shape of a driven oscillator in presence of a nonlinearity $\frac{2C_4}{C_2}z^3$ in arbitrary linear units. For $C_4 < 0$ the response to the drive is opened to frequencies $\omega < \omega_0$. If $C_4 > 0$, opposite behavior is observed. Note, that the maximum amplitude is achieved if $C_4 = 0$, which can be used for harmonicity tuning of a real Penning trap. b.) Illustration of the bi-stable response of a nonlinear oscillator in presence of a drive. Hysteresis due to "excitation history" is observed. For details see text.

- ...maximizing the particle signal on the detector if the particle is excited,

- ...minimizing the span of the frequency response if an rf-sweep is applied to the trap.

Both methods are applied in our experiment and discussed experimentally in chapter 7. Another interesting property of the nonlinearities is shown in Fig. 2.6 b.). The response of the particle to an excitation behaves bi-stable and depends on the "excitation-history". In the critical regime, where the resonance line shape obviously has two solutions, the behavior of the system depends on the initial conditions. Starting at a small orbit and exciting the particle with a frequency sweep $\omega + \Delta\omega t$, the system follows the black curve and at a certain frequency, which depends on the magnitude of the anharmonicity, jumps to lower amplitude. Sweeping the system then back with $\omega - \Delta\omega t$ it follows the red line and certainly jumps to a higher amplitude, which is effectively smaller and occurs at lower frequency as in case of the "up-sweep". This hysteresis behavior can be applied to measure the magnitude of the trap anharmonicities [46].

### 2.3.3 Anharmonic Electrostatic Potential and Particle Eigenfrequencies

Using the harmonic balance method, the shifts of the eigenfrequencies which occur due to the anharmonic electrostatic potential can be calculated [39] and for the modified cyclotron frequency are given by

$$\frac{\Delta\omega_+}{\omega_+} = \frac{1}{qV_0}\frac{3C_4}{C_2^2}\left(-\left(\frac{\omega_z}{\omega_+}\right)^4 E_+ + \frac{1}{2}\left(\frac{\omega_z}{\omega_+}\right)^2 E_z - \left(\frac{\omega_z}{\omega_+}\right)^2 |E_-|\right) , \tag{2.29}$$

for the axial frequency

$$\frac{\Delta\omega_z}{\omega_z} = \frac{1}{qV_0}\frac{3C_4}{C_2^2}\left(-\frac{1}{2}\left(\frac{\omega_z}{\omega_+}\right)^2 E_+ + \frac{1}{4}E_z - |E_-|\right) , \tag{2.30}$$

and for the magnetron frequency

$$\frac{\Delta\omega_-}{\omega_-} = \frac{1}{qV_0}\frac{3C_4}{C_2^2}\left(-\left(\frac{\omega_z}{\omega_+}\right) E_+ + E_z - |E_-|\right) . \tag{2.31}$$

In the static limit the Larmor frequency is not affected by electrostatic anharmonicities [3]. The effect of the anharmonicity on the cyclotron frequency is given by

$$\frac{\Delta\omega_c}{\omega_c} = \frac{\omega_+}{\omega_c^2}\Delta\omega_+ + \frac{\omega_z}{\omega_c^2}\Delta\omega_z + \frac{\omega_-}{\omega_c^2}\Delta\omega_- . \tag{2.32}$$

For a properly designed Penning trap the correction $C_4/C_2^2$ can be tuned to $\approx 10^{-5}$ or better. The particle energies during frequency measurements are typically about $300\,\mu$eV (see section 6.6) and thus, the electrostatic effects typically lead to shifts of the cyclotron frequency in the relative order of $10^{-11}$ or smaller. Our experiment aims at a relative precision of $10^{-9}$, therefore corrections caused by the electrostatic potential can be neglected.

### 2.3.4 Inhomogeneous Magnetic Field

In the presence of magnetic field inhomogeneities the eigenfrequencies of the particle become a function of energy as well. This is obvious for the cyclotron frequency $\omega_+$, which is defined by the magnetic field,

$$\omega_+ \approx \frac{e}{m}\left[B_0\vec{e}_z + \sum_k B_k r^k\left(P_k\left(\frac{z}{r}\right)\vec{e}_z + \frac{1}{k+1}P_k^1\left(\frac{z}{r}\right)\vec{e}_\rho\right)\right] \tag{2.33}$$

[3] in the relativistic limit there is indeed a shift of the Larmor frequency due to the electrostatic anharmonicity. The correction term is $\propto v^2/c^2 \approx 2\cdot 10^{-12}$ and can be neglected.

where $r = \sqrt{\rho^2 + z^2}$, $P_k, P_k^1$ are Legendre polynomials, and $B_k$ coefficients of the magnetic multipolar expansion. As shown in Eq. (2.7), the magnetron frequency is $\propto 1/B$, thus, a scaling of $\omega_-$ with magnetic field inhomogeneities is also obvious.

In the presence of a magnetic inhomogeneity the axial frequency $\omega_z$ also depends on the particle energy which is not as obvious as in the case of the radial modes. Due to their angular momentum, the radial modes carry Landau magnetic momenta

$$\mu_{z,\rho} = \mu_{z,+} + \mu_{z,-} = \frac{e}{2m} \left( L_{z,+} + L_{z,-} \right) \ . \tag{2.34}$$

These orbital magnetic momenta are coupled to the magnetic field $B_z$ and lead to a magnetic potential $\Phi_M = -\mu_{z,\rho} B_z$, which adds linearly to the electrostatic potential $\Phi_e$, defined by the voltages applied to the trap. The axial equation of motion in presence of a magnetic field thus becomes

$$\ddot{z} = -\frac{q}{m} \left( \vec{\nabla} \Phi_e | \vec{e}_z \right) - \frac{1}{m} \left( \vec{\nabla} \Phi_M | \vec{e}_z \right) \ . \tag{2.35}$$

If $\Phi_M$ scales $\propto z^k$ where $k > 1$, the axial frequency obviously scales proportional to powers of the radial energies.

The most important magnetic field perturbation is the second-order term

$$\vec{B}(z, \rho) = B_0 \vec{e}_z + B_2 \left( \left( z^2 - \frac{\rho^2}{2} \right) \vec{e}_z - \rho z \vec{e}_\rho \right) \ , \tag{2.36}$$

which will be called "magnetic bottle" in the following[4]. The cyclotron frequency $\omega_+$ shifts in presence of $B_2$

$$\Delta\omega_+ = \frac{\omega_+}{m\omega_z^2} \frac{B_2}{B_0} \left( -\frac{\omega_z^2}{\omega_+^2} E_+ + E_z - 2|E_-| \right) \ . \tag{2.37}$$

The scaling of $\Delta\omega_+$ with the radial energies $E_+$ and $|E_-|$ is obvious, since in the magnetic bottle the axial component of the magnetic field decreases with increasing radius. The scaling $\propto E_z$ is caused by the increase of $B_z$ with the axial coordinate $z$. The axial oscillation of the particle leads to a positive shift of the magnetic field seen by the particle since

$$\langle B_2 z(t)^2 \rangle = \langle B_2 z_0^2 \cos^2(\omega_z t) \rangle = \frac{B_2 z_0^2}{2} = \frac{B_2 E_z}{m\omega_z^2} \ . \tag{2.38}$$

[4] Actually, the term "magnetic bottle" is more general. All magnetic field inhomogeneities with a field-minimum at $z_0$ and larger fields $B(z_0 \pm \Delta z)$ are called "magnetic bottles". The term is not specially correlated to the quadratic scaling with the axial coordinate $z^2$. Nevertheless, since in our lab-language $B_2$ is called "magnetic bottle", this term will be used in the following

The shift of the Larmor frequency is

$$\Delta\omega_L = \frac{\omega_L^2}{\omega_+}\frac{\Delta\omega_+}{\omega_+} \ . \tag{2.39}$$

The arguments are the same as for the modified cyclotron frequency. For the modification of the magnetron frequency,

$$\Delta\omega_- = \frac{\omega_-}{m\omega_z^2}\frac{B_2}{B_0}\left(2E_+ - E_z + 2|E_-|\right) \tag{2.40}$$

is found. Again the arguments are the same as for the cyclotron frequency.

To discuss the axial frequency shifts, Eq. (2.36) has to be inserted into Eq. (2.35) yielding

$$\Delta\omega_z = \frac{1}{m\omega_z}\frac{B_2}{B_0}\left(E_+ + |E_-|\right) \ . \tag{2.41}$$

The coupling of the axial component of radial angular momentum to the axial frequency in presence of a magnetic bottle $B_2$ is the most important physical effect applied in our experiment, and will be discussed in the following section.

### *2.4 Continuous Stern-Gerlach Effect and Measurement of the Larmor Frequency*

The superposition of a magnetic bottle $B_2$ to a Penning trap, can be utilized to nondestructively determine the quantum number of the particle spin by measuring the axial frequency. As well as in case of the Landau magnetic momenta (Eq. (2.41)), the spin magnetic moment (Eq. (2.15)) is coupled to the axial frequency as well. Inserting this magnetic moment into Eq. (2.35) leads to the axial frequency

$$\omega_z^2 = \omega_{z,0}^2\left(1 + \frac{2\mu_s B_2}{m_p\omega_z^2}\right) \ . \tag{2.42}$$

Since the second term in the brackets is small compared to 1, it is sufficient to expanded this expression to first order

$$\omega_z \approx \omega_{z,0}\left(1 + \frac{\mu_s B_2}{m_p\omega_z^2}\right) = \omega_{z,0}\left(1 + g\frac{q m_s \hbar B_2}{m_p\omega_z^2}\right) \ , \tag{2.43}$$

where $m_s = \pm\frac{1}{2}$ is the spin quantum number. Therefore, a spin transition $\delta m_s = \pm 1$ leads to an axial frequency shift of

$$\Delta\omega_{\mathrm{z,SF}} = \frac{2\mu_s B_2}{m_p\omega_z} = g\frac{q\hbar B_2}{m_p\omega_z} \ . \tag{2.44}$$

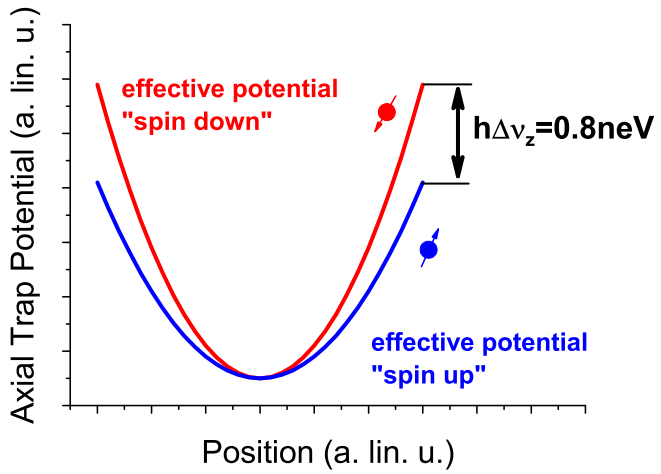


Figure 2.7: Illustration of the continuous Stern-Gerlach effect. Due to the coupling of the particle spin to the magnetic bottle, the axial frequency depends on the direction of the particle spin. For the parameters of our experiment, a spin transition causes $\Delta\nu_z = 191\,\mathrm{mHz}$ corresponding to 0.8 neV.

This principle is graphically shown in Fig. 2.7. This dependence can be applied to measure the Larmor frequency $\omega_L = \frac{g}{2}\frac{q}{m}B$, and thus, to determine the proton $g$-factor. The axial frequency is measured permanently and spin flips are driven by the well-known Rabi resonance principle [50]. When the spin flips, the axial frequency immediately changes by $\pm\Delta\omega_{\mathrm{z,SF}}$. The spin-flip probability $P_{\mathrm{SF}}$ can be measured as a function of frequency by tuning the radio frequency (rf) $\omega_{\mathrm{rf}}$ of the drive over the Larmor frequency $\omega_L$. The resulting curve $P_{\mathrm{SF}}(\omega_{\mathrm{rf}})$ has a maximum at the Larmor frequency of the single trapped proton.

This measuring principle was introduced by Dehmelt and Eckström [**?**] and called "Continuous Stern-Gerlach Effect". It was applied in several experiments to measure $g$-factors, as the $g$-factor of the electron [11], the positron [22] and that of the electron bound to highly charged ions [23, 24, 25].

In all these experiments magnetic moments at the level of the *Bohr magneton* were measured. A measurement of the magnetic moment of the proton or any other nuclear magnetic moment by the continuous Stern-Gerlach effect has up to now never been realized. To un-

derstand the reason, it has to be realized that the axial frequency shift which is caused by a spin flip $\Delta\omega_{z,\mathrm{SF}}$ depends on the ratio $\mu_s/(m_p\omega_z)$, which is in case of the proton approximately ten thousand times smaller compared to the electron. Obviously, the application of Dehmelt's method to measure the magnetic moment of the proton is an extremely challenging task.

Equation (2.44) has only two degrees of freedom, the value of the magnetic bottle strength

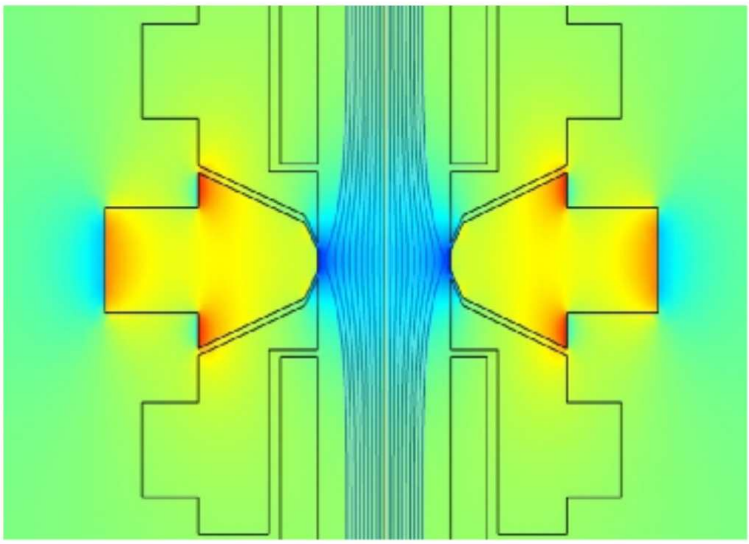

Figure 2.8: Magnetic field lines in the analysis trap of our experiment. The ferromagnetic ring electrode distorts the field lines to a large inhomogeneity $\vec{B}(z,\rho) = B_0\vec{e}_z + B_2\left((z^2-\rho^2/2)\,\vec{e}_z - z\rho\vec{e}_\rho\right)$. Such a magnetic field configuration is called "magnetic bottle". The color code indicates the absolute magnetic field strength and scales linearly from $B = 1.1\,\mathrm{T}$ (light blue) in the center of the "magnetic bottle" to $B = 4.5\,\mathrm{T}$ (dark red) at the edges of the ring electrode. The average background field is $B = 1.9\,\mathrm{T}$.

$B_2$ and the axial frequency $\omega_z$. Therefore, a Penning trap with a very strong superimposed magnetic bottle term $B_2 = 300000\,\mathrm{T/m^2}$ was designed. To translate this number to reality: This means that if the particle is shifted by $\approx 1.5\,\mathrm{mm}$ from the center of the inhomogeneity, the magnetic field changes by an amount of $1\,\mathrm{T}$ [5]. This is the strongest magnetic field inhomogeneity, which has ever been superimposed to a Penning trap. In [24] a $B_2$ term which is

[5] Detailed design-studies are presented in the PhD thesis of C. C. Rodegheri [47]

a factor of 30 smaller is used while in the free-electron experiments $B_2$ is even a factor of 200 smaller [22] compared to our value. A competing experiment located at Harvard University [30] also aims at measuring the $g$-factor of the proton. In that experiment a magnetic bottle of $B_2 = 78000\,\mathrm{T/m^2}$ is superimposed to the trap, which is still a factor of 3.8 smaller than ours. In Fig. 2.8 the design of this trap and the magnetic field lines are shown. In order to obtain such a large $B_2$ term, the cylindrical trap has an inner radius of only 1.8 mm leading to a large electrostatic trap coefficient $C_2 \approx 120000\,\mathrm{mm^{-2}}$. The trap is operated at a biasing voltage of $V_0 \approx -0.85\,\mathrm{V}$ leading to an axial frequency of $\omega_z/2\pi \approx 680\,\mathrm{kHz}$. At these conditions, the axial frequency-jump due to a spin flip is $\Delta\omega_{z,\mathrm{SF}}/2\pi = 191\,\mathrm{mHz}$, corresponding to a relative frequency change of about 0.3 ppm, and a tiny energy shift of only 0.8 neV.

## *2.5 Magnetic Bottle - Quantum Picture*

In the previous sections it was explained, that the magnetic bottle $B_2$ couples the radial energy as well as the spin energy to the axial frequency $\nu_z$. The energy dependent shifts of the axial eigenfrequency can be expressed in terms of the radial quantum numbers $n_+$ and $n_-$, and the spin quantum number $m_s = \pm\frac{1}{2}$

$$\begin{aligned}\Delta\nu_z(n_+, n_-, m_s) &= \\ \frac{h\nu_+}{4\pi^2 m_\mathrm{p}\nu_z}\frac{B_2}{B_0} &\cdot \left(n_+ + \frac{1}{2} + \frac{\nu_-}{\nu_+}\left(n_- + \frac{1}{2}\right) + \frac{g_\mathrm{p} m_s}{2}\right) .\end{aligned} \tag{2.45}$$

A cyclotron quantum jump $\Delta n_+ = \pm 1$ corresponds to a radial energy change of $\Delta E_+ = \pm 74\,\mathrm{neV}$ and causes an axial frequency shift of $\Delta\nu_z = \pm 68\,\mathrm{mHz}$. A change of the magnetron quantum number leads to $\Delta\nu_z = \pm 49\,\mu\mathrm{Hz}$. As already pointed out in the previous section, a spin-flip transition $\Delta m_s = \pm 1$ causes a jump of the axial frequency $\Delta\nu_{\mathrm{z,SF}} = \pm 191\,\mathrm{mHz}$.

## *2.6 Magnetic Bottle Lineshapes and Spin Transition Rates*

### *2.6.1 Lineshape*

As explained in sec. 2.2, the $g$-factor determination reduces to the measurement of the Larmor frequency $\omega_L$ and the free cyclotron frequency $\omega_c$ (see section 2.2). The standard

lineshape of a damped harmonic oscillator is a Lorentz curve. The linewidth is characterized by the damping constant $\gamma_l$. Nonlinearities lead to energy dependent eigenfrequencies modifying the form of the simple Lorentz curve. Furthermore, depending on the typical time scale of the nonlinear dynamics, the lines are broadened. The extraction of the eigenfrequencies from a nonlinear oscillator requires a detailed understanding of the lineshape. In this section the lineshape of the Larmor resonance in presence of a magnetic bottle $B_2$ is discussed.

The physics behind the lineshape is simple. The magnetic field seen by the particle changes on the time scale $\tau_z = 1/\omega_z$ of the axial oscillation. Assume that the amplitude of the axial oscillation is $z_0$, then

$$B(z_0, t) = B_0 + B_2 z_0^2 \sin^2(\omega_z t) \quad , \tag{2.46}$$

which obviously leads to a time dependent Larmor frequency

$$\omega_L = \frac{g}{2}\omega_{c,0}\left(1 + \frac{B_2}{B_0} z_0^2 \sin^2(\omega_z t)\right) = \omega_0\left(1 + \frac{B_2}{B_0} z_0^2 \sin^2(\omega_z t)\right) \ , \tag{2.47}$$

where $\omega_0$ is the Larmor frequency in the center of the trap. The Fourier spectrum of Eq.(2.47) has sidebands $\omega_0 \pm 2\omega_z$. This is discussed in [48], but not of interest for the parameters of the proton experiment [6]. Averaging of Eq. (2.47) gives

$$\omega_L = \omega_0\left(1 + \frac{B_2}{2B_0}\langle z_0^2\rangle\right). \tag{2.48}$$

As will be discussed in detail in chapter 4, the axial motion of the particle is coupled to the thermal heat bath of the axial detection system which has a temperature of $T_z \approx 9.5\,\mathrm{K}$. The coupling constant between the detection system and the particle is $\gamma_z = R_p/m_p \cdot q^2/D^2$ leading to a fluctuation of the particle's axial energy $E_z$ on timescales $\propto 1/\gamma_z$. Due to the equipartition theorem

$$\frac{1}{2}m\omega_z^2\langle z_0^2\rangle = \frac{k_B T_z}{2} \Leftrightarrow \langle z_0^2\rangle = \frac{k_B T_z}{m\omega_z^2} \tag{2.49}$$

[6] Compared to [48] we have lower temperatures and the linewidth of the Larmor resonance of the proton is much smaller compared to the electron.

where $k_B$ is the Boltzmann constant. For typical thermal amplitudes the correction term in Eq. (2.48)

$$\delta\omega_L = \omega_0 \frac{B_2}{B_0}\langle z_0^2\rangle = \omega_0 \frac{B_2}{B_0}\frac{k_B T_z}{m\omega_z^2} \ . \tag{2.50}$$

is

$$\delta\omega_L/2\pi \quad \approx \quad 5.9\,\mathrm{kHz}\cdot\mathrm{K}^{-1} \ . \tag{2.51}$$

In the following $\delta\omega_L$ is called "linewidth parameter".

The coupling of the particle motion to the heat bath of the axial detection system leads to a broadening of the resonance line. The lineshape is derived in a comprehensive paper by L. S. Brown [49] and given by

$$\chi(\omega) = \frac{4}{\pi}\mathrm{Re}\left[\frac{\tilde{\gamma}\gamma_z}{(\tilde{\gamma}+\gamma_z)^2}\sum_n \frac{(\tilde{\gamma}-\gamma_z)^{2n}(\tilde{\gamma}+\gamma_z)^{-2n}}{\left(n+\frac{1}{2}\right)\tilde{\gamma}-\frac{\gamma_z}{2}-i(\omega-\omega_0)}\right] \tag{2.52}$$

where $\tilde{\gamma} = \sqrt{\gamma_z^2 + 4i\gamma_z\delta\omega_L}$. Obviously, Eq. (2.52) is a series of Lorentz curves and the real part of $\tilde{\gamma}$ leads to the linewidth of the Larmor resonance while the complex part of $\tilde{\gamma}$ gives a frequency shift which is due to the fact that the linewidth parameter scales as $z^2$, and the axial oscillation does not average to zero.

The complex lineshape $\chi(\omega)$ simplifies in two limits

1. weak coupling $\delta\omega_L \gg \gamma_z$, and

2. strong coupling $\delta\omega_L \ll \gamma_z$ .

For the parameters of our experiment $\delta\omega_L/\gamma_z = 1350\,/\mathrm{K}\cdot T_z$ (see section 2.7), thus, the first case listed in the enumeration is applicable, and for the discussion of the second case we refer to [49]. In the case of weak coupling, the amplitude of the oscillation remains constant in a time window $\propto 1/\delta\omega_L$. In a sequence of idealized Larmor frequency measurements, the average observable lineshape is a convolution of the unperturbed infinitesimally narrow Lorentz lines with the thermal Boltzmann distribution. Solving the corresponding convolution integral leads to the total lineshape [49]

$$\chi_D(\omega) = \frac{\Theta(\omega-\omega_0)}{\delta\omega_L}\exp\left(-\frac{(\omega-\omega_0)}{\delta\omega_L}\right) \tag{2.53}$$

where $\Theta(\omega - \omega_0)$ is the Heaviside step function. The lineshape is an exponential function starting at a "trigger-point" which is defined by the zero temperature of the Boltzmann distribution. The linewidth is mainly defined by the parameter $\delta\omega_L$. The result Eq. (2.53), which includes the unit step is a consequence of integrating over Dirac-delta functions and does not fit to physical reality. For the condition $\delta\omega_L \gg \gamma_z$ the full lineshape Eq. (2.52) can be transformed to the smoother function

$$\begin{aligned} \chi_S(\omega) &= \frac{1}{\pi\delta\omega_L}\left(\arctan\left(\frac{\gamma_z\left(\omega-\left(\omega_0+\frac{\gamma_z}{2\mathrm{Re}\tilde{\gamma}}\delta\omega_L\right)\right)}{2\mathrm{Re}\tilde{\gamma}}\right)+\frac{\pi}{2}\right) \\ &\cdot \exp\left(-\frac{(\omega-\left(\omega_0+\frac{\gamma_z}{2\mathrm{Re}\tilde{\gamma}}\delta\omega_L\right))}{\delta\omega_L}\right) \end{aligned} \tag{2.54}$$

The derivation of Eq. (2.54) from Eq. (2.52) is mathematically complicated and physically not instructive, thus we just present the validity graphically, which is shown in Fig. 2.9. The filled circles represent the full calculation (Eq. (2.52)) and the red curve is the result

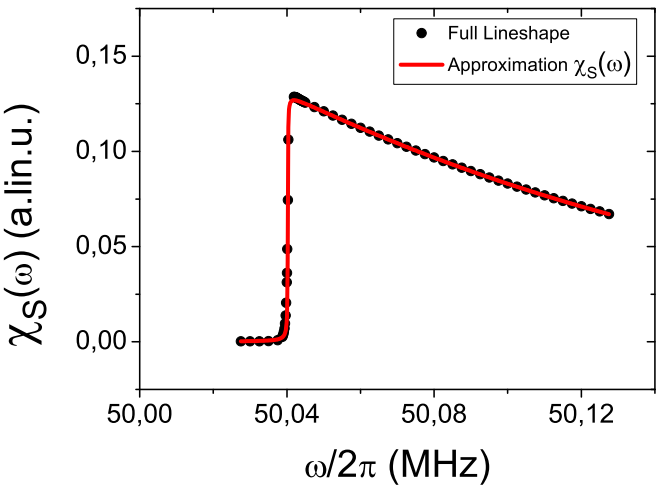


Figure 2.9: Lineshape of the Larmor resonance in arbitrary linear units. The filled circles represent the full result defined by Eq. (2.52), while the solid line represents the smooth approximation given in Eq. (2.54). The comparison is for the typical parameters of our experiment, but an increased temperature of $T_z = 100\,\mathrm{K}$, This demonstrates, that the approximation holds also for relatively high axial temperatures.

of the approximation given in Eq. (2.54). For this comparison, parameters typical for our

experiment are chosen but with a factor of 10 higher axial temperature $T_z$ in order to demonstrate the validity over a broad temperature range.

### *2.6.2 Transition Rates*

Spin flips are driven by the classical Rabi resonance principle [50]. A magnetic rf-field with amplitude $\vec{b}_{\mathrm{rf}}$ and resonance frequency $\nu_{\mathrm{rf}}$ is irradiated to the Penning trap. The vector $\vec{b}_{\mathrm{rf}}$ lies in the $(\rho, \phi)$-plane. Irradiating this field resonantly at the Larmor frequency $\nu_{\mathrm{L}}$, in its rest frame the particle sees a constant magnetic field in the $\rho$-direction and the spin vector starts to precess around this field component with the Rabi frequency $\Omega_R = 2\pi\nu_{\mathrm{L}} b_{\mathrm{rf}}/B_0$, effectively driving spin flips[7].

The spin transition rate in presence of an inhomogeneous magnetic field is discussed in [49] to exhausting detail. A more global but very simple and thus instructive explanation is given in [51]. In principle the dynamics of the Hamiltonian

$$H = H_0 + H_i = H_0 - \vec{\mu_s} \cdot \vec{b}_{\mathrm{rf}}(t) \tag{2.55}$$

has to be discussed in the interaction picture, where $H_0$ is the free Penning trap Hamiltonian and $\vec{\mu_s} \cdot \vec{b}_{\mathrm{rf}}(t)$ represents the interaction of the spin magnetic moment $\mu_s$ with the rf-drive. The additional time dependence arising from the inhomogeneity of the magnetic field can be averaged, leading to a spin-flip probability

$$P_{\mathrm{SF}} = \frac{1}{2}\left(1 - \exp\left(-\frac{1}{2}\Omega_R^2 t_0 \; \chi(2\pi\nu_{\mathrm{rf}}, B_2, T_z)\right)\right) \;, \tag{2.56}$$

where $t_0$ is the irradiation time of the rf-field. The maximum spin-flip probability $P_{\mathrm{SF}} = 50\,\%$ is achieved for resonant drive and adequate amplitude of the driving field $\vec{b}_{\mathrm{rf}}$. Figure 8.4 shows some arrays of curves of Eq. (2.56) with different array parameters. In a.) the spin-flip probability is shown as a function of frequency for constant temperature $T_z = 9.5\,\mathrm{K}$, constant irradiation time $t_0 = 10\,\mathrm{s}$ and varying $\vec{b}_{\mathrm{rf}}$. For high rf-amplitudes $b_{\mathrm{rf}} > 2\,\mu\mathrm{T}$ saturation occurs, leading to large linewidths. In b.) the axial temperature is varied. The reduction of the linewidth as a function of temperature is due to the reduction of the oscillation amplitude of the particle. Consequently the magnetic field variation scanned by the

[7] Due to the correspondence principle this classical explanation holds also in the quantum world

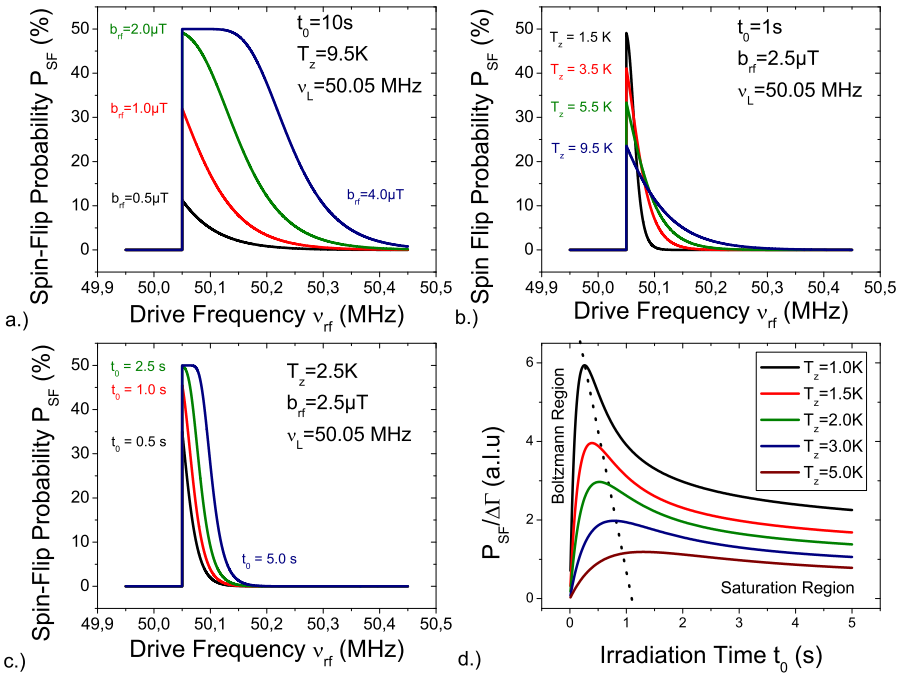


Figure 2.10: Spin-flip probability as a function of the drive frequency $\nu_{\mathrm{rf}}$... a.) for constant axial temperature of $T_z = 9.5\,\mathrm{K}$ and constant excitation time $t_0 = 10\,\mathrm{s}$ with the rf-amplitude as array parameter. b.) with axial temperature as array parameter, constant excitation time $t_0 = 1\,\mathrm{s}$, and constant rf-amplitude $\vec{b}_{\mathrm{rf}} = 2.5\,\mu\mathrm{T}$. c.) for variable excitation time $t_0$, constant axial temperature of $T_z = 2.5\,\mathrm{K}$ and constant rf-amplitude $\vec{b}_{\mathrm{rf}} = 2.5\,\mu\mathrm{T}$. d.) Ratio of the spin-flip probability $P_{\mathrm{SF}}$ and the linewidth defined by $\Delta\nu(P_{\mathrm{SF}}/2)$ in arbitrary linear units. For detailed explanation see text.

particle is reduced which leads to a decrease of the linewidth. In c.) the irradiation time is varied. Like in a.) the line saturates. Due to Eq.(2.56) compared to amplitude scaling, time scaling of the saturation is weaker.

To measure the Larmor frequency in the magnetic bottle with highest resolution, the temperature of the particle should be as small as possible. The particle temperature can be reduced by application of negatively phased feedback, as will be explained in section 4.5. Tuning the particle to the lowest accessible temperature $T_{\mathrm{min}}$ and irradiating $\vec{b}_{\mathrm{rf}}$ at constant amplitude, the excitation time has to be matched to optimum Larmor frequency resolution.

In order to choose the optimum irradiation time, the resolution $\Gamma = P_{\mathrm{SF}}/(\Delta\nu(P_{\mathrm{SF}}/2))$ is introduced, which is the quotient of the maximum spin flip probability and the frequency span $\Delta\nu(P_{\mathrm{SF}}/2)$ between the frequency cutoff and $P_{\mathrm{SF}}/2$:

$$\Delta\nu(P_{\mathrm{SF}}/2) = \frac{\delta\omega_L}{2\pi} \cdot \ln\left(-\frac{2\delta\omega_L}{\Omega_R^2 t}\ln\left(\frac{1}{2}\left(1+\exp\left(\frac{\Omega_R^2 t_0}{2\delta\omega_L}\right)\right)\right)\right) \ . \tag{2.57}$$

If the resolution $\Gamma$ is maximal the highest Larmor-frequency resolution is obtained from a mathematical function, which is fitted to a measured data set (see chapter 8). Figure 8.4 d.) shows $\Gamma$ as a function of the irradiation time. In the range where the resolution $\Gamma$ has a positive slope, the linewidth $\Delta\nu(P_{\mathrm{SF}}/2)$ is dominated by the thermal Boltzmann distribution and not affected by saturation. There, only the increase of $P_{\mathrm{SF}}$ due to an increase of irradiation time contributes to the scaling of $\Gamma$. Above the maximum saturation dominates. For irradiation times above the maximum $P_{\mathrm{SF}}$ increases only slightly while $\Delta\nu(P_{\mathrm{SF}}/2)$ increases due to saturation broadening, leading to the negative slope. Note that the maximum of $\Gamma$ corresponds to spin-flip probabilities of only $P_{\mathrm{SF}}(\Gamma_{\max}) \approx 40\,\%$. A transition probability of $50\,\%$ is always slightly broadened by saturation.

## *2.7 The Double-Penning Trap Method*

The continuous Stern-Gerlach effect is the crucial measuring technique applied in our experiment and requires the superposition of the Penning trap with a magnetic bottle $B_2$. On the other hand, as discussed in section 2.3.4, the presence of the magnetic bottle leads to energy dependent frequency shifts. The respective frequency shifts due to $B_2 = 3 \cdot 10^5\,\mathrm{T/m^2}$ are shown in Tab. 2.1 The question is, how the magnetic bottle modifies the result of a $g$-factor measurement. The relative error in the $g$-factor $\Delta g/g$ is given by

$$\frac{\Delta g}{g} = \frac{2}{g\nu_c}\left(\Delta\nu_L - \frac{g}{2}\Delta\nu_c\right) = \frac{1}{\nu_c}\left(\frac{\nu_L}{\nu_c}\Delta\nu_L - \Delta\nu_c\right) \ . \tag{2.58}$$

The cyclotron frequency is determined by means of the invariance theorem (Eq. (2.11)). The systematic frequency shift is

$$\Delta\nu_c = \sqrt{(\nu_+ + \Delta\nu_+(B_2))^2 + (\nu_- + \Delta\nu_-(B_2))^2 + (\nu_z + \Delta\nu_z(B_2))^2} - \nu_c \ . \tag{2.59}$$

Inserting the Eq. (2.37, 2.40, 2.41) into Eq. (2.59) and neglecting the contribution of the magnetron frequency, which contributes in all cases only a relative cyclotron frequency

Table 2.1: Respective frequency shifts in Hz/K due to the presence of the magnetic bottle with $B_2 = 3 \cdot 10^5\,\mathrm{T/m^2}$. For further discussion see text.

| Frequency Shift | $E_+$ | $E_z$ | $\lvert E_-\rvert$ |
|---|---|---|---|
| $\Delta\nu_+$ (Hz/K) | -3 | 2100 | -4220 |
| $\Delta\nu_z$ (Hz/K) | 80 | 0 | 80 |
| $\Delta\nu_-$ (Hz/K) | 3.1 | -1.5 | 3.1 |
| $\Delta\nu_L$ (Hz/K) | -8.4 | 5890 | -11780 |
| $\Delta\nu_c$ (Hz/K) | -0.023 | 2110 | -4210 |
| $\Delta\nu_L/\nu_L$ (1/K) | $-1.67 \cdot 10^{-7}$ | $1.18 \cdot 10^{-4}$ | $-2.36 \cdot 10^{-4}$ |
| $\Delta\nu_c/\nu_c$ (1/K) | $1.3 \cdot 10^{-10}$ | $1.17 \cdot 10^{-4}$ | $2.35 \cdot 10^{-4}$ |
| $\Delta g/g$ (1/K) | $-1.67 \cdot 10^{-7}$ | $1.67 \cdot 10^{-7}$ | $-5.01 \cdot 10^{-7}$ |

uncertainty $\Delta\nu_c/\nu_c \approx 10^{-10}$ /K or smaller, as well as terms $\propto \omega_z/\omega_+$, we find that

$$\Delta\nu_c = \frac{\nu_+}{4\pi^2 m\nu_z^2}\frac{B_2}{B_0}\left(E_z - 2|E_-|\right) \tag{2.60}$$

which is the modification due to the axial oscillation as well as the radius of the magnetron motion. Both terms lead to a cyclotron frequency shift in the $10^{-4}$ range.

The same calculation gives for the shift of the Larmor frequency

$$\Delta\nu_L = \frac{\nu_L}{4\pi^2 m\nu_z^2}\frac{B_2}{B_0}\left(E_z - 2|E_-|\right) \tag{2.61}$$

and therefore the relative shift of the $g$-factor

$$\frac{\Delta g}{g} = 2\left(\frac{\Delta\nu_L}{\nu_c} - \frac{\nu_L}{\nu_c^2}\Delta\nu_c\right) \tag{2.62}$$

$$= \frac{1}{4\pi^2 m\nu_z^2}\frac{B_2}{B_0}\left(\frac{1}{\nu_c}(\nu_L) - \frac{\nu_L}{\nu_c^2}(\nu_+)\right)\left(E_+ - 2|E_-|\right)\ . \tag{2.63}$$

Numerical values for $\Delta g/g$ are also given in Tab. 2.1. All relative shifts are in the range of $10^{-7}$ /K. By measuring the $g$-factor as a function of the mode energies and extrapolating to zero energy, higher resolution can be achieved. But these measurements require long measuring time, and are sensitive to external drifts.

To overcome this problem Häffner and Hermanspahn introduced the idea to separate the

precision measurement of the frequencies and the analysis of the spin state to two traps, a ***precision trap*** and an ***analysis trap*** [17]. The setup of such a double trap is shown

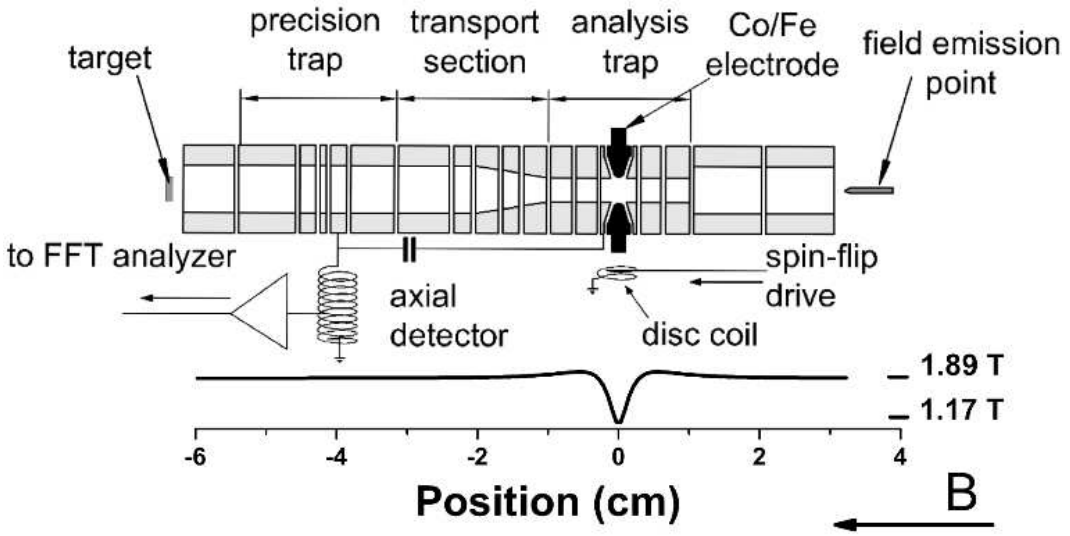


Figure 2.11: Schematic of the proton $g$-factor double Penning trap experiment. The trap tower consists of two Penning traps, the *precision trap* and the *analysis trap* connected by transport electrodes. The central ring electrode of the analysis trap is made of ferromagnetic Co/Fe material. The solid line below the Penning trap stack indicates the magnetic field strength $B_{0,z}$ in the axial direction. The ferromagnetic ring electrode in the center of the analysis trap distorts the magnetic field to a value $B_{0,z}$, which is in case of our experiment a factor of about 1.6 smaller than in the precision trap. For further details see text.

in Fig. 2.11. The Penning traps are connected by transport electrodes. The central ring electrode of the analysis trap is made of ferromagnetic Co/Fe material. The solid line below the Penning trap stack indicates the magnetic field strength $B_{0,z}$ in the axial direction. The ferromagnetic ring electrode distorts $B_{0,z}$ in the center of the analysis trap to a value which is in case of our experiment a factor of 1.6 smaller than in the precision trap. The field is reduced by nearly 1 Tesla in an axial range of 1.5 mm!

A time sequence of an experimental $g$-factor measurement with the double trap technique is illustrated in Fig. 2.12 [8]. In this schematic explanation it is assumed that the spin state of

[8] This description is concentrated to the essential elements, the real experimental procedure includes some additional parts as particle cooling after transport, additional axial frequency measurements, etc.

the particle is known. First the axial frequency is measured in the precision trap, afterwards the cyclotron frequency is measured and at the same time the spin flip is driven by irradiation of an rf-drive at $\nu_{rf}$ and an amplitude $b_{rf}$. Then the particle is transported to the analysis trap, applying adequate voltage ramps to the transport electrodes. Subsequently the axial frequency is measured in the analysis trap and afterwards the spin flip drive is irradiated until the axial frequency changes by an amount $\Delta\nu_{z,SF}$. If $\Delta\nu_{z,SF} > 0$ the spin flipped from "spin-down" to "spin-up", if $\Delta\nu_{z,SF} < 0$ the spin flipped from "spin-up" to "spin-down". This is the crucial measurement step and allows us to determine the eigenstate of the spin as the particle entered the analysis trap. In a final step the particle is transported back to the precision trap. Now the spin state is known and by repeating the sequence it can be decided whether the spin has flipped in the precision trap or not. For every irradiated drive frequency $\nu_{rf}$ this experimental sequence is repeated for several hundred times. In the

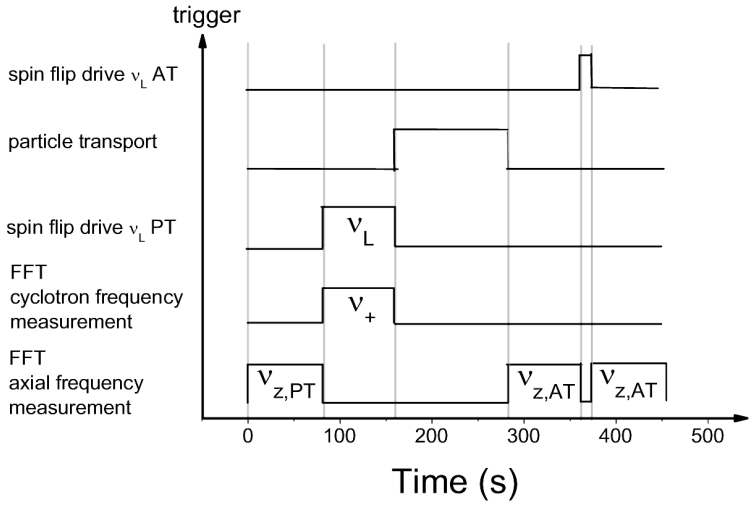


Figure 2.12: Measuring sequence for the $g$-factor determination. For details see text.

whole $g$-factor measuring sequence the rf-drive frequency is tuned in certain steps over the resonance. Finally, the spin-flip probability is evaluated as a function of the drive frequency $P_{SF}(\nu_{rf})$. This curve has a maximum at the Larmor frequency $\nu_L$. Together with the cyclotron frequency measurements performed during the irradiation of the spin-flip drive the $g$-factor can be extracted. This double-Penning trap measuring technique was developed

at the University of Mainz and was demonstrated for the first time in the framework of the measurement of hydrogen-like carbon $^{12}C^{5+}$ where a relative precision of $\Delta g/g = 2.5 \cdot 10^{-9}$ was achieved. Our Harvard-competitors have adopted this technique to their experiment [30].

Chapter 3

# EXPERIMENTAL SETUP

Starting my diploma-thesis [52] in 2005 with a superconducting magnet in an empty laboratory, the experiment was built in the following two years, including the Penning trap stack [53], the vacuum chamber, the cryo-mechanical support structure, temperature stabilization for the apparatus, radio frequency-electronics, filter-stages for trap biasing [47] etc.. This chapter gives a detailed overview of the experimental setup.

The key pieces of the experiment are the double Penning trap electrode-stack and the highly sensitive cryogenic detection systems. The Penning trap and the detection systems are located in the magnetic field of a superconducting magnet with a horizontal bore running a field of nominally $B_0 = 1.899\,\mathrm{T}$. The precision trap is adjusted to the homogeneous center of the magnet, where the magnetic field varies only by $1\,\mu\mathrm{T}$ in a volume of about $1\,\mathrm{cm}^3$.

These main pieces are the chocolate and the sugar in the experimental fancy cake but the recipe also asks for butter, eggs, flour and cream. Besides the trap-stack all less important components which are crucial for the successful accomplishment of a cryogenic Penning trap experiment are described in this chapter as well. Furthermore some useful hints about surface treatment of trap electrodes are given. The detection systems are described in-depth in chapter 4.

## *3.1 General Overview - Cryo-Mechanical Setup and Superconducting Magnet*

The experimental setup is shown in Fig. 3.1. The trap is located in the center of the magnetic field of a superconducting magnet. The horizontal cylindrical bore of the magnet has a diameter of $d = 88\,\mathrm{mm}$.

The cryogenic temperatures are provided by a two stage pulse-tube cryo-cooler (*Vericold 4-K cooler*). The cooler has two temperature reservoirs, the first stage and the second stage (also called *stage 1* and *stage 2* in the following text). The end temperatures reached by

the cooler depend on the heat load dissipated at the cryogenic stages. Values relevant for our experiment are $T_1 \approx 60\,\mathrm{K}$ for 6 W heat load at *stage 1* and $T_2 \approx 4\,\mathrm{K}$ for 0.35 W heat dissipation at *stage 2* [52].

The cryogenic apparatus is surrounded by a *CF-200* vacuum chamber providing an insulation vacuum of $p \approx 5 \cdot 10^{-8}\,\mathrm{mbar}$ if the apparatus is cooled to $T \approx 4\,\mathrm{K}$. The cryo-cooler is mounted on a *CF-200* double-cross which is placed on an aluminum table. The table is adjustable in all three spacial dimensions. The whole apparatus is mounted on rails. The

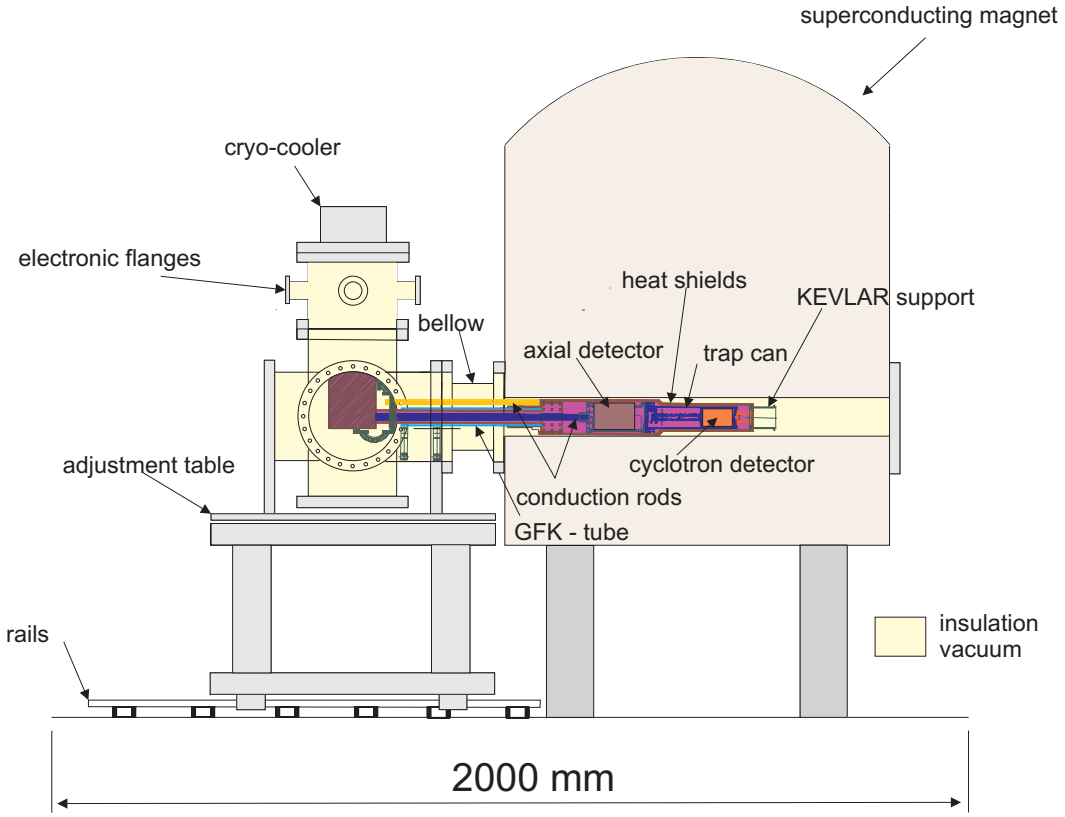


Figure 3.1: Sketch of the experimental setup. The cryogenic temperatures are provided by a 4 K pulse-tube-cooler. The superconducting magnet and the CF-200 double-cross are connected with a flexible bellow. The trap is mounted at the end of the horizontal arm and located in the center of the superconducting magnet. For a more detailed description of the apparatus see text.

magnet bore itself is part of the vacuum chamber. On one side the bore is closed with a window flange, on the other side it is connected to the double-cross with a flexible bellow,

making the system adjustable in the direction of the magnetic field vector.

With a high purity annealed copper rod the trap is connected to the second stage of the cryo-cooler and mounted in an aluminum heat shield. The shield is connected to *stage 1*, also by means of copper rods. In order to avoid mechanical friction during thermal cycling the rods are attached to the cryo-cooler by means of flexible copper strands.

Seen from the cryo-technical point of view the horizontal geometry of the experiment is challenging. Most cryogenic Penning trap experiments [23, 26, 30] are designed in vertical geometry. There the direction of gravitation makes the design simple since no stable carrying connections have to be used. For a horizontal design two contradicting constraints are given:

1. Mechanical stability of the system, and

2. low consumption of heat power.

The more massive and stable a support structure, the higher its heat conduction is. This problem is solved by combining the comparably high cooling power provided by the pulse tube cooler with highly-stable materials showing low heat conductance, as the glass fiber material *G10* [54], or the para-aramid synthetic fiber *Kevlar* [55].

With an aluminum claw, the heat-shield surrounding the trap is fixed to a custom made *G10*-tube [54] (*CG-TEC*[1]). On the other end, the tube is connected to a massive stainless steel support welded to the double-cross. The trap is fixed in the aluminum shield by means of *Kevlar* threads.

In order to keep the heat load due to thermal radiation as small as possible, the trap housing, as well as the cold stage support-structure are gold-plated and additionally shielded with numerous layers of super-insulation foil [56]. The surfaces of the *stage 1* shield are also sealed with super-insulation foil. It was measured that the use of several ten layers of super-insulation reduces the effective emissivity of the surfaces at least by a factor of 10. If the apparatus is setup with maximum carefulness with respect to cryogenics, within 12 h

[1]Important information for experimentalists: This company provides custom-made glass- and carbon-fiber tubes in very low piece numbers, starting from two tubes of one meter length.

of cooling time the end temperature of $\approx 65\,\mathrm{K}$ at the aluminum shield in the magnet bore and a trap temperature of 4.6 K is achieved.

Supply-, excitation- and detection-lines are guided into the double-cross vacuum chamber with standard Ni-pin feedthroughs mounted on *CF-40* flanges. Every single flange is shielded with a radio frequency (rf) shielding copper box with a copper-wall thickness of 2 mm. Inside these boxes filter stages for the DC-lines and attenuators for the rf-lines are located.

All wires connecting room-temperature with the cryogenic region are made from alloy with low heat conduction and comparably high electrical conductivity. The rf-lines have german silver shields, the inner conductors are made from brass. For the DC biasing manganin wires are used, which have a small heat conductance and excellent magnetic properties [2]. Starting from room-temperature the lines are guided to a second filter stage which is screwed to the mounting flange of the aluminum heat shield at $T_2$. A third filter stage is located at 4 K. The critical rf lines guiding the single-particle signals are additionally shielded with massive german silver tubes.

Around the whole apparatus shown in Fig. 3.1 a wooden box is built. The box protects the experiment against short term temperature fluctuations. Furthermore the temperature inside the box can be actively stabilized [59].

### *3.2 The Double Penning Trap Stack and the Cryogenic Vacuum Chamber*

The heart of the experiment is the double Penning trap-tower consisting of two traps and a transport section located between the traps. The mechanical concept, two traps and a first version of the transport section have been developed in the framework of the PhD thesis of Susanne Kreim [53]. In the following years this first design was improved. A new analysis trap [3] as well as a new transport section was designed (see section 6.13). Figure 3.2 shows a technical drawing of the current setup.

All electrodes have cylindrical symmetry. Every trap consists of five electrodes, a ring

[2] comparing constantan and manganin the electrical and thermal properties are nearly identical, but the constantan alloy consists of 30% Ni.

[3] The new analysis trap was designed in the framework of the PhD thesis of Cricia C. Rodegheri [47].

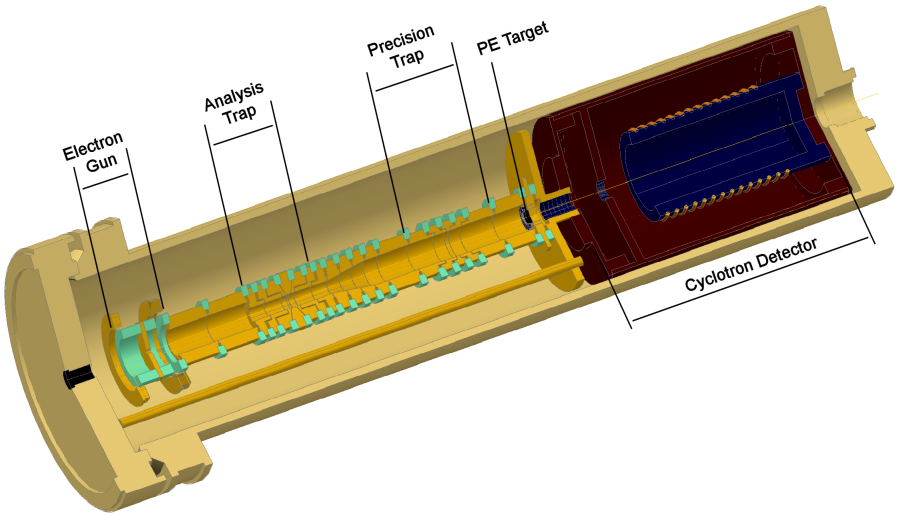


Figure 3.2: Sketch of the trap chamber including the trap-stack, the cryogenic electron source and the cyclotron detection system. The trap-stack is fixed to the sealing flange with three massive copper rods (not shown in the figure). For a more detailed description of the apparatus see text.

electrode, two correction electrodes and two end-caps. The inner radius of the precision trap (PT) is 3.5 mm, while the analysis trap (AT) has an inner radius of 1.8 mm. Both traps are in compensated, orthogonal design (see section 2.3.1). The geometrical parameters of the traps are listed in Tab. 3.1. The transport electrodes connect both traps. Along the transport section the inner diameter of the electrodes reduces and is matched to the inner radii of the traps. With these electrodes the particle can be moved between the traps adiabatically. The longitudinal distance between both trap centers is about 45 mm.

The electrodes are machined in the technical workshop in Mainz, and are made from oxygen-free electrolytic (OFE) copper. The parts of the small analysis trap are machined by the company *Blum-CNC, Heidelberg*. Working with temperature stabilized lathes and milling machines they achieve mechanical tolerances of $\leq 3\,\mu$m.

In order to protect the surfaces against oxidation, all electrodes are gold-plated electrolytically. Gold-plating was performed in cooperation with *Schlierholz-Galvanik*[4]. The average

[4]In a two-day crash-course the company-technicians introduced us into the equipment, allowed us to use all machines and do the gold-plating on our own - which is remarkably kind.

Table 3.1: Electrode geometry, typical biasing voltage and magnetic field of the precision trap and the analysis trap.

| Value | Precision Trap | Analysis Trap |
|---|---|---|
| Trap Radius | 3.5 mm | 1.8 mm |
| Length Correction Electrode | 2.85 mm | 1.36 mm |
| Length Ring Electrode | 0.92 mm | 0.39 mm |
| Typical Biasing Voltage | -3.197 V | -0.851 V |
| Magnetic Field in Trap Center | 1.901 T | 1.161 T |

thickness of the gold layer is $d_{\mathrm{Au}} \approx 5\,\mu$m. It is asserted [57] that a gold layer-thickness of $3 - 4\,\mu$m guarantees a closed surface. To avoid that the gold deposition diffuses into the copper, the parts are covered with a silver barrier-coating of $15\,\mu$m (in case of the five analysis trap electrodes, the barrier-coat is made of $5\,\mu$m $Ni$ layer) before gold-plating. Between machining and gold-plating the surfaces are mechanically polished with Q-tips.

In Fig. 3.3 two surfaces are shown. The pictures are made with a RE-microscope while the surfaces are analyzed per EDX measurements. The unpolished surface shown on the left side shows grooves caused by the machining tool. The dark stain is a not properly gold-plated copper area. The machining grooves obviously shield the electrical deposition fields in a way that the depletion of gold in the recess-area is suppressed. The polished surface shown on the right side of Fig. 3.3 has no grooves and is uniformly gold-plated. For our applications this result is of great importance, since the trap electrodes should represent ideal equipotential surfaces. This is only the case if the surfaces are covered uniformly with one material. Otherwise due to different work functions of different materials the equipotential-condition is not fulfilled anymore. The values of work functions of good metals differ in the range of 1 V (for example gold to silver) [58], which is roughly the voltage to be applied to tune the proton on resonance with the axial detector in the analysis trap. Thus, non-equipotential surfaces with work-function differences in the volt regime make controlled particle trapping and manipulation impossible.

All electrodes are stacked together to form the trap tower. Individual electrodes are sep-

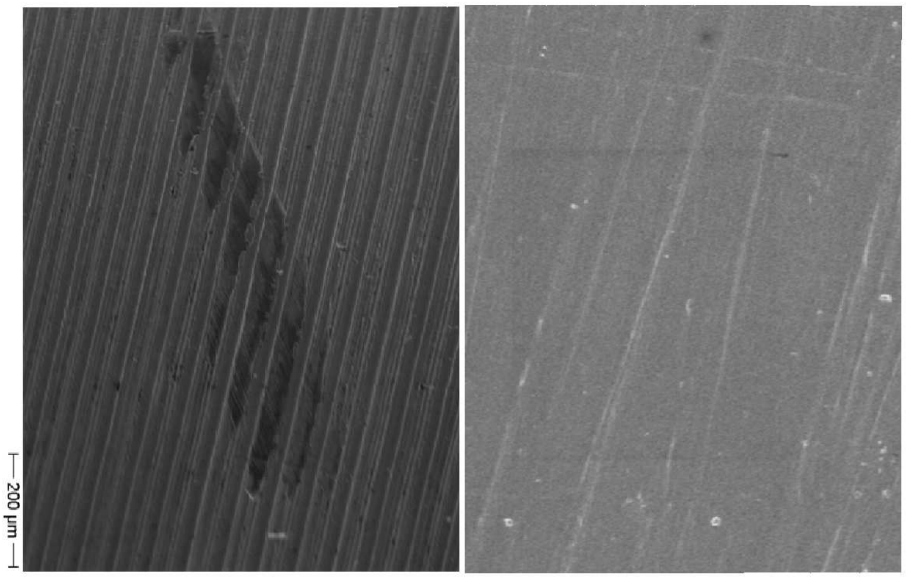


Figure 3.3: REM-photographs of electrode surfaces with different surface finishing. Left: Electrode surface which was gold-plated directly after machining. The grooves are caused by the machining tool. The black stain is a not adequately gold-plated area of copper. Right: Surface which was polished before gold plating. The surface is continuously gold plated.

arated by means of sapphire rings. Sapphire has excellent heat conduction properties at best electrical insulation properties, ultra-low dielectric loss tangent and high mechanical stability. The electrode geometry is designed in a way that on the inner surface the distance between two electrodes is $d = 140\,\mu$m. Stacked together the trap-tower is fixed to an OFE copper flange. Three massive copper rods screwed to the flange form the base frame for the mechanical fixture of the trap stack. Combined with a copper plate mounted at the end of the copper rods the stacked electrodes are centered and pressed together. Due to different heat expansion coefficients of copper and sapphire the stack stays tightened while cooling down from 300 K to 4 K.

The trap-stack is housed in a cylindrical cryogenic vacuum chamber (see Fig. 3.2), which is made from a massive OFE copper rod. On one side the chamber is closed by means of the upper described flange with an indium o-ring seal. Feedthroughs for biasing-, excitation-

and detection-lines are located (*Kyocera-Fine-Ceramics*) on this flange. The feedthroughs are soldered to the flange with standard Pb/Sn solder. In numerous thermal cycling tests we found that the feedthroughs, as well as the soldered connections, are very robust[5]
On the other side of the cryogenic vacuum chamber, a copper pinch-off tube is soldered to the trap can. After pumping the can to a pressure of at least $p \approx 1.0 \cdot 10^{-6}$ mbar, the tube is pinched-off, sealing the trap can hermetically. Cooled down to cryogenic temperatures, due to cryo-pumping the background pressure in such systems is typically $< 10^{-15}$ mbar. Proton's can be stored in our trap for arbitrarily long times (months). A photograph of the

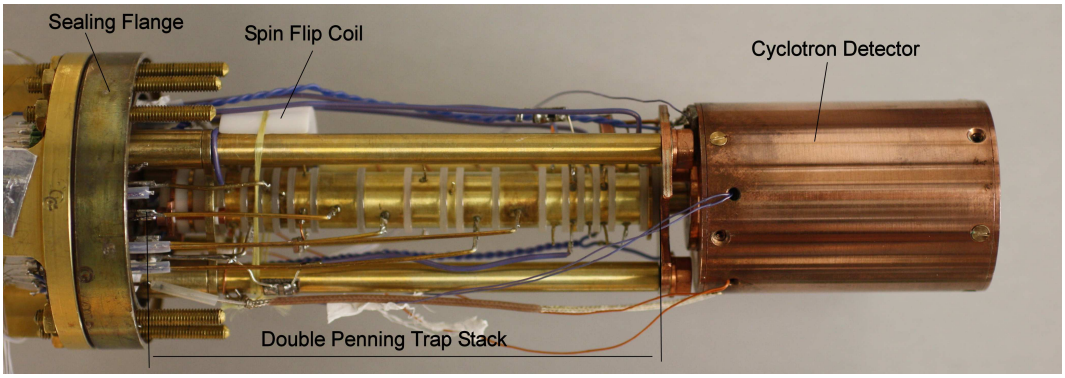


Figure 3.4: Photograph of the double Penning trap stack. For a detailed description see text.

mounted Penning trap, including the coil for the spin flip drive and the cyclotron detection system is shown in Fig. 3.4.

### *3.3 Basic Detection*

Besides the trap the highly sensitive detection systems are the most important components of the experiment. They provide all visible information about the particle stored in the Penning trap. A detailed description is found in chapter 4. In this section just the geometrical localization of the detectors and external hardware used to analyze the signals is described.

[5]Kyocera test-feedthroughs were cycled for fifty times down to 4 K without damage. The break-rate of feedthroughs delivered by other companies (*Ceramtech*, *Insulator Seal*) was found to be around 1% per cycle.

The detector for the modified cyclotron motion in the precision trap at $\nu_+ \approx 28.97\,\mathrm{MHz}$ is located inside the cryogenic vacuum chamber, see Fig. 3.2. The superconducting detection system for the axial motion at $\nu_z \approx 680\,\mathrm{kHz}$ is located outside the trap can as shown in Fig. 3.1. Caused by space problems due to the small diameter of the horizontal magnet bore, only one axial-frequency detector connected to both traps is used. In the analysis trap the cyclotron frequency is not measured directly, since the interaction of the particle with the thermal bath of the detection system causes instabilities of the axial frequency [48].

The detection systems consist of highly sensitive resonance circuits tuned to the proton's eigenfrequencies. The image-current signals induced by the oscillating particle in the trap electrodes are amplified with cryogenic amplifiers and guided to room temperature electronics, consisting of a second amplification stage (Axial: *Stahl Electronics*, Cyclotron: *Minicircuits ZFL500LN*) and a frequency down-converter (also *Stahl Electronics*). Behind the second amplification stage the rf-power is split. One signal is analyzed with an analog spectrum analyzer (*Rohde und Schwarz - FSP13*), the other portion of the signal is down converted to audio frequencies and analyzed with a Fast-Fourier-Transform (FFT) spectrum analyzer (*Stanford Research - SR780*).

All ingredients of the detection electronics are shown in Fig. 3.5. For frequency mixing *Agilent 33250* and *Rohde and Schwarz SML01* frequency generators are used. The generators are clocked with a *Stanford Research FS725* 10 MHz frequency standard.

### *3.4 Precision Voltage Source*

The aim of the experiment is the detection of spin flips of a single trapped proton by means of the continuous Stern-Gerlach effect. In the analysis trap, the axial frequency of the particle depends on the voltages applied to the trap electrodes, as well as the direction of the particle spin (see section 2.4)

$$\nu_z = \frac{1}{2\pi}\sqrt{\frac{2qC_2V_0}{m} + \frac{2\mu_p B_2}{m}}\ . \tag{3.1}$$

Voltage fluctuations $\Delta V_0$ affect the frequency stability $\delta\nu_z$ of the proton

$$\delta\nu_z = \frac{\nu_z}{2V_0}\Delta V_0\ . \tag{3.2}$$

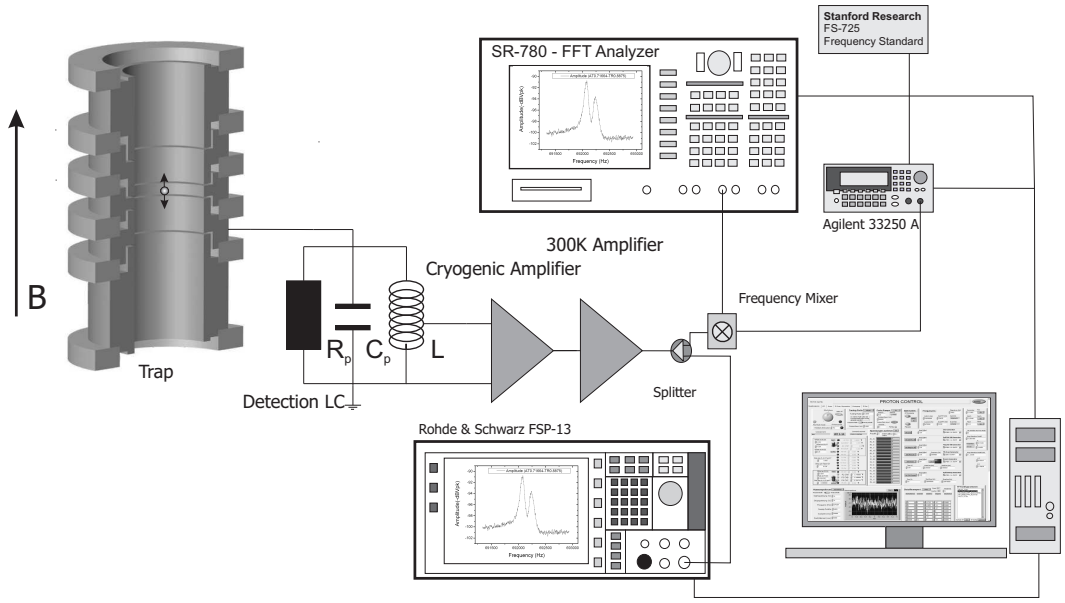


Figure 3.5: Basic setup for single particle detection. The detection-circuit is connected to a trap electrode. The voltage drop is amplified with a cryogenic low-noise amplifier. Behind this first amplification stage a second low-noise amplifier boosts the signal. This signal is split in two signal paths. One portion is down-converted and analyzed with an FFT-analyzer while the other portion is directly analyzed with an analogue spectrum analyzer.

A spin flip changes the axial frequency by $\Delta\nu_{\mathrm{z,SF}} = 191\,\mathrm{mHz}$ corresponding to $\Delta\nu_z/\nu_z = 0.3 \cdot 10^{-6}$. In order to resolve spin flips, a voltage stability of at least $\Delta V_0/V_0 = 0.6 \cdot 10^{-6}$ is required.

Thus, the trap electrodes are biased with an ultra-high-precision voltage source (*Stahl Electronics - UM1-14*). The electronic boards of the voltage source are housed in a cubic aluminum housing. The source has 16 channels - 10 *fast-mode channels* with a resolution of 16-bits supplying the electrodes of the transport section and the end-caps of the Penning traps, and 6 *precision-mode channels* with 24-bit resolution biasing the ring- and the correction electrodes. The voltage range of the fast mode channels as well as the three precision mode channels used for biasing of the precision trap is between 0 V and -14 V. The remaining three precision mode channels supplying the electrodes of the analysis trap have an output-range between 0 V and -4 V. The outputs of the voltage source are connected to a sub-D connector. The voltage source is designed to be directly connected to the apparatus.

Thus, no wire loops occur and the whole setup is not interference-prone to inductive effects. The voltage source is temperature stabilized. In order to suppress short-scale voltage fluctu-

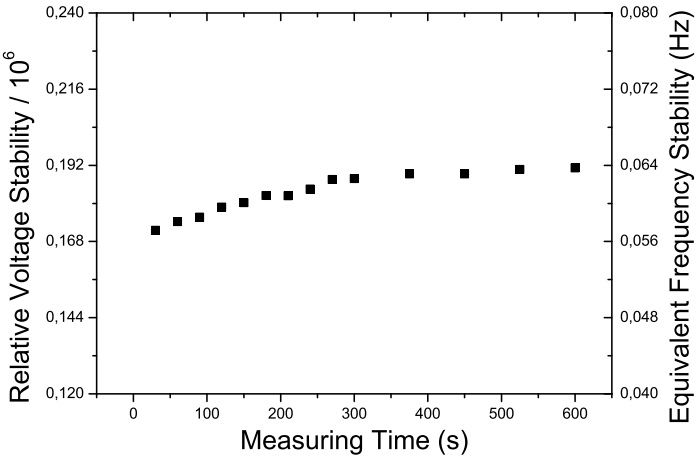


Figure 3.6: Stability of the ultra high precision voltage source as a function of measuring time. The left axis displays the voltage stability while the right axis shows the corresponding frequency stability.

ations due to abrupt temperature changes in the laboratory, the voltage source is thermally anchored to a massive copper housing with a total weight of 15 kg. This massive housing smoothes short-scale temperature fluctuations. In order to compensate typical day-night temperature fluctuations, the copper housing is temperature stabilized with a commercial P-I-D circuit (for details see [59]).

Figure 3.6 shows the relative voltage-stability of the temperature-stabilized DC-supply (measured with a *FLUKE-8508a-reference multi meter*), as well as the corresponding axial frequency stability as a function of measuring time. For typical measuring time-scales between 30 s and 10 min the voltage stability corresponds to an axial frequency stability between 55 mHz and 65 mHz. Thus, the detection of axial frequency shift caused by spin flips $\Delta\nu_{z,\mathrm{SF}} = 191\,\mathrm{mHz}$, should be possible. The frequency changes due to the fluctuation of the DC-voltage supply are a factor of 2.9 to 3.5 below $\Delta\nu_{z,\mathrm{SF}}$.

### *3.5 Control-System*

Most experimental ion trap routines are too complex to be controlled by one person with paper and pen. Thus, the whole experiment is controlled by means of a LabView 8.2. code based computer program named *Proton Control System (PCS)* [6]. A screen shot of the PCS is shown in Fig.3.7. It is operated on a DELL-PC with an Intel Core2-CPU, which is clocked with 2.13 GHz and has 1 GB RAM. The controllable devices are connected to the PC per USB or GPIB bus. The *PCS* controls the high-precision voltage source, arbitrary wave-form generators (*Agilent 33220a and 33250a / Rohde&Scharz SMY-02 and SML-01 / Stanford Research DS-345*) for particle excitation and manipulation, as well as voltage sources for the control of voltage controllable attenuators and amplifiers. Simple experimental routines such as particle cooling (see section 6.6), particle search in the magnetic bottle (see section 7.2), "single particle temperature measurements" (see section 7.4), and long time frequency recording (see section 7.5) are implemented. Furthermore readout of both analyzers and data storage is provided by the virtual instrument. For more complex routines as phase-sensitive detection (see section 6.12), particle cooling in the analysis trap (see section 7.1), and spin-flip measuring sequences (see section 8.2), external virtual instruments are individually written.

### *3.6 Wiring and Components*

As already mentioned in section 3.1 all DC lines for the trap supply are filtered with RC-circuits. The DC filters consist of two 820 kΩ resistors in parallel and a 2.7 nF capacitor connected to ground. All components are *0805*-surface mountable devices (SMD). The resistors are *Black-French-Snake*-components while the capacitors are *ECHU*. Both components are robust under thermal cycles and change their values down to 4 K in a range of only 10%. Filter stages are located at 300 K, at stage 2 temperature and on the copper flange closing the cryogenic vacuum chamber. All boards are made by standard etching technique and varnished with stop-lacquer. At 300 K and stage 2 standard FR4 boards are

[6] The main part of the control program was developed in the framework of Holger Krackes PhD thesis [59]. Thanks to Holger for his excellent work and his ability to transform every experimental idea into computer-code within seconds.

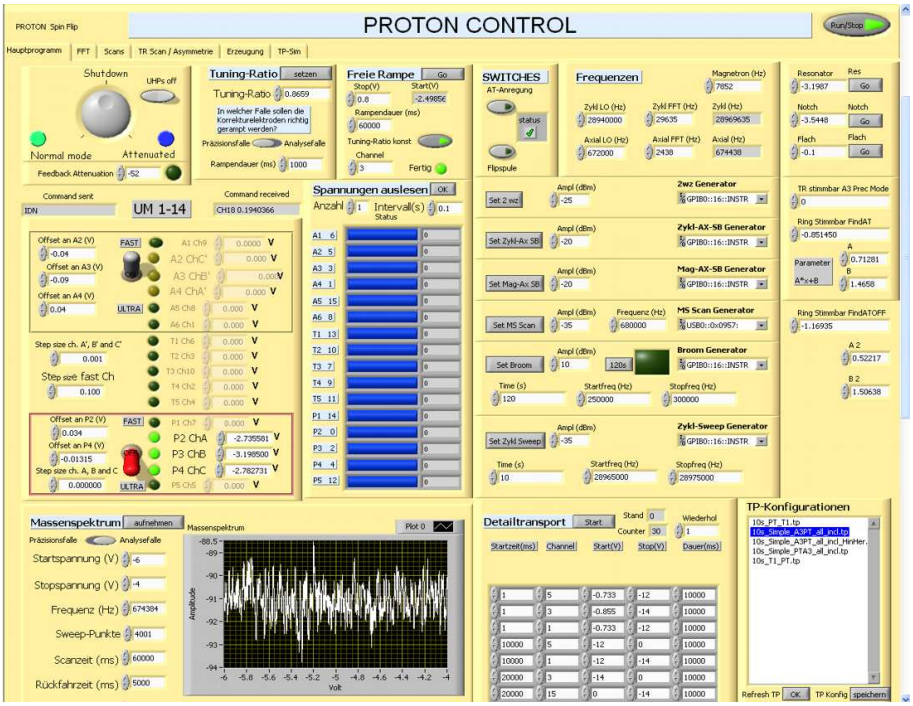


Figure 3.7: Screen-shot of the *proton control system (PCS)*. The virtual instrument is based on LabView 8.2. code.

used while the PCB at 4 K is made of low loss PTFE based laminate (*Tachonic TLC*). The excitation lines at the lab side are standard 50 Ω coaxial lines with BNC connectors. All lines are additionally shielded with copper meshwork, reducing the interference liability by additional 5 dB. Every rf-line is armed with a 20 dB attenuator. In order to suppress common-mode interference and to avoid ground-loops the lines are connected to the apparatus by means of 1/1-rf transformers.

The rf-signals for the spin-flip drive are guided to the trap by means of shielded cryogenic twisted-pair lines. The spin-flip coils have disk geometry and are fixed to PTFE holders. The holders are mounted to the copper rods, which form the base frame of the trap-stack. A detailed analysis and even more detailed description of this specific spin-flip geometry is given in [60]. A complete wiring diagram of the experiment and an even more detailed explanation is found in [47] and [53].

### *3.7 Cryogenic Electron Source*

This section describes the generation of charged particles by means of an electron beam hitting a target. The target is made of black poly-ethylene (PE). If the electron beam hits the target, neutral atoms are sputtered out of the solid and ionized in the center of the Penning trap. After ionization the particles are stored in the trap.

The electron beam is provided by a field emission electron source. A schematic of the source is shown in Fig.3.8 a.). A home made single field emission point (FEP) made from tungsten wire [7] is screwed to a cylindrical plate called base electrode . A photograph of the FEP is shown in Fig. 3.8 b.). Above the mounting plate for the FEP an acceleration-electrode is placed. Both plates are separated by a cylindrical MACOR ring. The distance between the tip of the FEP and the acceleration-electrode is adjustable and is tuned experimentally in a way that currents in the range of $I = 10\,\mathrm{nA}$ are achieved at moderate high-voltages between $V_{HV} \approx 0.5\,\mathrm{kV}$ and $V_{HV} \approx 1.5\,\mathrm{kV}$. Behind the acceleration-electrode, another electrode is

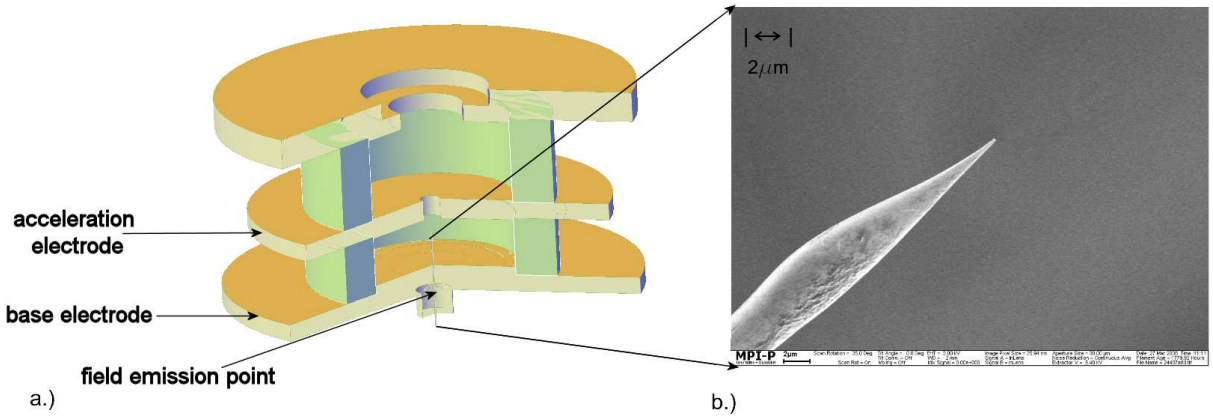


Figure 3.8: a.) Schematic of the cryogenic electron source. b.) REM-photograph of the home-made tungsten field emission point. With proper experimental setup the field emission point delivers currents between 10 nA and 100 nA at acceleration voltages between 0.5 kV and 1.5 kV.

placed, which is connected to ground potential. Applying a high voltage to the acceleration-

[7] The field emission points were manufactured by Bent Brueggemann in the framework of a training course in our lab. Thanks to Bent for the excellent job!

electrode, the intensity of the electron current can be adjusted. The energy of the electrons is defined by means of a negative voltage $V_{BE}$ applied to the base-electrode. In order to load the trap with ions we set $V_{BE} \approx 50\,\mathrm{V}$ at currents in the range of 20 nA to 50 nA. Depending on the application the electron beam-on time is varied between 2 s and 10 s.

# Chapter 4

# ELECTRONIC DETECTION AND REFRIGERATION

All visible information about the trapped proton is provided by highly sensitive detection systems [61, 62]. The higher the sensitivity of the detectors, the faster the measurement cycles needed to achieve the required frequency resolution. Therefore, besides the Penning traps, high-performance detection systems are the key-pieces of a high-precision experiment. In this chapter, the design, setup and characterization of the single particle detection systems are presented. Some parts of this chapter are extracted from [61] and [63].

## *4.1 Detection Principle*

A particle stored in a Penning trap oscillates with the eigenfrequencies $\nu_+$, $\nu_z$ and $\nu_-$, respectively (see chapter 2). The motion of a particle with charge $q$ leads to a tiny image-current flow $I_p$ induced in the trap electrodes [67]:

$$I_p = \frac{q}{D_i}\dot{\rho}_i = 2\pi\frac{q}{D_i}\nu_i\rho_i \ , \tag{4.1}$$

where $\rho_i$ is the coordinate, $\nu_i$ the eigenfrequency and $D_i$ the *effective electrode distance*[1] of the considered mode. $D_i$ depends on the trap geometry as well as the electronic signal pick-up design (see section 4.4).

The image-currents typically induced are in the fA range. These tiny signals can be detected connecting an inductor $L$ to the trap electrodes. Together with its parasitic self-capacitance $C_p$ and the capacitance of the trap $C_T$, the inductor forms a resonance circuit as shown in Fig. 4.1. On its resonance frequency $\nu_0$ the tank-circuit acts as an effective parallel resistance

$$R_p = 2\pi\nu_0 LQ \ , \tag{4.2}$$

[1] this term was introduced in the PhD thesis of S. Stahl [64] and is used in the Heidelberg-GSI-Mainz trap community.

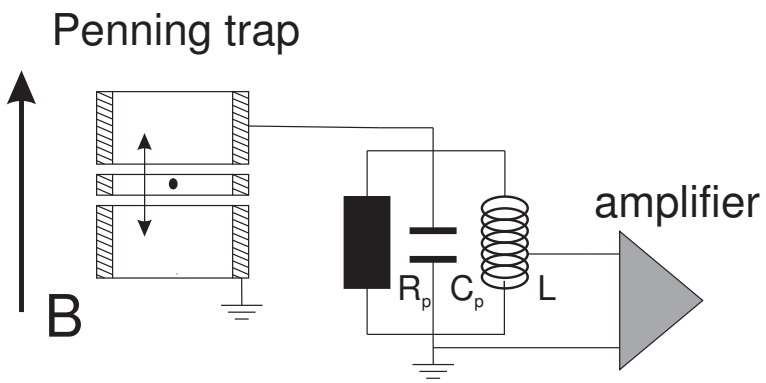


Figure 4.1: Schematic of single particle detection in a cylindrical Penning trap. The trap is represented by three cylindrical electrodes. The oscillation of the charged particle is indicated by the double arrow. The resonator is a parallel tank circuit consisting of an inductance $L$, an effective resistance $R_p$ and a parasitic capacitance $C_p$. The signal is coupled to a cryogenic amplifier.

where $Q$ is the *quality factor* or *Q-value* of the detection system. This number is defined as the ratio of stored energy to energy loss per cycle. Spoken in experimentally accessible quantities

$$Q = \frac{\nu_0}{\Delta\nu} \,, \tag{4.3}$$

where $\Delta\nu$ is the 3 dB width of the transfer function of the tank circuit. Tuning the detector's resonance frequency $\nu_0$ to the eigenfrequency $\nu_i$ of the particle a voltage drop

$$U_p = R_p I_p = 2\pi\nu_0 L Q I_p \tag{4.4}$$

is detected. This voltage drop is picked-up and amplified with a cryogenic ultra low-noise amplifier. Since the signal strength scales $\propto R_p$, to achieve high sensitivity of the detection system, this effective parallel resistance has to be as large as possible. Therefore, for optimum detector performance the inductance $L$ and the $Q$-value have to be maximized within the given experimental constraints.

### *4.2 Particle - Detector Interaction*

In the following the dynamics of a trapped charged particle is described for the axial coordinate $z$. The formalism also holds for the radial coordinates just by replacing $z$ by $\rho_{+,-}$

and $\omega_z$ by $\omega_{+,-}$, respectively.

The oscillating charged particle can be described by the newtonian equation of motion given by

$$\ddot{z} + \gamma_z \dot{z} + \omega_z^2 z = f(t)/m \tag{4.5}$$

where $f(t)$ is an arbitrary force and $\gamma_z$ is a damping constant due to the interaction between the particle and the detector. To analyze the correlation between the damping $\gamma_z$ and the parameters of the detector, the power $P$ dissipated by the particle current $I_p$ flowing through $R_p$ is considered.

$$P = U_p I_p = R_p I_p^2 = \frac{dE}{dt} \ . \tag{4.6}$$

This power is exactly the energy removed from the particle per unit time, due to the interaction with the detection system. Setting $f(t) = 0$ and multiplying the equation of motion by $m\dot{z}$, the expression

$$m\dot{z}\ddot{z} + m\gamma_z \dot{z}^2 + m\omega_z^2 \dot{z} z = 0 \tag{4.7}$$

is obtained. Time-integration of this result gives the first integral

$$\frac{1}{2} m\dot{z}^2 + \frac{1}{2} m\omega_z^2 z^2 = -\int dt \ \ m\gamma_z \dot{z}^2 \ . \tag{4.8}$$

The right hand side of Eq. (4.8) represents the total energy of the particle, while the left hand side is due to dissipation. Identifying

$$P = R_p I_p^2 = m\gamma_z \dot{z}^2 \tag{4.9}$$

and accounting for the coordinate-to-current relation given in Eq.4.1, the expression

$$\gamma_z = \frac{R_p}{m} \frac{q^2}{D^2} \Leftrightarrow \tau_z = \frac{m}{R_0} \frac{D^2}{q^2} \tag{4.10}$$

is found. This equation relates detector properties $R_p$, trap properties $D$, and particle properties $m$ an $q$ to damping $\gamma_z$.

Utilizing this relation, Eq. (4.5) can be rewritten as

$$m\frac{D^2}{q^2}\frac{d}{dt} I_p + R_p I_p + m\omega_z^2 \int dt \ \frac{D^2}{q^2} I_p = 0 \ . \tag{4.11}$$

The structure of this equation opens an interesting interpretation of the trapped charged particle. Identifying

$$l_p = m\frac{D^2}{q^2} \quad \text{and} \quad c_p = \frac{1}{m\omega_z^2}\frac{q^2}{D^2} \ , \tag{4.12}$$

Eq. (4.11) represents the differential equation describing a series tuned circuit! Actually, the particle-detector interaction shows properties legitimating this interpretation.

A clear understanding is obtained, taking into account that the particle in an ideal trap is an intrinsically undamped oscillator. Excited at its resonance frequency, it acts as a perfect short between the trap electrodes. This is exactly the behavior of a series tuned circuit at its resonance frequency.

## *4.3 Axial Detection - Noise-Dip*

### *4.3.1 Basic Concept*

The interpretation given at the end of the previous section is of great importance for single particle detection. This property is applied to measure particle frequencies in thermal equilibrium with the detection system. To describe this in detail, a charged particle represented by an undamped series tank circuit with inductance $l_p$ and capacitance $c_p$ is connected in parallel to a real resistor $R_p$ (Fig. 4.2). Regarding the transfer-function of the system and


Figure 4.2: a.) Trapped particle in interaction with the detection electronics. The trap is represented by two parallel plates in parallel to a resistor $R_p$. $e_{\text{th}}$ represents the thermal noise of the resistor. b.) equivalent circuit of a.). The particle is represented by a series lc-circuit with equivalent inductance $l_p$ and equivalent capacitance $c_p$ (see Eq.(4.2)).

calculating its real part

$$\text{Re}\,(Z) = \frac{R_p\left(\omega l_p - \frac{1}{\omega c_p}\right)^2}{R_p^2 + \left(\omega l_p - \frac{1}{\omega c_p}\right)^2} \tag{4.13}$$

is obtained. Introducing the resonance frequency of the particle $\omega_0 = (l_p c_p)^{-1/2}$, this can be rewritten as

$$Re\,(Z) = \frac{R_p}{1 + \frac{R_p^2}{\omega_0^2 l_p^2}\left(\frac{1}{\frac{\omega}{\omega_0} - \frac{\omega_0}{\omega}}\right)^2} = \frac{R_p}{1 + \frac{R_p^2}{\omega_0^2 l_p^2}\left(\frac{\omega\omega_0}{\omega^2 - \omega_0^2}\right)^2} \ . \tag{4.14}$$

From this form it can be read that

1. on resonance $\omega = \omega_0$ the real part of the total impedance vanishes, which means that the particle series *lc*-circuit acts as a perfect short (*particle-dip*), and

2. far from resonance the real part of the impedance is given by the value of $R_p$.

Calculating the full width at half maximum of the *particle-dip*,

$$\Delta\nu_z = \frac{1}{2\pi}\frac{1}{\tau_z} = \frac{1}{2\pi}\frac{R_p}{m}\frac{q^2}{D^2} \tag{4.15}$$

is obtained. Obviously, the tank-circuit damps the particle leading to a line-width which is defined by the properties of the detector. For few-particle ensembles with particle number $N$, the line-width is directly proportional to the number of particles stored in the trap [68]

$$\Delta\nu_z(N) = \frac{N}{2\pi}\frac{1}{\tau_z} = \frac{N}{2\pi}\frac{R_p}{m}\frac{q^2}{D^2} \ . \tag{4.16}$$

This is utilized later (see chapter 5) to count trapped protons and to reduce a proton cloud to one individual particle.

The phenomenon that the particle shorts the parallel resistance $R_p$ of the detector, is utilized experimentally to measure its axial frequency. To understand the measuring principle, thermal noise has to be taken into account. Due to the Johnson-Nyquist theorem [65, 66] the rms-power generated per unit bandwidth by a resistor $R_p$ at temperature $T$ is given by

$$u_n = \sqrt{4k_B T R} \quad [\mathrm{V}\cdot\mathrm{Hz}^{-0.5}] \ , \tag{4.17}$$

were $k_B$ is the Boltzmann-constant. Combining this formula with Eq. (4.14)

$$u_n = \sqrt{4k_B T \frac{R_p}{1 + \frac{R_p^2}{\omega_0^2 l_p^2}\left(\frac{\omega\omega_0}{\omega^2 - \omega_0^2}\right)^2}} \tag{4.18}$$

is obtained. This means that the thermal noise of the detection system is shorted by the particle in parallel. Consequently, in the thermal noise spectrum of the detector a dip at the particles resonance frequency occurs (see Fig. 4.3). Fitting Eq. (4.18) to such a noise spectrum, the eigenfrequency of the particle is yielded. Thus, particle detection by means of the *noise-dip method* provides frequency information in thermal equilibrium with the detection system. Typical thermal particle amplitudes are in a range of only one (cyclotron-mode) to fifty (axial-mode) microns. Compared to the detection of an excited particle, where amplitudes up to some millimeters are typical, noise-dip detection is "not"[2] sensitive to trap imperfections (see section 2.3.1) and special relativity [37].

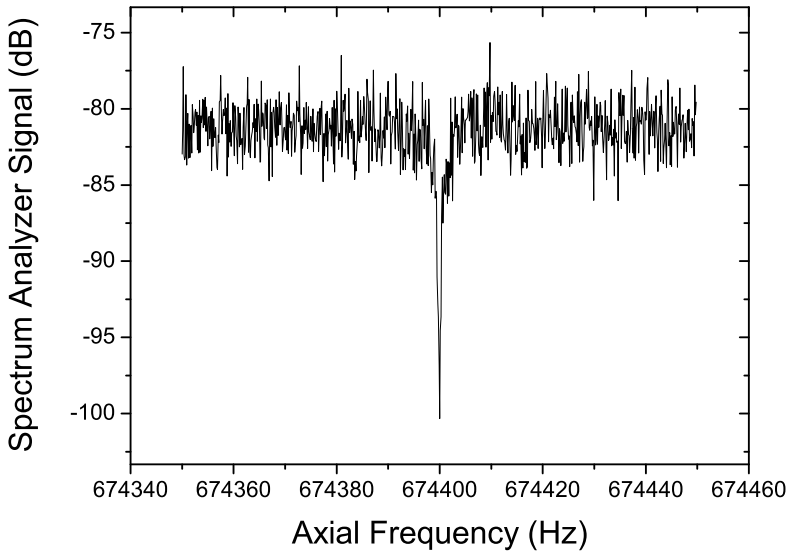


Figure 4.3: Simulated noise spectrum of a single particle in parallel to a resistor $R_p$.

### *4.3.2 Full Result*

In the simplified model presented above the complex impedance $Z$ of the detection system was replaced by a real resistance $R_p$. This describes the experimental reality only, if the

[2]...depending on the level of precision but in case of our experiment not to be taken into account.

eigenfrequency of the particle is tuned to resonance with the detection system exactly. In case of a detuning $\nu_0 \neq \nu_i$ the interaction of the complex impedances of the trapped particle and the detection system leads to a "dispersive" particle-dip which is shown in Fig. 4.4. Since frequency detection by means of dispersive spectra is not applied in our

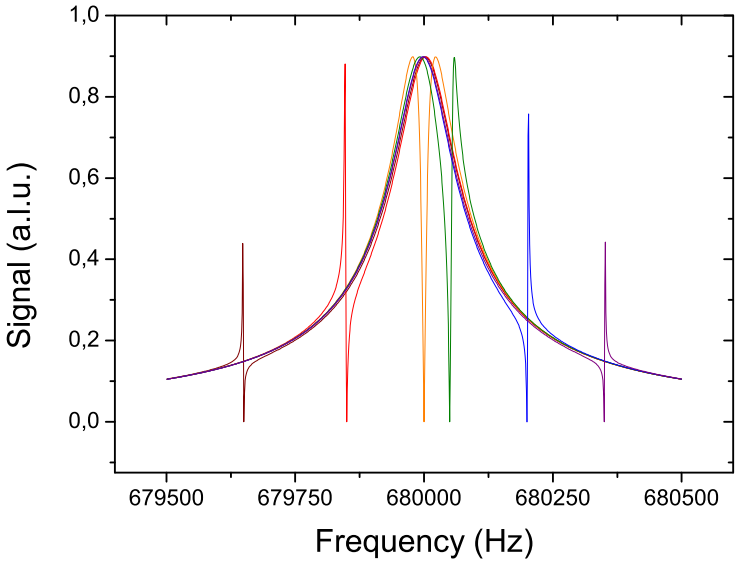


Figure 4.4: Result of the full solution of particle-detector interaction. If the particle is detuned against the resonance frequency of the detection system $\nu_0 \neq \nu_i$, "dispersive" dip-spectra are observed.

experiment, for further discussion we refer to the experimental work [42, 51]. A detailed theoretical discussion of the off-resonant particle-detector interaction, even for different particle numbers $N$ is found in [67] and [68].

### *4.4 Effective Electrode Distance*

In the previous sections expressions for the cooling time constant $\tau$ and the linewidth $\Delta\nu_z$ of the noise-dip were derived. Both expressions depend on the geometry of the trap indicated by introducing the parameter $D$, which is called *effective electrode distance*. For cylindrical Penning traps this parameter can be calculated analytically. The publication of the full

calculation is in progress [69]. In this section the basic mathematical idea and the results for different pick-up geometries are presented. In chapter 6, experimental results and their comparison to theory are discussed.

As explained in section 4.1, a charged particle stored in a Penning trap induces image charges on the surfaces of the trap electrodes. In order to calculate $D$, the portion of the total surface charge induced on a certain electrode has to be evaluated. In classical electrodynamics a simple expression relating the surface-charge $\sigma$ induced on a surface and the normal component of the induced electric field $E_n$ is derived [70]

$$\sigma = \frac{1}{4\pi} E_n = -q(\vec{\nabla} G_D|\vec{n}) \ , \tag{4.19}$$

where $G_D$ is the Green's-function for Dirichlet boundary conditions and $\vec{n}$ the normal vector of the surface. Inserting the Green's-function for a charge inside a cylindrical "box" [70],

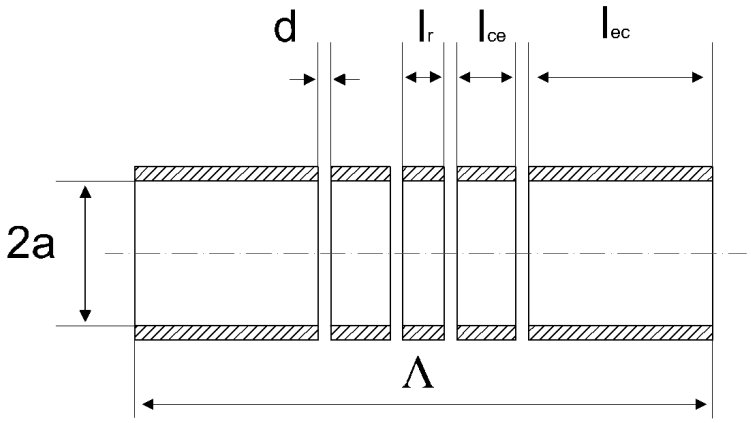


Figure 4.5: Schematic of a five-pole Penning trap for the definition of the variables used in Eq. (4.21) and (4.22).

the charge induced on the surface is expressed as

$$\begin{aligned} \sigma\left(\rho_1, \phi_1, z_1, \phi_2, z_2\right) &= \frac{q}{\pi a \Lambda} \sum_{m=0}^{\infty} \sum_{n=1}^{\infty} \cos\left(m\left(\phi_1 - \phi_2\right)\right)\left(2 - \delta_{m,0}\right) \\ &\times \left( \cos\left(\frac{(2n-1)\pi}{\Lambda} z_1\right) \cos\left(\frac{(2n-1)\pi}{\Lambda} z_2\right) \frac{I_m\left(\frac{(2n-1)\pi}{\Lambda}\rho_1\right)}{I_m\left(\frac{(2n-1)\pi}{\Lambda}a\right)} \right) \end{aligned}$$

$$+ \quad \frac{q}{\pi a \Lambda} \sum_{m=0}^{\infty} \sum_{n=1}^{\infty} \cos\left(m\left(\phi_1 - \phi_2\right)\right)\left(2 - \delta_{m,0}\right)$$
$$\times \quad \left( \sin\left(\frac{(2n)\pi}{\Lambda} z_1\right) \sin\left(\frac{(2n)\pi}{\Lambda} z_2\right) \frac{I_m\left(\frac{(2n)\pi}{\Lambda}\rho_1\right)}{I_m\left(\frac{(2n)\pi}{\Lambda}a\right)} \right) \ , \tag{4.20}$$

where $\Lambda$ is the length of the box, $\rho_1, \phi_1, z_1$ are the coordinates of the particle, $a, \phi_2, z_2$ are the coordinates of the surface, and $I_m(x)$ are modified Bessel-functions of first kind. Integrating this expression over the surfaces of a specific electrode geometry and combining the equations of motion with certain physically motivated approximations and series expansions, the effective electrode distance $D$ is obtained. Different expressions for axial pick-up or radial pick-up can be derived. The variables included in the given solutions are defined graphically in Fig. 4.5. For the detection of the axial frequency, where the signal is picked up with a cylindrical ring of length $l_k$ located at a distance $l_r/2 + d$ from the trap center, the result is

$$D_{\mathrm{eff,z}} = \frac{\Lambda}{8} \left( \sum_{n=1}^{\infty} \frac{\sin\left(\frac{n\pi}{\Lambda} l_{\mathrm{ce}}\right) \sin\left(\frac{n\pi}{\Lambda}\left(l_r + 2d + l_{\mathrm{ce}}\right)\right)}{I_0\left(\frac{2n\pi}{\Lambda}a\right)} \right)^{-1} \ . \tag{4.21}$$

For the detection of the cyclotron frequency where the signal is picked up with a radially segmented electrode located at a distance $l_r/2 + d$ from the trap center the calculation gives

$$D_{\mathrm{eff},+} = \frac{\pi\Lambda}{8} \left( \sum_{n=1}^{\infty} \frac{\left(\left(\cos\left(\frac{2n-1}{2\Lambda}\pi\left(l_r + l_{\mathrm{ce}}\right)\right) \sin\left(\frac{2n-1}{2\Lambda}\pi l_{\mathrm{ce}}\right)\right)\right)}{I_1\left(\frac{2n-1}{\Lambda}\pi a\right)} \right)^{-1} \ . \tag{4.22}$$

Picking up the cyclotron signal with the central ring electrode

$$D_{\mathrm{eff}} = \frac{\pi\Lambda}{4} \left( \sum_{n=1}^{\infty} \frac{\left(\left(\sin\left(\frac{2n-1}{2\Lambda}\pi l_r\right)\right)\right)}{I_1\left(\frac{2n-1}{\Lambda}\pi a\right)} \right)^{-1} \tag{4.23}$$

is obtained. These compact formulas can be evaluated easily with computer algebra systems as *Simulink-MatLab* or *Wolfram-Mathematica*.

In our experiment two Penning traps are operated, the precision trap and the analysis trap. The effective electrode distances $D$ for different pickup geometries are shown in Tab. 4.1. The results of the formalism are suited to decide which pickup geometry leads to optimum cooling time, and in case of dip-detection, to best signal-to-noise ratio. In our experiment all

Table 4.1: Overview on the effective electrode distances for the traps used in the proton $g$-factor experiment. Abbreviations: CE - Correction Electrode / EC - End Cap / RE - Ring Electrode.

| Pickup | Analysis Trap | Precision Trap |
|---|---|---|
| Axial CE (mm) | 4.12 | 7.60 |
| Axial EC (mm) | 4.53 | 8.69 |
| Axial CE + EC (mm) | 2.89 | 5.58 |
| Cyclotron RE (mm) | - | 23.96 |
| Cyclotron CE (mm) | - | 15.59 |
| Cyclotron EC (mm) | - | 42.49 |
| Cyclotron CE + EC (mm) | - | 14.23 |

signals, the axial- as well as the cyclotron signal, are picked up at the correction electrodes. Detection at only one electrode is favorable to keep resistive load on the detection system low.

Compared to endcap-pickup, the correction electrode signals lead in case of the axial detection system to nearly the same damping. Since the endcaps have a larger geometry, leading to higher system capacitance, signal pickup at the correction electrode is favored.

### *4.5 Feedback - Active Particle-Temperature Control*

The setup of an amplifier with a high-$Q$ tank circuit connected to its input is challenging work, since such a system combines an oscillator (tank circuit) with a drive (amplifier). Such combinations tend to oscillate.

What seems to cause problems at the first glance, can be utilized experimentally to manipulate particle temperature by controlled feedback [71, 72] (experimental results are presented in section 6.11 and 7.4). The concept of active electronic feedback is shown in Fig.4.6. The detector is represented by an ideal resistor $R_p$ with a thermal noise source $e_{th}$ in series. The amplifier is modeled as an ideal amplifier with equivalent input noise $e_n$. The signal is picked-up, amplified, phase shifted and fed back to the trap. The feedback-strength (also

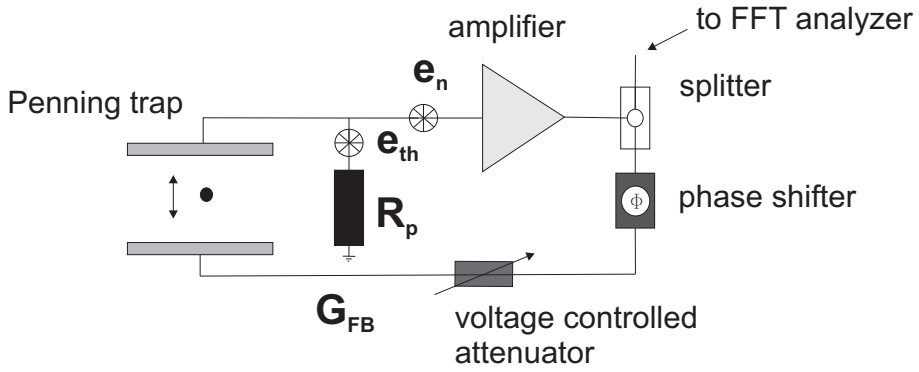


Figure 4.6: Experimental realization of active particle-temperature control by application of phased feedback. The detector is represented by the ideal resistor $R_p$ in series to a thermal noise source $e_{th}$. The amplifier is represented by a noiseless amplifier with effective input noise $e_n$. The signal is amplified and fed back to the trap. The feedback gain is adjusted with a voltage controlled attenuator. The phase is adjusted with a phase shifter.

feedback-gain) $G_{\mathrm{FB}}$ is adjusted by a voltage controlled attenuator.

Consider a voltage drop $V_p$ due to the particle current $I_p$ flowing through a resistor $R_p$. If the signal is instantaneously fed-back to the particle with feedback-gain $G_{\mathrm{FB}}$, the feedback signal manipulates its motion as indicated in Fig. 4.7 a.). For the particle itself the effect of $G_{\mathrm{FB}}$ looks like a resistor with modified absolute value $R_{\mathrm{eff}}$ and temperature $T_{\mathrm{eff}}$ as shown in Fig. 4.7 b.).

To evaluate how these effective values are affected by $G_{\mathrm{FB}}$, we take into account that the po-

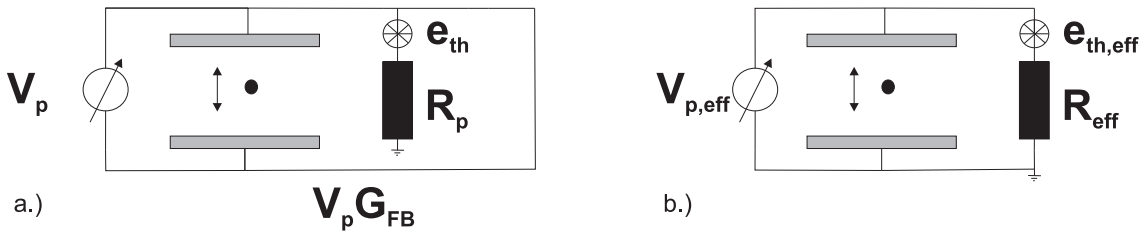


Figure 4.7: a.) Schematic of a particle in a Penning trap with application of feedback. The detector signal is fed back to the particle with a feedback gain $G_{\mathrm{FB}}$. In b.) the details shown in a.) are replaced by an effective voltage $V_{\mathrm{p,eff}}$ and an effective parallel resistance $R_{\mathrm{p,eff}}$.

tential difference $V_p$ in case of active feedback has to be identical to the case where effective

values $R_{\mathrm{eff}}$ are used

$$V_p = I_p R_p \pm G_{\mathrm{FB}} I_p R_p \tag{4.24}$$

$$V_{\mathrm{p,eff}} = I_p R_{\mathrm{eff}} \ . \tag{4.25}$$

Equating both relations it is found that

$$R_{\mathrm{eff}} = R_p \left(1 \pm G_{\mathrm{FB}}\right) \tag{4.26}$$

defining the effective resistance seen by the particle if feedback is applied. To derive the effective temperature the same argumentation as in case of the resistance is used for the fluctuating voltages seen by the particle, leading to

$$T_{\mathrm{eff}} = T_0 \left(1 \pm G_{\mathrm{FB}}\right) \ . \tag{4.27}$$

The ratio $T_i/R_i$ is a fluctuation-dissipation invariant. Active electronic feedback applied to the detection system obviously modifies the temperature of the particle. Negative feedback reduces, while positive feedback increases the particle temperature, respectively. Therefore, by application of negative feedback, the particle can be cooled to temperatures far below the physical temperature of the apparatus. For precision Penning trap experiments this is an important result, since linewidths, and thus, experimental precision scales with temperature (see chapter 2). Reducing the temperature of the particle by means of negatively phased feedback, the linewidths of the cyclotron resonance, and the Larmor resonance are reduced and thus, the experimental precision is increased (see chapter 7 and 8).

For real experimental conditions amplifier noise has to be taken into account. At a certain level of feedback-gain $G_{\mathrm{FB}} \approx 1$, the noise added by the amplifier causes additional heating and the linear scaling of temperature $T_{\mathrm{eff}}$ and detector resistance $R_{\mathrm{eff}}$ modifies. The minimum temperature, which is achieved by active electronic feedback, depends on the signal-to-noise ratio of the detection system. For a detailed discussion of noisy feedback we refer to [73].

## 4.6 Noise Matching

### 4.6.1 Peak-Detection

For the experimental realization of a highly-sensitive detection system amplifier noise and effects of $Q$-value degeneration have to be considered. In order to characterize the quality of a detection system the signal-to-noise ratio (SNR)

$$\mathrm{SNR} = \frac{2\pi\nu Q L I_p}{\sqrt{\sum_k e_k^2}} \tag{4.28}$$

is introduced. Here the coefficients $e_k$ account for different noise sources as thermal noise [65] and active electronic noise [74].

To built a detector with high signal-to-noise ratio a detailed understanding of the system is necessary. Therefore the model shown in Fig.4.8 is introduced. The oscillating particle

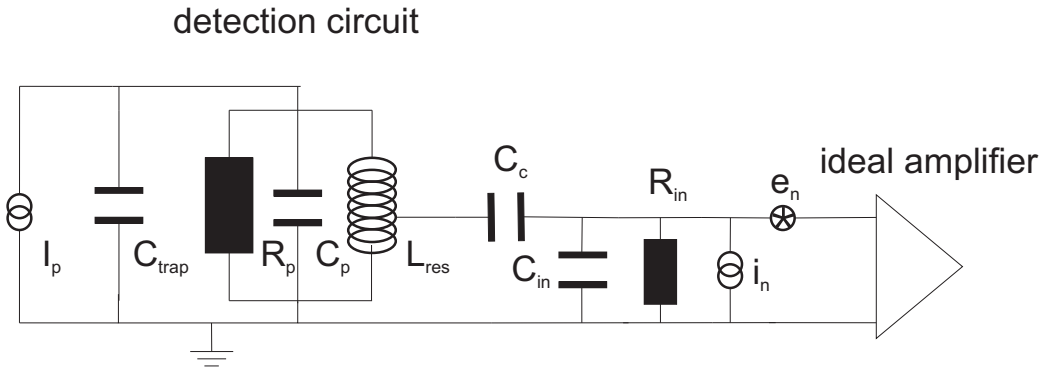


Figure 4.8: Detailed schematic of a single particle detection system. The particle is modeled as a current source $I_p$ in parallel to the parallel tank circuit represented by an inductance $L$, an effective parallel resistance $R_p$ and a parallel capacitance $C_p$. The trap is represented by its capacitance $C_{\mathrm{trap}}$. The amplifier is modeled as a parallel $RC$ circuit with the components $R_{in}$ and $C_{in}$. The noise characteristics of the amplifier is taken into account by the current noise source $i_n$ and the voltage noise source $e_n$. Amplifier and tank circuit are connected by the coupling capacitance $C_c$.

is modeled as a current source $I_p$ in parallel to the tank circuit represented by the effective parallel resistance $R_p$, the inductance $L$ and the capacitance $C_p$. The signal is connected to the amplifier with a coupling capacitance $C_c$. The input of the amplifier is modeled

as a parallel $RC$ circuit with input resistance $R_{\mathrm{in}}$ and input capacitance $C_{\mathrm{in}}$. The noise characteristics of the amplifier is modeled by a current source $i_n$ in parallel to the input $RC$ and a voltage source $e_n$.

In [74] a very similar model is presented including approximations for low $R_p$, very high $R_{\mathrm{in}}$ and low frequencies in the MHz range. For the setup of detection systems with very high performance and high frequencies, e.g. the modified cyclotron frequency of 28.9 MHz, the damping of the tank circuit by means of the input of the amplifier has to be taken into account. Due to the coupling of $R_{\mathrm{in}}$ to the resonator, the parallel resistance of the system is

$$R_{\mathrm{sys}} = \left(\frac{C_c + C_{\mathrm{in}}}{C_c}\right)^2 \frac{R_p R_{\mathrm{in}}}{R_p + \left(\frac{C_c+C_{\mathrm{in}}}{C_c}\right)^2 R_{\mathrm{in}}} \ . \tag{4.29}$$

Furthermore, the effective system capacitance $C_{\mathrm{sys}}$ modifies

$$C_{\mathrm{sys}} = C_p + \frac{C_c}{C_c + C_{\mathrm{in}}} C_{\mathrm{in}} \ , \tag{4.30}$$

due to $C_{\mathrm{in}}$. Defining the coupling factor $\kappa = \frac{C_c}{C_c+C_{\mathrm{in}}}$ the voltage signal at the input of the amplifier can be written as

$$V = I_p R_p \left(\frac{1}{1 + \kappa^2 R_p / R_{\mathrm{in}}}\right) \kappa \ . \tag{4.31}$$

The total spectral noise density applied to the input of the amplifier $e_{tot}$ is a combination of the thermal noise of the tank circuit $e_{th} = \sqrt{4k_B T R_{\mathrm{sys}}}$, the voltage noise $e_n$ and the current noise $i_n$. At the typical parameters of our experiment the current noise can be neglected, since $e_{\mathrm{th}} \gg \kappa^2 R_p i_n$. Thus, the total noise of the system denotes

$$e_{tot}^2 = e_n^2 + 4k_B T R_{\mathrm{sys}} \kappa^2 \ , \tag{4.32}$$

leading to the explicit form of the signal-to-noise ratio

$$\mathrm{SNR}^2 = \frac{\left(I_+ R_p \kappa\right)^2}{\left(1 + \kappa^2 R_p / R_{\mathrm{in}}\right)^2 e_n^2 + 4k_B T R_p \left(1 + \kappa^2 R_p / R_{\mathrm{in}}\right) \kappa^2} \ . \tag{4.33}$$

Adjusting the coupling factor $\kappa$, this expression can be maximized, leading to optimum signal-to-noise ratio. A simple calculation gives the ideal coupling factor

$$\kappa_{\mathrm{opt}} = \left(\frac{2e_n^2}{8k_B T R_p^2 / R_{\mathrm{in}} + 2R_p^2 / R_{\mathrm{in}}^2 e_n^2}\right)^{1/4} \approx \left(\frac{e_n^2}{4k_B T R_p^2 / R_{\mathrm{in}}}\right)^{1/4} \ . \tag{4.34}$$

The last approximation $4k_BTR_{\rm in} \gg e_n^2$ holds for technically realistic situations. Combining this expression with Eq. (4.33), and accounting for $1 \gg \kappa^2 R_p/R_{\rm in}$, results in

$$\mathrm{SNR} = I_p \sqrt{\frac{R_p}{4k_BT\left(1+\frac{e_n}{k_BTR_i}\right)}} = \frac{I_p R_p}{e_{\rm th}(R_p)\sqrt{\left(1+\frac{e_n}{k_BTR_i}\right)}} \ . \tag{4.35}$$

The signal to noise ratio certainly depends on the excitation amplitude of the particle. But the larger the factor

$$\mathrm{SNR}/I_p = \sqrt{\frac{R_p}{4k_BT\left(1+\frac{e_n}{k_BTR_i}\right)}} \tag{4.36}$$

the more sensitive the detection system.
This expression is crucial for the setup and optimization of a single particle detector.
Summarizing the meaning of Eq.(4.35):

1. Within given experimental constraints the unloaded parallel tank circuit should be optimized to maximum $R_p$.

2. It is aimed to built an amplifier with high input resistance $R_{in}$ at low equivalent input noise $e_n$.

3. Cryogenic operation of the detection system increases the sensitivity, since thermal noise, and in most cases (see section 4.11) active electronic noise is lowered. Furthermore, superconducting materials can be used, leading to higher $R_p$.

The experimental techniques to obtain optimum $Q$ for the tank circuits is described in section 4.9. Details of the amplifier design and experimental realization are presented in section 4.7 and 4.10ff..

### *4.6.2 Dip-Detection*

For the discussion of the axial dip detection the same model as described in the previous subsection is used. In contrast to the considerations made there, the signal-to-noise ratio has to be defined in a different way. For the detection of the noise-dip, the difference between

the noise floor caused by the equivalent input voltage noise $e_n$ of the amplifier and the thermal noise maximum in the center of the resonance is of interest (see Fig. 4.24). Since voltage noise $e_n \ll e_{th}$, it can be neglected in the numerator of the signal-to-noise ratio

$$\mathrm{SNR}_{Dip} = \frac{\sqrt{e_{th}^2 + (R_p i_n \kappa^2)^2}}{e_n} = \sqrt{\frac{4k_B T \left(\frac{\kappa^2 R_p}{1+\kappa^2 R_p/R_{in}}\right) + \left(\frac{\kappa^2 R_p}{1+\kappa^2 R_p/R_{in}}\right)^2 i_n^2 \kappa^4}{e_n^2}} \,. \tag{4.37}$$

Due to the scaling at least with powers of

$$\propto \sqrt{\left(\frac{\kappa^2}{1+\kappa^2 R_p/R_{in}}\right)} \tag{4.38}$$

a maximum of this expression does not exist, or in other words:
If $\kappa$ is small, the total parallel resistance $R_p$ rises but simultaneously signal strength is lost. These two effects compensate in the signal-to-noise ratio. Ideal matching for dip detection has many degrees of freedom, since the eigenfrequency of the particle is obtained from a fit to the dip in the noise spectrum of the detector. The coupling factor $\kappa$ modifies the signal-to-noise ratio, the linewidth of the dip, and the noise temperature of the detection system due to current-noise feedback. We optimize the coupling factor for dip detection by means of a data-simulation algorithm, based on experimental data as input parameters (input resistance, current noise, and voltage noise of the amplifier / parameters of the free resonator). The algorithm gives the coupling factor for best frequency resolution at fastest measuring time.

### *4.7 Amplifiers*

The application of knowledge about rf-amplifier design, which is found in textbooks, does not really fit experimental reality. Setting up a classical textbook amplifier on a standard pin board and connecting a high-$Q$ resonator to its input will lead to oscillations or $Q$-value degeneration. The lower the $Q$-value degeneration the higher the probability that the systems tends to oscillate. To setup a high-performance detection system the challenge is to combine both, high-$Q$ and stable performance. Therefore, it is crucial to understand the mechanisms, which cause the undesirable effects described.

The amplifiers built for the detection systems are two stage amplifiers based on GaAs-field effect transistors (FET). Due to the small band-gap of GaAs these devices work under cryogenic conditions [75, 76, 77]. The first stage of the amplifier is in common source layout, giving high voltage gain at high input impedance. As a second stage a source follower is used. While the first stage provides the voltage gain, the second stage matches the high output impedance of the first stage to the $50\,\Omega$ impedance of the rf-lines.

### *4.7.1 Parasitic Feedback and Regeneration*

Stability problems of the detection system are caused by parasitic electronic feedback. The mechanism is the same as described in section 4.5. If the parasitic feedback gain $G_{\mathrm{FB}}$ is $> 1$, the system starts to oscillate. To develop a deeper understanding of the mechanisms a model-FET is introduced. In Fig.4.9 a.) the model of a "real" FET is shown. The input of

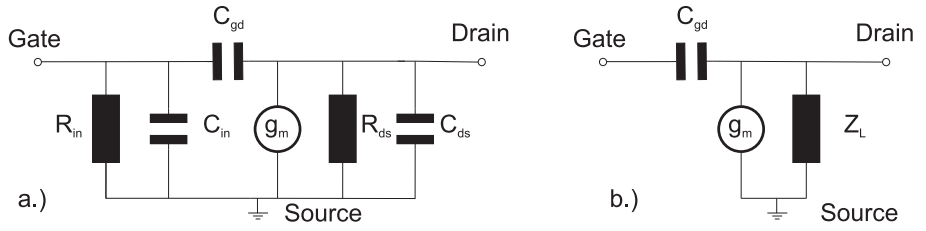


Figure 4.9: a.) Model of a real FET. The input of the FET is modeled as a RC-circuit with input resistance $R_{in}$ and input capacitance $C_{in}$. The amplification characteristics is modeled by the transconductance $g_m$, which is in parallel to a drain to source resistance $R_{DS}$. These components are coupled to the input by means of the gate-to-drain capacitance $C_{GD}$.
b.) Simplified model of the FET, which is used for the discussion of parasitic feedback. The FET has an ideal input, which is coupled to the drain-to-source resistances $R_{DS}$ and the tranconductance $g_m$.

the FET is modeled as an RC-circuit with input resistance $R_{\mathrm{in}}$ and input capacitance $C_{\mathrm{in}}$. The amplification characteristics is modeled by the transconductance $g_m$ which is in parallel to a drain to source resistance $R_{\mathrm{DS}}$. These components are coupled to the input by means of the gate-to-drain capacitance $C_{\mathrm{GD}}$. For the description of parasitic feedback the simplified model shown in Fig.4.9 b.) is used. The FET is an ideal amplifier with transconductance

$g_m$ connected to a load impedance $Z_L$. Drain and gate are connected by means of $C_{\mathrm{GD}}$. In this context, it is interesting to evaluate the effective input impedance of the FET seen by the resonator if the load impedance is varied at given $C_{\mathrm{GD}}$.

The behavior of the model-FET, including the load-impedance, is described by four equations:

$$I_S = I_G + I_D \tag{4.39}$$

$$I_G = \frac{1}{\chi_{\mathrm{GD}}}(V_G - V_D) \tag{4.40}$$

$$V_D = -I_D Z_L \tag{4.41}$$

$$I_S = g_m V_G \tag{4.42}$$

The first three equations are simply due to Kirchhoffs laws, while the fourth equation accounts for the performance of an ideal FET [75]. From these equations, the effective series-input impedance looking into the gate of the amplifier is yielded:

$$Z_{in} = \frac{V_G}{I_G} = \frac{Z_L + \chi_{GD}}{1 + g_m Z_L} \; . \tag{4.43}$$

To discuss the meaning of this equation different loads $Z_L$ are inserted. Transforming the series impedance to a parallel input-RC circuit we obtain:

1. Resistive load at the output of the FET leads to an additional capacitance $C_{\mathrm{in}}$ and an effective parallel resistance $R_{\mathrm{in}}$. With increasing resistive load the parallel input resistance decreases.

2. Purely capacitive load puts resistive load to the input of the amplifier effectively lowering the $Q$-value of the system.

3. Inductive load adds negative resistive load to the amplifier input being equivalent to positive feedback and increasing the $Q$-value of the system. This leads effectively to an increase of particle temperature. If the feedback is strong, the amplifier starts to oscillate.

In conclusion, parasitic reactive loads should be avoided. Especially inductive loads cause positive feedback and lead to instability.

### *4.7.2 Resistive- and Dielectric Losses*

Another enemy of highly sensitive detection systems are resistive loss mechanisms. Connecting a high-$Q$ resonator to a lossy component decreases $Q$. Therefore, the input resistance of the amplifier should be high.

Besides the obvious resistive losses in conductors another loss mechanism exists - dielectric losses. Due to polarization currents occurring in every dielectric material, power is dissipated. The quantity which characterizes the rf-quality of a material is the dielectric loss tangent defined as

$$\tan(\delta) = 2\pi\nu C_s R_s = \frac{1}{2\pi\nu C_p R_p} \,, \tag{4.44}$$

being the ratio of reactive to dissipative power in a device with capacitance $C_s$ or $C_p$, respectively. The first expression defines the loss tangent for a series circuit while the second is the same for a parallel circuit.

Adequate materials for rf-applications with low loss tangents are PTFE ($\tan(\delta) = 10^{-4}$) or sapphire ($\tan(\delta) = 10^{-5}$). Standard PCB materials as FR4 or G10 have larger loss tangents (typically $\tan(\delta) = 0.02$).

As an example, the self capacitance of a standard amplifier board is around 2 pF. Machined from FR4 the equivalent series resistance at 28.9 MHz is around 50Ω! Coupled 1/1 to the cyclotron resonator, this would lower the $Q$-value to $\approx 20$.

Due to the simple scaling of Eq. (4.44) with capacitance it could be concluded, that the higher the capacitance of the lossy component, the smaller the effect of the loss-factor, which is not true. The lossy material is only one component in a composition. Connecting a lossy component with given $\tan(\delta) \approx \delta$ and capacitance $C_{\text{loss}}$ in parallel to a lossless capacitor $C_0$ the equivalent series resistance of the whole system is given by:

$$R_{\text{S,eff}} = \frac{1}{(1 + C_0/C_{\text{loss}})^2 + \delta^2 (C_0/C_{\text{loss}})^2} \frac{\delta}{\omega C_{\text{loss}}} \approx \frac{1}{(1 + C_0/C_{\text{loss}})^2} \frac{\delta}{\omega C_{\text{loss}}} \,. \tag{4.45}$$

This expression has a maximum for $C_{\text{loss}} = C_0$. The slope in case of $C_{\text{loss}} < C_0$ is much steeper as if $C_{\text{loss}} > C_0$. Since the total system capacitance should be reduced to the possible minimum, the capacitance of the lossy element should be kept small in comparison to the total system capacitance.

### *4.8 Experimental Realization - Test Setup*

In the following sections results of noise-, amplification-, and $Q$-value measurements are presented. Data at room temperature and 4 K are shown. All results are based on measurements with a *HP3755* network analyzer. For the $Q$-value determination the transfer function of the device under test (DUT) is recorded. The quality factor is obtained by measuring the resonance frequency $\nu_0$ and the 3 dB width $\Delta\nu_{3dB}$ where

$$Q = \frac{\nu_0}{\Delta\nu_{3dB}} \ . \tag{4.46}$$

For the $Q$-value measurements care is taken to focus on avoiding limitations due to the input load of the network analyzer. Therefore the analyzer is weakly coupled to the DUT. The excitation signal is loosely coupled to the input of the tank circuit by means of an air capacitor with $C_p < 0.1$ pF. The signal is picked up with a single conducting loop near the cold end of the resonator and amplified with an rf amplifier (*MiniCircuits ZFL-500LN*).
The network analyzer is also used to measure the amplification factor of the tested amplifiers. For every amplification measurement the transmission characteristics of the signal lines were normalized.
Amplifier noise measurements are performed with a *Rohde and Schwarz FSP 13* spectrum analyzer, which directly gives the spectral noise density applied to its input. To avoid that the background noise of the analyzer $e_A$ modifies the experimental result, the signals are amplified with an ultra low noise amplifier (*MiniCircuits ZFL-500LN*). Measuring the amplification factor $G_A$ of the amplifier and the noise amplitude $e_F$ at the input of the spectrum analyzer, the equivalent input-noise of the DUT is obtained

$$e_n = \frac{1}{G_A}\sqrt{\frac{1}{G_Z^2}\left(e_F^2 - e_A^2\right) - e_Z^2} \ . \tag{4.47}$$

In order to test the quality of our noise measurements the equivalent input noise was measured for different amplifiers and compared with datasheet values, which were reproduced by our measurements.
The amplifiers are biased with home made ultra stable voltage sources, alternatively with a battery based voltage source. The experimental result did not depend on the biasing

technique. For cryogenic test measurements the devices under test are cooled by means of a pulse tube cooler (*Vericold Technologies - 4 K Pulse Tube*) [52]. The temperature is measured with *Lakeshore* sensors (*CERNOX CU CX-1050*) mounted to the DUT.
The radio frequency signals are guided into the vacuum chamber with standard BNC-feedthroughs. Inside the vacuum chamber special cryogenic coaxial rf-lines with brass conductor and german silver shields (*GVL-Cryoenineering*) are used. The transmission lines are adequately heat sunk at the 50 K stage of the cooler.

## *4.9 Experimental Realization - Resonators*

### *4.9.1 Basic Remarks and Geometrical Design*

The detection systems consist of two key-pieces, a cryogenic ultra low-noise amplifier and a high-$Q$ tank circuit. What has been described as an effective parallel RLC-circuit, is in experimental reality a solenoidal coil with inductance $L$ wound on a PTFE core and mounted in a cylindrical housing [78]. The tank circuit properties of such a system arise from parasitic effects as the self capacitance $C_p$ of the inductor, the series resistance $R_s$ of the coil's wire and resistive losses in the cylindrical housing.
For our experiment two detectors are designed, one for the axial frequency of $\nu_z \approx 680\,\mathrm{kHz}$ and another for the cyclotron frequency $\nu_+ \approx 28.9\,\mathrm{MHz}$. Drafts of both resonators are shown in Fig. 4.10 a.) and b.) respectively. The cyclotron tank circuit is made of oxygen-free electrolytic (OFE) copper, while the resonator for the axial frequency is machined from superconducting NbTi. This alloy is a type II superconductor with a critical temperature of $T_c \approx 9.5\,\mathrm{K}$ and an upper critical field strength of $B_{c2} \approx 14.5\,\mathrm{T}$. Therefore, the superconducting phase does not collapse in the magnetic field of the Penning trap. In vanishing magnetic field, the only loss mechanism in superconducting material is due to the inertial mass of the cooper pairs. The mass affects the appearance of electrical stray fields interacting with the normal fluid component of the superconductor. Adding a magnetic field to the superconductor, additional loss mechanisms as flux-flow and flux-creep resistances occur[81]. These loss mechanisms scale proportional to $\nu^3$. For low frequencies as the axial frequency $\nu_z$ these resistances are much smaller than the resistances of good metals as copper or silver.

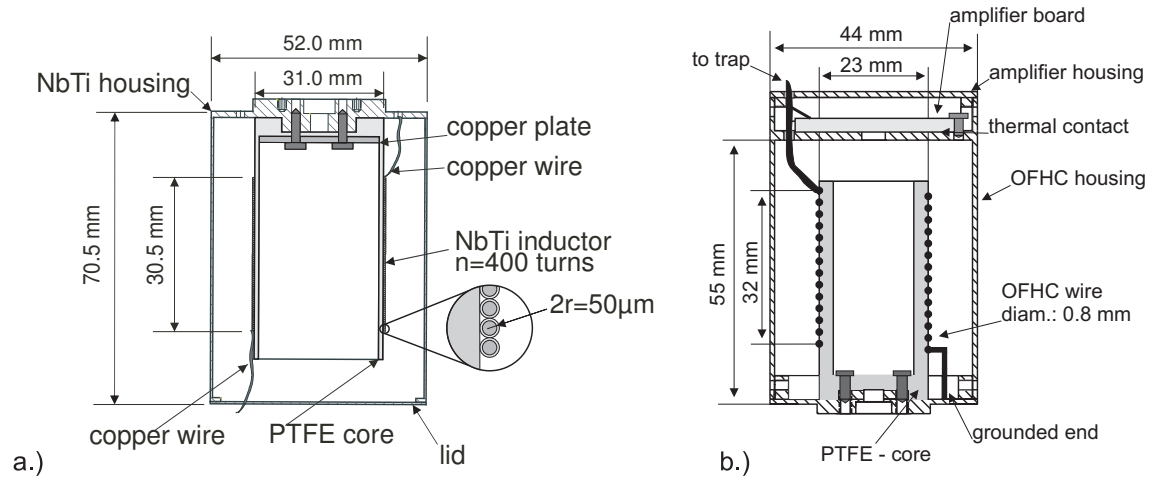


Figure 4.10: a.) Draft of the superconducting resonator used for detection of the axial frequency. b.) Draft of the copper resonator used for the detection of the modified cyclotron frequency.

At higher frequencies as the cyclotron frequency $\nu_+$ the copper resistances are smaller as the superconducting resistances [61].

Both tank-circuits are setup in *helical resonator* design. A detailed theoretical treatment of such a device is given in [78]. For a given geometry, defined by experimental constraints, an optimum geometry of the resonator can be derived. For the construction of our resonators the design chart given in [80] was used. Tabular 4.3 shows the parameters of the resonators.

### *4.9.2 Optimization*

Driving the performance of the free resonators to the maximum and understanding the limitations is the first crucial step for the setup of a highly sensitive detection system. The basic optimization for both resonators is the same. A detailed discussion is found in [61]. For both resonators the following steps are crucial:

- Low loss materials (PTFE) are used for the cores of the coil. With sapphire even better results as presented here should be possible[3]. Furthermore the amount of material

[3]One sapphire core costs about 4000,- Euros.

Table 4.2: Parameters of the helical resonators used for the axial- and the cyclotron detection system.

| | Axial Resonator | Cyclotron Resonator |
|---|---|---|
| Metals | NbTi | Cu |
| Core Material | PTFE | PTFE |
| Inner Diameter Housing (mm) | 52 | 42 |
| Inner Length Housing (mm) | 70.5 | 54 |
| Outer Diameter Coil (mm) | 32 | 23 |
| Length Coil (mm) | 30 | 32 |
| Number of Windings | 300 | 13 |
| Diameter Wire (mm) | 0.05 | 1 |
| Wire Insulation | FORMVAR | bare wire |
| Inductance ($\mu$H) | 1450 | 1.68 |
| Self Capacitance (pF) | 4.3 | 3.32 |
| Free Resonance Frequency (MHz) | 2.0 | 68.2 |
| Unloaded Q-value (4 K) | 25800 | 4700 |
| Effective Parallel Resistance $R_p$ (M$\Omega$) | 473 | 3.38 |

should be reduced to the possible minimum.

- Metallic surfaces should be kept clean. Both resonators are mechanically polished on a lathe. In case of the cyclotron circuit the surface of the bare wire is polished as well. This cleans the surfaces and reduces its effective area. To dissolve polishing greases, the resonators are cleaned in an ultra-sonic acetone-tri-chloral-ethylene bath afterwards.

*Axial Resonator - Optimization*

Above the transition temperature $T_c$, superconducting alloys are bad conductors. To assure that all superconducting components are properly thermalized, adequate thermal anchoring is of exceeding importance. Therefore the coil's wire is fixed to the core with PTFE thread seal tape. A loose superconducting wire, which is not fixed to a cold surface, does not thermalize below the critical temperature. The ends of the wire are soldered to copper wires with a diameter of $500\,\mu$m. One copper wire is soldered to the housing of the coil, the other wire is soldered to a cryogenic feedthrough. This assures proper thermalization. To assure that the housing is also properly thermalized, the whole resonator is surrounded by copper netting which is thermally anchored to the cryogenic region of the experiment [4]. After these optimization steps a $Q$-value of 42000 was measured at an inductance of 2.3 mH and a resonance frequency of 1.6 MHz. In a detailed analysis presented in [61] it was found that this value is limited by the FORMVAR insulation of the superconducting wire [5]. This coil was finally tuned to an inductance of 1.45 mH and $Q = 25800$ was measured. The degeneration of the $Q$-value is due to the frequency dependency of the dielectric loss resistance.

---

[4] Maybe this explanation appears to be exaggerated to some readers. But we worked some weeks with superconductos without success until we realized that all $Q$-value problems observed were due to improper thermal anchoring. Having realized this $Q$-values around 40000 were achieved within a few additional days.

[5] This result was proven by Andreas Mooser [79] who setup coils with PTFE insulated wire showing $Q$-values of 160000 at comparable frequencies and inductances.

*Axial Resonator - Quality Factor as a Function of the Magnetic Field*

In this section the investigation of the optimized $Q$-value as a function of the average magnetic dc field is described. The results are shown in Fig. 4.11. These data were recorded at a resonator temperature of $T$=3.9 K. In general, a decrease of the $Q$-value with increasing magnetic field is observed.

In a first measurement series the resonator was cooled below the critical temperature $T_c$

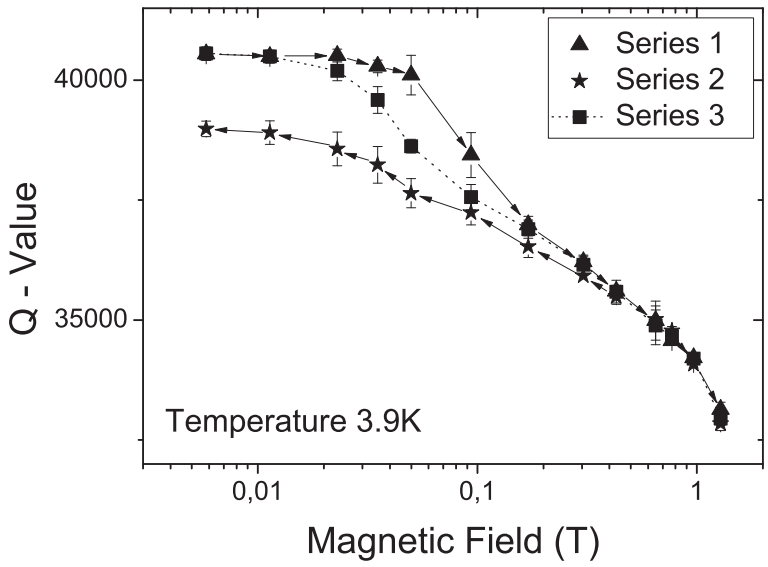


Figure 4.11: Quality factor of the superconducting axial tuned circuit as a function of the external magnetic field $B$. Series 1: Resonator cooled in vanishing magnetic field ($B \ll B_{c1}$). Series 2: Resonator cooled in high magnetic field. Series 3: Resonator cooled in ambient magnetic field of actual position. All data sets show a $Q$-value decrease with increasing magnetic dc-field. For further details see text.

outside the magnet bore and afterwards moved into the high field (filled triangles). In a second experiment the system was cooled down in the maximum available field of $B$ =1.2 T. Subsequently the apparatus was moved out of the magnet (filled stars). In the third measurement series (filled squares) for every data point, the circuit was heated above the critical temperature, then moved to the smaller field region and finally cooled down in that position. The data show a hysteresis and can be explained as follows: Below the lower critical field $B_{c1}$ the dc field is screened by means of the Meissner effect [82]. In this region the $Q$-value

remains constant. Above $B_{c1}$ the Shubnikov phase is reached and flux tubes penetrate the superconductor. The interaction between the rf currents $\mathbf{j}$ in the superconductor and the penetrating flux leads to a Lorentz force density acting on the vortices. Thus, the flux lines move perpendicular to the current and generate a motional electric field in direction of the supra-current. The interaction of this field with the normal conducting phase in the center of the flux tubes causes dissipative losses. In a second dissipative mechanism the flux tube motion results in breaking and reformation of Cooper pairs. In this non-equilibrium process, additional heat is dissipated since, compared to the breaking, the pairs reform in a lower field [81]. Increasing the external dc field raises the total penetrating flux which entails a magnification of surface resistance followed by $Q$-value degeneration. From the first measurement series, the lower critical field $B_{c1}$ was determined to lie between 20 mT and 30 mT, which is in agreement with the value $B_{c1} = 24\,\mathrm{mT}$ given in [83].

Between the first and the second measurement series a hysteresis effect is observed. Above the irreversibility field $B_{irr}$ [84], when the superconductor is homogeneously penetrated with flux lines, the $Q$-values of the different measurements are equivalent. Below $B_{irr}$ the quality factors of the second measurement series are smaller. This behavior can be explained by means of an irreversible magnetization of the superconductor. If the resonator is moved to lower fields, magnetic flux remains trapped in the material. Since the trapped flux lines contribute to the surface resistance, it doesn't relax to its initial value.

This effect can be understood in the Bean picture of the critical state [85]. The application of an external magnetic field to a bulk superconductor generates eddy currents which screen the external dc field. Thus, the effective magnetic field strength decreases in the superconductor. If the external field is decreased, the magnetization cannot be compensated and residual magnetic flux remains in the material.

The third measurement series (filled squares) can be understood as an intermediate between the two afore mentioned measurements. Above the irreversibility field the data are equivalent to the other measurements. Below $B_{c1}$, where the Meissner phase expels the external field, the surface resistance is equal to the one in the first measurement. Between these regions the surface resistance is smaller than in the second measurement series, but higher than observed in the first. This is to be expected since the resonator is cooled in the

ambient field. No screening Bean state is formed, thus, compared to the first measurement, more field lines penetrate the material leading to a higher surface resistance.

For a quantitative analysis of the data the formerly described model was combined with

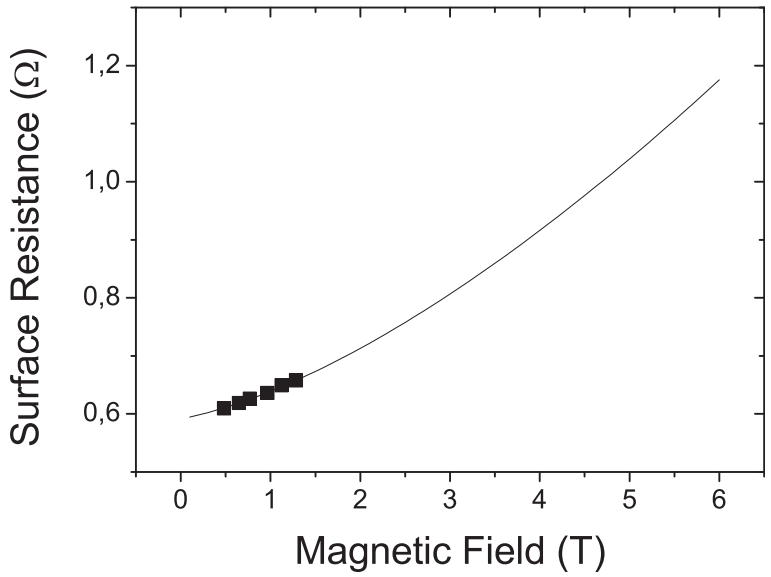


Figure 4.12: Residual resistance as a function of the average magnetic DC-field. The squares represent the measured data, the solid line is the result of a fit based on the combination of our model with the Coffey Clem theory. For further details see text.

the Coffey Clem theory (CCT) [86]. This comprehensive model yields an expression for the complex penetration depth in the framework of the two-fluid-model. Since the CCT is only valid for homogeneous field penetration, only the data points above the irreversibility field were taken into account for the analysis. As input parameters the London depth $\Lambda_L = 50\,\mathrm{nm}$ [87] and the upper critical field $B_{c2} = 14\,\mathrm{T}$ [88] were taken. Two more input parameters for the CCT were measured. In a 4-wire measurement the conductivity of Nb/Ti at 10.5 K was determined to be $\approx \sigma_{\mathrm{Nb/Ti}} = 1.625 \cdot 10^6\,\mathrm{S{\cdot}m^{-1}}$. In the same experiment the critical temperature of $T_c \approx 9.5\,\mathrm{K}$ was measured. Thus, the data were fitted with two free parameters, the residual resistance due to dielectric losses etc. and the critical current density $J_C$ of NbTi. The result is shown in Fig. 4.12. The residual resistance obtained from the fit is $0.59\,\Omega$. This is in good agreement with the measured one of $0.58\,\Omega$. The critical current

density resulting from the fit is $J_C$=9 300 A·cm$^{-2}$·T$^{-1/2}$, which agrees with the values given in [89].

From these results the variation of the residual resistance as a function of the magnetic field can be extrapolated to higher ambient dc fields, as shown in Fig. 4.12. These data may be of interest for comparable experiments working in higher magnetic fields. If the $Q$-value degeneration due to the magnetic field is small compared to other damping effects, caused by the trap, cryogenic feedthroughs, amplifiers etc. , the placement of the resonator as close as possible to the trap has to be preferred. Otherwise, placement outside the high magnetic field should be favored.

Based on these results, the surface resistance can be calculated as a function of the reso-

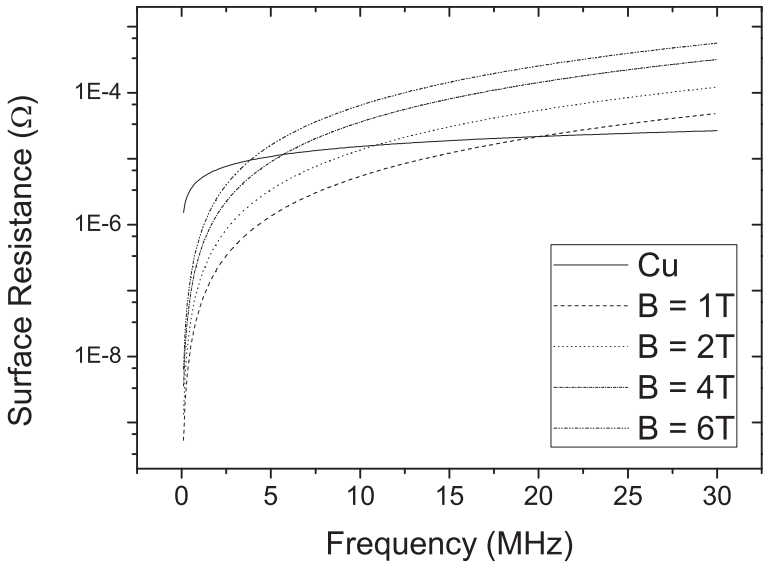


Figure 4.13: Comparison of the surface resistance of copper with a residual resistance ratio of 140 (solid line) and field penetrated NbTi as a function of the resonance frequency of the tuned circuit.

nance frequency of the tuned circuit. Figure 4.13 shows the results for different magnetic dc fields and compares them to the surface resistance of copper with a residual resistance ratio ($RRR$) of 140. This value is typical for commercial high purity wire. In low magnetic dc fields, the use of superconducting material is favorable, since the surface resistance lies below that of copper. In higher fields and frequencies copper resonators are more favorable.

At our experiment, the axial resonator will finally be located in a magnetic field of $\approx 0.5\,\mathrm{T}$. It will be shown later, that $Q$-value limitations due to the rf-resistance of a superconductor in a magnetic field will finally not limit the detector performance.

*Cyclotron Resonator*

The optimization of the cyclotron resonator is by far not as critical as in case of the axial resonator. The 1 mm copper wire is a good conductor and thermalization problems do not occur. Due to the high cyclotron frequency special care is taken to keep the amount of dielectric materials low.
With the optimized cyclotron resonator at 4 K a $Q$-value of 4700 was measured at a free resonance frequency of $\nu \approx 68\,\mathrm{MHz}$, corresponding to an inductance of $L_c = 1.68\,\mu\mathrm{H}$ and a self capacitance $C = 3.32\,\mathrm{pF}$. The limitation is given by the residual resistance of the copper and the dielectric loss resistance of the PTFE-core.

## *4.10 Experimental Realization - Cyclotron Amplifier*

In the next sections experimental results are described. An analysis of loss mechanisms is given. This analysis is based on electronic algebra-calculations performed with *Wolfram Mathematica 6.0.*. The explicit mathematical formulas of these calculations are not denoted explicitly. All results are based on highly sensitive high frequency measurements. Systematic errors arising from different measurement setups occur. The reproducability of the measured quantities is consistent within an error bar of 5 %.

### *4.10.1 Amplifier Setup - Basic Rules*

In sections 4.7.1 and 4.7.2 the main problems of high-$Q$ detector design were discussed. In conclusion the points mentioned there lead to design rules for the setup of the cryogenic amplifiers.

1. Choose a GaAs-FET with a small gate-to-drain capacitance.

2. The PCB-board contributes parasitic parallel-, and gate-to-drain capacitance. Thus,

use board materials with low dielectric permittivity and a layout with small dimensions. To avoid limitations by the PCB-material, use high performance rf-laminates (*Taconic / Rogers*).

3. Avoid parasitic reactive contributions. Therefore, use surface mountable devices (SMD). The components should have intrinsically low loss tangents.

4. Avoid parasitic signal paths coupling the output to the input. Therefore, define a proper ground.

5. Eliminate interaction of the rf signals with the impedances of the dc biasing supplies used to operate the FET. Therefore, ground the dc-ports adequately.

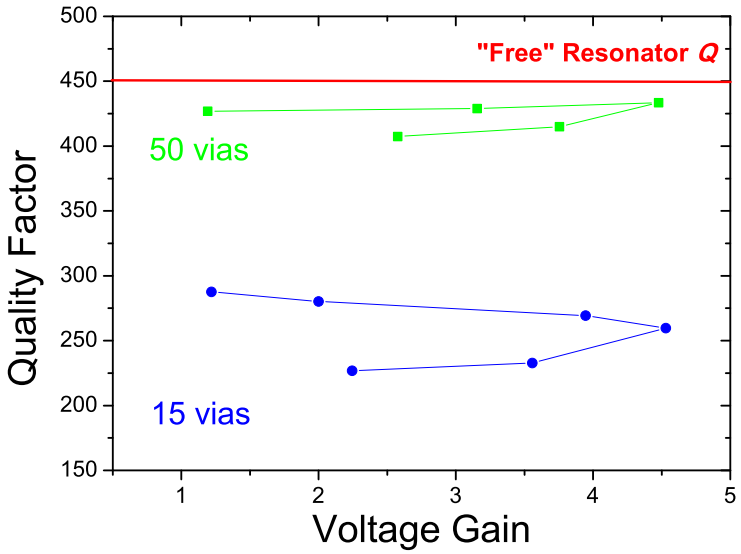


Figure 4.14: Quality factor as a function of voltage gain of the connected amplifier. The filled circles represent a measurement where only 15 "vias" connected upper and lower clad of the board. The filled squares represents the same measurement but for 50 "vias" connecting the clads.

To fulfill these demands, dual-gate GaAs FET's are used. Compared to single gate transistors in these IC-cascoded devices $C_{\mathrm{GD}}$ is smaller, furthermore the cascode surpresses the Miller-effect [75]. For the boards double-clad copper *Taconcic TLC*-laminate is used having a dielectric permittivity of only 2.75 at a loss tangent of $\delta_{\mathrm{TLC}} = 0.002$. At cryogenic temperatures $\delta_{\mathrm{TLC}}$ is nearly one order of magnitude lower. To avoid dielectric losses caused by chemical residuals from etching, the boards are made with a mill. No stop-lacquer is used. Numerous "vias" connect the upper- and the lower-clad, which is screwed to ground. This defines adequate ground, reduces the total board capacitance and limitations caused by the dielectric material, furthermore parasitic signal paths are suppressed [6]. In Fig. 4.14 the quality factor of a copper resonator connected to a simple amplifier is shown for different voltage gains. The two curves are for different numbers of "vias" connecting the upper and the lower plate of the amplifier board. Two effects are observed. The $Q$-value increases with increasing numbers of "vias" and the effective feedback to the resonator is reduced, indicated by a smaller total $Q$-value range in the $Q(G)$ data. The increase of the value is due to reduction of the effective series resistance of the board. The feedback reduction is due to reduction of the parasitic coupling of the output to the input by means of the board. The amplifier is setup with 08/05 SMD components. For small value capacitors between 1 pF and 220 pF high-$Q$ Johanson-Techchnology components are used while *ECHU*-plastic components are used for the large capacitances (1 nF to 1 $\mu$F). The resistors are 0805-SMD (*Blackstar-components*). All components are robust under thermal cycling and change their values only by $\approx 10\,\%$ during cool-down from room temperature to 4 K.

### *4.10.2 Cyclotron Amplifier and Varactor*

The cyclotron frequency is defined by the field-strength of the superconducting magnet, the detector is tuned to resonance with the particle by means of a varactor diode (a voltage controlled capacitor $C_{var}(V)$). Connecting the device in parallel to the resonator, its resonance frequency can be tuned. A *MACOM MA46H072* varactor diode is used. Details are described in [47].

---

[6] I worked several weeks having stability problems. Setting numerous vias solved this problem

Table 4.3: Overview on measured GaAs-FET parameters. $C_{\mathrm{in}}(pF)$ is the input capacitance, $R_{\mathrm{in,DC}}$ the DC-input resistance, $C_{\mathrm{GD}}$ the gate-to-drain capacitance and $e_n$ the equivalent input noise density per unit bandwidth.

| FET | $C_{\mathrm{in}}(pF)$ | $R_{\mathrm{in,DC}}$ (MΩ) | $C_{\mathrm{GD}}$ (pF) | $e_n$ (nV/Hz$^{1/2}$) |
|---|---|---|---|---|
| Sony 3SK166 | 1.4 | 2.2 | - | - |
| NEC 3SK206 | 1.6 | 6.9 | - | - |
| Sanyo 3SK164 | 1.2 | 68 | - | 2.2 (0.1) |
| Siemens CF739 | 1.1 | 52 | 0.055 | 0.85 (0.05) |
| NEC NE25139 | 0.95 | 48 | 0.03 | 0.83 (0.05) |

For input stage of the amplifier different n-channel dual gate GaAs MES-field effect transistors were tested, namely *Siemens CF739*, *NEC NE25139*, *NEC 3SK206*, *Sony 3SK166* and *Sanyo 3SK164*. Pre-selection criteria were datasheet-values as noise figure and input capacitance. All transistors are housed in an SOT-143 package. As characterizing quantities the input capacitance $C_{in}$, the DC input resistance $R_{in,DC}$ were measured. The results are shown in Tab. 4.3.

The input capacitance $C_{in}$ was measured putting a resonator of known inductance $L$ and capacitance $C$ in parallel to the transistors. Measuring the resonance frequency $\nu_{FET}$ of the system with the FET in parallel $C_{in}$ can be derived.

From these measurements, the *Sony 3SK166*, as well as the *NEC 3SK206*, were excluded since the low input resistances would limit the $Q$-value of the system.

The measurements of the equivalent input noise of the FET's were performed at 4 K. The results are also shown in Tab. 4.3. Due to the comparably large equivalent input noise $e_n = 2.2\,\mathrm{nV}\cdot\,\mathrm{Hz}^{0.5}$ the *Sanyo 3SK164* transistor was excluded too.

Compared to the *Siemens CF739* the *NEC NE-25139* has a slightly lower input capacitance at smaller DC-input resistance $R_{\mathrm{in}}$. To select the best FET, additionally the gate to drain capacitance $C_{\mathrm{GD}}$ was measured. This capacitance couples the drain-to-source resistance $R_{\mathrm{DS}}$ of the FET to the input of the device, resulting in an effective input resistance $R_{\mathrm{in,eff}} < R_{\mathrm{in,DC}}$. Connecting a high-$Q$ resonator to the input of the FET and measuring

the $Q$-value as a function of $R_{\mathrm{DS}}$ the value $C_{\mathrm{GD}}$ can be extracted. The data are shown in Fig.4.15. From these measurements for the *CF739* transistor $C_{\mathrm{GD}} = 0.055\,\mathrm{pF}$ and for the *NE25139* transistor $C_{\mathrm{GD}} = 0.03\,\mathrm{pF}$ is yielded. Despite of the higher DC input resistance

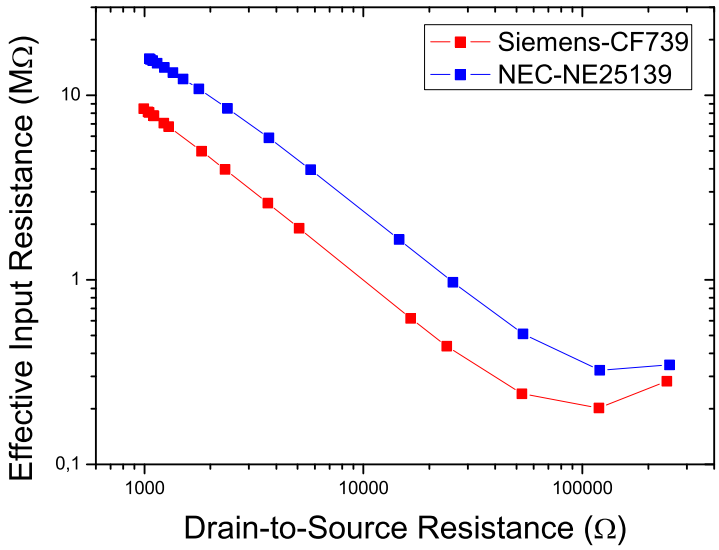


Figure 4.15: Effective input resistance as a function of the drain-to-source resistance for the *Siemens CF739* transistor (red squares) and the *NEC NE25139* (blue squares) GaAs FET. From these measurements the gate-to-drain capacitance $C_{\mathrm{GD}}$ can be extracted resulting in 0.055 pF for the *CF739* and 0.03 pF for the *NE25139*.

the effective input resistance $R_{\mathrm{in,eff}}$ is larger for the NEC transistor. Thus, this part was chosen for the final layout.

The output impedance of the first amplification stage is matched to the 50 Ω signal lines with a low noise *AVAGO-ATF35143* source follower. Compared to the alternative matching CLC-$\pi$-net [91], resistive matching leads to higher stability of the detection system.

The final layout of the amplifier is shown in Fig. 4.16. Having measured $g_m$ of the transistors at cryogenic temperatures, the stages were designed by standard methods [92]. With that electronically straight forward design a voltage amplification of 19 dB at a power consumption of only 4.5 mW is achieved.

The system capacitance is tunable in a range between $C_{in} = 2.75\,\mathrm{pF}$ and $C_{in} = 4.2\,\mathrm{pF}$.

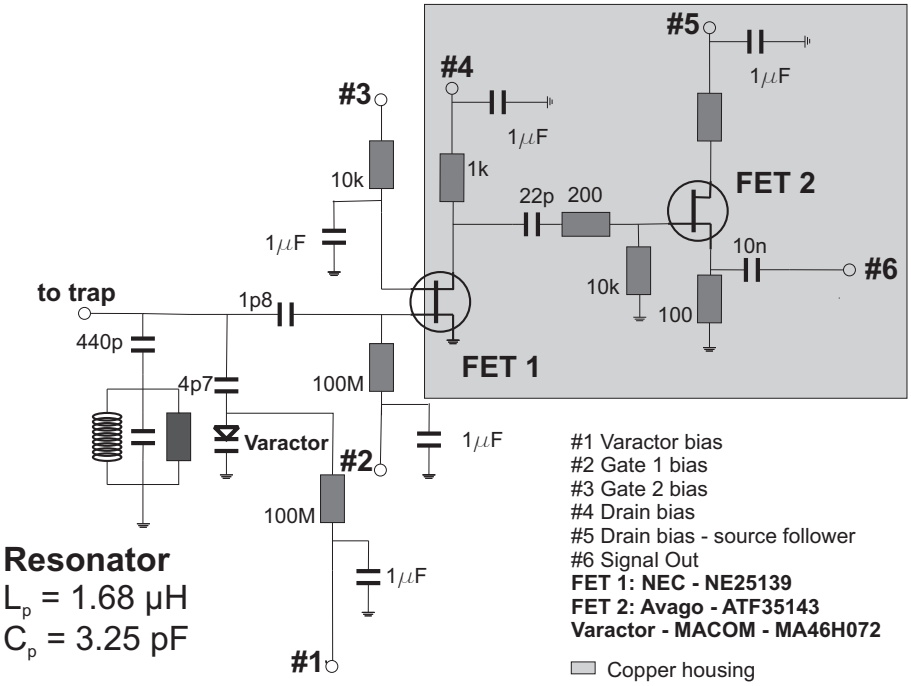


Figure 4.16: Layout of the cyclotron GaAs-FET amplifier. For detailed description see text.

Coupling the varactor in parallel to the detection system by means of a 4.7 pF capacitor, it was found to contribute an effective parallel resistance of $R_{p,V} = 1.7\,\mathrm{M\Omega}$. Combining all the information as a coupling factor for optimum signal-to-noise matching $\kappa = 0.58$ is calculated (see section 4.6). Different coupling techniques are possible, inductive pickup, capacitive pick-up or both techniques in combination. Inductive pickup can be realized tapping a wire in a certain position of the inductor (auto-transformer) or by a real secondary coil. Both techniques were tested but finally not used since additional wire material in the resonator housing leads to a higher effective capacitance. Furthermore, the additional wire modifies the inductance, which complicates detector tuning in this low inductance range ($\mu$H). Purely capacitive pickup leads to the smallest system capacitance and thus, to the highest effective parallel resistance. For the capacitive coupling, a high-$Q$ capacitor with $C_c = 1.8\,\mathrm{pF}$ is used (*Johanson-Technologies S-series*) [93].

The board has circular geometry with a diameter of $d_b = 40\,\mathrm{mm}$ and is screwed by six

brass screws to the bottom of the cylindrical housing of the resonator, shown in Fig. 4.17. This ensures both, good electrical contact between the ground plate of the board and the copper housing as well as good thermal contact between amplifier and housing. Thus the heat produced in the drain-to-source channel is adequately sunk.

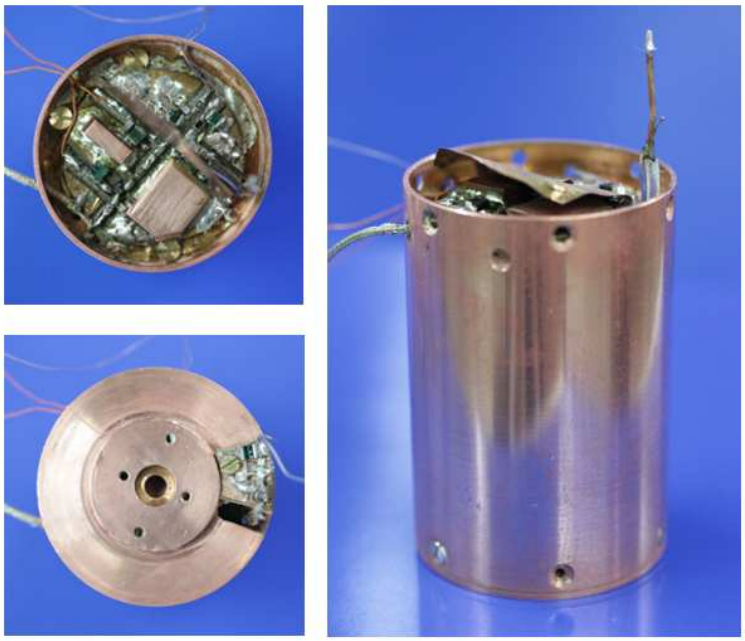

Figure 4.17: Photographs of the cyclotron detection system. Upper left.) View on the circular amplifier board. Lower left.) The same view, but closed with a copper-cap. On the cap the varactor board is mounted. right.) Cylindrical housing of the detection system.

### *4.10.3 Cyclotron Detector without Trap*

Connecting the amplifier to the resonator and tuning it with an additional capacitor to the aimed resonance frequency of 28.9 MHz, the $Q$-value decreases at 300 K from $Q_{68\,\mathrm{MHz}} = 740$ to $Q_{29\,\mathrm{MHz}} = 430$. Due to the relation $Q(\nu) = Q_0\sqrt{\nu/\nu_0}$ [78] loss free down tuning should result in a quality factor of $Q_{29\,\mathrm{MHz}} = 470$. The additional loss resistance is due to the equivalent series resistance of the tuning capacitor, the coupling capacitors and

the varactor diode. Cooling the device down to 4 K $Q$-values between 1500 and 2050 are measured, depending on the biasing conditions. Results are shown in Fig. 4.18. Besides

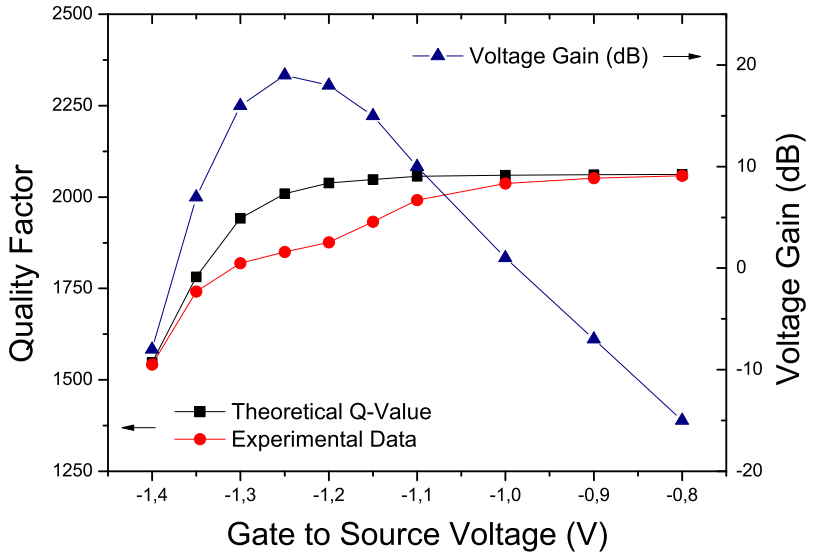


Figure 4.18: System performance without trap. The detector is tuned to the aimed resonance frequency of $\nu_0 = 28.9\,\mathrm{MHz}$ with a capacitor. The filled squares represent the theoretical $Q$-value accounting for the limitation due to coupling of the varactor and the drain-to-source resistance $R_{DS}$ by means of $C_{GD}$ to the input. The filled triangle represent the measured voltage amplification. The filled circles represent the measured data. The data can be explained by introducing a tiny negative feedback gain $g_{FB} \approx -0.01$ to the input. This modifies the particle temperature only by 1%.

the quality factor (filled dots) the amplifier voltage gain (filled triangles) and the drain to source resistance were measured. The filled squares represent the theoretical $Q$-value, taking the effective series resistance of the coupling network and the coupling of $R_{\mathrm{DS}}$ by means of $C_{\mathrm{GD}} = 0.03\,\mathrm{pF}$ to the input resistance of the amplifier into account. The measured quality factor can be explained combining the theoretical $Q$-value $Q_0$ with a feedback gain of $g_{FB} \approx -0.01$, since $Q(g_{FB}) = Q_0(1 - g_{\mathrm{FB}})$ [72] (see section 4.5). This tiny negative feedback gain would reduce the effective particle temperature by $\approx 1\%$ and is not critical for our application.

Compared to the lossless down-tuning, which should result in an equivalent series resistance of $0.1\,\Omega$, the cryogenic equivalent series resistance of the system including amplifier and varactor is $\Delta R_{\mathrm{amp,vacator}} = 0.06\,\Omega$ larger. Replacing the varactor with a lossless capacitor $\Delta R_{\mathrm{amp}} = 0.01\,\Omega$ was measured, thus, the varactor is the main limitation of the detection system.

### *4.10.4 Performance of the Detection System and Limitation*

The detector is mounted near the precision trap in the cryogenic vacuum chamber (see chapter 3). A drawing is shown in Fig. 4.19. . The distance between the hot end of the

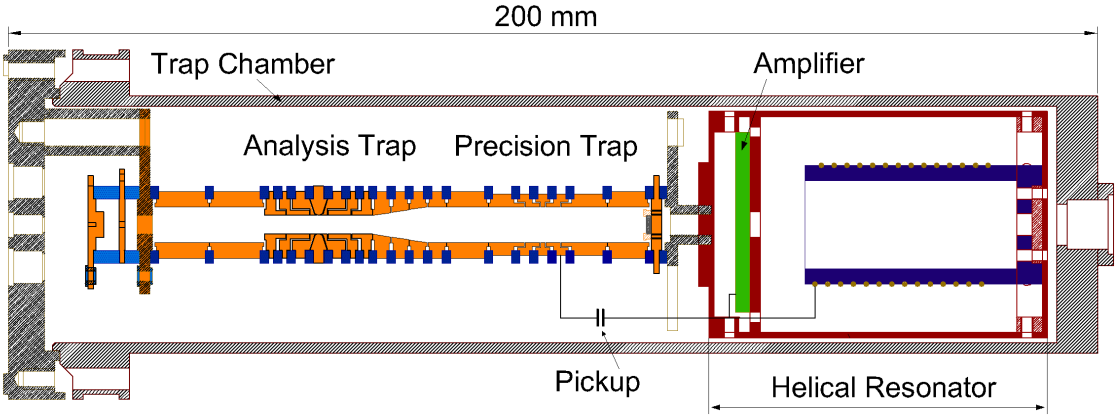


Figure 4.19: Cryogenic vacuum chamber of the experiment. The traps and the cyclotron resonator are housed in the "trap can". The distance between the hot end of the resonator and the detection electrode is only 10 mm.

detector and the detection electrode is only about 10 mm. Thus, the additional parasitic capacitance due to connection wires is below 1 pF. Furthermore, due to the assembling of the detector in the trap chamber it is avoided that cryogenic feedthroughs with $C_F = 2.5\,\mathrm{pF}$ and cryogenic loss tangent of $\tan\delta_F \approx 0.001$ [61] are put in parallel to the detector. With the decoupled amplifier capacitance of $C_{\mathrm{amp}} = 0.75\,\mathrm{pF}$, the resonator capacitance of $C_p = 3.32\,\mathrm{pF}$, the total trap capacitance $C_T = 12.7\,\mathrm{pF}$ and the capacitance of the varactor network $C_V = 2.2 \pm 1.3\,\mathrm{pF}$, the resonance frequency of the cryogenic system is $\nu_0 = 28.8 \pm 0.505\,\mathrm{MHz}$. The $Q$-value of the whole system was measured to be $Q_{4\mathrm{K}} = 1250$,

corresponding to an effective parallel resistance of 380 kΩ and an equivalent series resistance of $R_{\mathrm{s,system}} = 0.244\,\Omega$. Expressed in effective series resistance, this value is $0.14\,\Omega$ higher as it should be achieved with a loss free system. This value consists of the amplifier limitations discussed above with $\Delta R_{\mathrm{amp,varactor}} = 0.06\,\Omega$ and limitations of $\Delta R_{\mathrm{trap}} = 0.08\,\Omega$ due to coupling of the detector to resistive biasing elements of the trap.

To compare the quality of this detection system to other copper machined GaAs-FET detectors as figure of merit

$$\alpha = \frac{1}{\omega_0^{3/2} L} \frac{R_p}{D} \tag{4.48}$$

is used, where $D$ is the diameter of the resonator. At a given geometry $D$ the $Q$ value is given by $Q = \alpha D \sqrt{\omega_0}$, where $\alpha$ is a scaling factor characterizing losses [78].

In [24] a detection system for the modified cyclotron frequency measurement of hydrogen-like carbon at 24 MHz is described. With a resonator diameter of 35 mm and an inductance of L=1.32$\mu$H a cryogenic $Q$-value of 400 is achieved, leading to $\alpha = 14.7$. For the measurement of the axial frequency of an electron in [73] another detection system with $L = 0.3\,\mu$H operating at a frequency of $\nu = 64\,$MHz is described. Here a $Q$-value of 400 is measured at 4 K where the diameter of the resonator is $D = 35\,$mm, leading to $\alpha = 9$. The detection system used for comparison of the proton to antiproton massratio [91] $\alpha = 25$ is obtained. With the detection system presented in this work $\alpha = 35$ is achieved. Thus, among the detection systems compared in the upper text, our cyclotron detection system has the highest quality.

### *4.10.5 Possible Improvements*

For the discussion of further improvements of the detection system the loss resistances of the detection system are summarized in Tab. 4.4. By proper annealing of the copper resonator the measured residual resistance ration value of 130 may be improved by at least a factor of 10. The losses in the PTFE core located in the resonator housing can be reduced replacing the PTFE core with a sapphire core which should result in a decrease of the equivalent series resistance by a factor of 6 to 10.

Currently the varactor diode is coupled to the resonator by means of a 4.7 pF capacitor.

Table 4.4: Overview on measured experimental loss resistances and expected values after optimization. For details on the optimization we refer to the text.

| Loss Source | Experimental $R_s$ at 28.9 MHz($\Omega$) | Optimized $R_s$ at 28.9 MHz($\Omega$) |
|---|---|---|
| Helical Resonator | 0.1 | $\approx 0.03$ |
| PTFE Core | 0.007 | $< 0.001$ |
| Varactor | 0.05 | $\approx 0.025$ |
| Amp | 0.01 | 0.01 |
| Trap | 0.08 | $< 0.01$ |
| Cryogenic $Q$-value | 1250 | 4000 |

Reducing the value of this capacitor will also lead to an effectively smaller equivalent series resistance seen by the resonator. Note that this decoupling also affects the tunability of the system. Using a weaker coupling factor for the varactor, which will reduce the tunability, the amount of equivalent series resistance carried by that component can be reduced (f. e. 300 kHz tunability 0.025 $\Omega$).

Changing the electronic trap design to higher impedances or purely reactive components the trap losses should also decrease by a factor of 10.

With these modifications an increase of system $Q$ by a factor of 3 to 4 should be possible. The major limitation of the current setup is the varactor diode.

## *4.11 Experimental Realization - Axial Detection System*

### *4.11.1 Axial Amplifier*

Compared to the cyclotron amplifier, the setup of the axial amplifier is simple. At the axial frequency of $\nu_z \approx 680$ kHz parasitic reactive effects are reduced by a factor of 40 ($\nu_+/\nu_z$). Following the design rules described in section 4.10.1 the axial amplifier works immediately. Seen from amplifier side, in case of the axial detection system noise is critical, since $\nu_z = 680$ kHz is below the *1/f*-cutoff of GaAs transistors [94, 95]. In this frequency range active electronic noise shows arbitrary behavior. Temperature reduction does not necessarily

reduce noise. In contrast, for some devices the equivalent input noise increases if temper-

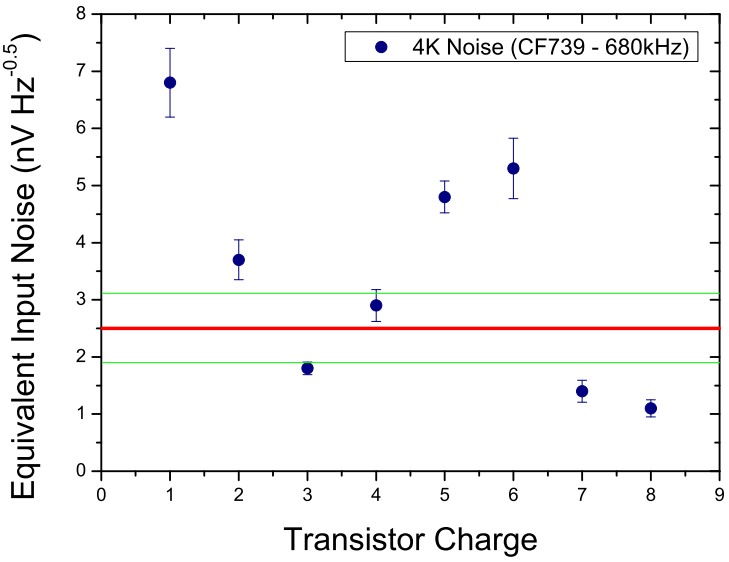


Figure 4.20: Results of noise measurements performed with different *CF739* transistors at room-temperature indicated by the red line and 4 K. The cryogenic equivalent input noise is represented by the filled circles.

ature is lowered. Figure 4.20 shows the equivalent input noise for different charges of a *CF739* transistor. At 680 kHz and room temperature, all transistors show the same behavior $e_n = 2.5 \pm 0.5\,\mathrm{nV{\cdot}Hz^{-0.5}}$. The results from the measurements at 4 K are represented by the filled circles. The 4 K-noise values scatter in a span of $7\,\mathrm{nV}/\sqrt{\mathrm{Hz}}$. No correlation between 300 K and 4 K-noise seems to exist. From room temperature measurements, it is not possible to predict how the transistor behaves at 4 K. This experimental result is in accordance to [75, 94] and still under discussion.

To find a suited FET, several transistor charges were tested. A NEC-*NE*25139 with $e_n = 1.3\,\mathrm{nV{\cdot}Hz^{-0.5}}$, $i_n = 4.5 \pm 3\,\mathrm{fA{\cdot}Hz^{-0.5}}$ and input resistance of 43 MΩ at 680 kHz was found, this device is used for the common-source input stage. For the second stage a *Siemens-CF739* with $e_n = 1.7\mathrm{nV{\cdot}Hz^{-0.5}}$ is used. The slightly higher noise of the second stage is not critical, since it contributes to the total noise only $e_n/G_1$, where $G_1$ is the am-

plification of the first stage. The design procedure is the same as for the cyclotron amplifier.

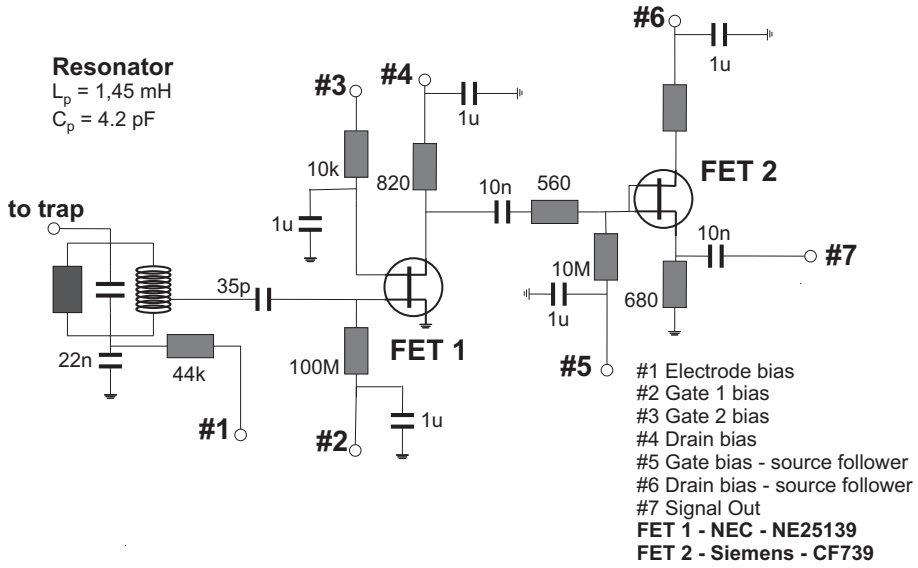


Figure 4.21: Layout of the axial GaAs-FET amplifier. For detailed description see text.

The layout of the amplifier is shown in Fig. 4.21. At a power consumption of 5.2 mW a voltage gain of 17 dB is obtained.

Since the axial amplifier is connected directly to the superconductor, adequate heat sinking is of tremendous importance. Therefore the whole amplifier board is soldered to a massive copper plate of 1.5 mm thickness which is screwed to the cold stage of the apparatus. Figure 4.22 shows photographs of the axial detection system. For details see figure-caption

### *4.11.2 Matching and Coupling*

As shown in section 4.6, perfect noise matching depends on the effective parallel resistance of the system and the input resistance of the amplifier. The parallel resistance $R_p$, which has to be taken into account for matching is not that of the unloaded resonator. The Penning trap and additional components have to be taken into account. Since in case of the axial detection system the parallel resistances included are in the range of 100 MΩ it is of importance to take all limitations into account before matching.

The wiring schematic of the axial detection system including the double Penning trap stack

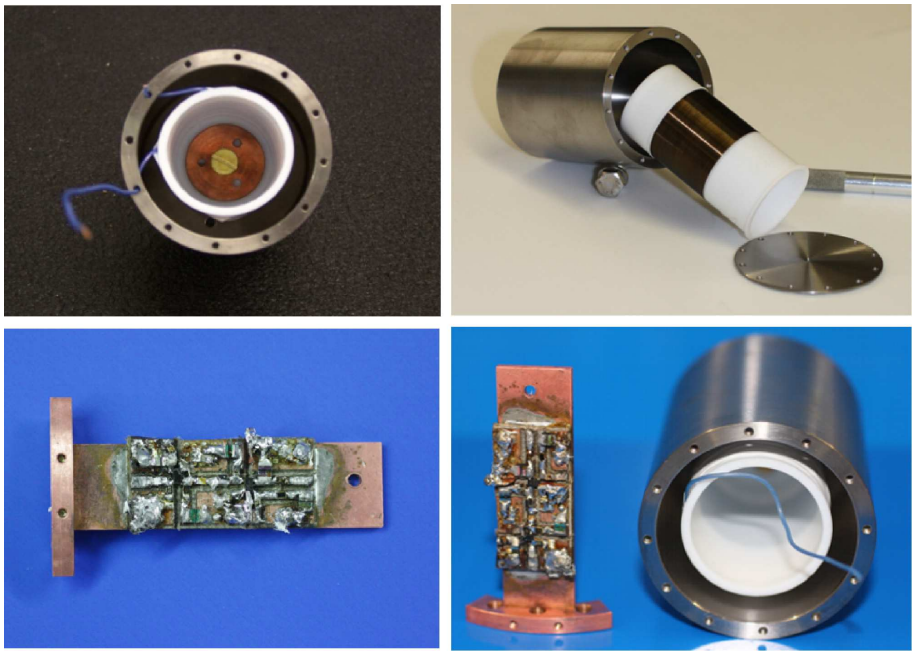

Figure 4.22: Photograph of the axial detection system. upper left.) Coil mounted in the superconducting housing. upper right.) Superconducting resonator and the solenoidal FORMVAR insulated NbTi inductor, which is wounded on a PTFE core . lower left.) Cryogenic amplifier. The amplifier's ground clad is directly soldered to a massive copper plate. lower right.) Cryogenic amplifier and superconducting resonator.

is shown in Fig. 4.23. The axial detection system is connected to both traps, the signal is picked-up with the correction electrodes (see section 4.4). To block dc voltages the resonator is connected to the precision trap with a 440 pF capacitor. Furthermore, to avoid capacitive load, the dc-biasing network of the precision trap electrode is blocked by a 100 M resistor. The proton signal is guided to the detector by an alumina feedthrough soldered to a copper flange (see chapter 3). The feedtrough has a loss-tangent of $\delta_F \approx 3 \cdot 10^{-4}$ at a parallel capacitance of 2.5 pF. At 680 kHz an effective series resistance of $R_{s,F} \approx 0.12\,\Omega$ is obtained. The effective series resistance of the 100 M$\Omega$ block resistor (140 M$\Omega$ at 4 K) is $R_{s,B} \approx 0.29\,\Omega$ and that of the free resonator is $R_{s,R} \approx 0.7\,\Omega$, respectively. Therefore the total effective parallel resistance for matching is $R_p \approx 35\,\mathrm{M}\Omega$.

To achieve optimum signal-to-noise ratio the formulas derived in section 4.6 for peak detection is used, giving a coupling factor of $\kappa_{peak} = 0.12$. Since the signal-to-noise ratio for peak

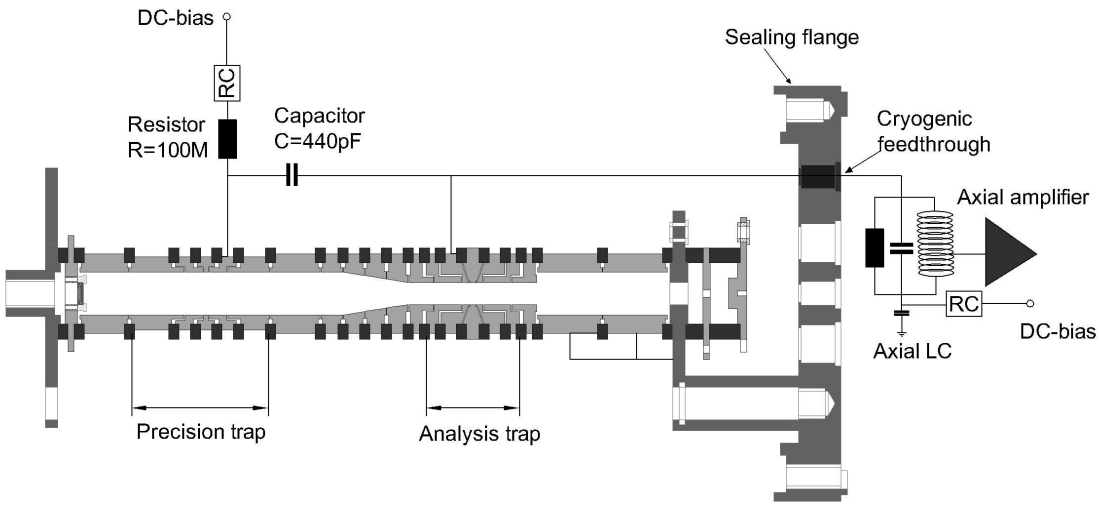


Figure 4.23: Detailed wiring diagram of the axial detection system. One detection system for both Penning traps is used. To avoid capacitive load from the dc-biasing of the precision trap the network is blocked with a 100 MΩ resistor effectively lying in parallel to the resonator.

detection is a smooth function around its maximum, the coupling was slightly increased to $\kappa = 0.15$, which gives 2 dB more in signal-to-noise ratio for dip detection, leading to an effective design value of 21 dB. The coupling factor is adjusted with a tap (see section 4.10.2). Due to the lower frequency and the very high inductance, the tapping wire does not contribute to the total inductance.

### *4.11.3 Detector Performance*

Connected to the Penning trap, in different experimental runs quality factors between 3200 and 5800 at a resonance frequency of $\nu_z \approx 680$ kHz were measured. The higher $Q$-values are achieved, when special care on proper cabling is taken. Guiding of low-impedance excitation and dc-biasing lines near the signal line should be avoided. The best measured quality factor of 5800 corresponds to an effective parallel resistance of $R_p \approx 36$ MΩ. Transformed in a series resistance we find $R_S = 1.06\,\Omega$.

From run to run the frequency sightly fluctuates in a span of 15 kHz. This is due to differences in the effective parallel capacitance of $\Delta C_p \approx 1.8$ pF, caused by slightly varying

wiring geometries. With the discussion of the limitations given in the last section (see Fig. 4.23)

$$Q = \frac{2\pi\nu_z L}{R_S + R_{S,F} + R_{S,B}} \approx 5600 \ . \tag{4.49}$$

The 5 % difference between measured and calculated quality factor corresponds besides the known contributions to a reduction of effective series resistance by $\Delta R_S = -0.045\,\Omega$. This small deviation is consistent to zero within the error bars of the limitations.
This shows that the limitations are understood very well. The takeaway information of this section is that:

- Apart from the 100 MΩ resistor, which blocks the DC-biasing of the precision trap, no limiting effects of the Penning trap are observed if the trap is adequately wired.

- Replacing the alumina- by a sapphire-feedthrough, would improve the loss tangent of this component by at least one order of magnitude.

- Introducing a geometry allowing us to use one independent detector for every trap would increase the detector-inductance by a factor of 2. Furthermore the 100 MΩ block resistor would not be needed anymore.

- As discussed in section 4.9.2 the limitation of the free resonator is due to dielectric losses in the FORMVAR insulation of the wire. With PTFE insulated wire higher $Q$-values can be achieved.

For further developments of the axial detection system based on these results, see [18, 79].

### *4.11.4 Axial Signal-to-Noise Ratio*

With the measured effective parallel resistance of 36 MΩ, the coupling factor $\kappa = 0.15$, the physical temperature of $T_{exp} \approx 4.5\,\mathrm{K}$, and the equivalent input noise $e_n = 1.4\,\mathrm{nV{\cdot}Hz^{0.5}}$ a signal-to-noise ratio 21 dB is calculated. Taking the room-temperature amplifier into account which adds 1.5 dB to the noise floor 19.5 dB should be measured.

A noise resonance of the axial detection system connected to both traps is shown in Fig.

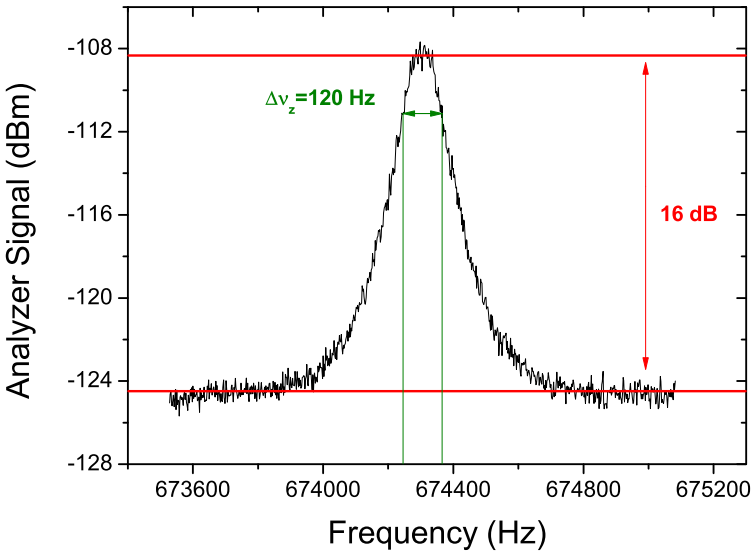


Figure 4.24: Noise resonance of the superconducting axial detection system. The signal-to-noise ratio is 16 dB the measured $Q$-value in this case is 5600. The theoretical signal-to-noise ratio is 20 dB. For detailed discussion of this discrepancy see text.

4.24. A signal-to-noise ratio of 16 dB is measured, which means that 3.5 dB are missing, being equivalent to a factor of 1.5 in the voltage ratio. Assuming that the error of the amplifier noise measurements as well as the error of the coupling factor is $\approx 10\,\%$, 2 dB in deviation can be explained. Giving an error of 10 % for the effective coupling-factor is convenient since the parasitic capacitance of the tap wire may be in the range of 2 pF which would explain the deviation. Nevertheless, calculating the expected signal-to-noise ratio based on the test measurements, within the final signal-to-noise of the real experiment does not fit to the experimental results within the error bars. The experimental data are in agreement with adding 300 pV to the noise measured in test experiments. A comparable value of an increase of background-noise has also been observed in other experiments [7]. In [97] a possible explanation is given. There, the effect of a magnetic field on amplifier noise

[7] Private communication with Sven Sturm who built an ultra low-noise amplifier for the detection of the axial frequency of hydrogen-like Ca. The axial signal-to-noise ratio measured in his experiment accords to 200 pV increase of amplifier noise compared to preliminary test measurements.

is discussed. Due to the Hall effect the effective gate length is increased, resulting in higher effective input noise [75]. For a detailed discussion, we refer to [98].

### *4.12 Detection Systems - Summary*

Both detection systems presented in this thesis show excellent performance. Compared to other detection systems, the cyclotron detector presented in this work has very high quality (see section 4.10.2).

In case of the axial detection system, despite of the challenging experimental constraint that it is connected to both traps, a very large effective parallel resistance of 36 MΩ is obtained. This was achieved by detailed experimental investigation of loss mechanisms. It will be shown in the next chapters, that both detection systems have single proton sensitivity and fulfill the requirements of a precision experiment.

The characterizing parameters of both detection systems are summarized in Tab. 4.5.

Table 4.5: Summary of the parameters of the detection systems. The axial detection system is connected to both traps. The fist value is for the precision-, the second for the analysis trap respectively.

| | Cyclotron Detector | Axial Detector |
|---|---|---|
| Resonance Frequency (MHz) | 28.969 | 0.680 |
| Inductance ($\mu$H) | 1.68 | 1450 |
| Quality Factor | 1250 | 5800 |
| Effective Parallel Resistance (MΩ) | 0.382 | 36 |
| Effective Electrode Distance (mm) | 15.5 | 7.7 and 4.5 |
| Cooling Time Constant (s) | 40 | 0.105 and 0.037 |
| Dip-Line-Width (Hz) | 0.004 | 1.5 and 4.3 |
| Signal-to-Noise Ratio (dB) | 18 | 16 |
| Power Dissipation (mW | 4.5 | 5.3) |

# Chapter 5

# SINGLE PARTICLE PREPARATION

In this chapter experimental routines for the preparation of one individual proton are described. This includes the preparation of an ion cloud, the analysis of the trap content, cleaning the trap from contaminants and reducing the clean proton cloud to one individual particle. All routines described here are performed in the Precision trap.

## *5.1 Trap Loading, Mass Spectra and Trap Cleaning*

To load the Penning trap with ions a trapping potential is applied to the electrodes and the electron beam is turned on for several seconds (section 3.7). To analyze the trap content, a voltage ramp $V(t) = V_0 \pm \Delta V/\Delta t \cdot t$ where $t \in [0, \Delta t]$, is applied to the electrodes. Due to the definition of the axial frequency by the trapping voltage

$$\nu_z(t) = \frac{1}{2\pi}\sqrt{\frac{2qC_2\left(V_0 \pm \frac{\Delta V}{\Delta t}\cdot t\right)}{m}} \tag{5.1}$$

ion species of different $m/q$-ratio are tuned to resonance with the detector. There, the particles dissipate energy, leading to a peak in the power-spectrum of the spectrum analyzer. Such a *mass-spectrum* or *voltage ramp* is shown in Fig. 5.1 a.). In order to record such a spectrum typically 10 V are ramped in 30 s.

The trap content shows the typical composition of frozen air. In addition a proton peak occurs being due to the effect of the black PE target.

To reduce the composition of trapped ions to a clean proton cloud, a negative voltage of $-7$ V is applied to the target. Then the trap voltage is adjusted to tune the protons to the center of the axial resonator. The protons are resistively cooled, while contaminants are not affected. Afterwards the trapping voltage is lowered to -100 mV and hot particles are evaporated. In the next step the protons are tuned to the center of a steep homemade notch filter ($\nu_0 = 710$ kHz). There applied rf-signals are attenuated by 60 dB. Subsequently a

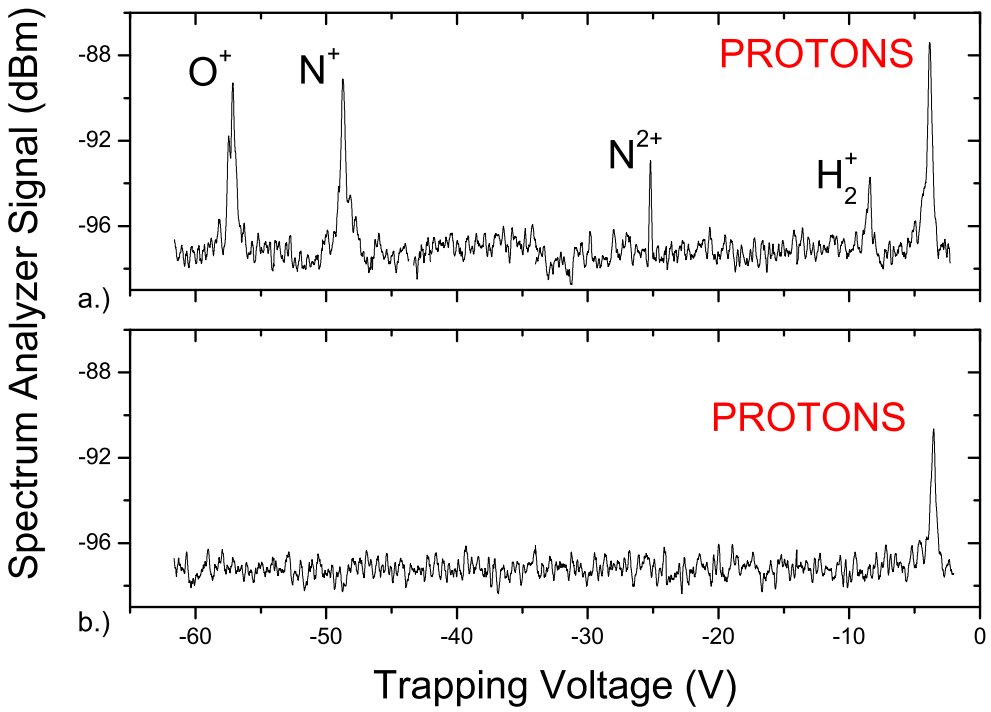


Figure 5.1: a.) Mass-spectrum after trap loading and b.) after the cleaning-procedure described in the text. After cleaning no contaminations are visible anymore and only a clean cloud of protons is observed in the "mass-spectrum".

broadband frequency modulated stored wave inverse fourier transform (SWIFT) noise signal [99] [1] with an amplitude of 10 dBm and an upper cutoff frequency of 500 kHz is applied to the axial dipolar excitation electrode for about 20 s. This heats all the contaminants with $m/q > 1$ while the proton is not affected. The signal applied to the trap including SWIFT signal and notch filter is shown in Fig. 5.2. Afterwards the trapping voltage is lowered again to $-100$ mV for hot particle evaporation. In the next step the protons are tuned to the resonator and the magnetron mode of the cloud is cooled (see section 6.6). To heat heavy particles out of the trap, finally a 2 min. rf-sweep in a frequency span between 40 kHz

[1] In frequency space SWIFT signals appear to be a composition of discrete peaks in the defined excitation region. The frequency modulation broadens the frequency spectrum of the SWIFT signal to a quasi-continuous signal over the defined bandwidth.

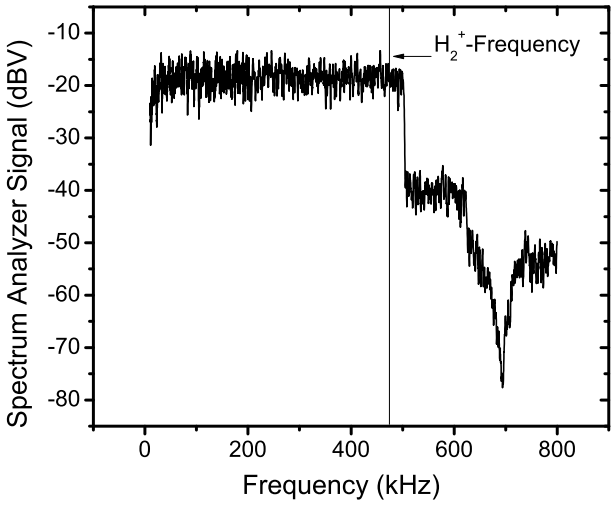


Figure 5.2: Combined SWIFT-notch signal applied to the axial dipolar excitation electrode for cleaning of contaminants.

and 140 kHz is applied. After this sweep the trapping voltage is lowered again. A mass spectrum recorded after such a cleaning procedure is shown in Fig. 5.1 b.).

In order to ensure that all contaminants are heated out of the trap, the procedure described above is repeated for several times. Having reduced the particle cloud to a few individual protons, the particles are transported to the analysis trap, and the ring voltage is ramped down to -48 V with a *HP-6629A* DC-voltage source (the maximum voltage that can be applied to the filter capacitors is $\pm 50$ V). The magnetic bottle distorts the field of the superconducting solenoid to $B_{0,AT} \approx 1.16$ T. Furthermore, due to the smaller diameter of the trap compared to the precision trap, the potential coefficient $C_2$ is a factor of 4 larger. Thus, the described voltage ramp makes the trap for all particles above $m/q > 5.5$ unstable (see Eg. (2.9)). Subsequently, the particles are transported back to the precision trap and the $m/q$-range $2 < m/q < 5.5$ is cleaned again with rf-sweeps.

### *5.2 Trap Optimization with a Particle Cloud*

To resolve a single particle tuned to resonance with the axial detection system by means of noise-dip detection, it is important to tune the trap to high harmonicity (see section 6.3). First tuning is performed with voltage scan records. After loading, the particle-cloud has a certain energy distribution. As shown in Eq. (2.28) in presence of anharmonicities the energy distribution leads to a frequency distribution. In case of a harmonic trap, ramping an excited particle cloud over the axial detection leads to a narrow, large response, since all particles are at the same resonance frequency. In presence of anharmonicities the signal of the peak is smeared-out, due to the energy dependent frequency distribution. The trap can be optimized recording voltage scans for different tuning ratios. For the best tuning ratio the highest signal is recorded. Figure 5.3 shows two voltage scans, recorded with the same

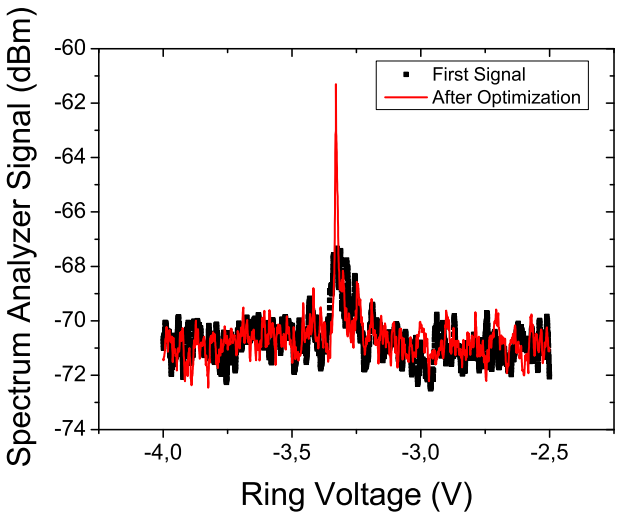


Figure 5.3: Voltage scans recorded with a proton cloud. The filled circles show a result, where the trap is anharmonic. After trap-tuning the spectrum indicated by the red solid line is measured.

proton cloud. The filled black squares represent the spectrum analyzer signal before trap optimization. The signal is smeared-out towards smaller absolute values of the ring voltage, indicating that $C_4 > 0$. The solid line represents the signal after optimization. By means of that method, the tuning ratio can be optimized quickly to about 1 mUnit. For further

optimization more sensitive methods have to be applied (see section 6.3).

### *5.3 Single Proton Preparation*

To reduce the clean proton cloud to one individual particle different experimental procedures can be applied. Axial heating and evaporation gradually reduces the number of particles. Another possibility is proton reduction by means of cyclotron excitation.

This is shown in Fig. 5.4. If the cyclotron motion of a proton cloud is excited, a broad

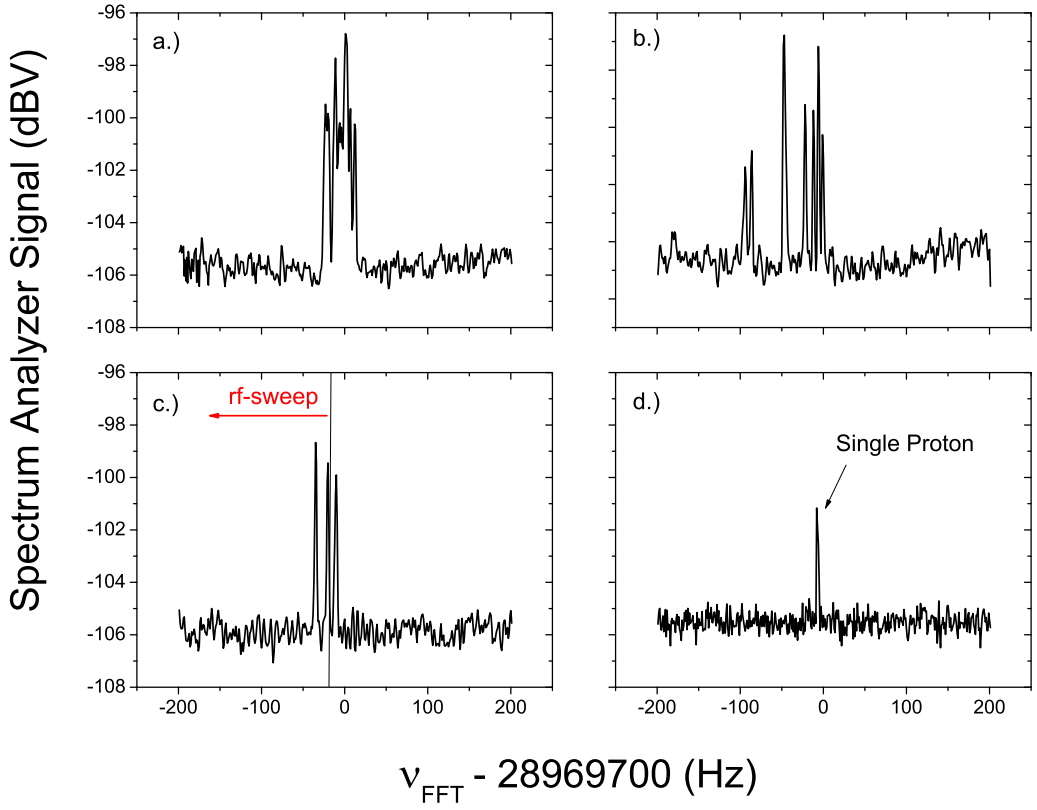


Figure 5.4: Proton reduction by means of rf-drives. a.) shows a cloud of excited protons. If rf-drives are applied repeatedly, protons are heated out of the trap (b.) and c.)) until one individual particle remains in the Penning trap (d.)). For further information see text.

particle peak appears on the cyclotron detection system (Fig. 5.4 a.)). Applying such an

excitation for several times the protons are heated [19]. The broad peak degenerates and narrow peaks, representing individual protons become visible (Fig. 5.4 b.)). This splitting is due to the energy dependence of the cyclotron frequency $\nu_+(E_+)$ caused by trap imperfections (see chapter 2). If the trap voltage is lowered, hot particles evaporate. This driving-lowering sequence is applied until only a few protons are left. Figure 5.4 c.) shows the signals of three individual trapped protons. Subsequently an rf down-sweep at high amplitude and a starting frequency below the resonance frequency $\nu_{+,1}$ of the coldest proton is applied, as indicated by the solid line and the arrow in Fig. 5.4 c.). This sweep heats all particles except of the coldest proton out of the trap. Fig. 5.4 shows the cyclotron peak-signal of an excited individual proton.

In order to proof that the signal is due to one *single* proton, the linewidth $\Delta\nu_z$ of the

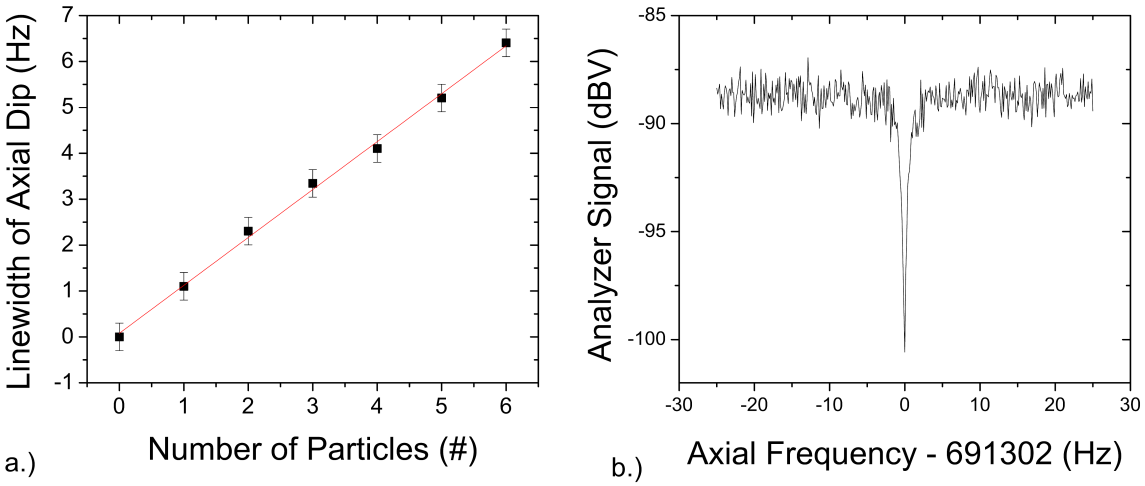


Figure 5.5: a.) Linewidth of the dip in the axial noise spectrum as a function of the number of particles stored in the Penning trap. b.) Axial noise-dip due to a single proton stored into the precision trap. The linewidth of the single-proton dip is $\Delta\nu_z = 1.2\,\mathrm{Hz}$.

dip in the axial noise spectrum is used. As explained earlier (Eq. (4.16)), for small particle numbers $N$ the linewith is given by

$$\Delta\nu_z = N\Delta\nu_{z,1}, \tag{5.2}$$

where $\Delta\nu_{z,1}$ is the linewidth of a single proton. For the calibration the linewidth of the axial noise-dip is measured for different, preliminary unknown particle numbers. Since every measured linewith has to be a multiple of the single-proton linewith $\Delta\nu_{z,1}$, after several measurements $\Delta\nu_{z,1}$ is yielded, just by solving simple algebraic equations. Having determined $\Delta\nu_{z,1}$, the noise-dip can be used as "particle-counter". Figure 5.5 a.) shows the linewidth of the axial noise-dip as a function of the particle number. The dip in the noise-spectrum shown in Fig. 5.5 b.) is due to one individual proton stored in the precision trap.

Chapter 6

# EXPERIMENTAL RESULTS - A SINGLE PROTON IN THE PRECISION TRAP

An experiment dedicated to a high-precision measurement has to be tuned to measure all quantities of interest fast, precisely and reliably. Most important for our experiment is the measurement of the Larmor frequency (discussed in chapter 8) and the measurement of the eigenfrequencies $\nu_+$, $\nu_-$ and $\nu_z$ of the trapped proton in the precision trap. Together with the invariance theorem (see Eq. (2.11)), these frequencies yield the free cyclotron frequency $\nu_c$. In this chapter the measurements of these eigenfrequencies are described. Moreover, systematic studies in the precision trap with its homogeneous magnetic field are presented.

## *6.1 Direct Measurement of the Cyclotron Frequency*

Having prepared a single proton in the precision trap, the direct measurement of the modified cyclotron frequency is as simple as described in chapter 4. By means of an rf-sweep the particle is excited to an energy $E_{+,0}$ and the cyclotron detection system (see chapter 4) is tuned to the proton's resonance frequency $\nu_+(E_+)$. Figure 6.1 a.) shows a peak on the noise spectrum of the detector, which is due to a single excited proton. Recording the frequency of the peak as a function of time, an exponential curve

$$\nu_+(t) = \nu_{+,0}\left(1 - \alpha_+ E_{+,0}\exp\left(-\frac{t}{\tau_+}\right)\right) \tag{6.1}$$

is measured. This is due to resistive cooling with the damping time constant

$$\tau_+ = \frac{m_p}{2\pi\nu_+ L_+ Q_+}\frac{D_{\mathrm{eff},+}^2}{q^2}\ . \tag{6.2}$$

$\alpha_+$ is due to trap imperfections (see chapter 2). Such a "cooling curve" $\nu_+(t)$ is shown in Fig. 6.1 b.). Fitting an exponential to the data, yields the cooling time constant $\tau_+ = 39.8(4)\,\mathrm{s}$. Since the parameters of the detection system are known, from such a measurement the effective electrode distance $D_{\mathrm{eff},+}^{\mathrm{exp}} = 15.3(2)\,\mathrm{mm}$ can be determined, which perfectly agrees

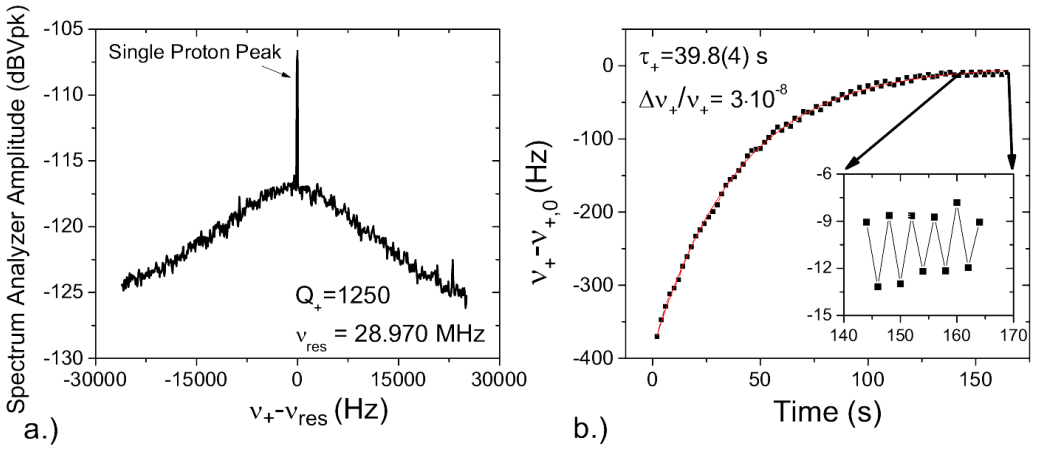


Figure 6.1: a.) Single proton peak signal on the noise resonance of the cyclotron detection system. b.) Measurement of the cyclotron frequency $\nu_+$ as a function of time. The drift described by Eq.(6.1) is due to a magnetic field inhomogeneity in the center of the precision trap which is caused by the ferromagnetic ring electrode of the analysis trap. The inset in b.) is a zoom to the last data points. The cyclotron frequency fluctuates with $\pm 1.6\,\mathrm{Hz}$, which is due to vibrations of the pulse tube cooler.

to the theoretical value calculated with Eq. (4.22), where $D_{\mathrm{eff},+}^{\mathrm{theo}} = 15.6(2)\,\mathrm{mm}$ is obtained. The inset in Fig. 6.1 b.) is a zoom of the last data points of the measuring sequence. The cyclotron frequency fluctuates by $\approx \pm 1.6\,\mathrm{Hz}$. This corresponds to a periodic fluctuation of the magnetic field with an amplitude of $\approx 100\,\mathrm{nT}$, which arises from diamagnetic currents induced in the apparatus by the vibration of the pulse tube cooler[1]. For a measurement of the cyclotron frequency by means of direct detection, the cooling curve is fitted with an exponential and $\nu_+(t = \infty)$ is extracted. Due to averaging by the fit, the cyclotron frequency can be determined to a relative precision of $\Delta\nu_+/\nu_+ = 3 \cdot 10^{-8}$. In order to improve the precision, which can be achieved by our experiment, the pulse tube cooler will be replaced by a liquid helium cryostat in one of the next experimental runs [79].

[1] In the first experimental runs we measured at magnetic field fluctuation amplitudes in the $\mu$T range. The improvement by a factor of 10 is due to vibration decoupling of the pulse tube cooler from the apparatus. This is described in detail in the diploma-thesis of C. Mrozik [100].

### *6.2 Contaminating Ions*

The cyclotron frequency measurement as a function of time $\nu_+(t)$ is an important tool to decide whether the trap is "clean". In presence of a contaminating ion, the trapping potential is modified by the coulomb-interaction monopole shift

$$\Delta V = \alpha\hbar c \frac{Z}{\sqrt{(\rho_p - \rho_c)^2 + (z_p - z_c)^2}} \ , \tag{6.3}$$

where $Z$ is the charge of the contaminating ion. Indices $p$ describe the proton indices $c$ the contaminant coordinates, respectively. The potential modification is repulsive leading to an increase of the axial frequency and a decrease of the cyclotron frequency. Harmonic balance averaging leads to average frequency shifts [101]

$$\Delta\nu_z = \frac{1}{8\pi^2}\frac{\alpha\hbar c}{\nu_z m_p}\frac{Z}{R_r^3} \tag{6.4}$$

and

$$\Delta\nu_+ \approx -\frac{\nu_z}{\nu_c}\Delta\nu_z \ , \tag{6.5}$$

where the relative distance $R_r = (\rho_p - \rho_c)$ between the proton and the contaminant was defined. If the proton is excited and cools resistively, the relative coordinate $R_r$ between the contaminant and the proton changes. In addition to $\alpha_+$ the effect of the monopole shift adds to the cooling characteristics Eq. (6.1). An example of a cooling curve in presence of a contaminant is shown in Fig. 6.2. First, the curve looks like an exponential, this is the case for large distances $R_r$, where the contribution of the monopole shift is small compared to the trapping fields. If the proton is cooled, the distance to the contaminant reduces, the monopole shift starts to contribute, and the cyclotron "cooling curve" shows a negative slope. Cooling the particle further, $\nu_+$ increases again. By observation of such cooling curves, at the AD-TRAP III experiment $H^-$ ions were discovered in an antiproton Penning trap, which led to an ultrahigh-resolution mass comparison of the proton and the antiproton mass at the sub-ppb level [102].

Note that the observation of such modifications of the cooling characteristics $\nu_+(t)$ indicates the presence of contaminants. If not observed, it does not necessarily indicate that the trap

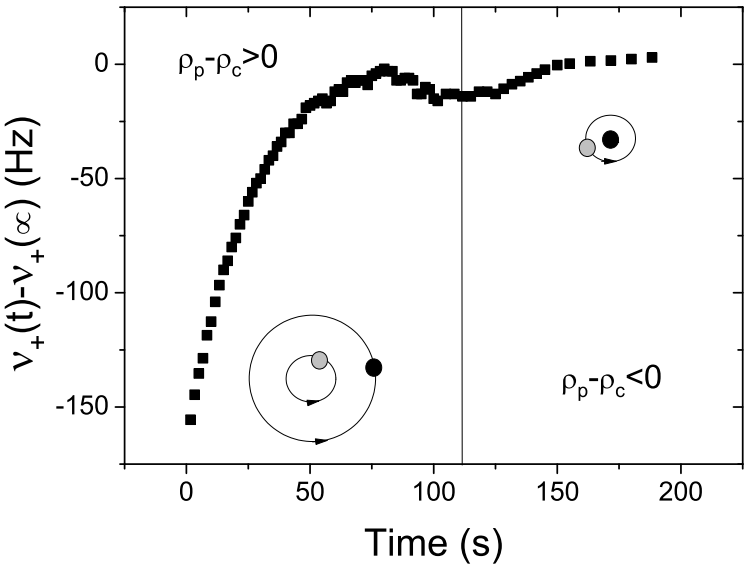


Figure 6.2: Cyclotron frequency as a function of time in presence of a contaminating ion. The proton is indicated as a black, the contaminant as a grey dot. For large distances between the proton and the contaminant, the cooling curve looks exponential. If $R_r = \rho_p - \rho_c$ becomes smaller, the monopole shift due to coulomb interaction modifies the cyclotron frequency and the cooling curve shows a negative slope.

is clean. If the contaminant is on a large radius, it cannot be detected by means of that method. For a very detailed discussion of particle-particle interaction in a Penning trap see [101, 103].

## *6.3 Basic Trap Tuning*

### *6.3.1 Harmonicity Tuning*

The modified cyclotron frequency $\nu_+$ and the magnetron frequency $\nu_-$ of the proton will finally be measured by sideband coupling to the axial mode, which will be discussed in section 6.6. The basis for fast and accurate frequency measurements by means of the axial detection system, is the perfect optimization of the trapping potential, i. e. the minimization of anharmonic potential terms.

When the particle is tuned to resonance with the axial detection system, the axial mode is

thermalized to the temperature $T_z$ of the detector, and shorts its thermal noise (see chapter 4). The resulting line shape is a convolution of the Lorentz-like lineshape (see Eq. (4.18)) of the single particle dip with the thermal Boltzmann distribution [42]. In presence of a trap anharmonicity $C_4$, the lineshape becomes

$$\chi(\omega) = \frac{A}{\pi k_B T_z} \int_0^\infty dE_z \exp\left(-\frac{E_z}{k_B T_z}\right) \frac{\gamma_z/2}{\left(\omega - \omega_z\left(1 + \frac{3}{4}\frac{C_4}{C_2^2}\frac{E_z}{qV_0}\right)\right)^2 + \gamma_z^2/4}\,, \tag{6.6}$$

where $A$ is a normalization factor, $E_z$ is the axial energy, and $\gamma_z$ the damping constant of the axial detection system. With increasing anharmonicity $C_4$, the convolution Eq. (6.6)

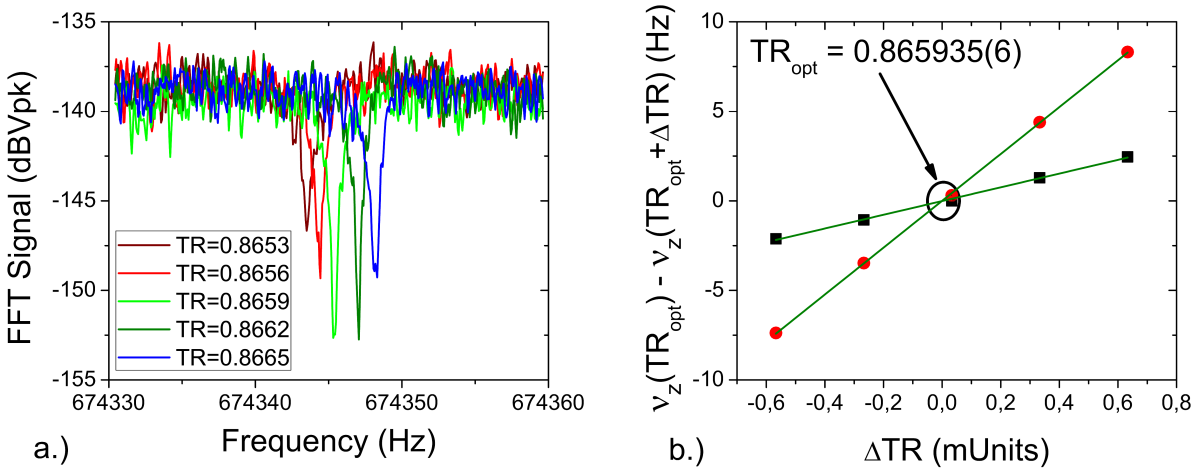


Figure 6.3: a.) Axial noise-dip spectra recorded for different tuning ratios. The frequency shift is due to a non-zero $D_2$. The narrowest and at the same time the deepest dip approximates the condition $C_4 = 0$ best. b.) Axial frequency as a function of the tuning ratio. The filled squares are due to the sequence described in a.), the red squares represent the same measurement principle but with broadband white noise added to the detector. The steeper slope is caused by the higher axial energy. From the crossing-point the ideal tuning ratio is obtained. By means of that method, the optimum tuning ratio can be determined with an absolute resolution of $6 \cdot 10^{-6}$.

leads to a broadening of the line and a reduction of the depth of the noise dip.

The trap can be tuned by measuring axial frequency spectra for different tuning ratios TR $= \frac{V_{ce}}{V_0}$ (see section 2.3.1). Figure 6.3 a.) shows axial noise-dip spectra of a single trapped proton for different tuning ratios applied to the trap electrodes. The frequency changes due to a non-vanishing orthogonality parameter $D_2$ (see section 2.3.1). The data

shown in the figure correspond to $D_2 = 3.83(8)\,\mathrm{Hz/\,mUnit}$ (for a detailed discussion of $D_2$ see section 6.4). With this fast and easy experimental method, the tuning ratio can be optimized with a precision of $100\,\mu$Units in about 3 minutes.

After this optimization a linewidth of the noise-dip of $1.23(5)\,\mathrm{Hz}$ is measured, which corresponds to an effective electrode distance $D^{\mathrm{exp}}_{\mathrm{eff,z}} = 7.73(15)\,\mathrm{mm}$. The theoretical result given by Eq. (4.21) is $7.61(2)\,\mathrm{mm}$ and agrees perfectly with the experimental result.

To optimize the trap to even higher harmonicity, broadband uniform white noise provided by an arbitrary wave-form generator *(Agilent 33250A)* is added to the detection system. This increases the axial energy $E_z$ of the proton, and thus, the sensitivity of the optimization to the correction $\frac{3}{4}\frac{C_4}{C_2^2}\frac{E_z}{qV_0}$. Therefore, the axial frequency is measured as a function of the tuning ratio, first without noise, and second with added noise. The result of such a measurement is shown in Fig. 6.3 b.). The filled squares are axial frequency records without additional noise, while in the sequence represented by the filled circles noise was added. The steeper slope of the filled circles is due to an increase of the average axial energy, caused by the added noise. The solid lines are linear fits to the data. From the crossing-point of both curves the ideal tuning ratio can be determined to an absolute precision of $0.006\,\mathrm{mUnits}$.

### *6.3.2 Trap Orientation*

The mechanics of our apparatus are designed in a way, that the trap can be adjusted in all three spacial dimensions (see chapter 3). If the electrostatic axis of the trap is misaligned with respect to the axis of the magnetic field, the effective axial potential seen by the particle is smoother compared to a perfectly oriented trap, leading to a smaller axial frequency. In a tilted trap, the effect of the decrease of the axial frequency is exactly compensated by an increase of the magnetron frequency leading to the same relation for the free cyclotron frequency for the tilted as for the ideal trap

$$\nu_c = \sqrt{\nu_+^2 + \nu_-^2 + \nu_z^2} = \sqrt{\tilde{\nu}_+^2 + \tilde{\nu}_-^2 + \tilde{\nu}_z^2}. \tag{6.7}$$

Here $\tilde{\nu}_i$ are the eigenfrequencies of the proton in the tilted trap. For this reason, Eq. (6.7) is called *invariance theorem* [37, 38]. Nevertheless, it is of great importance to work with a perfectly oriented trap since particle transport along the axis of a tilted Penning trap tower

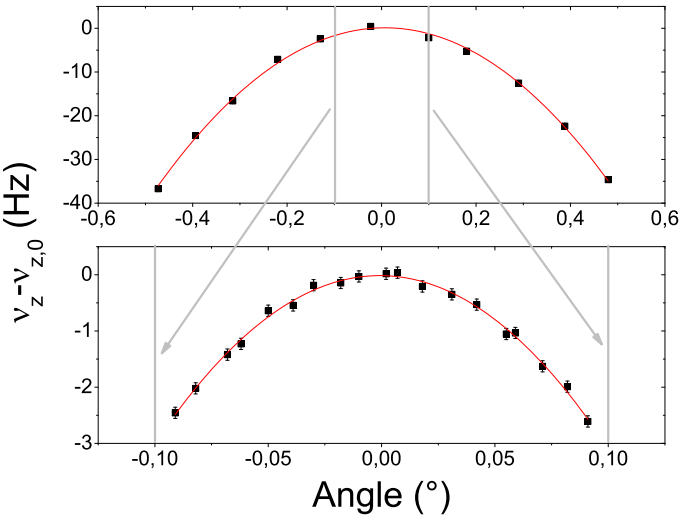


Figure 6.4: Axial frequency as a function of the tilt angle between the electrostatic axis defined by the electrodes and the magnetic field axis.

leads to accumulation of magnetron radius. To adjust the angle $\theta$ between the magnetic field axis and the electrostatic axis to zero, the axial frequency is measured as a function of $\theta$, and the relation

$$\tilde{\nu}_z(\theta) = \nu_{z,0}\sqrt{1 - \frac{3}{2}\sin^2(\theta)} \Rightarrow \tilde{\nu}_z(\theta) \approx \nu_{z,0}\left(1 - \frac{3}{4}\theta^2\right) \tag{6.8}$$

is applied [37]. The axial frequency-maximum $\nu_{z,\max}$ obtained from such an experimental sequence corresponds to $\theta = 0$. In Fig. 6.4 experimental results are shown. For the orientation, first a low-resolution measurement is recorded to roughly determine the maximum. Subsequently, the region around the maximum is scanned with higher resolution. The angle is obtained by the parameters of the best fit. Limited by the axial frequency resolution, the stability of the DC-voltage supply and hysteresis in the adjustment mechanics, the apparatus can be adjusted within an angle of $\leq 0.02°$. With the new orientation of the apparatus, no effect of the particle transport on the magnetron radius $\rho_-$ is observed anymore. Thus, cooling of the magnetron motion after particle-transport is not necessary, which is crucial for the optimization of the analysis trap (see section 7.1) and will finally allow a fast measuring sequence for the $g$-factor determination.

### *6.4 Advanced Trap Tuning - Asymmetry Compensation*

The electrodes of a cryogenic Penning trap are biased with the high-precision DC voltage supply located at room temperature (see chapter 3). The biasing lines underlie a temperature gradient of $\approx 300\,\mathrm{K}$. Under such experimental conditions, contact potentials in a range up to several 100 mV occur. Additionally, voltage drops due to leakage currents take place, being in the range of tens of millivolts. Under typical experimental conditions the voltages effectively applied to the electrodes differ by that amount resulting in an asymmetric trap potential, which is neither orthogonal nor compensated (see section 2.3.1). A technique to measure these offset voltages with the single trapped proton was developed.

Offset potentials $\Delta V$ are applied to the Penning trap electrodes and the axial frequency $\nu_z(\Delta V)$ is measured. Assume that the trap is perfectly harmonic in its initial state and no offset potentials are applied to the electrodes. Then, if $\Delta V$ is applied for example to the upper correction electrode *UCE*, the axial frequency shift $\Delta\nu_z(\Delta V) = \nu_z(0) - \nu_z(\Delta V)$ will be the same as if $\Delta V$ will be applied to the lower correction electrode *LCE*. If different offset potentials $\Delta\tilde{V}_{\mathrm{UCE}}$ and $\Delta\tilde{V}_{\mathrm{LCE}}$ are initially present at the electrodes, this will not be the case and $\Delta\nu_{z,\mathrm{UCE}}(\Delta V) \neq \Delta\nu_{z,\mathrm{LCE}}(\Delta V)$. How the frequency shifts behave in detail, can be calculated by potential theory (see chapter 2). The basic idea is, that the potential minimum $Z_{\mathrm{min}}$ is not at the center of the trap anymore, if asymmetric potentials are applied to the electrodes, but in the position[2]

$$Z_{\mathrm{min}}(V_{\mathrm{UEC}}, V_{\mathrm{UCE}}, V_{\mathrm{ring}}, V_{\mathrm{LCE}}, V_{\mathrm{LEC}}) = -\frac{C_1(V_{\mathrm{UEC}}, V_{\mathrm{UCE}}, V_{\mathrm{ring}}, V_{\mathrm{LCE}}, V_{\mathrm{LEC}})}{2C_2(V_{\mathrm{UEC}}, V_{\mathrm{UCE}}, V_{\mathrm{ring}}, V_{\mathrm{LCE}}, V_{\mathrm{LEC}})}\,. \tag{6.9}$$

Therefore, the series expansion of the potential given in Eq. (2.23) has to be modified to

$$\Phi(0,z) = V_{\mathrm{ring}} \sum_{j=0}^{\infty} C_{j,\mathrm{asm}}(V_i)(z - Z_{\mathrm{min}})^j \tag{6.10}$$

where the modified potential coefficients $C_{j,\mathrm{asm}}(V_i)$ are

$$\begin{aligned} C_{j,\mathrm{asm}}(V_i) &= \frac{2}{j!\Lambda V_{\mathrm{ring}}} \sum_{n=1}^{\infty} \left[ \frac{V_1\cos(k_n z_0) - V_5\cos(k_n\Lambda)}{k_n} + \sum_{i=2}^{5} \frac{V_i - V_{i-1}}{k_n^2 d}\left(\sin(k_n z_{2i}) - \sin(k_n z_{2i-1})\right) \right] \\ &\times \frac{1}{I_0(k_n a)} \left[ \frac{d^j}{dz^j} \sin\left(k_n\left(z + \frac{\Lambda}{2}\right)\right) \right]_{Z_{\mathrm{min}}} . \end{aligned} \tag{6.11}$$

[2]This is a first order shift of the potential minimum. If larger offset voltages occur at the trap electrodes, higher order shifts which arise from $C_3$ and $C_5$ have also to be taken into account.

Here, $\Lambda$ is the total length of the trap, $d$ is the distance between two adjacent electrodes, and $z_i$ are the electrode coordinates (for a more detailed description see section 2.3.1). In the experiment, the axial frequency $\nu_z(\Delta V_i)$ is measured for different offset voltages $\Delta V_i$ applied to different trap electrodes $i$. Figure 6.5 shows the axial frequency shift $\nu_z(\Delta V_i) - \nu_z(0)$ as a function of the offset potential applied to electrode $i$. In the

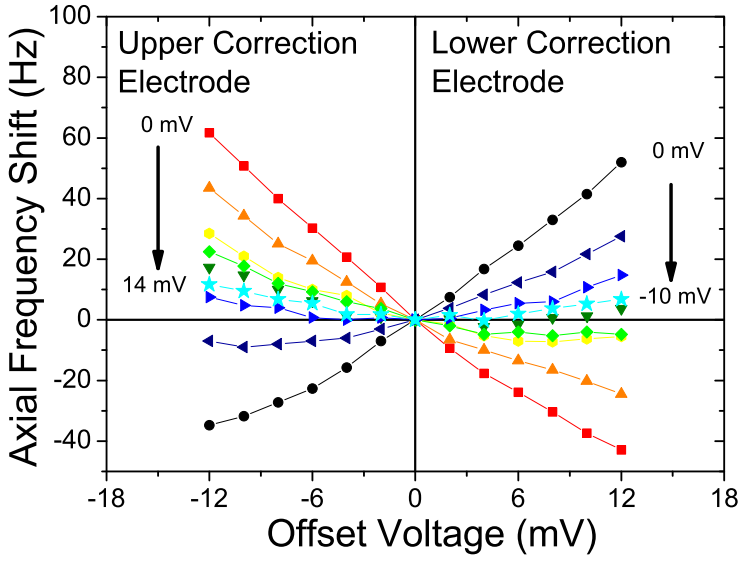


Figure 6.5: Asymmetry Compensation. Axial frequency shift $\nu_z(\Delta V_i) - \nu_z(0)$ as a function of the offset potential applied to electrode $i$. In the data sets showing a negative slope, the offset voltage was applied to the upper correction-electrode. The data with positive slopes are due to an offset voltage which is applied to the lower correction-electrode. Due to the asymmetry compensation algorithm which is described in the text, the trap can be symmetrized. By means of that method, asymmetric voltages which are initially present at the trap electrodes can be directly measured with the single trapped proton.

data set, which is represented by the red squares, the offset voltage $\Delta V_{\mathrm{UCE}}$ was applied to the upper correction electrode. The negative slope of the curve is due to a negative offset voltage being initially present at the upper correction electrode. In the next measuring sequence, a constant positive offset potential $\Delta V_{\mathrm{off,1,UCE}} = 3\,\mathrm{mV}$ is applied to this electrode, and $\nu_z(\Delta V_{\mathrm{UCE}} + \Delta V_{\mathrm{off,1,UCE}}) - \nu_z(\Delta V_{\mathrm{off,1,UCE}})$ is measured. The re-

sulting data are represented by the filled orange triangles. Compared to the first sequence, the slope of the data is still negative but smaller. The voltage asymmetry is partly compensated by the added offset potential $\Delta V_{\mathrm{off,1,UCE}}$. This measuring sequence is repeated for different offset voltages $\Delta V_{\mathrm{off,k,UCE}}$, where $k$ is an iteration index, until the trap behaves symmetric, meaning that an offset voltage $\Delta V_{\mathrm{off,k,UCE}}$ is found for which $\nu_z(\Delta V_{\mathrm{UCE}}+\Delta V_{\mathrm{off,k,UCE}})-\nu_z(\Delta V_{\mathrm{off,k,UCE}}) = \nu_z(-\Delta V_{\mathrm{UCE}}+\Delta V_{\mathrm{off,k,UCE}})-\nu_z(\Delta V_{\mathrm{off,k,UCE}})$ and $\nu_z(\Delta V_{\mathrm{LCE}} + \Delta V_{\mathrm{off,k,UCE}}) - \nu_z(\Delta V_{\mathrm{off,k,UCE}}) = \nu_z(-\Delta V_{\mathrm{LCE}} + \Delta V_{\mathrm{off,k,UCE}}) - \nu_z(\Delta V_{\mathrm{off,k,UCE}})$. This is the case for the cyan-filled stars, where at the upper correction electrode an offset potential of $\Delta V_{\mathrm{off,k,UCE}} = 14\,\mathrm{mV}$, and at the lower correction electrode $\Delta V_{\mathrm{off,k,UCE}} = -10\,\mathrm{mV}$ is applied. In this case we call the trap *asymmetry-compensated*. The data points with the positive slopes represent the same measuring sequence, but for the lower correction electrode.

Note, that this way of asymmetry compensation is arbitrary in a certain way. If a negative net-offset voltage is initially present for example at the upper correction electrode, it may be compensated by applying a positive offset voltage to this electrode, or alternatively, by applying a negative compensation voltage to the lower correction electrode. The absolute value and sign of the offset voltages which are present initially, cannot be determined by the technique described so far. But it is important to note, that the algorithm presented here leads to a locally symmetrized trap. If the asymmetry measurement curves shown in Fig. 6.5 are fitted with the function

$$\nu_z = \frac{1}{2\pi}\sqrt{\frac{2qC_{2,\mathrm{asm}}(V_i)V_0}{m}}\ , \tag{6.12}$$

where for $C_{2,\mathrm{asm}}(V_i)$ Eq.(6.11) has to be inserted, geometrical errors and all asymmetry voltages are obtained from the fit[3]. One free parameter is left which defines zero potential. Therefore in the fit routine $V_{\mathrm{LEC}}$ is defined to be zero. From the fit to the data the values shown in Tab. 6.1 are obtained. The errors given for the endcap electrodes exceed the errors given for the correction-electrodes by a factor of 5, which is due to the larger distance of

[3]Since $C_{2,\mathrm{asm}}$ is a product of a series expansion with at least 1600 coefficients it is in fact not simple to find a convergent fit without giving sharp constraints. This problem was solved by a numerical simulation which simulated potentials and fitted finally curve arrays to the data.

the endcap electrodes to the particle, and therefore the reduced sensitivity.

In order to test the results, other parameters are measured and the results are compared

Table 6.1: Geometrical errors and offset potentials present at the precision trap of our experiment. For the geometrical values also a comparison is between the measured value and the design value given which shows that the work performed by the technicians from the workshop in Mainz is excellent.

| | Value | Error | Design Value |
|---|---|---|---|
| Voltage Offset Ring Electrode | -21 mV | ±2 mV | - |
| Voltage Offset Upper Correction Electrode | -14 mV | ±2 mV | - |
| Voltage Offset Lower Correction Electrode | 10 mV | ±2 mV | - |
| Voltage Offset Upper Endcap Electrode | 23 mV | ±10 mV | - |
| Voltage Offset Upper Endcap Electrode | 0 mV | 0 mV | - |
| Length of Ring Electrode | 0.916 mm | ±5 $\mu$m | 0.92 mm |
| Length of Upper Correction Electrode | 2.852 mm | ±5 $\mu$m | 2.850 mm |
| Length of Lower Correction Electrode | 2.839 mm | ±5 $\mu$m | 2.850 mm |

to potential theory. Therefore, the orthogonality coefficient $D_2$, as well as the resonance voltage, which has to be applied to center the axial frequency of the proton on the axial resonator, is measured as a function of the offset voltage applied to the upper correction electrode. The results of these measurements are represented by the filled squares in Fig. 6.6. Note, that the solid lines are not due to fits, but from to analytic calculations based on the parameters shown in Tab. 6.1. Obviously, the experimental data points behave exactly as predicted. This excellent agreement is of importance, since such a remarkable understanding of the electrostatic properties of the trap can be utilized for systematic studies. Based on that detailed knowledge of trap errors and thus, the trapping potential, the particle energy can be calibrated (see section 6.10), which has never been done before, using the argument that a Penning trap has unknown machining errors and unknown applied offset potentials (see f. e. [17] or [103]). With the asymmetry compensation method presented here, the single trapped proton itself is used as an electro-mechanical probe to measure these errors!

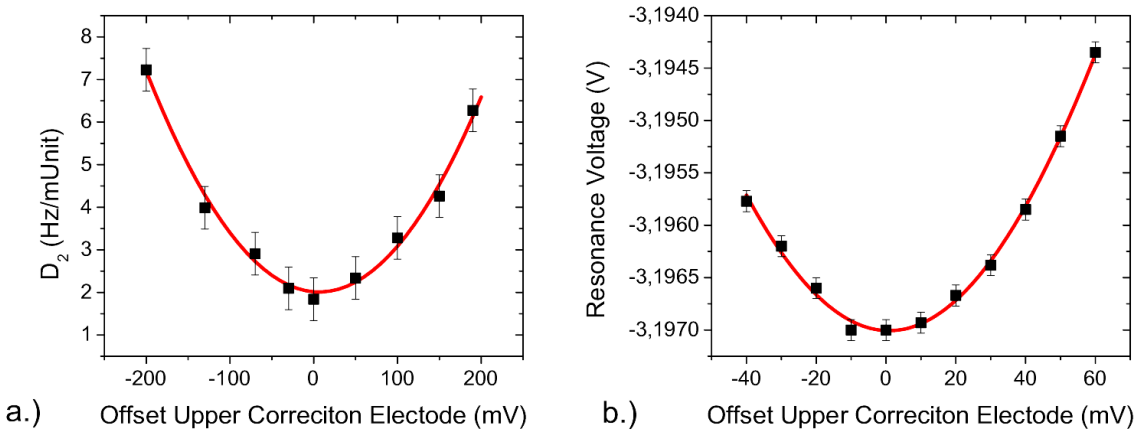


Figure 6.6: Consistence test of the asymmetry compensation. a.) The orthogonality coefficient $D_2$, and b.) resonance voltage to set the proton in resonance with the axial detection system as a function of an offset potential which is applied to the upper correction-electrode. Note, that the solid lines are not due to fits anymore but only due to analytic calculations based on the parameters shown in Tab. 6.1.

With that detailed knowledge the proton can now be shifted along the $z$-axis of the trap with sub-$\mu$m resolution which can f. e. be utilized to measure the magnetic field $B$ of the trap as a function of the particle position $z$ (see section 7.3). Furthermore, it is possible to "taylor" the Penning trap to certain experimental constraints.

Note that in presence of asymmetric offset voltages, all trap specific parameters change. This has been shown in Fig. 6.6 for the orthogonality parameter $D_2$. But the anharmonicity coefficients $C_4$ and $C_6$ vary as well with the offset potentials. Asymmetric offset voltages break the simultaneous compensation $C_4(\mathrm{TR_{opt}}) = C_6(\mathrm{TR_{opt}}) = 0$ of the five-pole Penning trap. The asymmetry compensation method can be utilized to compensate this breaking, being crucially important, if measuring techniques are applied which require large particle amplitudes where the effect of $C_6$ on the axial frequency is substantial. In Fig. 6.7 the ideal tuning ratio setting $C_4 = 0$ (filled squares) and $C_6 = 0$ (filled circles), respectively, is shown as a function of the asymmetry applied to one of the correction electrodes. For this simulation an extreme example was chosen, assuming that both compensation electrodes show machining errors of 100 $\mu$m. Two offset voltages exist, where $C_4$ and $C_6$ simultaneously

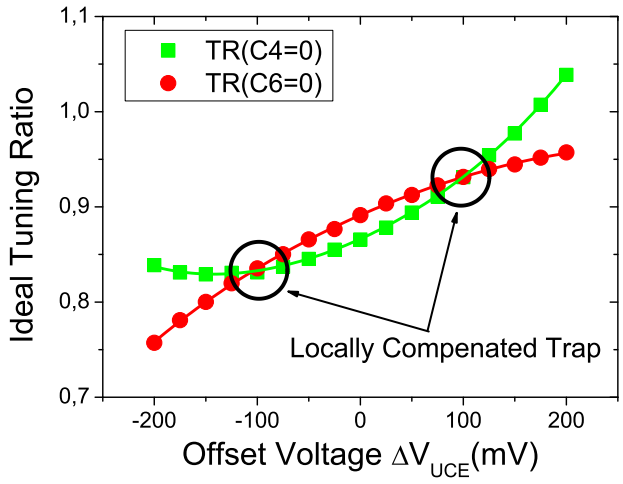


Figure 6.7: Calculation Results. Ideal tuning ratio to set $C_4 = 0$ (filled squares) and $C_6 = 0$ (filled circles) as a function of the offset potential $\Delta V_{\mathrm{UCE}}$ applied to the upper-correction electrode. In this example, it was assumed that the correction electrodes of the trap have machining errors of 100 $\mu$m. Two tuning ratios exist, which simultaneously compensate the first higher order coefficients $C_4$ and $C_6$.

vanish for a certain tuning ratio, and thus, locally compensate the trap. The understanding and application of asymmetry compensation leads to the possibility to perform challenging experiments with imperfect Penning traps.

### *6.5 Optimization of Spectrum Analyzer Averaging Time*

For the noise-dip detection method of the axial frequency an FFT spectrum is recorded for an averaging time $\Delta t$ and a Lorentz-curve is fitted to the data. It is obvious that the axial frequency resolution is a function of averaging time, since for very short $\Delta t$ the result will be noisy due to thermal and spectrum analyzer noise. With increasing measuring time the results are smoothed by analyzer averaging, but long-term fluctuations add up, which increase the fluctuation. To characterize the frequency stability obtained by noise-dip detection, the axial frequency fluctuation

$$\Xi = \sqrt{\frac{1}{N}\sum_n (\alpha_n - \bar{\alpha})^2} \tag{6.13}$$

is introduced, where $\alpha_n = \nu_z(n\Delta t) - \nu_z((n-1)\Delta t)$. $N$ is the total number of measurements and $\bar{\alpha}$ is the mean value of all $\alpha_n$, which typically vanishes for large $N$. If no additional frequency drift effect is present, the total axial frequency fluctuation $\Xi_{tot}$ is the root of the square-sum $\Xi_{\mathrm{tot}} = \sqrt{\Xi_{\mathrm{FFT}}^2 + \Xi_{\mathrm{DC}}^2}$, where $\Xi_{\mathrm{FFT}}$ is the fluctuation caused by averaging of the FFT analyzer and $\Xi_{\mathrm{DC}}$ is the fluctuation due to the DC-voltage supply (see chapter 3). In Fig. 6.8 the fluctuation is shown as a function of averaging time. The green dashed line represents simulation results of $\Xi_{\mathrm{FFT}}$. In the simulation Gaussian white noise is added to the theoretical noise dip curve. The data are averaged, a Lorentz-line is fitted to the noise dip and $\Xi_{\mathrm{FFT}}$ is evaluated. The dash-dotted line is due to the measured voltage fluctuation of the DC-supply, while the solid line is $\Xi_{\mathrm{tot}}$. The filled stars and the filled circles are experimental results. For every data point a measuring sequence with $N = 200$ was evaluated. In the experimental sequence which is represented by the filled stars, the tuning ratio was detuned from the optimum by 400 $\mu$Units, while in case of the filled circles the optimum tuning ratio was used. For long averaging times both data sets converge to the same fluctuation limit of $\approx 75$ mHz. The sequence where the tuning ratio was detuned from the optimum (filled stars) converges slower but to the same limit. The reason is, that for a detuned trap the noise-dip does not short the thermal noise of the axial resonator (see section 6.3) and, thus, the relative fluctuation effect caused by averaging noise is increased. Note that this effect is only due to spectrum analyzer averaging and not caused by an active "self-drive" [42], which may be caused by the non-vanishing $C_4$ term.

The filled dots, which represent the measuring sequence for optimized tuning ratio, follow the solid line $\Xi_{\mathrm{tot}}$ obtained from the simulation results. Hence, the total axial frequency stability is well understood. The principal resolution limit is achieved at a measuring time of about 100 s, which is two times faster compared to the sequence where the tuning ratio was detuned from the optimum. This demonstrates, again, that for a high-precision experiment it is crucial to tune the trap to high harmonicity. Fast measuring sequences are only possible in adequately optimized traps. In practice, for measurements in the precision trap averaging times between 80 s and 110 s are used.

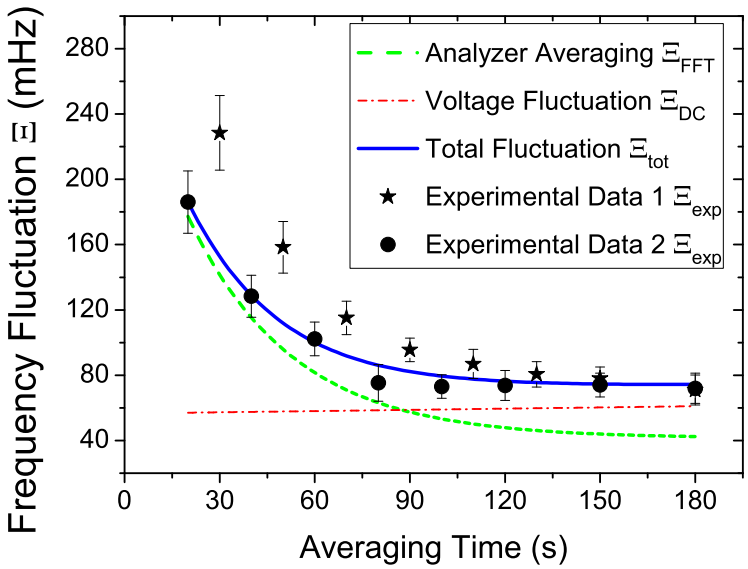


Figure 6.8: Axial frequency fluctuation $\Xi$ as a function of averaging time. The dashed line represents the result of FFT data-averaging simulations, while the dash-dotted line is due to fluctuations of the DC-voltage supply. The solid line is the resulting total fluctuation $\Xi_{\rm tot} = \sqrt{\Xi^2_{\rm FFT} + \Xi^2_{\rm DC}}$. The filled circles and the filled stars represent experimental results. In case of the circles the optimized tuning ratio was applied to the compensation-electrodes, while in the sequence represented by the stars, the tuning ratio was detuned from the optimum by $400\,\mu$Units.

### *6.6 Sideband Coupling, Cooling, and Frequency Measurements in "Thermal Equilibrium"*

One of the most important techniques applied at our experiment is *sideband coupling*. In [37, 104] the technique is described in detail. In [105] a very technical but fully quantum mechanical approach including the discussion of the transition to the classical limit is found. The technique is used for frequency measurements, mode cooling, temperature measurements and mode-temperature calibration, -manipulation and -preparation. Applying rf-drives[4] with a frequency $\omega_{\rm rf}$ and a field amplitude $E_0$ to the trap electrodes, which couple

[4] I will follow the convention, that in calculations for the "frequencies" $\omega$ is used. In the data presentation, frequencies $\nu$ will be used, since these are the measured quantities. For the Rabi frequency we will explicitly write $\Omega$ and $\Omega/2\pi$.

the coordinates

$$\vec{E}\left(x_i, x_k\right) = \mathrm{Re}\left(E_0 \exp\left(i\omega_{\mathrm{rf}} t\right)\right)\left(x_i \vec{e}_k + x_k \vec{e}_i\right) \tag{6.14}$$

at the sum and the difference frequency $\omega_{rf} = \omega_i \pm \omega_k$ of two modes described by the coordinates $x_{i,k}$ and frequencies $\omega_{i,k}$, energy can be transferred form one mode $i$ into the other $k$. The system of differential equations describing the dynamics is given by

$$\ddot{x}_i + \omega_i^2 x_i = \frac{qE_0}{m} \exp\left(i\omega_{\mathrm{rf}} t\right) x_k \tag{6.15}$$

$$\ddot{x}_k + \omega_k^2 x_k = \frac{qE_0}{m} \exp\left(i\omega_{\mathrm{rf}} t\right) x_i \ . \tag{6.16}$$

If possible, such systems are typically solved by two different ansatzes:

1. A transformation to a system, where the dynamical matrix has only non-diagonal terms, or

2. a transformation to a system, where the dynamical matrix is diagonal.

Both transformations lead to valid solutions, focussing different aspects of physical reality. While the non-diagonal form focuses on energy transfer between the modes and leads to a "time-like" interpretation of the dynamics, the diagonal form is "energy-like" and points out that the mode energies are shifted due to the superposition of the trap with the coupling field[5]. Assuming that the field amplitude of the rf-drive is small compared to the field strengths defining the unperturbed mode dynamics, which is valid for typical experimental conditions (typical frequencies due to coupling are in the range of Hz, only, compared to kHz to MHz trap frequencies), the transformation

$$x_i \rightarrow \frac{X_i(t)}{\sqrt{\pi m \omega_i}} \exp\left(i\omega_i t\right) \tag{6.17}$$

$$x_k \rightarrow \frac{X_k(t)}{\sqrt{\pi m \omega_k}} \exp\left(i\omega_k t\right) \tag{6.18}$$

[5]Both ansatzes are well known from the quantum mechanical discussion of a two-level system in presence of a resonant coupling field. The solution of the first ansatz leads to Rabi-oscillations, while the second ansatz focusses on shifts of the energy levels due to the ac-Stark effect.

leads to a non-diagonal system matrix with vanishing trace and complex eigenvalues, being equivalent to an oscillating system. The transfer rate is defined by the strength of the drive and can be expressed in terms of a "Rabi frequency"

$$\Omega_0 = \frac{qE_0}{2m\sqrt{\omega_i\omega_k}} . \tag{6.19}$$

In the following we concentrate on the coupling of the magnetron mode to the axial mode. Assume that the particle has initially zero axial amplitude and non-vanishing radial amplitude, and a resonant coupling drive $\omega_{\mathrm{rf}} - (\omega_z + \omega_-) = \delta = 0$ is turned on. Due to the energy transfer between the modes, the mode trajectories can be parameterized as

$$z(t) = z_0 \sin\left(\frac{\Omega_0}{2}t\right) \sin\left(\omega_z t + \phi_z\right) \tag{6.20}$$

$$\rho_-(t) = \rho_{-,0} \cos\left(\frac{\Omega_0}{2}t\right) \sin\left(\omega_- t + \phi_-\right) , \tag{6.21}$$

where $\phi_{z,-}$ are arbitrary phases. The mode amplitudes $z$ and $\rho_-$ are modulated with the frequency $\Omega_0/2$. A frequency analysis of Eq. (6.21) gives modified eigenfrequencies $\omega_{l,r} = \omega_z \mp \Omega_0/2$. Actually, if a coupling drive is applied, the single particle dip in the noise spectrum of the axial resonator splits into two dips. This is shown in Fig. 6.9 a.) for coupling of the magnetron mode to the axial mode via a coupling field with $\omega_{\mathrm{rf}} = \omega_z + \omega_-$. This structure is called "double-dip". For resonant coupling $\omega_{\mathrm{rf}} - (\omega_z + \omega_-) = \delta = 0$ the separation of the two dips in the frequency spectrum is exactly the resonant Rabi frequency $\Omega_0$. For non-resonant coupling $\delta \neq 0$ the system oscillates at the modified Rabi frequency $\Omega = \sqrt{\Omega_0^2 + \delta^2}$ and the energy is not transferred completely from one mode into the other. In order to investigate how non-resonant coupling affects the new eigenfrequencies $\omega_l$ and $\omega_r$, the system is diagonalized by the assumption that the axial mode oscillates at $\omega = \omega_z + \epsilon$ and the magnetron mode at $\omega - \omega_p$, where $\omega_p = \delta + \epsilon + \omega_- - \omega$ [104]. Inserting this ansatz into the system Eq. (6.18), it is found that the frequency values $\omega_l$ and $\omega_r$ of the dips are given by $\omega_{l,r} = \omega_z + \epsilon_{l,r}$, where

$$\epsilon_{l,r} = -\frac{1}{2}\left(\delta \pm \Omega\right) = -\frac{1}{2}\left(\delta \pm \sqrt{\Omega_0^2 + \delta^2}\right) . \tag{6.22}$$

If $\omega_{\mathrm{rf}}$ is tuned over the resonance $\omega_z + \omega_-$, it is observed, that the $\omega_l$ and $\omega_r$ vary as predicted by Eq. (6.22). The result of such a measurement is shown in Fig. 6.9 b.). The

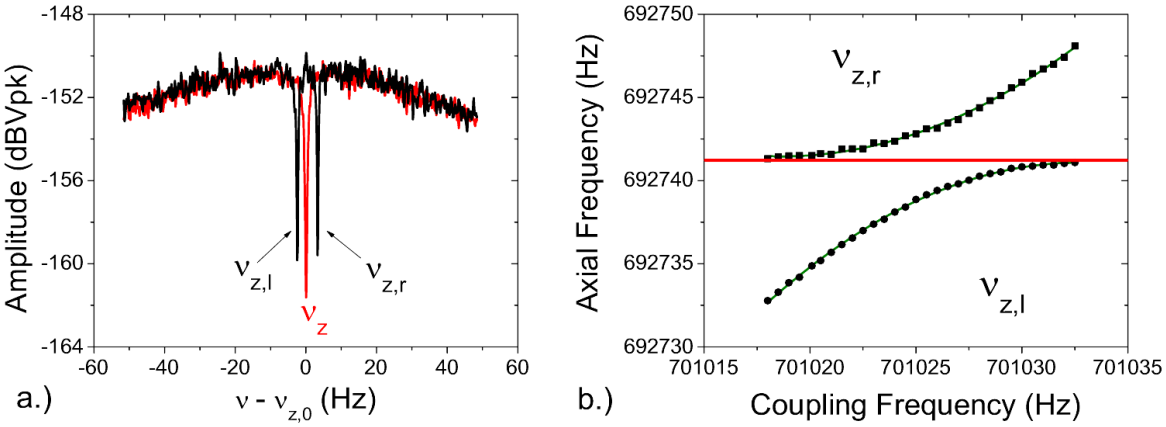


Figure 6.9: a.) Single- and double-dip in the noise spectrum of the axial detector. The double-dip is due to an irradiated coupling drive with frequency $\nu_{\mathrm{rf}} \approx \nu_z + \nu_-$. Such a drive transfers energy between the axial and the magnetron mode, leading to an amplitude modulation with the Rabi frequency $\Omega/4\pi$ and consequently to frequencies $\nu_l = \nu_z - \Omega/4\pi$ and $\nu_r = \nu_z + \Omega/4\pi$ in the noise spectrum of the axial resonator. b.) "Classical avoided crossing" recorded by a coupling of the magnetron mode to the axial mode. The frequency $\nu_{rf}$ of the coupling drive is tuned in steps over the resonance $\nu_z + \nu_-$ and the frequencies $\nu_l$ and $\nu_r$ of the respective dips are measured. For further details see text.

filled circles represent the measured frequency values of the left dip while the filled squares are the frequencies of the right dip. Fitting Eq. (6.22) to such a "classical avoided crossing" the magnetron frequency $\omega_-$, as well as the Rabi frequency and thus, the effective coupling strength of the rf-drive to the particle can be extracted.

For the measurement of the radial eigenfrequencies by means of sideband coupling to the axial mode, it is not necessary to record a full avoided crossing. If $\omega_{\mathrm{rf}}$ is irradiated, and the frequencies $\omega_l$ and $\omega_r$ are measured, from Eq. (6.22),

$$\omega_l + \omega_r = 2\omega_z - \delta = \omega_z + \omega_{rf} - \omega_- \tag{6.23}$$

is obtained. This equation bears two unknown quantities, the axial frequency $\omega_z$ and the magnetron frequency $\omega_-$. If the axial frequency is measured independently, the magnetron frequency is yielded. Thus, a measurement of the radial frequencies by means of sideband coupling requires two independent measurements.

All arguments and techniques presented for magnetron-to-axial coupling, are also valid for

the modified cyclotron frequency, except for the sign in the coupling frequency. If the particle is driven with a sideband $\omega_{\mathrm{rf}} = \omega_+ - \omega_z$ the same argumentation holds and the cyclotron frequency can be determined

$$\omega_l + \omega_r = 2\omega_z - \delta = \omega_z - \omega_{rf} + \omega_+ \ . \tag{6.24}$$

Thus, applying sideband-coupling, within three measurements of typically 80 s all eigenfrequencies of the trapped proton are obtained. Tabular 6.2 shows results obtained from sideband frequency measurements. Note that the precision of the free cyclotron frequency

Table 6.2: Results of the frequency measurements achieved with the sideband method. Note that the precision of the free cyclotron frequency is defined by the precision achieved by the measurement of the modified cyclotron frequency.

| | Result | Error | Relative Precision |
|---|---|---|---|
| Modified Cyclotron Frequency $\nu_+$ | 28 970 274.66 Hz | 0.14 Hz | $4.8{\cdot}10^{-9}$ |
| Axial Frequency $\nu_z$ | 674 408.05 Hz | 0.05 Hz | $7.4{\cdot}10^{-8}$ |
| Magnetron Frequency $\nu_-$ | 7 854.12 Hz | 0.07 Hz | $9.8{\cdot}10^{-6}$ |
| Free Cyclotron Frequency $\nu_c$ | 28 978 124.54 Hz | 0.14 Hz | $4.8{\cdot}10^{-9}$ |
| Magnetic Field $B$ | 1.900 804 710 T | $9.2{\cdot}10^{-9}$ T | $4.8{\cdot}10^{-9}$ |

is dominated by the precision achieved by the measurement of the modified cyclotron frequency, which is due to the relation

$$\Delta\nu_c = \sqrt{\left(\frac{\nu_+}{\nu_c}\Delta\nu_+\right)^2 + \left(\frac{\nu_z}{\nu_c}\Delta\nu_z\right)^2 + \left(\frac{\nu_-}{\nu_c}\Delta\nu_-\right)^2} \ , \tag{6.25}$$

and $\nu_+/\nu_c \approx 1$, $\nu_z/\nu_c \approx 1/43$, and $\nu_-/\nu_c \approx 1/3700$. To measure the free cyclotron frequency with a relative precision in the ppb range, the magnetron frequency has only to be known to about 100 Hz. Therefore, the measurement of the magnetron frequency is neglected in most $g$-factor measuring cycles and routinely just determined once per day [42, 51]. By means of the sideband technique the modified cyclotron frequency can be determined with one order of magnitude higher precision compared to the direct measuring method described in section 6.1. This is due to averaging of the FFT analyzer during the dip detection. The

error $\Delta\nu_+$ of the modified cyclotron frequency measurement is larger than $\sqrt{2}\Delta\nu_z$, which should potentially be achieved. This is due to the fluctuation of the magnetic field caused by the vibration of the cryo-cooler, which leads to a broadening of the linewidths of the cyclotron sideband dips, increasing the error of $\Delta\nu_+$. With these measurements it has been shown, that the final experimental aim, the measurement to a relative precision of $10^{-9}$ has nearly been achieved.

So far it has been shown, that sideband-coupling is a strong tool for the measurements of the eigenfrequencies of the trapped proton. It is of special interest, since the frequencies are measured by mode coupling to the thermal bath of the axial detection system, which is nearly at ambient physical temperature of $\approx 5\,\mathrm{K}$[6]. Thus, a detailed understanding of mode temperature in case of a frequency measurement by means of sideband coupling is crucial. In the thermodynamic limit the radial mode is "thermalized" in an interesting way. On a first look it may be assumed that the equipartition theorem holds and that both modes coupled to the axial heat bath are at the same temperature. Surprisingly, this is not true. If the particle is initially in the state $(n_z, n_-)$ and interacts with an rf-photon with energy $\hbar(\omega_z + \omega_-)$ a transition to the states $(n_z + 1, n_- - 1)$ or $(n_z - 1, n_- + 1)$ is possible. The matrix element of the process $(n_z, n_-) \to (n_z + 1, n_- - 1)$ "heats" the magnetron mode and goes as $(n_z + 1)n_-$ while the process $(n_z, n_-) \to (n_z - 1, n_- + 1)$ "cools" the magnetron mode and a proportionality of the transition rate $\propto n_z(n_- + 1)$ is found[7]. Thus, as long as $n_- > n_z$ the cooling transition dominates, until the equilibrium state characterized by equal quantum numbers of the modes $n_z = n_-$ is reached. For the limit temperature the relation

$$T_- = \frac{\omega_-}{\omega_z} T_z \tag{6.26}$$

is found. It will be shown in section 7.4 that average magnetron temperatures down to $T_- = 1\,\mathrm{mK}$ can be achieved and that the particle can be prepared to magnetron energies of $T_- = |E_-|/k_B \approx 100\,\mu\mathrm{K}$ within a few minutes[8].

---

[6] In fact it is slightly higher which will be discussed later in this chapter and in section 7.4

[7] Heating means that the magnetron radius increases, while cooling leads to a decrease of $\rho_-$.

[8] Sometimes the mode energies $E_i$ are expressed in terms of the "temperature" scale $T_i = E_i/k_B$. For low energies the term "temperature" is more intuitive as energy. One Kelvin corresponds to $86\,\mu\mathrm{eV}$.

In case of the modified cyclotron frequency $\omega_+$ the same argumentation holds, leading to the equilibrium cyclotron temperature of

$$T_+ = \frac{\omega_+}{\omega_z} T_z \tag{6.27}$$

being a factor of $\approx 40$ larger than the temperature achieved by direct resistive cooling with the cyclotron detector.

Indeed, measuring frequencies by means of sideband coupling the particle is cooled to a tiny volume. The thermal amplitude of the axial mode is about $20\,\mu\mathrm{m/K}^{0.5} \cdot \sqrt{\mathrm{T}_z}$, the magnetron as well as the cyclotron mode amplitudes are in the range of $4\,\mu\mathrm{m/K}^{0.5} \cdot \sqrt{\mathrm{T}_z}$. For such tiny proton-amplitudes, the relative eigenfrequency-shifts are far below the ppb range (see chapter 2).

### *6.7 Advanced Coupling*

Frequency shifts arising from trap-errors can be neglected if the eigenfrequencies are determined by means of sideband-coupling. A remaining problem is, that sideband measurements require a certain amount of averaging time - typically $\Delta t_{\mathrm{FFT}} \approx 100\,\mathrm{s}$ per measurement. For a determination of the cyclotron frequency $\nu_+$, first the axial frequency is measured ($\Delta t_{\mathrm{FFT}} = 80\,\mathrm{s}$). Subsequently an rf-field with $\nu_{\mathrm{rf}}$ is irradiated and a double-dip spectrum is measured ($\Delta t_{\mathrm{FFT}} = 120\,\mathrm{s}$) yielding $\nu_l$ and $\nu_r$

$$\nu_l + \nu_r = 2\nu_z - \frac{\delta}{2\pi} = \nu_z - \nu_{\mathrm{rf}} + \nu_+ \ . \tag{6.28}$$

Combining both results, the cyclotron frequency

$$\nu_+ = \nu_l + \nu_r - \nu_z + \nu_{\mathrm{rf}} \tag{6.29}$$

is obtained. In this measuring-time window external systematic drifts due to voltage- and magnetic field fluctuations occur, which is illustrated in Fig. 6.10 a.)[9]. Both measurements give time averages of the measured frequencies. In the first part of the measuring sequence ($t < 80\,\mathrm{s}$), indicated by the red part of the drift curve, the axial frequency $\nu_{z,1}$ is measured.

[9]The example is based on voltage drift measurements with the DC-voltage supply used to bias the trap electrodes.

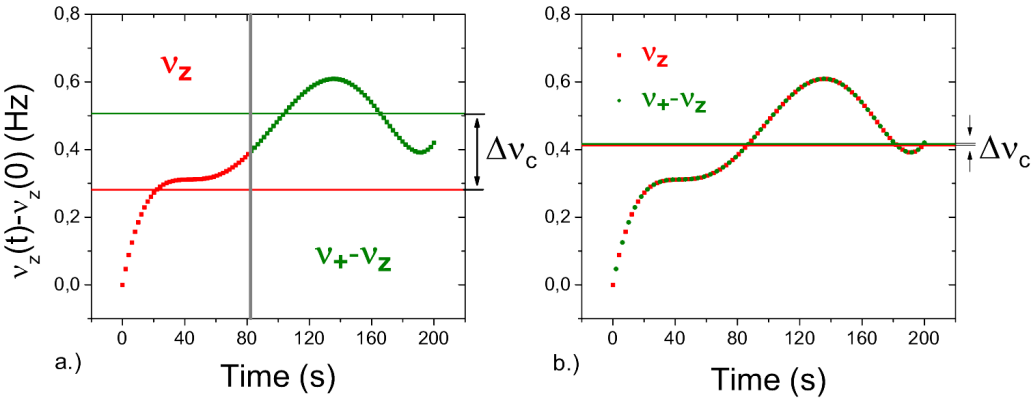


Figure 6.10: a.) Illustration of the drift problem due in a sideband frequency measurement. First the axial frequency is measured. Subsequently the double-dip spectrum is measured and the cyclotron frequency is evaluated by means of Eq. (6.30). The shift of the average axial frequency between both measurements directly shifts the result of the cyclotron frequency $\Delta\nu_+ = \Delta\nu_{z,\mathrm{DC}} \approx \Delta\nu_c$. b.) Toothed sequence. The axial frequency and the sideband-frequencies $\nu_l$ and $\nu_r$ are measured alternatingly. The FFT spectra are routed and evaluated after the measuring sequence. This reduces the systematic error in the cyclotron frequency measurement.

Subsequently a double-dip spectrum is recorded, indicated by the green part of the drift curve ($t > 80\,\mathrm{s}$). The cyclotron frequency is evaluated by

$$\nu_+ = \nu_l + \nu_r - \nu_{z,1} + \nu_{\mathrm{rf}} \; . \tag{6.30}$$

Note that the real cyclotron frequency is

$$\nu_+ = \nu_l + \nu_r - \nu_{z,2} + \nu_{\mathrm{rf}} \; , \tag{6.31}$$

where $\nu_{z,2}$ is the average axial frequency during the second sequence, while the sideband drive was applied. The axial frequency shift arising from the drift of the DC-voltage supply $\Delta\nu_{z,\mathrm{DC}} = \nu_{z,1} - \nu_{z,2}$ directly shifts the value of the cyclotron frequency by $\Delta\nu_+ = \Delta\nu_{z,\mathrm{DC}} \approx \Delta\nu_c$ (see Fig. 6.10 a.)).

To overcome this drift problem, in earlier $g$-factor measuring sequences [23, 24, 25], the axial frequency was measured twice, before $\nu_{z,1}$ and after sideband-coupling $\nu_{z,3}$, and the average of both frequencies was used to evaluate the cyclotron frequency. A much more elegant solution of this drift problem is a "toothed" measuring sequence. The idea was originally

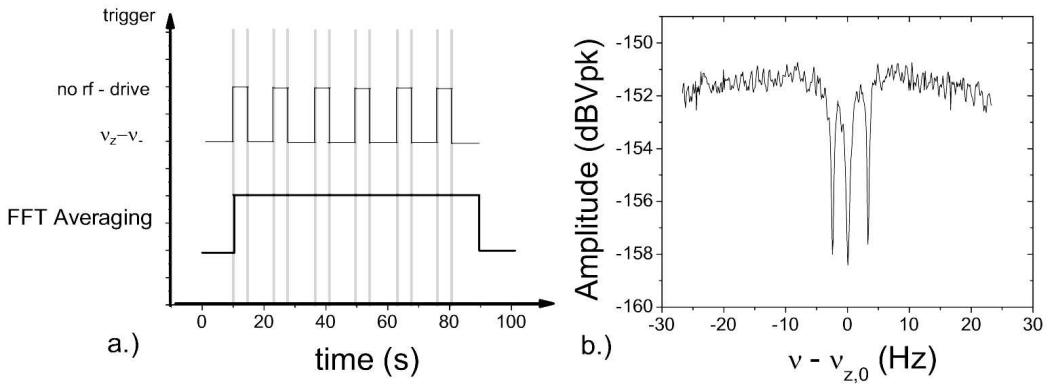


Figure 6.11: a.) Timing scheme for the "toothed" measuring sequence b.) Triple-dip FFT spectrum. The averaged result of a "toothed" measuring sequence. For details see text.

introduced by J. Verdu [42]. The whole measuring-time sequence is split into $N$ subintervals. In every interval $2k$ no sideband is irradiated and the axial frequency is measured. In the intervals $2k+1$ the sideband is irradiated and the double dip spectrum is measured. The respective FFT spectra of the subsequences $2k$ and $2k+1$ are routed with a software routine and averaged after the measurement. This sequence corresponds to the conditions shown in Fig. 6.10 b.). Since the measurement is "toothed" the average value of the axial frequency is nearly identical for both measurements and systematic shifts due to voltage drifts are suppressed. In Fig. 6.11 a.) the time sequence for such a toothed measurement is shown while Fig. 6.11 b.) shows the result of such a "toothed" measurement, where the FFT analyzer averaged over the whole coupling sequence, as indicated in Fig. reffig:TripleDip a.). The interval length for the unperturbed axial frequency measurement was $\Delta t_z = 2\,\mathrm{s}$, while for the coupling interval $\Delta t_{\mathrm{sideband}} = 2\Delta t_z = 4\,\mathrm{s}$ was chosen. Note that this "triple-dip" spectrum is not due to physics in the sense that a third "eigenstate" is produced by the coupling, but only due to spectrum analyzer averaging. Figure 6.12 compares the results of a toothed sequence with the "traditional" measuring sequence. The average value of the cyclotron frequency $\langle\nu_+\rangle$ of $N = 50$ measurements $i$ is evaluated and $\langle\nu_+\rangle - \nu_{+,i}$ is plotted to a histogram. The narrow histogram, with a standard deviation of $\sigma = 55\,\mathrm{mHz}$, results from the toothed sequence, while the broad histogram, with $\sigma = 75\,\mathrm{mHz}$, is due to

the "traditional" method. In the final $g$-factor experiment the toothed sequence will be applied.

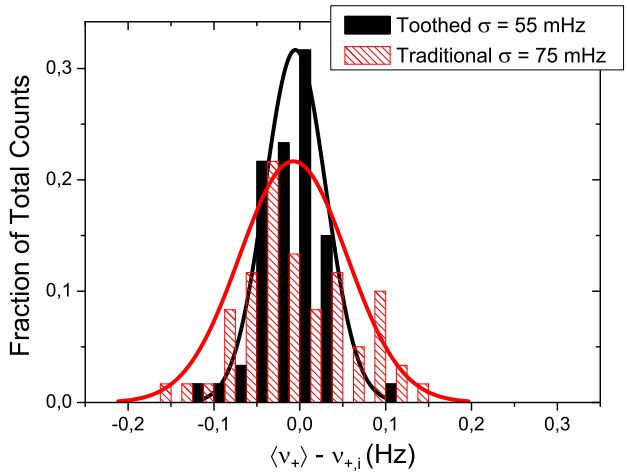


Figure 6.12: Results of sequential and toothed cyclotron frequency measurement. The histograms show the difference of the mean value $\langle \nu_+ \rangle$ and individual frequency measurements $\nu_{+,i}$. The narrow histogram shows results of the toothed measuring sequence while the broad histogram is due to the "traditional" measuring method. For details see text.

### *6.8 Crossed-Coupling*

The toothed sequence described in the last section can be interpreted as a "simultaneous" measurement of two eigenfrequencies of the proton. In the following a new idea is presented, which can be used to measure *all* eigenfrequencies of the particle "simultaneously". A very intuitive understanding of the basic idea is developed, if every dip of the double dip spectrum is interpreted as a new "dressed" Penning trap mode [109]. The "dressing" of the axial mode with one of the radial modes leads to two new Penning trap "eigenstates". Every state of these new eigenstates can be dressed with the remaining radial mode, which means, that every double dip splits again into two additional modes. The principle is illustrated in Fig. 6.13 a.), where the axial state is resonantly dressed by the cyclotron mode with a Rabi frequency $\Omega_+/2\pi$, and subsequently the new "cyclotron-dressed" axial states are resonantly

dressed by the magnetron mode with a Rabi frequency $\Omega_-/2\pi$.

In the experiment, a coupling field with a frequency $\nu_{\mathrm{rf},+} = \nu_+ - \nu_z + \frac{\delta_+}{2\pi}$ is irradiated,

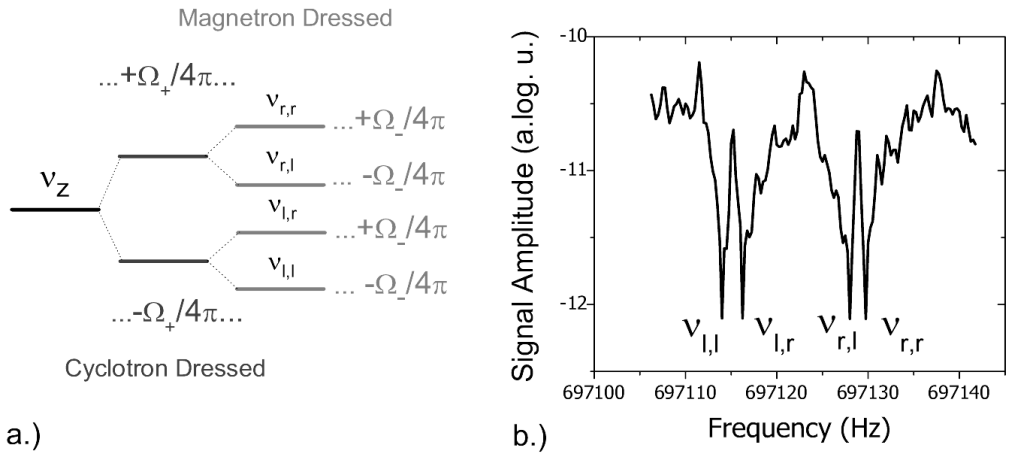


Figure 6.13: a.) Illustration of the basic principle for the simultaneous measurement of all eigenfrequencies of the trapped proton in one single shot. For further details see text. b.) Experimental result of a double-dressing, the "fourfold-dip". Applying adequate rf-drives to the trap both radial modes are simultaneously coupled to the axial mode, resulting in a "double-dressing".

dressing the axial mode with the cyclotron mode. From this coupling the new eigenstates at the frequencies

$$\nu_{l,+} = \nu_z - \frac{\delta_+}{4\pi} - \frac{\Omega_+}{4\pi} \tag{6.32}$$

$$\nu_{r,+} = \nu_z - \frac{\delta_+}{4\pi} + \frac{\Omega_+}{4\pi} \tag{6.33}$$

are defined ($\delta_+$ and $\Omega_+$ are as explained in section 6.6). Every single-dressed mode is subsequently dressed with the magnetron mode, irradiating the rf-frequencies $\nu_{\mathrm{rf},1} = \nu_{l,+} + \nu_- - \delta_{l,-}$ and $\nu_{\mathrm{rf},2} = \nu_{r,+} + \nu_- - \delta_{r,-}$, respectively. These drives obviously couple the magnetron mode to the left and the right frequency dip of the cyclotron dressing. Consequently, the left, as well as the right dip $\nu_{l,+}$ and $\nu_{r,+}$ are split in two dips

$$\nu_{l,l} = \nu_{l,+} - \frac{\delta_{l,-}}{4\pi} - \frac{\Omega_{l,-}}{4\pi} \tag{6.34}$$

$$\nu_{l,r} = \nu_{l,+} - \frac{\delta_{l,-}}{4\pi} + \frac{\Omega_{l,-}}{4\pi} \tag{6.35}$$

and

$$\nu_{r,l} = \nu_{r,+} - \frac{\delta_{r,-}}{4\pi} - \frac{\Omega_{r,-}}{4\pi} \tag{6.36}$$

$$\nu_{r,r} = \nu_{r,+} - \frac{\delta_{r,-}}{4\pi} + \frac{\Omega_{r,-}}{4\pi} \ , \tag{6.37}$$

where $\Omega_{l,-} = \sqrt{\Omega_-^2 + \delta_{l,-}^2}$ and $\Omega_{r,-} = \sqrt{\Omega_-^2 + \delta_{r,-}^2}$ are the off-resonant Rabi frequencies of the double-dressing. The result of such a double-dressing, the "fourfold-dip", is shown in

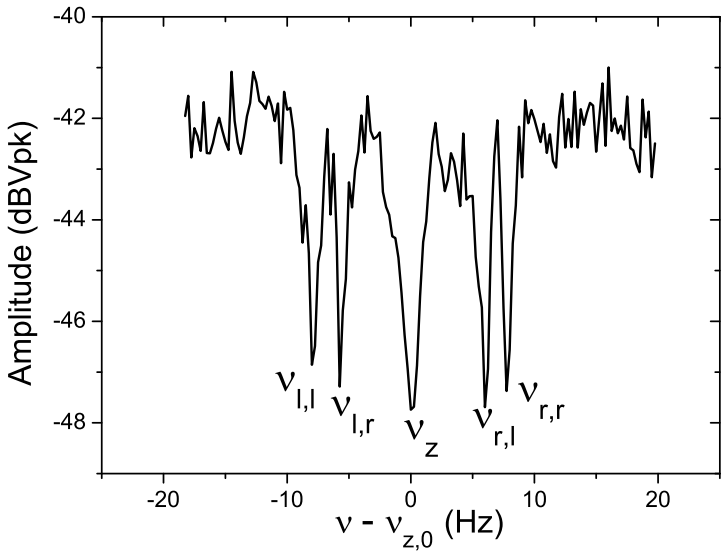


Figure 6.14: This fivefold-dip spectrum was recorded in one shot and carries all information of the eigenfrequencies of the trapped proton.

Fig. 6.13 b.). The equations Eq. (6.34) to Eq. (6.37) relate four measured quantities $\nu_{l,l}$, $\nu_{l,r}$, $\nu_{r,l}$, and $\nu_{r,r}$ with five unknown quantities, the eigenfrequencies of the trapped proton $\nu_+$, $\nu_z$, and $\nu_-$, and the resonant Rabi frequencies $\Omega_+/2\pi$ and $\Omega_-/2\pi$. To obtain an additional quantity, the axial frequency $\nu_z$ is measured. Applying the idea described in the previous section for the toothed measurement sequence, a "fivefold-dip" spectrum is obtained. Figure 6.14 shows such a fivefold-dip. This spectrum carries all eigenfrequency-information of the trapped proton, and thus, this measuring sequence can be understood as the very first demonstration of the direct determination of the free cyclotron frequency $\nu_c$ of a charged

Table 6.3: Comparison of the results of the frequency measurements obtained with the "traditional" sideband-coupling method, and the double-dressing method.

| Frequency | Triple-Dip Method (Hz) | Double-dressing Method (Hz) |
|---|---|---|
| $\nu_+$ | 28 965 737.98(14) | 28 965 737.8(12) |
| $\nu_z$ | 694 345.46(5) | 694 345.37(5) |
| $\nu_-$ | 8 322.76(7) | 8 322.84(8) |

particle stored in a Penning-trap.

To test the proposed method, the results of frequency measurements obtained by the triple-dip method are compared with the results obtained by application of the described double-dressing method. The results of both measurements are shown in Tab. 6.3. All eigenfrequencies are identical within the errors. Compared to the triple-dip method for the determination of the cyclotron frequency $\nu_+$, the double-dressing method requires a longer averaging time to achieve the same frequency resolution. Furthermore, as discussed in section 6.6, the magnetron frequency determination is not required for the aimed precision of $10^{-9}$, thus, the method will not be applied in the $g$-factor measuring sequence. Nevertheless, to date, this novel measuring scheme to determine the free cyclotron frequency $\nu_c$ in one single measurement, and the simultaneous dressing of the axial mode with both radial modes has never been demonstrated before in Penning trap physics. One individual trapped proton simultaneously delivers four frequency-response signals due to energy transfer between all three eigenmodes.

### *6.9 "Classical Rabi Oscillations" and Nonlinear Dynamics*

So far, sideband coupling was applied to measure oscillation frequencies of a trapped proton in "thermal equilibrium" with the axial detection system. Another important aspect of the sideband-coupling dynamics is the property, that coupling pulses can be applied to transfer energy from one mode into another. Following the terms of quantum mechanics, the pulse which transfers all energy from one mode into another is called "$\pi$"-pulse. To calibrate the

pulse front, the magnetron mode is excited and afterwards a coupling-pulse at frequency $\nu_{\mathrm{rf}} = \nu_z + \nu_-$ is applied for a coupling time $t_{\mathrm{couple}}$. After this pulse the FFT analyzer is triggered to measure the amplitude of the axial signal. In Fig. 6.15 the axial signal of such a measuring sequence is shown, as a function of the coupling time $t_{\mathrm{couple}}$. In the figure, the signal is in linear units and scaled to one for the largest amplitude. Obviously the coupling

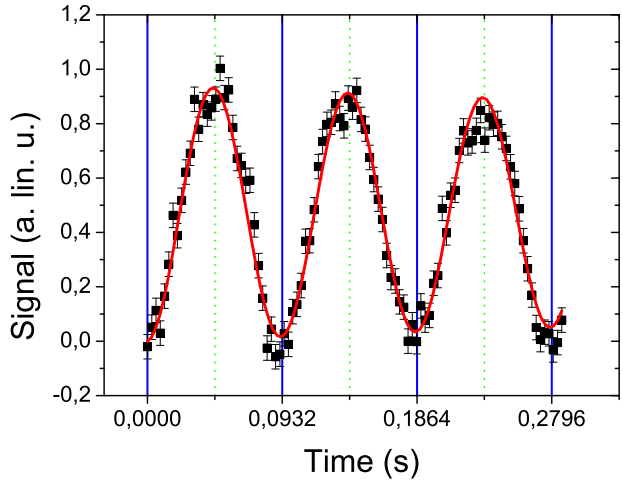


Figure 6.15: "Classical Rabi Oscillations" recorded for magnetron-to-axial coupling. For details see text.

dynamics show the oscillations predicted in section 6.6 - "classical Rabi oscillations". In section 6.10 classical "$\pi$" pulses will be applied to calibrate the axial energy. Now, it will be investigated, how the Rabi-like dynamics behave, when a nonlinearity is superimposed to the Penning trap. In the case discussed here, the nonlinearity can be tuned by adjusting the tuning ratio. Then, nonlinear terms add up to the dynamical system Eq. (6.16) which becomes

$$\ddot{z} + i\omega_z^2 \left(1 + \frac{C_4}{C_2}\left(z^2 - \frac{3}{2}\rho_-^2\right)\right) z = \frac{qE_0}{m} \exp\left(i\omega_{\mathrm{rf}} t\right) \rho_- \tag{6.38}$$

$$\ddot{\rho}_- - i\omega_-^2 \left(1 - \frac{3C_4}{2C_2}\left(\rho_-^2 - 4z^2\right)\right) \rho_- = \frac{qE_0}{m} \exp\left(i\omega_{\mathrm{rf}} t\right) z \ . \tag{6.39}$$

Using the same ansatz as given above and extracting the slow dynamics, these equations can be transformed to a clearer system

$$\dot{Z} + \omega_z^2 \left( \frac{C_4}{C_2} \left( Z^2 - \frac{3}{2} R_-^2 \right) \right) Z = -i\Omega(C_4, E_z, E_-) \exp\left(i\delta(C_4, E_z, E_-)t\right) R_- \quad (6.40)$$

$$\dot{R}_- - \omega_-^2 \left( \frac{3C_4}{2C_2} \left( R_-^2 - 4Z^2 \right) \right) R_- = i\Omega(C_4, E_z, E_-) \exp\left(-i\delta(C_4, E_z, E_-)t\right) Z \quad (6.41)$$

The solution of such a system is complicated mathematics. Since we do not use this phenomenon anymore and a full discussion would require several ten pages, just the qualitative behavior is discussed. Both systems of equations are of interest, since in the first system (Eq. (6.39) and (6.39)) a sideband aspect is shown. The frequency of the solution will be modulated by the $C_4$ term leading to higher harmonics in the original oscillation, and thus, in the coupling dynamics. The second system (Eq. (6.41) and (6.41)) shows the "concurrence" between the Rabi coupling and the nonlinear dynamics, $\Omega$ and $\frac{2C_4}{mC_2}E_z$.
The behavior of the system can be summarized:

1. If $C_4$ is smal,l the dynamics described in section 6.6 will occur.

2. If $0 \neq \frac{2C_4}{mC_2}E_z \ll \Omega$, controllable nonlinear dynamics will occur, which means that second-order perturbation theory can be applied and that due to the proportionality $Z^3$ and $R_-^3$ sidebands at odd harmonics $(2k+1)\Omega$ will occur in the Rabi oscillations. A faster "damping" is expected, which is due to de-phasing.

3. If $0 \neq \frac{2C_4}{mC_2}E_z \gg \Omega$, the dynamics is dominated by the nonlinearities, which will finally lead to chaotic behavior.

This is exactly what is observed if the experimental sequence described above is repeated for increasing $C_4$ terms. The results of such a sequence are shown in Fig. 6.16. The aspect that the nonlinearities increase the damping of the system can be observed in the data. The red solid lines in a.) to d.) are due to a fit of the unperturbed Rabi oscillations. Figure a.) shows unperturbed Rabi oscillations. Increasing $C_4$, the dynamics becomes structured and finally only arbitrary peaks are observed. Figure 6.17 shows the corresponding frequency spectra. In the first spectrum a.), a single peak at the Rabi frequency occurs. With

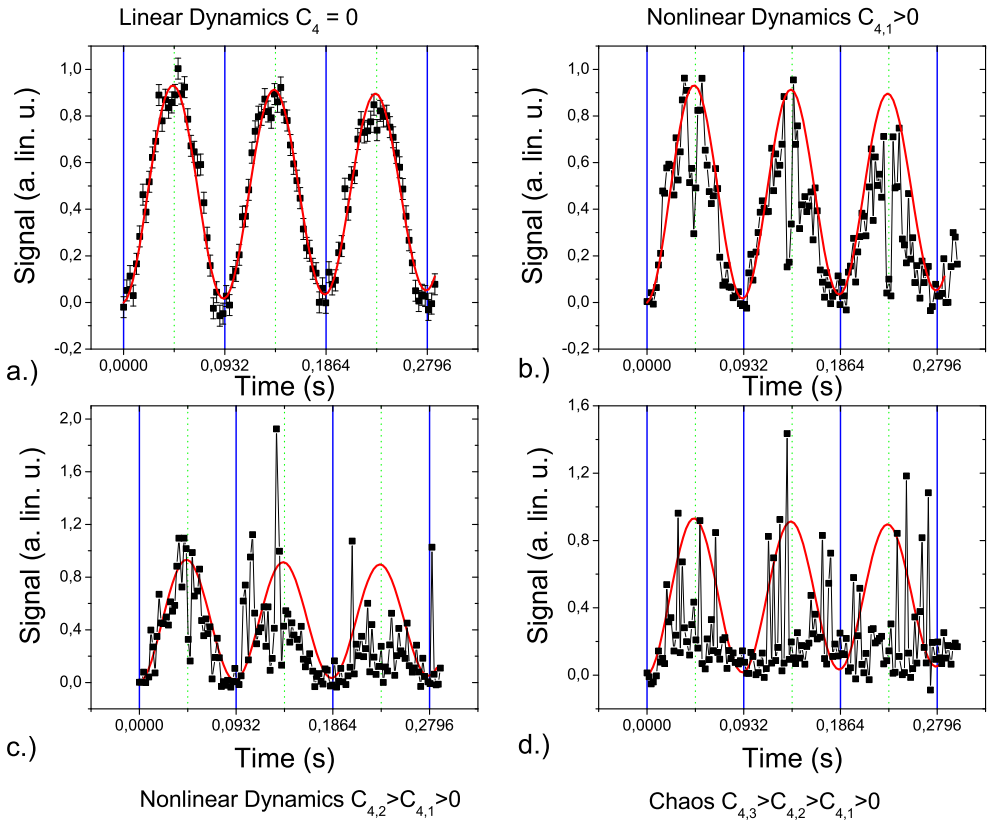


Figure 6.16: Rabi oscillations in presence of a nonlinear potential. From a.) to d.) the anharmonic ptoential term $C_4$ is increased. a.) shows linear Rabi oscillations. Increasing $C_4$ finally leads to chaos.

increasing $C_4$, the peak height decreases and additional peaks at odd multiples of $\Omega$ become visible (b.)). In spectrum c.) the peaks nearly vanish, while the frequency spectrum d.) is flat, corresponding to arbitrary "chaotic" behavior. These measurements have the potential to study the transition from controlled nonlinear dynamics to chaos with a single trapped proton stored in a Penning trap. Moreover, in combination with the magnetic bottle trap (see chapter 7), thermalization of quasi-classical chaotic systems can be investigated.

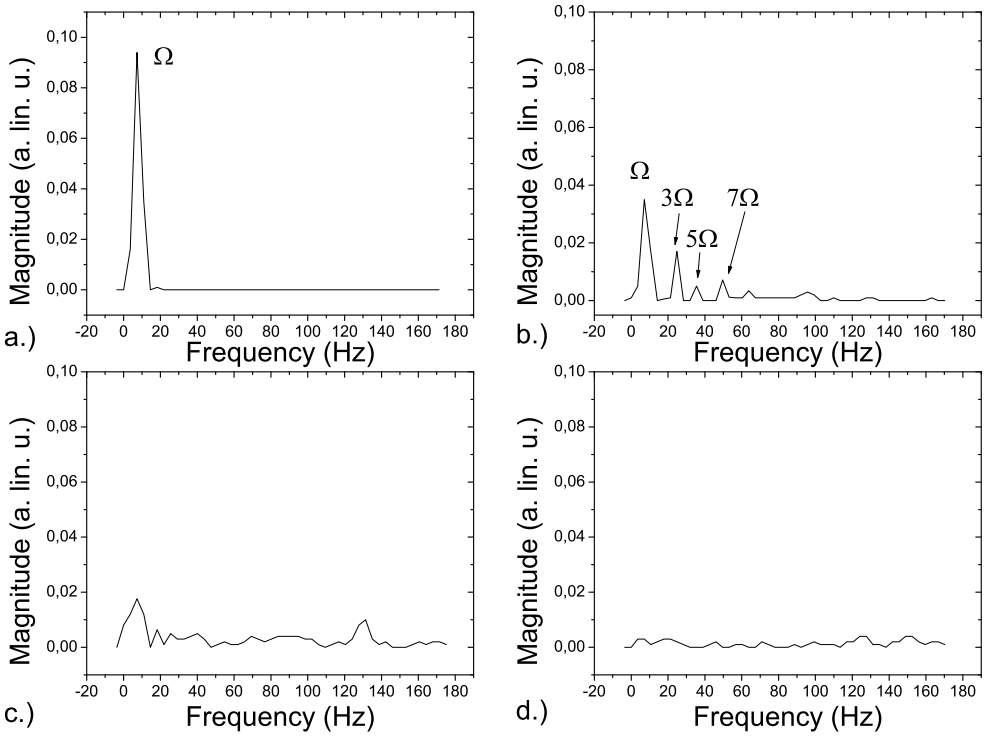


Figure 6.17: Fourier spectra of the dynamics shown in Fig. 6.16. For discussion, see text.

### *6.10 Energy Calibration*

As explained in section 6.4 with the precise knowledge of the trap errors which were measured with the proton, the mode energies can be calibrated. Here the calibration of the magnetron energy $|E_-|$ and the axial energy $E_z$ is presented. For this purpose, the magnetron radius is first cooled and excited afterwards with a burst signal of $N$ cycles and an amplitude of $-23\,\mathrm{dBm}$ at the frequency generator output[10]. Then the axial frequency of the particle is measured as a function of the tuning ratio. This measurement sequence

[10]With the burst function of a frequency generator the particle can be excited at a frequency $\nu_{rf}$ for $N$ rf-cycles.

is repeated for different burst cycles $N_i$. Figure 6.18 shows the axial frequency shift as a

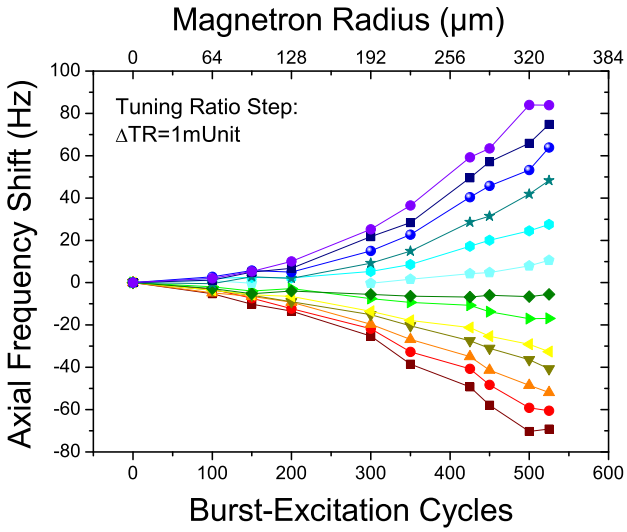


Figure 6.18: Axial Frequency shift as a function of the burst excitation cycles $N$. The array parameter is the tuning ratio which has been detuned in steps of 1 mUnit. The dark green curve shows the weakest scaling with $N$. It corresponds to the optimum tuning ratio.

function of $N_i$. The different curves correspond to different tuning ratios applied to the trap. The quadratic scaling with the number of burst-excitation cycles is due to excitation dynamics. The amplitude of an undamped, resonantly excited oscillator increases linearly with the excitation time,

$$\rho_- = \alpha N_i \ , \tag{6.42}$$

where $\alpha$ is an unknown experimental scaling factor depending linearly on the excitation amplitude of the frequency generator and the coupling strength of the excitation to the Penning trap electrodes. Comparing these results to potential theory, the energy due to an excitation can be calibrated.

The axial frequency shift $\Delta\nu_z$ as a function of the magnetron radius $\rho_-$ is given by

$$\Delta\nu_z = -\frac{3\pi^2 m\nu_z^3}{C_2^2}\cdot(E_4 + D_4\cdot \mathrm{TR})\,\frac{\rho_-^2}{qV_0} = -\frac{3\pi^2 m\nu_z^3}{C_2^2}\cdot(E_4 + D_4\cdot \mathrm{TR})\,\frac{(\alpha N)^2}{qV_0}\ , \tag{6.43}$$

where $C_4 = E_4 + D_4\cdot \mathrm{TR}$ was used (see section 2.3.1). Fitting the data shown in Fig. 6.18 with parabolas $A + B\cdot N^2$, the function $B(\mathrm{TR})$ (shown in Fig. 6.19 a.)) is obtained, whereas

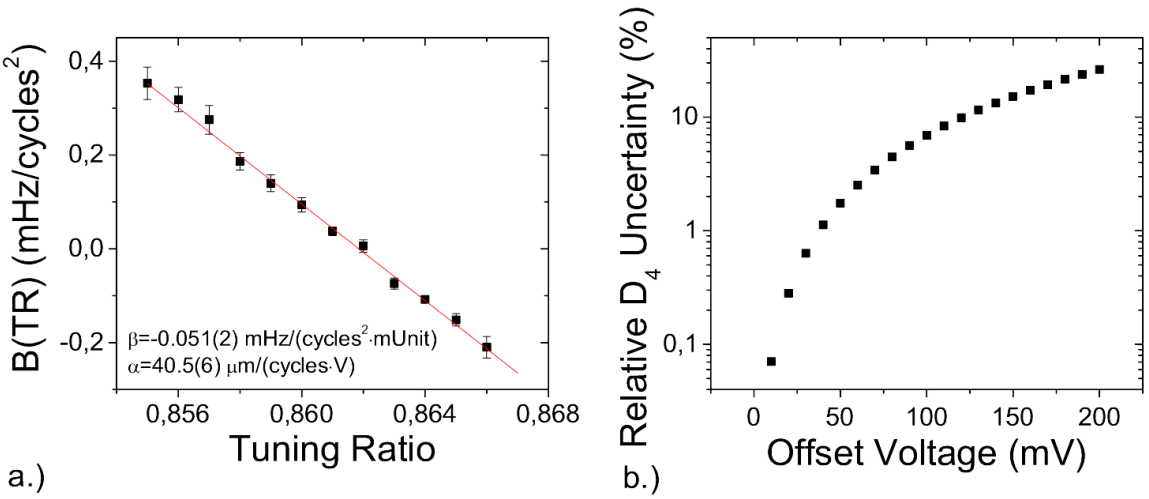


Figure 6.19: a.) The function $B(\mathrm{TR})$, which is derived from the energy calibration data. For details see text. b.) (Calculation result) Relative error of the $D_4$ parameter of the trap as a function of an offset potential, which is applied to a correction electrode. The parameter is very robust in the presence of typical trap errors.

the derivative of this function can be expressed as

$$\beta := \frac{d}{d\mathrm{TR}} B(\mathrm{TR}) = -\frac{3\pi^2 m\nu_z^3}{C_2^2} D_4 \frac{(\alpha)^2}{qV_0} \Rightarrow \alpha^2 = -\frac{C_2^2}{3\pi^2 m\nu_z^3} \frac{qV_0}{D_4} \frac{d}{d\mathrm{TR}} B(\mathrm{TR}) \ . \tag{6.44}$$

Therefore, the calibration of the scaling factor $\alpha$ is reduced to the knowledge of coefficient $D_4$, which is a very robust parameter, especially combined with the knowledge achieved by the asymmetry compensation of the trap. In Fig. 6.19 b.) calculation results for the uncertainty of $D_4$ are shown as a function of the offset potential, which is applied to one of the correction electrodes. For offset potentials below 40 mV the relative error of $D_4$ is below 1 %. Thus, combined with the asymmetry compensation described in section 6.4, this "$D_4$-method" is suited perfectly for energy calibration.

From this experiment the value

$$\alpha = 40.5(6) \, \frac{\mu\mathrm{m}}{\mathrm{cycle} \cdot \mathrm{V}} \tag{6.45}$$

is obtained. The uncertainty is due the error of $\beta$ and $D_4$.

Combining this knowledge with the Rabi pulse calibration described in section 6.9, the axial energy can be calibrated as well. For this purpose, the particle is excited by a magnetron

pulse and subsequently a $\pi$-pulse is applied to couple the radial energy to the axial mode. Afterwards the FFT analyzer is triggered to measure the axial peak signal. By this sequence the signal-to-noise ratio of the axial peak can be measured as a function of the axial energy. If the equivalent input noise $e_n$ of the FET-amplifier is neglected, the signal-to-noise ratio measured with the FFT spectrum analyzer, which averages for a measuring time $t_{\mathrm{FFT}} = 1/\mathrm{BW}$, where BW is the resolution bandwidth per bin, is given by (see chapter 4)

$$\mathrm{SNR} = \sqrt{\frac{2\pi\nu_z QL}{4k_B T_z}}\frac{q}{D_{\mathrm{eff}}}\sqrt{\frac{E_0}{m}}\frac{1}{\sqrt{t_{\mathrm{FFT}}}}\int_0^{t_{\mathrm{FFT}}}\exp\left(-\frac{t}{2\tau}\right)dt \tag{6.46}$$

$$= \sqrt{\frac{2\pi\nu_z QL}{4k_B T_z}}\frac{q}{D_{\mathrm{eff}}}\sqrt{\frac{E_0}{m}}\frac{2\tau}{\sqrt{t_{\mathrm{FFT}}}}\left(1-\exp\left(-\frac{t_{\mathrm{FFT}}}{2\tau}\right)\right)\ . \tag{6.47}$$

$E_0$ is the initial excitation energy of the magnetron mode. All parameters of this equation are known except for the temperature $T_z$ of the detection system. Thus, from these data the temperature of the axial detection system is obtained. The data are shown in Fig. 6.20,

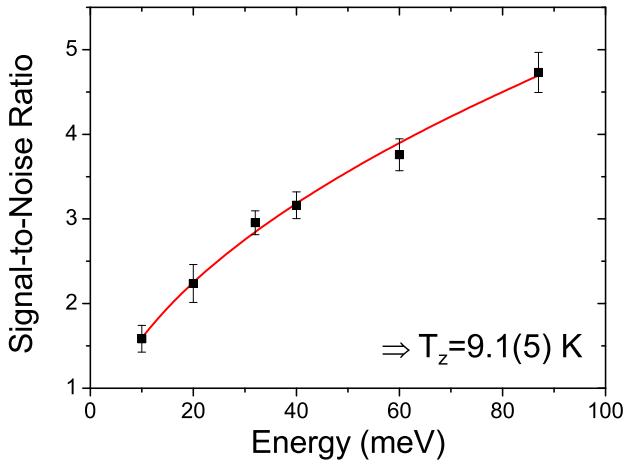


Figure 6.20: Signal-to-noise ratio of the axial peak signal in linear units as a function of the axial energy. From these data the axial temperature can be derived and is given by $T_z = 9.1(5)\,\mathrm{K}$.

every data point is an average of twenty coupling sequences. From the fit $T_z = 9.1(5)\,\mathrm{K}$ is yielded. This temperature is about 4 K above the physical temperature of the apparatus.

Measuring the quality factor of the axial detection system as a function of amplifier gain (see chapter 4), only a positive feedback effect of $G_{\mathrm{FB}} \approx 0.1$ is measured, explaining only a temperature increase of about 1 K (for a detailed discussion of the effects of amplifier feedback on temperature see chapter 4). The origin of the higher temperature may be due to broadband background noise on the ground of the apparatus, but currently the details are not understood yet. The temperature of the proton can be reduced by the application of active electronic feedback, which will be described in the next section.

### *6.11 Application of Active Electronic Feedback*

As explained in chapter 4, the temperature of the proton can be varied by the application of active electronic feedback. Experimentally, a portion of the amplified detector-signal is picked up and fed back to the resonator. Details are shown in Fig. 6.21 a.). The axial

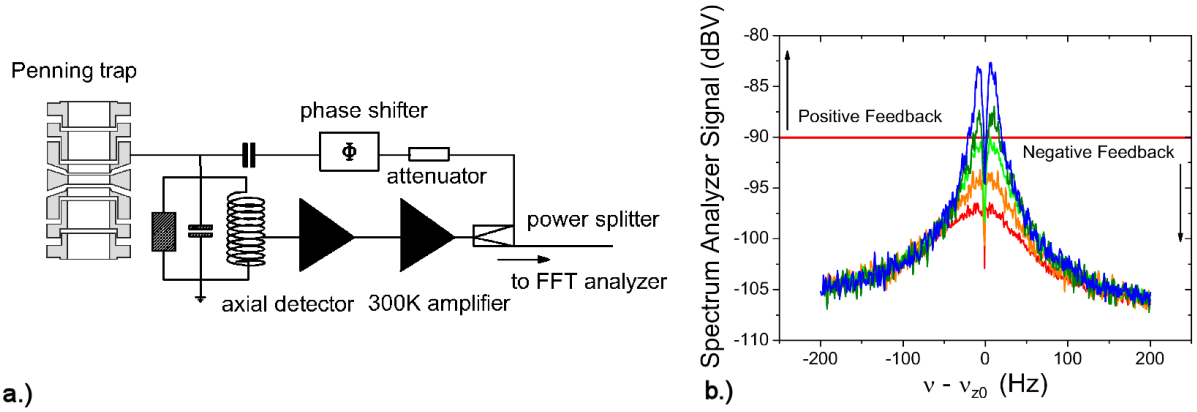


Figure 6.21: a.) Simplified schematic of the ingredients used for the application of active electronic feedback. The signal is picked up at the output of the room temperature amplifier and fed back to the detection system. The phase of the signal is adjusted with a phase shifter. The feedback gain can be regulated with a voltage-controlled attenuator. b.) Noise spectra of the axial detection systems for different feedback gains. The solid red line indicates $G_{\mathrm{FB}} = 0$. Above the solid red line positive feedback is applied, while the noise spectra below this line are measured with negative feedback.

signal of the trapped proton is picked up at the output of the room temperature amplifier of the axial detection system, and fed back to the resonator. The phase $\Phi$ of the feedback

signal is adjusted with a home-made voltage controlled $IQ$-modulator. The signal strength can be controlled with an also home-made voltage controlled attenuator.
To adjust the feedback phase $\Phi$ a certain feedback gain is applied to the loop and the noise spectrum of the resonator is recorded as a function of $\Phi$. The largest signal is obtained for $\Phi = 0°$, while for $\Phi = 180°$ the lowest signal is measured. Figure 6.21 b.) shows axial noise spectra which are recorded at different loop settings. For the spectra, where the maxima are above the red solid line positive feedback is applied, while the spectra where the maxima are below this line are due to negative feedback. For a very detailed discussion of feedback temperature see section 7.4.

## *6.12 Phase-Sensitive Detection*

Phase-sensitive detection is a very important technique for our experiment. It was introduced by S. Stahl to resolve spin flips of an electron bound to a highly charged ion [106]. In our experiment the method will finally be applied to resolve the axial frequency jump $\Delta\nu_{\mathrm{z,SF}}$ due to a proton spin flip in the analysis trap (see chapter 2). In this section the application of phase-sensitive detection in the precision trap is presented. The resolution of a frequency change of 200 mHz out of 680 kHz within a measuring time of only 1 s is demonstrated. In the $g$-factor measuring sequence, this will reduce the time needed for the axial frequency measurements in the analysis trap from $\approx 2 \cdot 80$ s to $\approx 2 \cdot 1$ s (see Fig. 2.12). All experimental techniques applied in the precision trap can be transferred to the analysis trap.

### *6.12.1 Experimental Principle*

The basic idea of phase-sensitive detection is shown in Fig. 6.22. The axial motion of the proton with frequency $\nu_z$ is excited resonantly with an rf drive. Afterwards it is decoupled from the axial detection system for a free phase evolution time $t_{\mathrm{evol}}$. Subsequently the particle is re-coupled to the detection system and the relative phase $\Delta\phi$ between the particle signal and the drive signal is measured

$$\Delta\phi_1(^\circ) = 360(\nu_{\mathrm{drive}} - \nu_z) \cdot t_{\mathrm{evol}} \ . \tag{6.48}$$

If the axial frequency changes by $\Delta\nu_z$ a relative phase

$$\Delta\phi_2(^\circ) = 360(\nu_{\mathrm{drive}} - (\nu_z + \Delta\nu_z)) \cdot t_{\mathrm{evol}} \tag{6.49}$$

will be measured. Finally, the difference of the relative phases of both measurements will be evaluated

$$\Delta\phi(^\circ) = \Delta\phi_1(^\circ) - \Delta\phi_2(^\circ) = 360\Delta\nu_z \cdot t_{\mathrm{evol}} \ . \tag{6.50}$$

The comparison of two subsequent phase measurements lets us decide, whether the proton spin has flipped or not. In case of the expected axial frequency change of $\Delta\nu_{\mathrm{z,SF}} \approx 200\,\mathrm{mHz}$ caused by a proton spin flip, the phase difference is given by $\Delta\phi(t_{\mathrm{evol}}) = 72\,^\circ/\mathrm{s}$. The experimental aim is to obtain such good experimental control, that the phase shift caused by such a tiny axial frequency shift can be detected clearly in only one single experiment.

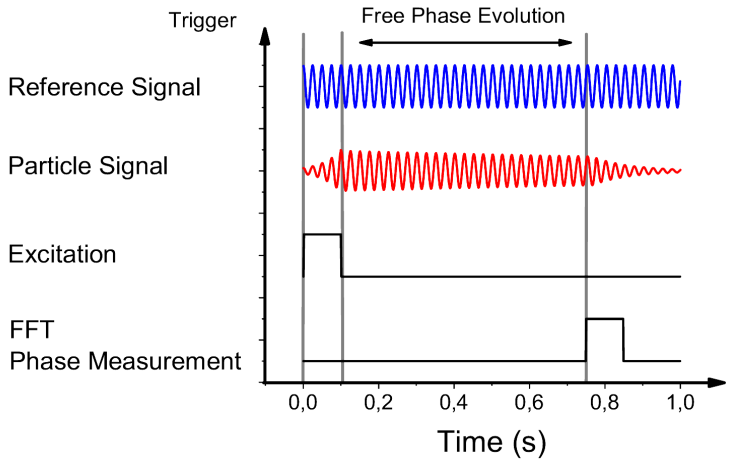


Figure 6.22: Illustration of the basic idea of the phase-sensitive detection method.

### *6.12.2 Preliminary Considerations - Phase Fluctuation*

What sounds very simple in the explanation given above is challenging work seen from the experimental point of view.

Before the discussion is started the term *phase fluctuation* $\sigma_\phi$ is introduced, which is defined

as the standard deviation of a series of $N$ phase measurements. It is important to think about mechanisms, which are responsible for phase fluctuations. The final experimental aim is to find a configuration, where $\sigma_\phi$ is small compared to the phase shift which is caused by an axial frequency shift of $\Delta\nu_z = 200\,\mathrm{mHz}$. The smaller the value $\sigma_\phi$, the shorter the measuring time which is required to resolve an axial frequency change caused by a spin flip. A very obvious aspect causing phase fluctuation, is the signal-to-noise ratio between the particle peak and the noise floor of the detection system. In the experiment the particle is excited to an amplitude $z_0$ such that a peak signal above the thermal background noise of the detection system becomes visible. Then the phase between the external reference and the axial signal of the proton is measured with the cross-correlation function of the spectrum analyzer. The FFT-analyzer, as well as the thermal noise of the axial detection system, add noise with an amplitude $A$ and a random phase $\phi_{\mathrm{noise}}$. The effective signal is given by (see chapter 4)

$$S = \frac{q}{D_{\mathrm{eff}}} z_0 \exp\left(i\left(2\pi\nu_z t + \phi_{\mathrm{exc}}\right)\right)\left(1 + \frac{A}{z_0}\exp\left(i\left(\phi_{\mathrm{noise}} - \phi_{\mathrm{exc}}\right)\right)\right) \ . \tag{6.51}$$

This is schematically shown in Fig. 6.23 a.). The effectively measured amplitude $R$ and phase $\phi_{meas}$ can be calculated by the cosine theorem and are given by

$$R = \sqrt{z_0^2 + A^2 + 2z_0 A\cos\left(\phi_{\mathrm{noise}} - \phi_{\mathrm{exc}}\right)} \tag{6.52}$$

$$\phi_{meas} = \phi_{\mathrm{exc}} \pm \arccos\left(\frac{R^2 + z_0^2 - A^2}{2Rz_0}\right) \approx \phi_{\mathrm{exc}} \pm \arccos\left(1 - \frac{A^2}{2z_0^2}\right) \ , \tag{6.53}$$

where the last approximation holds only for $R \approx z_0 \gg A$. Thus, to achieve small phase fluctuation $\sigma_\phi$, it is crucially important to measure at large signal-to-noise ratio. The principal phase resolution achieved as a function of the signal-to-noise ratio is shown in Fig. 6.23 b.). The red line is due to a numerical convolution of Eq.(6.53) with uniform white noise, the filled squares are experimental data measured with an rf-drive, which simulates the proton signal. To achieve a phase resolution below 10°, a signal-to-noise ratio between 15 dB and 20 dB is required. This means, that the proton has to be excited to energies between 100 meV and 200 meV corresponding to axial oscillation amplitudes of 1 mm to 1.5 mm, which is already one half of the trap diameter, bringing us to the second mechanism, which causes phase fluctuations - the harmonicity of the Penning trap.

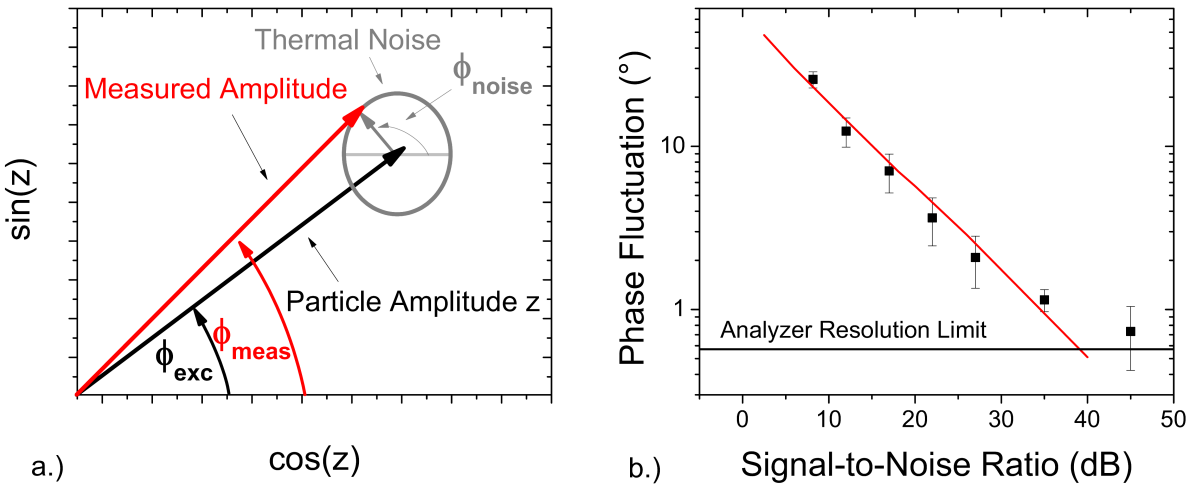


Figure 6.23: a.) Schematic for the explanation how thermal background noise affects the phase resolution of the measurement. The black arrow indicates the amplitude of the proton and its phase $\phi_{exc}$. The added noise is indicated by the circle around the tip of the arrow. The effective phase $\phi_{\mathrm{meas}}$ and amplitude $R$ can be calculated as described in the text. b.) Phase resolution as a function of the signal-to-noise ratio. The red line is due to a numerical convolution of Eq.(6.53) with uniform white noise. The filled squares are experimental data measured with an rf-drive which simulates the proton signal.

For such large proton amplitudes the $C_6$ term cannot be neglected anymore. Assume, that the trap is not optimized and $C_4$ and $C_6$ do not vanish, and remember, that the initial oscillation amplitudes before the excitation are thermally distributed due to the heat contact between the single trapped proton and the axial detection system, leading to an initial energy uncertainty $\langle E_{z,th}\rangle = k_B T_z$, where $T_z$ is the axial temperature of the detection system. Furthermore, the average amplitude of the proton after excitation has a distribution due to amplitude fluctuations of the rf generator and rise-time accuracy of included rf-switches, leading to a total experimental energy distribution $\langle E_z\rangle = \langle E_{z,th}\rangle + \langle E_{z,tech}\rangle$. Then the principal phase fluctuation $\sigma_\phi$, which can be achieved, is given by

$$\sigma_\phi(\langle E_z\rangle, t) = 360\Delta\nu_z(\langle E_z\rangle)t = 360\nu_{z,0}\left(\frac{3}{4}\frac{\langle E_z\rangle}{qV_0}\left(\frac{C_4}{C_2^2} + \frac{5}{4}\frac{C_6}{C_2^3}\frac{\langle E_z\rangle}{qV_0}\right)\right)t\ . \tag{6.54}$$

The particle energies in many single measurements are distributed in the interval $[0,\infty]$ with an expectation value of $\langle E_z\rangle$. Therefore, it is of importance to compensate the Penning trap

in such a way, that $C_4$ and $C_6$ vanish simultaneously for a given energy $E_z$.
Here a numerical example is given to provide the reader with a detailed picture:
Assume, that the tuning ratio is optimized locally, in the way described in the upper text. The average axial temperature of the detection system should be $T_z = 10\,\mathrm{K}$ leading to an initial amplitude uncertainty of $\approx 70\,\mu\mathrm{m}$. The machining errors of the trap are $10\,\mu\mathrm{m}$ for the correction electrode and the ring electrode, and an offset potential of $-30\,\mathrm{mV}$ is applied to one of the correction electrodes. Under these assumptions, the axial frequency spread due to the thermal energy spread defined by the temperature reservoir is $\approx 150\,\mathrm{mHz}$, which is already in the range of the axial frequency difference caused by a spin flip.
In section 6.4 it was shown, that asymmetry compensation can be applied to tune the trap locally in a way, that both higher order coefficients $C_4 = C_6 = 0$ vanish simultaneously for a certain tuning ratio. This property is crucial for the successful application of phase sensitive detection.

### *6.12.3 Experimental Setup and Detailed Measuring Sequence*

The experimental setup is shown in Fig. 6.24. The measuring sequence is triggered by a *National Instrument PCI-6602* Card (indicated in the figure as "timing unit"). All frequency generators included in the sequence are phase locked by means of a *Stanford Research FS725* frequency standard. The cross-correlation function of the two-channel FFT analyzer (*Stanford Research SR-780*) compares the phases between two signals connected to its inputs A and B, respectively. The decoupling of the particle from the detection system is realized by application of negatively phased feedback to the resonator. In this way, the quality factor $Q$ can be switched down to values around 100, giving axial cooling time constants around 5 s which is sufficiently large to apply the phase-sensitive detection method.
The measuring sequence goes as follows:
In order to keep the scatter of the initial conditions small, the resonator is tuned to a cooling time constant of $\approx 500\,\mathrm{ms}$ which sharpens the initial energy spread by a factor of $\approx 4$ compared to the feedback-free conditions, and the proton is thermalized for 1 s. Afterwards the particle is excited. The excitation signal is also the reference for the relative phase

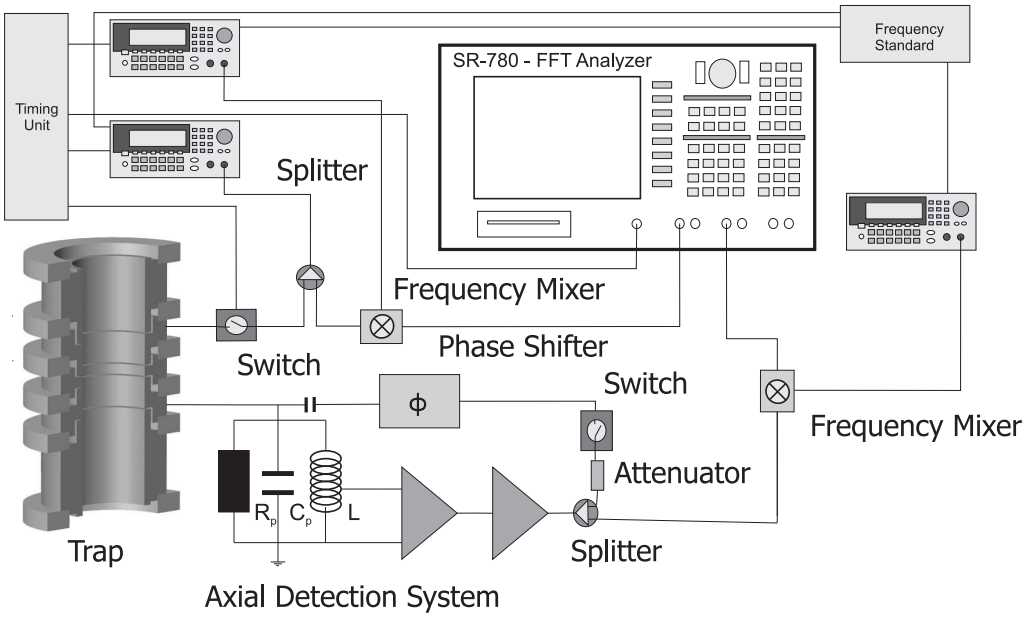


Figure 6.24: Experimental setup used for the phase sensitive detection technique. For a detailed description see text.

measurement. Thus, it is split into two signal ways, one is down-mixed and analyzed with the FFT analyzer, the second is guided to the Penning trap. In this second path a triggered rf switch is located connecting the signal to ground during the free evolution time and pre-cooling of the axial mode of the proton before the next experimental run[11]. Subsequently negative feedback is turned on, also with a triggered switch and the particle evolves freely. Finally the detector is re-coupled to the particle and the relative phase between the particle and the reference is measured.

### *6.12.4 Signal-to-Noise Ratio*

Up to now the phase-sensitive detection method was applied at the highly charged ion experiments in Mainz where the ions have charge states in the range of 5 to 19. In case of the proton the charge state is 1 and thus to measure at a comparable signal-to-noise ratio

[11] The switch attenuates the signal by more than 70 dB. It is based on a double-balanced mixer and has a rise time in the range of 10 ns which is only 1/100 of an axial oscillation cycle and can be regarded to be instantaneous.

and principal phase resolution the particle has to be excited to much larger amplitudes, making the application of the method more challenging compared to the HCI experiments. Therefore, for the application of the phase-sensitive detection method with a single proton, optimization of the signal-to-noise ratio is crucial.

The signal-to-noise ratio of an FFT analyzer measurement is given by Eq. (6.47). It is important to note, that higher signal-to-noise ratios can be achieved with lower quality factors. The quality factor of the detection system is adjusted by the application of phased feedback. The signal-to-noise ratio was measured as a function of the FFT averaging time $t_{\mathrm{FFT}} = 800/(6.25 \cdot 2^n)\,\mathrm{s}$, where $n$ is a positive integer, for different quality factors. The particle was excited for 2 ms with an rf amplitude of -20 dBm. For every time point $t_{\mathrm{FFT}}$, 100 data points were measured. The results are shown in Fig. 6.25, the solid lines are best fits of Eq. (6.47) to the data. Obviously, the data behave exactly as predicted by

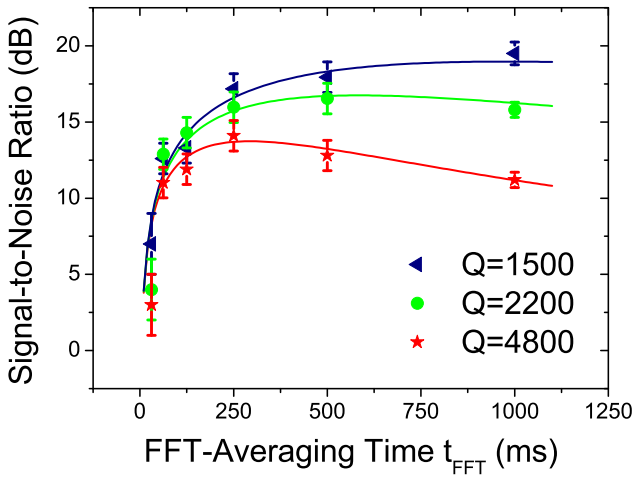


Figure 6.25: Signal-to-noise ratio as a function of measuring time recorded for different quality factors of the axial detection system. The quality factor was adjusted by application of negatively phased feedback.

Eq. (6.47). Below $t_{\mathrm{FFT}} = 250\,\mathrm{ms}$ the data have a steep slope which is due to the scaling $\mathrm{SNR} \propto \left(1 - \exp\left(-\frac{t_{\mathrm{FFT}}}{2\tau}\right)\right)$. Above 250 ms a weak scaling with time is observed which is mainly caused by the proportionality $\propto 1/\sqrt{t_{\mathrm{FFT}}}$. The final experimental aim is to measure

fast and at high signal-to-noise ratios. Therefore, all further results presented in this section are measured with an FFT-averaging time of 250 ms. For all peak measurements the quality factor is tuned to a value of $Q = 2200$. During the "free" phase evolution time the resonator is switched to a $Q$-value of about 150 which corresponds to a cooling time of $\tau_z = 4.2\,\mathrm{s}$. At these experimental settings the average signal-to-noise ratio is 16(1) dB corresponding to a noise limited phase resolution of 10°. Together with the knowledge that the feedback-free temperature of our axial detection system is 9.5(5) K (see section 7.4) from the fits to the data it can be evaluated that this signal-to-noise ratio corresponds to an axial energy of $E_z = 110(11)\,\mathrm{meV}$.

### *6.12.5 Phase Fluctuation as a Function of Tuning Ratio and Trap Asymmetry*

As explained in section 6.12.2, to achieve low phase fluctuation $\sigma_\phi$, it is important to tune the Penning trap to high harmonicity. Since dip optimization is not sensitive to the $C_6$ term, it is not sufficient to optimize the trap in the way described in section 6.3. It rather has to be optimized locally for a certain excitation energy. For this purpose, the particle is excited and the phase is measured for 30 times. Afterwards the phase fluctuation $\sigma_\phi$ is evaluated. This sequence is repeated for different tuning ratios. The results of such a measuring sequence is shown in Fig. 6.26, for a free evolution time of $t_{\mathrm{evol}} = 300\,\mathrm{ms}$, and an axial proton energy of 110(11) meV. The green filled circles are due to a measurement where the trapping potential was asymmetric. The best measured phase-fluctuation in this case is $\sigma_{\phi,\mathrm{opt}} = 35°$. The black squares represent a measurement where the trapping potential was asymmetry-compensated. There, the phase resolution, defined by the signal-to-noise ratio is achieved. An explanation has already been given in section 6.4 and 6.12.2. This shows the tremendous importance of the asymmetry-compensation method. Without asymmetry-compensation, clear spin-flip resolution in just one measuring sequence would not be possible. Comparing the scaling of the phase resolution $\sigma_\phi$ with the tuning ratio to potential theory, the slopes are consistent with an average run-to-run amplitude fluctuation of 12(2) meV. This is about 10 % of the absolute axial energy. A portion of 3 % can be explained by the amplitude accuracy of the frequency generator (*Agilent 33220A*) and rise

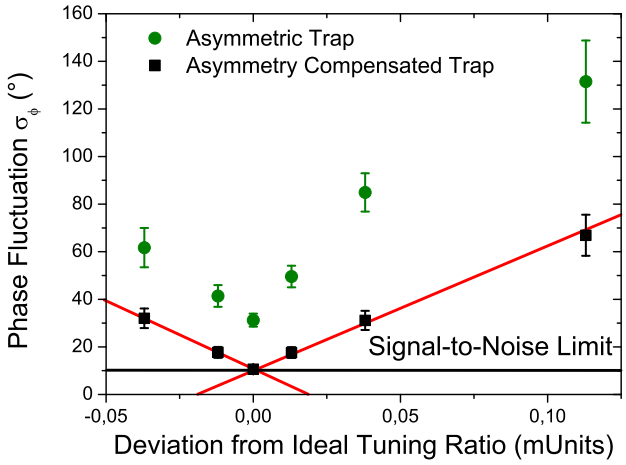


Figure 6.26: Phase fluctuation as a function of the deviation from the ideal tuning ratio recorded for an axial proton energy of 110(11) meV and a free evolution time of $t_{\mathrm{evol}} = 300\,\mathrm{ms}$. The green filled circles are due to a measurement where the trapping potential was asymmetric. The best measured phase-fluctuation in this case is $\sigma_{\phi,\mathrm{opt}} = 35°$. The black squares represent a measurement where the trapping potential was asymmetry-compensated. There, the phase resolution, defined by the signal-to-noise ratio is achieved.

times of the switches. The remaining 7 % may be due to the nonlinear response of the excited proton, caused by the anharmonicity [43]. Nevertheless, in the asymmetry compensated trap and for the optimized tuning ratio, in this measuring sequence the resolution level defined by the signal-to-noise ratio is achieved.

### *6.12.6 Achieving Spin Flip Resolution by Phase Sensitive Detection*

Applying the optimized tuning ratio found in the previous section to the trap, spin flip resolution in one second is achieved. To experimentally demonstrate the detection of a frequency jump of 200 mHz out of 680 kHz, the measuring sequence described in section 6.12.3 is performed, where alternatingly the reference signal is detuned by a frequency shift of 200 mHz [12]. In Fig. 6.27 a.) the phases measured in a sequence with $N = 28$ at a free evolution time of $t_{\mathrm{evol}} = 1\,\mathrm{s}$ is shown as a function of the sequence number. In Fig.

[12] Alternatively the proton can be detuned by the trapping potential.

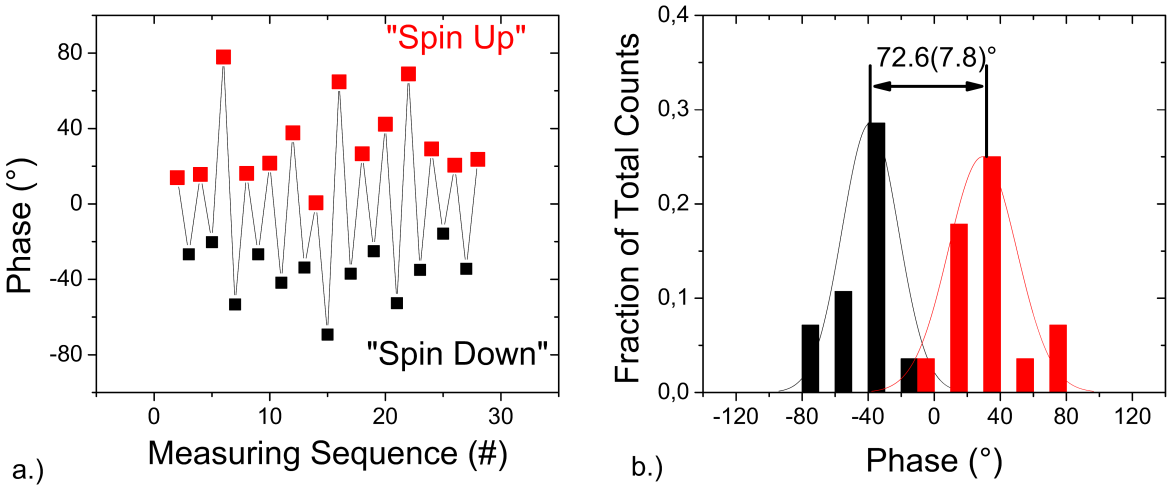


Figure 6.27: Experimental demonstration of the resolution of a frequency jump of 200 mHz in one second by phase-sensitive detection in the precision trap. a.) Measured relative phase as a function of the measuring sequence for a free phase evolution time of $t_{\mathrm{evol}} = 1\,\mathrm{s}$. Obviously two phase levels are observed, corresponding to a frequency shift of 200 mHz. b.) The data shown in a.) plotted to two histograms. The overlap of the histograms is only $\approx 3\,\%$. Thus, only in 3 out of hundred measuring sequences it cannot be decided whether the spin has flipped or not.

6.27 b.) the data are plotted to histograms. It is important to note, that the overlap of the histograms is only about 3 %, which means that in only 3 out of 100 measurements it cannot be decided, whether the spin has flipped or not. The phase difference between "spin up" and "spin down" is 72.6(7.8)° where the error is due to statistics. This is in perfect agreement with the expected theoretical value of 72°.

### *6.13 Particle Transport*

To detect spin flips of the proton by means of the continuous Stern-Gerlach effect, the particle has to be transported to the analysis trap. Therefore, adequate voltage ramps are applied to the electrodes of the transport section.

Transporting particles between both traps sounds straight forward, but we spent half a year working on particle transport until we succeeded for the first time. The first design of the

transport section is shown in Fig. 6.28 a.). It consists of three electrodes: two electrodes with the 3.5 mm-radius of the precision trap and one long electrode reducing the radius to the 1.8 mm-radius of the analysis trap. After this *reduction electrode* the long endcap of the analysis trap follows. In the experiment we never succeeded in transporting the protons

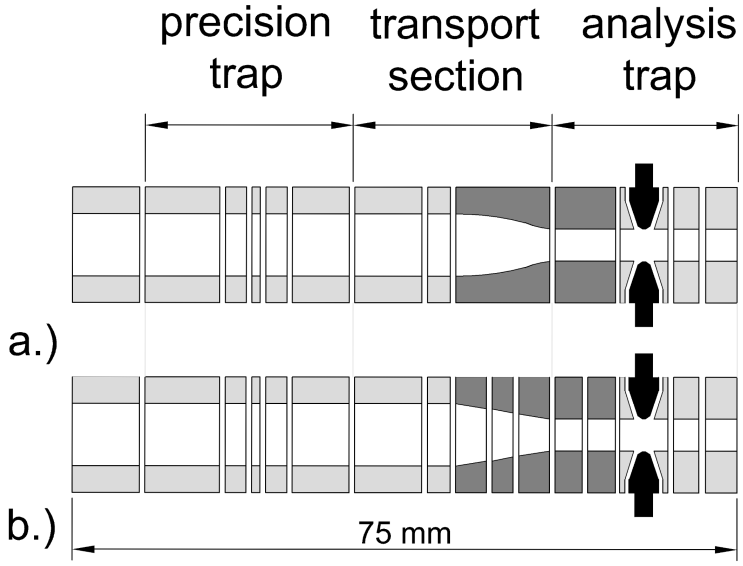


Figure 6.28: a.) Geometry of the old transport section and b.) geometry of the modified transport section. For details see text.

through the long electrodes. In numerous experiments it was found that

1. in short electrodes short voltage ramp times (several 10 ms) heat the magnetron mode of the proton,

2. in long electrodes short voltage ramp times (several 10 ms) heat the magnetron mode, but are the only recipe to transport the proton through the reduction electrode, and

3. transporting at small absolute voltages is for short electrodes more lossy than transporting at large absolute voltages. For the long electrodes the particles are lost in general.

Possible loss mechanisms are:

- **Resonances** where one eigenfrequency is a multiple of another $\omega_i = n\omega_j$ ($n$ is a positive integer). In case of resonances, the particle loss should depend on the values $V_{\mathrm{ramp}}$ of the voltage ramps. This was investigated but no correlation between "transport efficiency" and transport voltage in the sense, that a clear resonance occurred was found. In numerous SimIon simulations no particle loss due to a resonance ever occurred [13].

- **Non-ideal surfaces:** Metals have different work functions [58]. The electrodes are made out of copper, then plated with a silver-barrier-coat and finally gold-plated. The work functions of silver and gold or copper and silver differ by 1 V. If the surface is not coated properly, the particle sees inside a long electrode abrupt potential changes and non-symmetrical electric fields-strengths up to 1 V/mm. These fields enlarge the magnetron radius and lead to particle loss after some axial oscillation cycles.

Combining the experimental observations with the simulation results hints that *imperfect surfaces are responsible for the particle loss*. Thus, the reduction electrode as well as the long endcap of the analysis trap were divided in shorter sections (see Fig. 6.28 b.)). Shorter electrodes affect better control of the transport potential, furthermore, the deposition fields of the plating bath are not shielded in the inner of the electrode leading to better coating quality. After the modification the transport worked immediately [14].

[13] Simulation results and more details are presented in the PhD thesis of Cricia C. Rodegheri [47].

[14] The lab team measuring the $g$-factor of the electron in highly charged ions [26], had the same problem afterwards, which has also been solved by separation of the long transport electrodes to smaller lengths.

# Chapter 7

# EXPERIMENTAL RESULTS - MAGNETIC BOTTLE EXPERIMENTS

In this chapter, experiments in the strong "magnetic bottle" field

$$\vec{B} = B_0\vec{e}_z + B_2\left(\left(z - \frac{\rho^2}{2}\right)\vec{e}_z - z\rho\vec{e}_\rho\right) \tag{7.1}$$

are presented. The magnetic bottle coefficient is $B_2 = 3 \cdot 10^5\,\mathrm{T}\cdot\mathrm{m}^{-2}$. This is the strongest magnetic field inhomogeneity ever superimposed to a Penning trap. As explained in chapter 2, it is required to resolve spin flips of a single proton by means of the continuous Stern-Gerlach effect. The magnetic bottle couples the magnetic moment of the proton to the axial frequency. A spin flip will cause an axial frequency shift of $\Delta\nu_{z,\mathrm{SF}} = 191\,\mathrm{mHz}$.
The controlled storage of charged particles in such a large magnetic field inhomogeneity has never been demonstrated before. It is challenging work to get single particle resolution under such extreme experimental conditions.

1. The strong magnetic bottle $B_2$ leads to a highly sensitive dependency of the axial frequency on the energy stored in the radial modes,

   $$\Delta\nu_z = \frac{1}{4\pi^2 m\nu_z}\frac{B_2}{B_0}\left(E_+ + |E_-|\right) \approx 0.92\,\mathrm{MHz}\cdot\mathrm{eV}^{-1}\ . \tag{7.2}$$

   This strong coupling leads to large axial frequency shifts and complicates the optimization of the Penning trap.

2. Due to the small radius of the magnetic bottle trap of only 1.8 mm the biasing voltage to tune the proton to resonance with the axial detector is only $-0.85\,\mathrm{V}$. As explained in section 6.4, typical offset potentials due to leakage currents, patch effects, and thermal contact potentials are in the range of 100 mV. This is already about 10 % of the respective biasing voltage, making the initial experimental conditions rather undefined. Thus, preliminary theoretical calculations do not help too much for the experimental operation.

Results of an example calculation shown in Fig. 7.1 point out the experimental difficulties. An offset voltage of $\Delta = 100\,\mathrm{mV}$ is initially present to the ring electrode. The effective

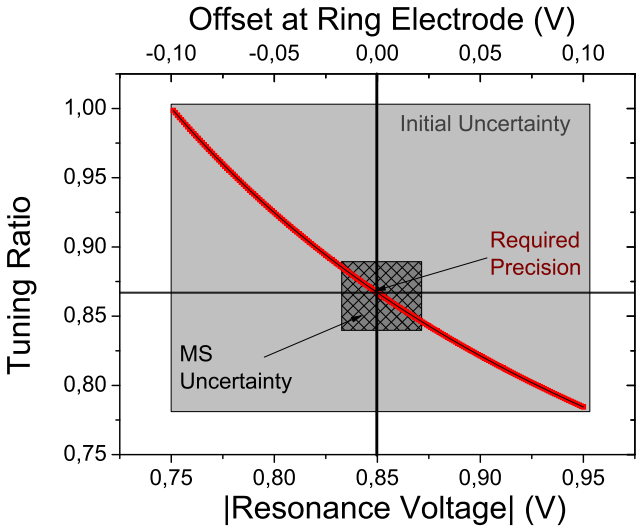


Figure 7.1: Scatter of the experimental initial conditions in the analysis trap. The upper axis shows the offset voltage, which is initially present at the ring electrode of the trap. The red solid line shows the effective tuning ratio, which is applied at the trap, as a function of the offset voltage, being present at the ring electrode. The lower x-axis shows the resonance voltage to tune the particle on resonance with the axial detector. The light grey rectangle marks the initial experimental uncertainty, which is caused by this offset - 220 mUnits in tuning ratio, and 200 mV in the resonance voltage. To resolve the proton in the analysis trap, the voltage has to be known with an absolute precision of 0.25 mV, and the tuning ratio has to be optimized to at least 0.5 mUnits. This makes the optimization of the analysis trap challenging. The optimization described in section 7.1 reduces this parameter space to the dark-grey meshed rectangle.

tuning ratio which is applied to the trap in presence of an offset voltage $\Delta$ at the ring electrode is given by

$$\mathrm{TR} = \mathrm{TR}_0 \left( \frac{1}{1 + \frac{\Delta}{V_R}} \right) \ , \tag{7.3}$$

where $\mathrm{TR}_0$ is the tuning ratio, applied at the DC-voltage supply, and $V_R$ is the voltage of the ring electrode. Equation (7.3) is represented in the graph by the red line. An offset potential span of $\pm 100\,\mathrm{mV}$ is plotted. To detect a proton-dip in the analysis trap, the ring voltage has to be known at a level of at least 0.04 % and the tuning ratio at 0.06 %. This means that

the difference between the required precision to resolve a single particle in the bottle trap and the preliminary knowledge differs by a factor of $\approx 200$. The light-grey rectangular area in Fig. 7.1 visualizes the spread of the initial conditions. With the techniques described in section 7.1 the uncertainties can be reduced to a smaller area represented by the dark meshed rectangle. The size of the crossing point of the solid orthogonal lines represents the precision required to resolve a single proton dip in this trap.

Besides the technical problems arising from offset voltages, the axial frequency dependency on the radial energy (Eq. (7.2)) complicates the optimization additionally. The magnetic bottle couples the radial energies of the proton to the axial motion and thus to the axial frequency. The parameters to observe a proton on resonance with the axial detection system are therefore a function of the particle energy, which underlies a Boltzmann distribution. In different experimental runs the proton has slightly different cyclotron energies, leading to an axial frequency spread in the range of about 5 kHz and the optimum trap parameters vary from run to run. Since initially nothing is known about the trap, the combination of both effects makes the optimization of the trap very challenging. In this chapter procedures to prepare a single proton in the analysis trap, as well as experiments with a single proton in the magnetic bottle are presented.

## *7.1 Proton Cloud in the Magnetic Bottle*

The first step to detect particles in the magnetic bottle is to determine the ring voltage $V_R$ which tunes the particles on resonance with the axial detector. Therefore, a cold clean cloud of protons is prepared in the precision trap and transported into the analysis trap. There a voltage scan (as explained in chapter 5.1) is recorded. To get valuable experimental information about the trap, it is important to ramp the voltage form negative voltages towards zero. If the other direction is chosen, hotter particles are excited first and interact with the colder particles before they are excited. This smears-out the results obtained for the cutoff voltage.

A typical result of such a measurement is shown in Fig. 7.2. This curve is a direct picture of the thermal Boltzmann-distribution of the cyclotron mode which is indicated by the red line. The cutoff voltage defines the voltage $V_R$ which has to be applied to the ring electrode

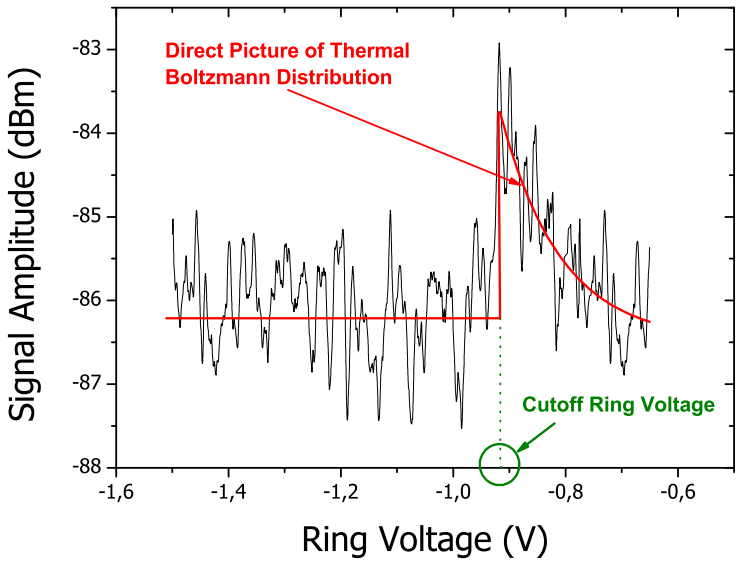


Figure 7.2: Mass Spectrum of a particle cloud in the magnetic bottle trap. The cutoff defines the ring voltage, which has to be applied to tune one single cold proton to resonance with the detection system.

to tune one single cold particle on resonance with the detection system. From the voltage scan, this resonance voltage can be determined to a precision of $\pm 20\,\mathrm{mV}$. It is important to mention again, that the proton cloud before the record of such a scan has to be cold and clean, otherwise the mass spectra show confusing results and no valuable information about the trap is obtained. Figure 7.3 a.) shows two histograms of measured resonance voltages. The narrow histogram corresponds to data, extracted from voltage scans obtained with cold clean clouds. The broad histogram is extracted from data, were the initial conditions of the cloud were not well-defined. These results scatter in a voltage range of about $100\,\mathrm{mV}$ and do not narrow the parameter space. After a voltage scan, the particles are excited and due to Coulomb-coupling in the cloud, energy is pumped to the radial modes. Thus, after every single experiment in the analysis trap the cloud is transported back to the precision trap to cool the modes for the next experimental run, making the initial optimization of the trap

time-consuming[1].

A tuning ratio optimization with a particle cloud in the magnetic bottle as described

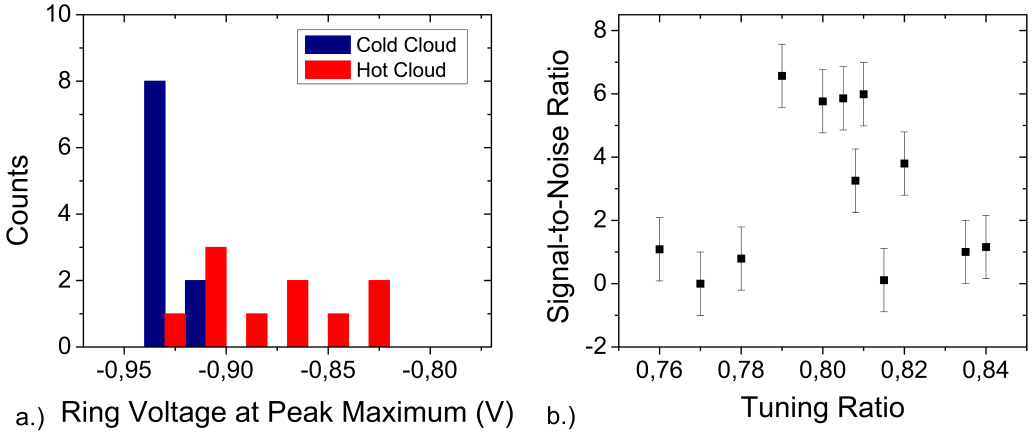


Figure 7.3: a.) Results of measured resonance voltages binned to histograms. The narrow histogram corresponds to data extracted from voltage scans obtained with cold clean clouds. The broad histogram is extracted from data were the initial conditions of the cloud were not well-defined. b.) Signal-to-noise ratio for different tuning ratios. By voltage scans the tuning ratio can only be determined with an uncertainty of about 40 mUnits, where 0.5 mUnits are required to resolve a single proton in the trap.

in section 5.2 reduces the initial tuning-ratio uncertainty to about 40 mUnits, only, where 0.5 mUnits are required to resolve a single proton (see Fig. 7.3 b.)). This is due to a $B_4$ term. The optimum tuning ratio scales with the cyclotron energy $E_+$ [42].

### *7.2 Optimization with a Single Particle*

The optimization of the trap by means of voltage scans defines the optimum parameters only in boundaries which is represented by the dark-grey meshed rectangle shown in Fig. 7.1. To get the trap under better control and to achieve dip resolution, it has to be optimized with one single proton. The basis for successful optimization is a clean and in all modes adequately cooled particle.

For the optimization $2\nu_z$-*parametric resonance* is used. The basic physics is described in

[1]From cool-down of the experiment to single particle dip resolution, typically two to three weeks are used, depending on the "luck" to choose the right parameters already at the beginning of the optimization.

[44]. In Penning trap physics, parametric resonance was applied in [46] and [107]. A detailed discussion is presented in [45].

Parametric resonance occurs, if a (damped) harmonic oscillator with eigenfrequency $\nu$ is driven with an excitation at its second-harmonic $2\nu$. Two aspects of the parametric drive are of importance for the optimization of the analysis trap.

1. **Saturation free particle observation:**

   If an excitation is tuned to the second-harmonic of the axial detector $\nu_{res}$ and a proton is tuned on resonance, a response of the particle due to parametric excitation is observed. Therefore, by application of that method, particle excitation can be observed, where at the same time saturation of the axial detection system is avoided. Anharmonicities shift the axial frequency as a function of energy, arresting the rapid growth of the amplitude. Consequently the particle can be observed non-destructively.

2. **Dependence of the signal-to-noise ratio on** $1/C_4$**:**

   The signal strength of the parametrically excited particle scales as $1/C_4$ (see section 2.3.1). Scanning the tuning ratio while observing parametric resonance, the trap can be tuned to high harmonicity. Best harmonicity is indicated by the highest signal-to-noise ratio.

One crucial feature of damped parametric resonance is shown in Fig. 7.4 a.). The inset shows a parametrically pumped proton and defines the signal-to-noise ratio. Below a threshold amplitude $h_T = \gamma_z/\omega_z$, the parametric resonance does not occur. Above the threshold amplitude, the signal increases exponentially with the excitation amplitude, and reaches an almost constant value, which is defined by the anharmonicity of the trap [46]. For $h > h_T$, where $h$ is the excitation amplitude, the frequency span where parametric resonance occurs, is given by

$$\Delta\nu_z = \nu_z h \sqrt{1 - \frac{h_T^2}{h^2}} \ . \tag{7.4}$$

Thus, to get high resolution for the trap optimization, the excitation amplitude has to be adjusted to a value above, but near the threshold amplitude $h_T$. Figure 7.4 b.) shows a

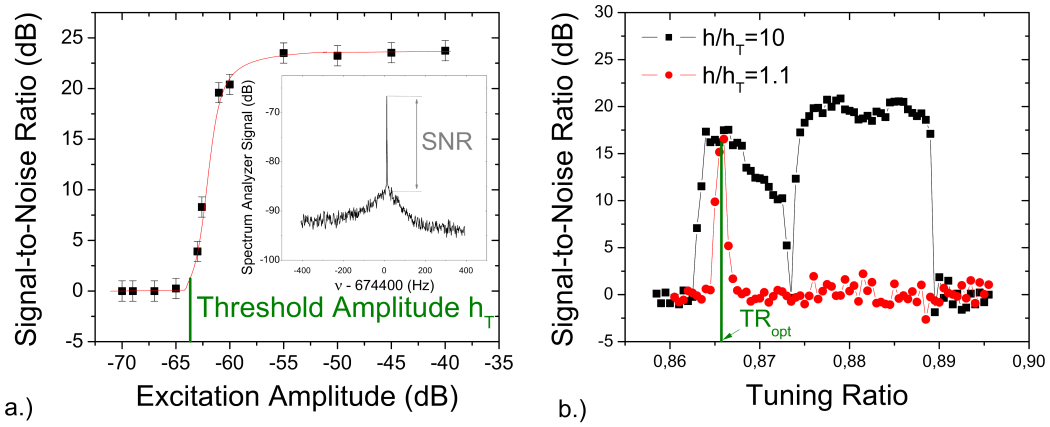


Figure 7.4: Illustration of two features of parametric resonance. a.) Signal-to-noise ratio of a parametrically pumped proton as a function of the drive amplitude. Below a threshold amplitude $h_T$, no response of the particle can be observed. Above $h_T$, the signal increases exponentially and reaches its maximum amplitude "immediately". The maximum signal-to-noise ratio is defined by the harmonicity of the trap. The inset in a.) shows a parametrically pumped proton and defines the signal-to-noise ratio. b.) Parametric resonance for $h/h_T = 1.1$, (filled red circles) and $h/h_T = 10$ (filled black squares), where $h$ is the drive amplitude. For $h/h_T = 1.1$, the resonance behaves as expected, parametric resonance occurs only in a narrow tuning ratio span. For $h/h_T = 10$, the parametric response around the optimum tuning ratio is broad. Furthermore another region occurs were parametric resonance is possible, corresponding to a locally harmonic trap $\sum_k \alpha_k C_k A^k = 0$.

feature which occurs if the excitation amplitude of the drive is far above $h_T$. In the figure the signal-to-noise ratio of a parametrically driven proton is shown as a function of the tuning ratio applied to the trap. For the filled red circles where $h/h_T = 1.1$, parametric resonance is only observed in a small tuning ratio span. In case of the filled black squares where $h/h_T = 10$, besides the broad response near the optimum tuning ratio parametric pumping is also observed in another tuning ratio region. This occurs if the excitation is that high, that the particle is excited to an amplitude $A$, where higher order coefficients simultaneously vanish $\sum_k \alpha_k C_k A^k = 0$. At the respective amplitude, the particle behaves as a quasi-harmonic oscillator [108]. In that case no valuable information for the dip-optimization is obtained. Consequently, large excitation amplitudes should be avoided.

Having mentioned these special features of parametric resonance, a parametric rf-drive is turned on at moderate amplitude ($-45\,\mathrm{dBm}$ which corresponds to $\approx 3h_T$) and a software

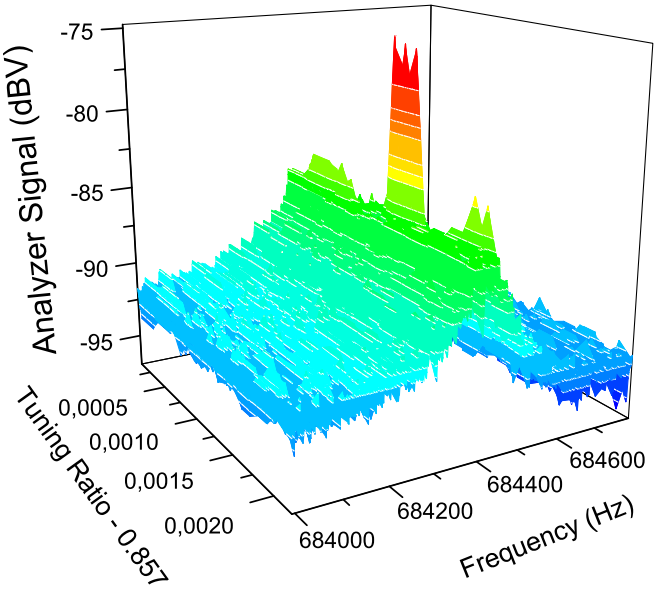


Figure 7.5: Surface plot of axial frequency spectra in presence of a parametric drive. The different spectra were recorded for different tuning ratios which were applied to the trap. The particle response can only be observed in a narrow tuning ratio span. In this span the trap behaves approximately harmonic.

routine is started, which scans the remaining parameter space in voltage steps of 250 $\mu$V and tuning ratio steps of 5 mUnits. As soon as a peak occurs on the resonator, the routine is stopped and the ring voltage, as well as the tuning ratio, are optimized manually until the maximum signal is obtained. Figure 7.5 shows a surface plot of axial frequency spectra in presence of a parametric drive. The spectra were recorded for different tuning ratios. The parametric response only occurs in a tuning ratio range of 0.5 mUnits. In that tuning ratio window the trap behaves nearly harmonic.

Having found this tuning ratio interval, the drive is turned off and a dip occurs on the noise spectrum of the axial detection system. Subsequently, the magnetron mode is feedback-cooled and the tuning ratio is optimized as described in section 6.3. Figure 7.6 shows the very first dip signal of a single charged particle, which has ever been observed in a Penning

trap with a superimposed magnetic bottle of $B_2 = 3 \cdot 10^5\,\mathrm{T/m^2}$.[2] The dip in the analysis

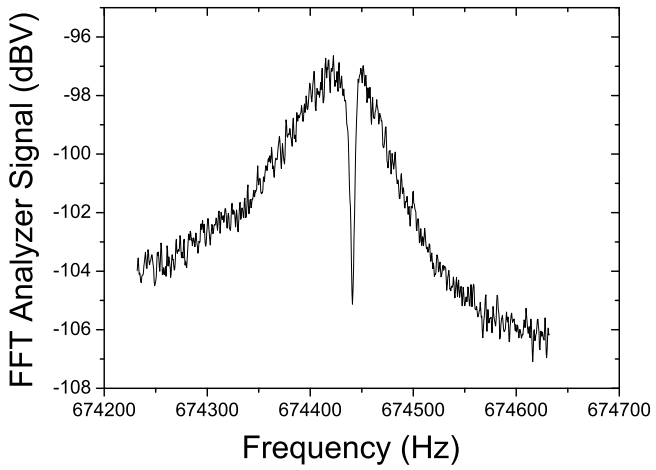


Figure 7.6: Very first dip signal of a single charged particle which has ever been observed in a Penning trap with a superimposed magnetic bottle of $B_2 = 3 \cdot 10^5\,\mathrm{T/m^2}$.

trap has a width of $\Delta\nu_{\mathrm{z,AT}} \approx 3.5\,\mathrm{Hz}$, being again in perfect agreement with theory (see section 4.4). Compared to the single-proton noise-dip in the precision trap this is about a factor of three larger, being due to the smaller diameter of the analysis trap, which leads to a stronger coupling of the detection system to the proton.

### *7.3 Magnetic Bottle Measurement*

For systematic studies such as energy calibration and single-particle temperature measurements it is crucial to determine the strength $B_2$ of the magnetic bottle experimentally. To obtain high-resolution data, first, the trap asymmetry is investigated as described in section 6.4. With the knowledge obtained from the asymmetry compensation, the proton can be moved in the trap with sub-$\mu$m-resolution. The particle is moved along the $z$-axis by application of asymmetric potentials to the trap electrodes and subsequent measurement of the cyclotron frequency (and therefore the magnetic field). For the determination of the

[2] February 12, 2010 - 4.53 am.

cyclotron frequency, the axial frequency is measured continuously, and an rf-drive is applied to excite the particle. If the proton absorbs energy from the drive, a drastic change of the axial frequency is observed, which indicates resonant energy absorption from the drive. The result of such a frequency measurement is shown in Fig. 7.7 a.), where the axial frequency is plotted as a function of the excitation frequency $\nu_{\mathrm{drive}}$. Below the resonance frequency

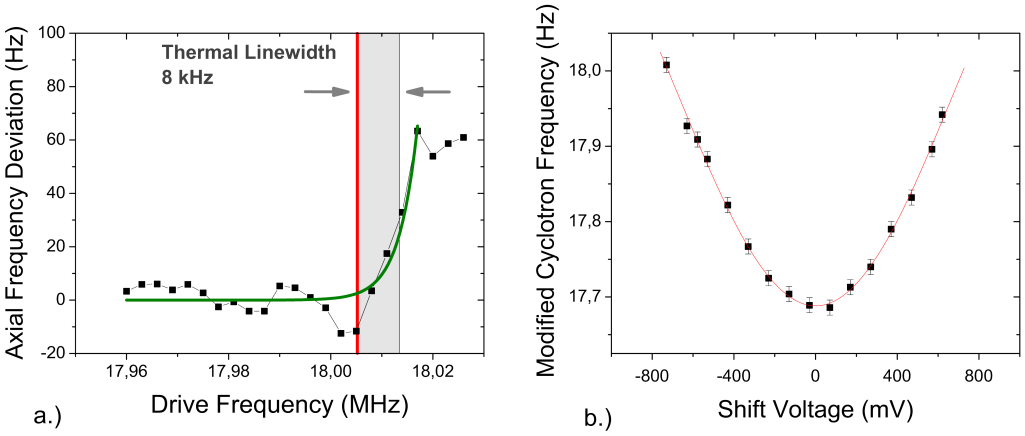


Figure 7.7: a.) Axial frequency as a function of the drive frequency $\nu_{\mathrm{drive}}$, which is irradiated to excite the cyclotron motion. Below $\nu_+$ the axial frequency $\nu_z$ is constant. If the particle resonantly absorbs energy from the drive, the axial frequency drastically changes according to Eq.(7.2). The frequency response in a window of about 8 kHz is due to the linewidth of the cyclotron resonance. b.) Cyclotron frequency as a function of the offset voltage applied to the endcap electrode. The offset shifts the particle along the z-axis of the trap. From these $\nu_+(\Delta V)$ data, the magnetic field $B(z)$ is extracted.

$\nu_{\mathrm{drive}} < \nu_+$, the axial frequency is constant. At a frequency of $\nu_+ = 18.05\,\mathrm{MHz}$ the axial frequency drastically changes, which is due to resonant absorption of the drive signal. A response is observed in the frequency span of the thermal cyclotron linewidth. Above this span, $\nu_z(\nu_{\mathrm{drive}})$ becomes "quiet" again. Due to the Boltzmann convoluted lineshape of the cyclotron frequency (see chapter 2), the "first axial frequency jump" indicates the "cold" cyclotron frequency [23, 48]. To achieve high-resolution, the axial motion of the particle is feedback cooled, which reduces the linewidth of the cyclotron resonance curve (see chapter 2 and [49]).

The particle is excited with a burst signal of 3 kHz linewidth (1000 burst-cycles at 18 MHz),

while the frequency step between different excitations was also 3 kHz. This limits the principal resolution of the measurement to 1.5 kHz. Due to the strong dependence of the magnetic field with the position in the strong magnetic bottle, where frequency changes of several hundred kHz occur (see Fig. 7.7), this resolution is sufficient for the measurement of the magnetic bottle. Repeating this measuring sequence for different offset potentials $\Delta V$ applied to the upper endcap-electrode, $\nu_+(\Delta V)$ is measured. The results of the whole sequence are shown in Fig. 7.7 b.). The error bars are a combination of the resolution limit and the statistical average over several measuring cycles at the same position. With the information obtained from the asymmetry compensation (see section 6.4), $\nu_+(\Delta V)$ is transformed into a function of the position $\nu_+(z)$. Applying the invariance theorem (Eq. (2.11)) the magnetic field $B(z)$ is yielded. The result of the magnetic field as a function of the position is shown in Fig. 7.8. From a 4th-order polynomial-fit to the data, the magnetic bottle coefficient

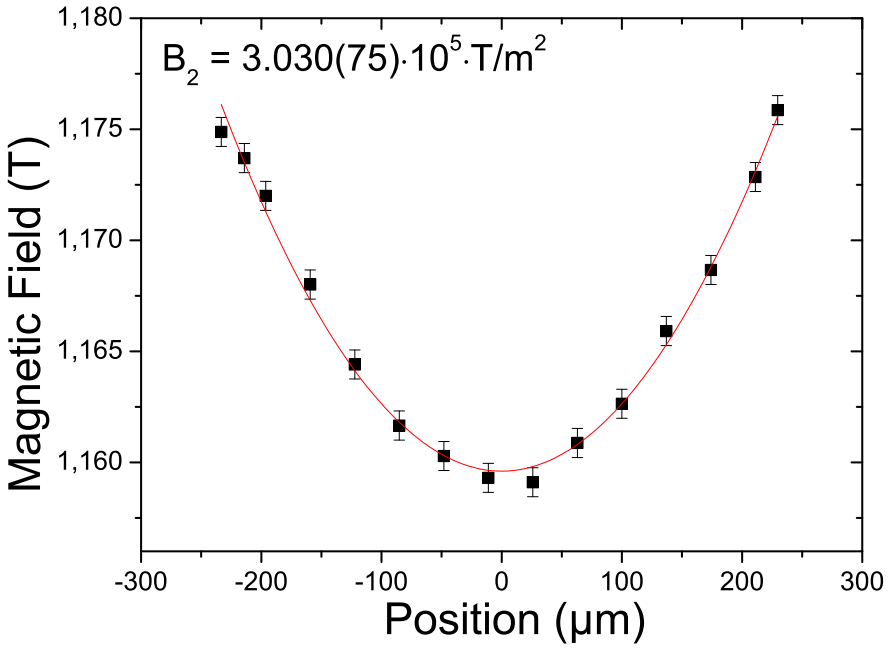


Figure 7.8: Result of the magnetic bottle measurement. From a fit to the data $B_2 = 3.030(75) \cdot 10^5\,\mathrm{T/m^2}$ is extracted. This value agrees perfectly to the design value of $B_2 = 2.99 \cdot 10^5\,\mathrm{T/m^2}$ [47].

$B_2 = 3.030(75) \cdot 10^5\,\mathrm{T/m^2}$ is obtained being in perfect agreement with the numerically simulated design value of $B_2 = 2.990 \cdot 10^5\,\mathrm{T/m^2}$ [47].

## 7.4 "Single-Particle-Temperature" Measurements

### 7.4.1 Magnetron and Axial Temperature

Temperature $T$ is known to be a global state variable of a thermodynamic system and, thus, is defined as an average over many degrees of freedom of a system consisting of a large number of particles. Due to the ergodic hypothesis, which indicates that the time average of a statistically defined quantity $\langle A \rangle_t$ is equivalent to its array average $\langle A \rangle_a$, it is possible to relate the properties of a single trapped proton to temperature.

If the proton is coupled to a bath with fluctuating energy, for a certain amount of thermalization time and afterwards the energy of the particle is measured, the particle can be used as a probe which directly maps the energy distribution of the bath.

The presence of the magnetic bottle $B_2$ and the fact that radial energy is directly visible in the axial frequency, compare Eq. (7.2), leads to the possibility to map the energy of the

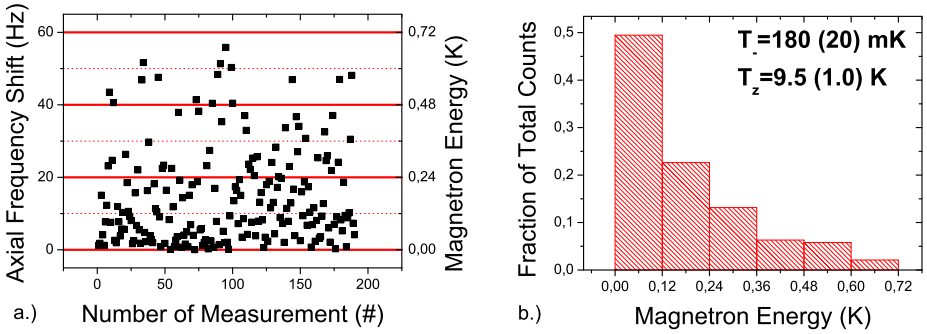


Figure 7.9: a.) Sequence of axial frequency measurements in presence of the magnetic bottle $B_2$. Between two subsequent measurements, the magnetron motion is coupled to the thermal bath of the axial detection system via a resonant sideband $\nu_{\mathrm{rf}} = \nu_z + \nu_-$. Due to this coupling, the thermal energy distribution of the axial detector is directly mapped by magnetron energy, which can be observed measuring the axial frequency $\nu(E_-)$. The left axis indicates the frequency shift; the right axis is scaled to the equivalent magnetron energy. b.) Histogram of the measured axial frequencies. The energy shifts are scaled to the magnetron energy. From this histogram, a "magnetron temperature" of $T_- = 180(20)\,\mathrm{mK}$ and by the relation $T_z = T_- \cdot \nu_z/\nu_-$ an axial temperature $T_z = 9.5(1.0)\,\mathrm{K}$ is obtained.

particle and thus, the temperature of a heat bath which was coupled to the radial modes. In the magnetic bottle $B_2 = 3.030(75) \cdot 10^5\,\mathrm{T/m^2}$ the axial frequency dependence on the radial mode energies is $\Delta\nu_z \approx 0.92\,\mathrm{Hz}\cdot\mu\mathrm{eV}^{-1}$. Since the axial frequency can be measured with a precision of about 60 mHz, in principle a temperature resolution of 700 $\mu$K can be achieved.

For the measurement of the temperature of the axial detection system, the magnetron mode of the particle is coupled to the thermal bath of the axial detection system by means of a sideband drive (see section 6.6). Subsequently, the axial frequency $\nu_z$ is measured. This coupling-measuring cycle is repeated for several hundred times. Figure 7.9 a.) shows the results of axial frequency measurements as a function of the sequence number. Between each single axial frequency measurement, the magnetron mode of the proton was coupled to the axial heat bath. Binning these frequency data into a histogram, which is shown in Fig. 7.9 b.), gives a direct map of the thermal Boltzmann distribution

$$w(E_z, T_z) = \frac{1}{k_B T_z} \exp\left(-\frac{E_z}{k_B T_z}\right) = \frac{1}{k_B T_z} \exp\left(-\alpha \frac{E_-}{k_B T_-}\right) \ , \tag{7.5}$$

of the energy of the axial detection system. A recorded frequency shift $\Delta\nu_z$ directly pictures the corresponding magnetron energy according to

$$|E_-| = 4\pi^2 m_p \nu_z \frac{B_0}{B_2} \Delta\nu_z \ . \tag{7.6}$$

The energy $|E_-|$ can be calibrated absolutely, by evaluating the slope $\kappa$ of the natural logarithm of the histogram-counts by a best fit. From that slope the magnetron- as well as the axial temperature are obtained

$$T_- = \frac{4\pi^2 m_p \nu_z}{\kappa k_B} \frac{B_0}{B_2} \Rightarrow T_z = \frac{\nu_z}{\nu_-} T_- \ . \tag{7.7}$$

The histogram shown in Fig. 7.9 b.) corresponds to a magnetron temperature of $T_- = 180(10)\,\mathrm{mK}$ and an axial temperature of $T_z = 9.5(1.0)\,\mathrm{K}$. Together with the temperature result obtained by phase-sensitive detection (see section 6.12), where $T_z = 9.1(5)\,\mathrm{K}$ was obtained, this result can be interpreted in several ways: first of all as a verification of the temperature determination method presented in section 6.12. Moreover, reversing the argumentation, this result can be seen as a direct experimental proof of the ergodic hypothesis.

In this section the temperature was determined by a time average. The determination of the axial temperature $T_z$ described in section 6.12 corresponds to a temperature determination by means of an array-average. There, the temperature of the noise floor of the axial detector was measured. Since both temperatures are identical within their error bars this independent determination of $T_z$ can also be understood as a direct proof of the relation $T_z = \frac{\nu_z}{\nu_-} T_-$.

In chapter 4 it was claimed, that negative feedback applied to the axial resonator reduces its effective temperature, and due to the interaction of the proton and detection system, the axial temperature of the particle. This can be proven directly by this temperature measuring method, as shown in Fig. 7.10 a.).
Feedback is applied to the resonator, and the procedure described in the upper text is repeated for different feedback-gains $G_{\mathrm{FB}}$ and -phases $\Phi$. Increasing $G_{\mathrm{FB}}$ at $\Phi = 180°$ (see section 6.11) reduces the temperature of the particle and the width of the histograms. As described in chapter 4.5 the effective particle temperature $T_{\mathrm{eff}}$, as well as the effective parallel resistance $R_{\mathrm{eff}}$ are in a wide range linear functions of feedback gain $G_{\mathrm{FB}}$

$$R_{\mathrm{eff}} = R_p \left(1 \mp G_{\mathrm{FB}}\right) \tag{7.8}$$

$$T_{\mathrm{eff}} = T_0 \left(1 \mp G_{\mathrm{FB}}\right) \ . \tag{7.9}$$

These relations lead to a thermalization-dissipation invariant $R_{\mathrm{eff}}/T_{\mathrm{eff}}$ [72].
Figure 7.10 a.) shows three histograms where negative feedback was applied to the axial detection systems and the measuring sequence described above was performed. The narrowest histogram corresponds to the highest feedback gain $G_{\mathrm{FB}}$ at $\Phi = 180°$, resulting in an axial temperature of $T_z = 1.75(0.25)\,\mathrm{K}$. In every second measurement, the magnetron energy is cooled to the lowest frequency bin which has a width of only 20 mK. Thus, experimentally only about 10 s are required to cool the magnetron mode of the particle to such low energies. In section 7.5 it will be shown that this will be crucial for a fast performance of the final $g$-factor measuring sequence.
In Fig. 7.10 b.) the linewidth $\Delta\nu_z \propto R_{\mathrm{eff}}$ of the axial noise-dip is shown as a function of feedback gain $G_{\mathrm{FB}}$ which is directly proportional to $R_{\mathrm{eff}}$. Figure 7.10 c.) shows the axial temperature as a function of $G_{\mathrm{FB}}$. The results $T_z(G_{\mathrm{FB}})$ are obtained from histograms as de-

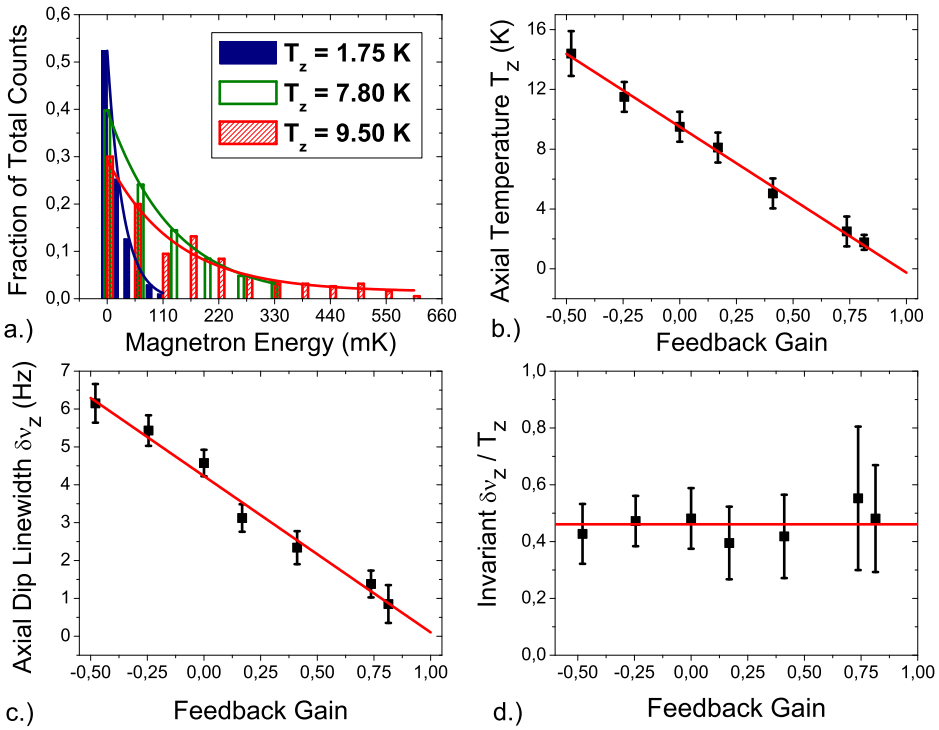


Figure 7.10: Results of temperature measurements in presence of active electronic feedback. a.) Temperature histograms for different feedback gains. b.) shows the axial temperature as a function of $G_{\mathrm{FB}}$. c.) Linewith $\Delta\nu_z \propto R_{\mathrm{eff}}$ of the axial dip as a function of feedback gain $G_{\mathrm{FB}}$. In d.) the fluctuation-dissipation invariant $\Delta\nu_z(G_{\mathrm{FB}})/T_{\mathrm{eff}}(G_{\mathrm{FB}})$ obtained from the data b.) and c.) is shown. For further discussion see text.

scribed above. In Fig. 7.10 d.) the fluctuation-dissipation invariant $\Delta\nu_z(G_{\mathrm{FB}})/T_{\mathrm{eff}}(G_{\mathrm{FB}})$ is shown, the constant value of the data proves the invariance. After this feedback-temperature calibration, the temperature can be extracted directly from the measurement of the dip-linewidth $\Delta\nu_z$.

### *7.4.2 Cyclotron Temperature*

The measurement of the axial as well as the magnetron temperature is carried out in the analysis trap. In this trap no cyclotron detection system is present for obvious reasons.

The interaction of the detection system with the single tapped proton would lead to axial frequency drifts. Details are discussed in [48]. For the measurement of the temperature of the cyclotron detection system $T_+$, the particle is transported to the precision trap. There the cyclotron mode is thermalized for a time $\approx 3\tau_+$, where $\tau_+$ is the resistive cooling time constant of the cyclotron mode. Subsequently, the proton is transported back to the analysis trap, where the axial frequency $\nu_z$ is measured. Before such a measuring sequence the effect of the transport on particle temperature is investigated. The average heating due to particle-transport between both traps is only 80 mK, which is less than 2 % of the expected temperatures and thus, neglected in the following discussion. The axial frequency shift as a function of the cyclotron temperature is $\Delta\nu_{z,\mathrm{cyc}} \approx 80\,\mathrm{Hz/K}$. This means that after thermalization of the cyclotron mode, the axial frequency typically scatters in a range of 3 kHz. Since the axial resonator has a line-width of only 120 Hz, the ring voltage to detect the particle has to be adjusted. Combining a calibration measurement of the frequency shift as a function of the voltage shift $\Delta\nu_z/\Delta V = 435\,\mathrm{Hz/mV}$, $\Delta\nu_z(E_+)$ is obtained. The temperature is calibrated assuming again, that the ergodic hypothesis holds. From a linear fit to the natural logarithm of the histogram-counts, the temperature of the cyclotron detection system $T_+$ is obtained. The result of such a measurement is shown in Fig. 7.11 a.). The red histogram corresponds to a cyclotron-temperature of $T_+ = 8.87(85)\,\mathrm{K}$. This result is obtained if no feedback is applied to the cyclotron detection system. Obviously, a temperature is obtained which is about 4 K above the physical temperature of the trap. Also in this case no detectable active feedback is present on the resonator. As already mentioned in case of the axial detection system, up to now the slight increase of the detector temperatures has not been understood yet and still under experimental observation.

The blue histogram is obtained if negative feedback is applied to the detection system[3]. Here a temperature of $T_+ = 3.15(11)\,\mathrm{K}$ is extracted. In this case, in every second measurement, the particle is cooled to the lowest temperature bin. In order to get an even higher temperature resolution for the cyclotron mode, in a sequence of measurements the lowest

[3]Compared to axial feedback, successful application of negative feedback to the cyclotron detector is much more complicated, since at the higher frequencies parasitic couplings, which may heat the particle are more critical.

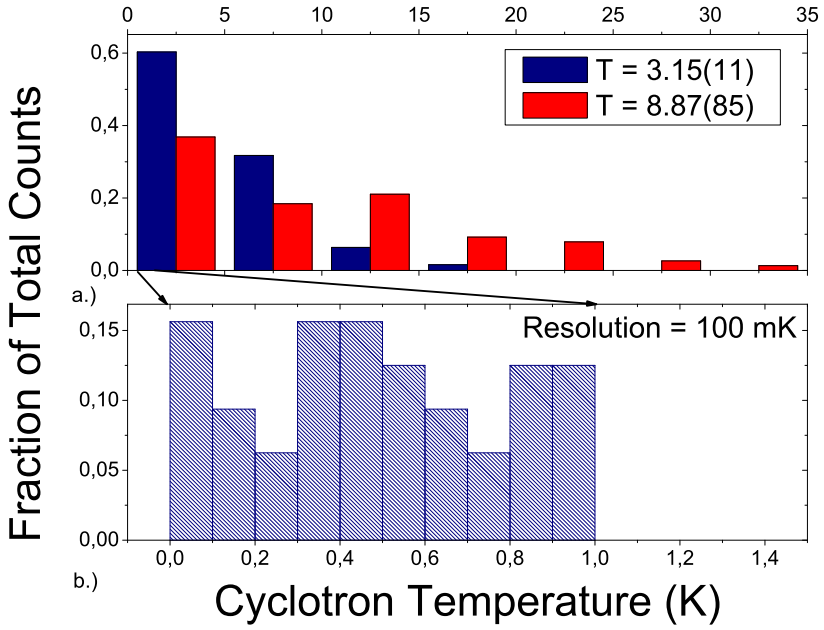


Figure 7.11: a.) Cyclotron temperature histograms for two different cyclotron feedback temperatures $T_+ = 8.87(85)\,\mathrm{K}$ and $T_+ = 3.15(11)\,\mathrm{K}$. The errors are due to statistics. The measuring sequence is described in the text. b.) High-resolution measurement of the lowest temperature bin. With this measurement, a temperature calibration of 100 mK is achieved. This calibration gives the possibility to prepare the particle to a cyclotron quantum state with an uncertainty of only $\Delta n_+ = \pm 60$.

temperature bin was calibrated with a resolution of only 100 mK as shown in Fig. 7.11 b.). In this frequency-bin, the results are approximately equally scattered, which means that in one out of twenty tries the particle can be prepared to a cyclotron energy which is below a corresponding temperature of 100 mK. It will be shown in section 7.5, that this will become very important for the final $g$-factor measuring sequence.

### *7.4.3 Importance of Temperature Calibration*

The measurement of the temperature of a thermal heat bath using a single particle as a probe and the fact that the experimental results represent the predictions of the ergodic hypothesis is fascinating. Reversing the matter of fact that the experimental results represent

these predictions, the energy of the particle can be measured directly. In that sense, the Boltzmann histograms obtained in the last two sections can be understood as an absolute calibration of the particle energy. If the magnetron mode is cooled to the lowest bin above the Boltzmann cutoff the axial frequency measurement is especially a direct measure of the cyclotron energy, giving us the possibility to investigate how experimental results behave as a function of the radial energies.

## *7.5 Axial Frequency Drifts*

### *7.5.1 Initial Conditions and Optimization*

It was explained in chapter 2, that for a $g$-factor measurement the axial frequency shift $\Delta\nu_{z,SF} = 191\,\mathrm{mHz}$, which is induced by a spin flip of the proton in the analysis trap, has to be resolved. Consequently, it is important to characterize the axial frequency stability of the proton trapped in the magnetic bottle. The result of the first frequency measurement $\nu_z(t)$ is shown in Fig. 7.12 a.) (red line). In this measurement the axial frequency drifts during a measuring time of 12 h in a range of $\approx 70\,\mathrm{Hz}$. In a time window of $\Delta t = 200\,\mathrm{s}$, which is typically needed to detect a spin flip by means of noise-dip detection, the average drift from measurement to measurement is about 3 Hz, being more than a factor of 10 above the resolution required.

In order to decrease the frequency fluctuation $\Xi$ (as defined in section 6.5) the apparatus was optimized in several steps leading to the rules that...

- ...rf-transmission lines for particle excitation and cooling should be connected to ground whenever possible,
- ...all DC lines should be filtered to high order,
- ...ground loops should be avoided,
- ...everything which is not urgently used - temperature monitors, pump controllers, pressure gauges, high-voltage lines,..., should not be connected to the apparatus during a precision measurement,

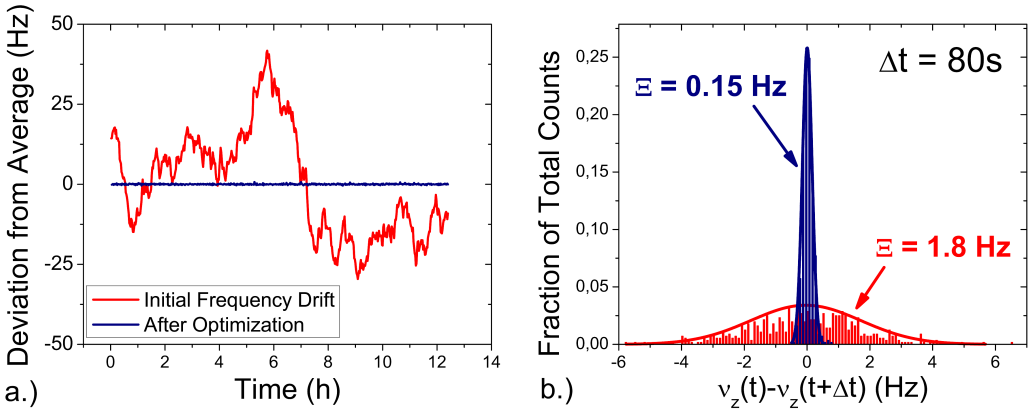


Figure 7.12: a.) Axial frequency drift directly after trap loading and after the optimization procedure. b.) Histograms of axial frequency fluctuation before and after optimization. The optimization procedure described in the text leads to a decrease of the frequency fluctuation $\Xi$ by a factor of 12.

- ...the radial mode-energies of the proton $E_+$ and $|E_-|$ should be cooled to the cutoff (see section 7.4).

The result of a frequency measurement $\nu_z(t)$ after these optimization steps is indicated by the blue line in Fig. 7.12 a.). Figure 7.12 b.) shows the frequency fluctuation $\Xi$ for the first measurement and after the optimization. An improvement by more than a factor of 10 is achieved, being a success, but still not enough to clearly resolve spin flips in one single frequency measurement.

### *7.5.2 Origin of Axial Frequency Drifts*

In numerous test experiments no correlation of the frequency fluctuation to an external parameter as temperature, pressure in the liquid-He and liquid-$N_2$ reservoirs of the magnet, vibrations of the cryo-cooler, or voltage fluctuation of the DC supply biasing of the trap electrodes was found. In one of these test experiments the Co/Fe ring electrode of the analysis trap was replaced by a copper electrode, leading to a frequency stability which agrees with the fluctuations of the DC voltage supply, and which was also achieved in section 6.5 in case of the precision trap. From these test experiments it is concluded, that the axial

frequency fluctuation is due to the strong coupling of the radial angular momentum to the axial mode, by means of the magnetic bottle $B_2$. A change of the radial energy by only 12 mK changes $\nu_z$ already by 1 Hz. Spurious heating of the radial mode by background noise may be responsible for the axial frequency drifts.

Having clearly identified the strong magnetic bottle as the origin of the frequency drifts,

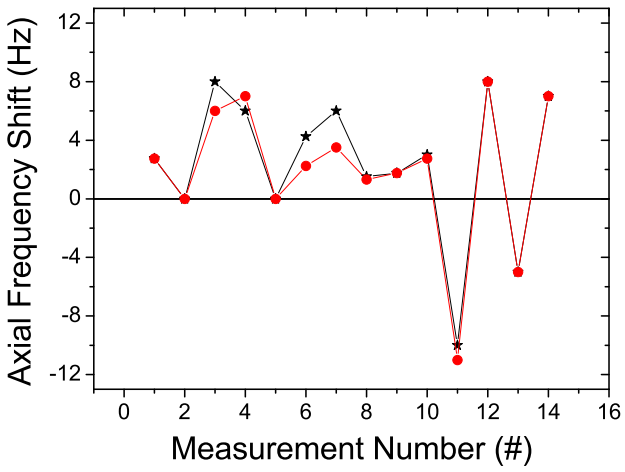


Figure 7.13: Every data point represents the axial frequency shift after a 12 h drift measurement. The filled stars are the shifts $\nu_{z,\mathrm{stop}} - \nu_{z,0}$ while the filled circles indicate difference between the start frequency and the frequency after re-cooling the magnetron mode $\nu_{z,\mathrm{re}} - \nu_{z,0}$. These results allow the conclusion, that the axial frequency drifts are mainly caused by variation of the cyclotron energy.

it was investigated, whether the axial frequency fluctuation is caused by heating of the cyclotron- or the magnetron mode. For this purpose, the magnetron mode of the proton was feedback-cooled to the minimum possible temperature indicated by the Boltzmann cut-off. Then a frequency drift was recorded for $\approx 12$ h. Afterwards the magnetron mode was re-cooled. In such a sequence the start frequency $\nu_{z,0}$, the stop frequency $\nu_{z,\mathrm{stop}}$ and the frequency after re-cooling $\nu_{z,\mathrm{re}}$ are recorded. If the magnetron mode causes the frequency drifts it should be possible to prepare the particle to its initial frequency $\nu_{z,\mathrm{re}} = \nu_{z,0}$. If the fluctuations are due to heating of the cyclotron mode, magnetron cooling will not affect the frequency $\nu_{z,\mathrm{stop}} = \nu_{z,\mathrm{re}}$. If the drifts are due to heating of both modes the proton cannot be

prepared to its initial state. The stop frequency $\nu_{z,\mathrm{stop}}$ will neither be equal to the frequency $\nu_{z,\mathrm{re}}$ after re-cooling of the magnetron mode nor the start frequency $\nu_{z,0}$. The experimental results for fourteen independent 12 h drift records are shown in Fig. 7.13. The filled stars indicate the difference $\nu_{z,\mathrm{stop}} - \nu_{z,0}$ while the filled circles show $\nu_{z,\mathrm{re}} - \nu_{z,0}$. Obviously, in most of the experimental sequences $\nu_{z,\mathrm{stop}} = \nu_{z,\mathrm{re}}$, indicating that the observed axial frequency fluctuations are due to heating of the cyclotron mode.

### *7.5.3 Investigation of Averaging Time*

In section 6.5 it was discussed that the measured axial frequency fluctuation is a function of the FFT averaging time $\Delta t_{\mathrm{FFT}}$. With increasing time the fluctuation decreases due to averaging. On the other hand, long term drifts cause an increase of fluctuation with time. To achieve smallest frequency fluctuation, $\Xi(t)$ is measured. The particle is prepared to the lowest temperature bin of the respective radial mode. The results are shown in Fig. 7.14. With increasing averaging time the fluctuation decreases to a minimum of 150 mHz at an averaging time of $\Delta t_{\mathrm{opt}} = 100\,\mathrm{s}$. Afterwards an increase of $\Xi(t)$ is observed being much steeper as in case of the precision trap. The dashed red line with the negative slope is due to a simulation which models the fluctuation $\Xi_{\mathrm{FFT}}$ caused by averaging.

To achieve a detailed understanding of the increase of $\Xi(t)$ above the minimum, the axial frequency drift caused by cyclotron quantum-noise was simulated. One cyclotron quantum jump $n_+ = \pm 1$ changes the axial frequency $\nu_z$ by $\Delta\nu_{z,+} = 68\,\mathrm{mHz}$. In the simulation the transition rate per second $p_{\mathrm{cyc}}$ is combined with a random-number generator which defines the sign of a quantum jump. Based on that simulation, the fluctuation $\Xi_{\mathrm{cyc}}(t, p_{\mathrm{cyc}})$ is evaluated. The blue dotted line with the increasing slope is a simulation result corresponding to a cyclotron transition rate of $p_{\mathrm{cyc}} = 0.035$ per second. The solid green line is the statistical sum $\Xi_{\mathrm{tot}}(t) = \sqrt{\Xi_{\mathrm{FFT}}(t)^2 + \Xi_{\mathrm{cyc}}(t, p_{\mathrm{cyc}})^2}$ of both effects, which obviously fits the measured data perfectly. With these agreements, a semi-quantitative understanding of the axial frequency drifts is obtained.

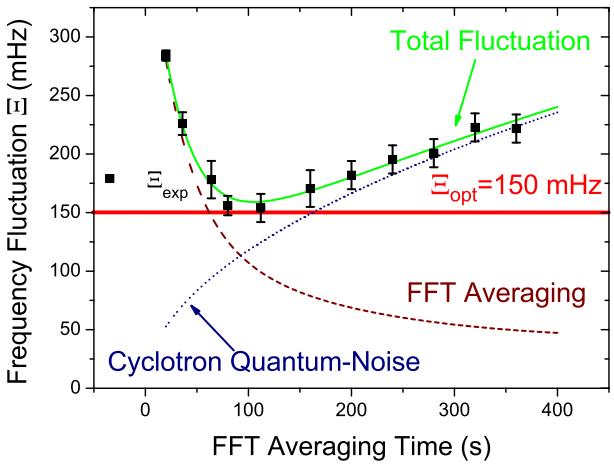


Figure 7.14: Axial frequency fluctuation in the analysis trap as a function of the FFT averaging time. For details see text.

### *7.6 Axial Frequency Fluctuation as a Function of the Cyclotron Temperature*

To obtain an even more detailed understanding of the processes behind the fluctuation, $\Xi$ in presence of cyclotron quantum jumps is calculated. Assume, that for the evaluation of the fluctuation the measuring interval is so small, that maximally one cyclotron quantum jump occurs per cycle, and let $N$ be the number of measuring sequences, furthermore $\bar{\alpha} = 0$ (see section 6.5). Then the fluctuation caused by noise-induced cyclotron transitions is

$$\Xi_{\mathrm{cyc}} = \sqrt{\frac{1}{N}\sum_{k}^{N}(\nu_{z,k} + \Delta\nu_{z,+} - \nu_{z,k})^2} = \sqrt{\frac{1}{N}\sum_{k}^{N}\Delta\nu_{z,+}^2}\ . \tag{7.10}$$

Let us now assume that in $M$ out of $N$ sequences a cyclotron quantum jump occurred, then

$$\Xi_{\mathrm{cyc}} = \sqrt{\frac{1}{N}\left(\sum_{k}^{M}\Delta\nu_{z,+}^2\right)} = \sqrt{p_{\mathrm{cyc}}\Delta\nu_{z,+}^2}\ . \tag{7.11}$$

Scaling the cyclotron transition rate $p_{\mathrm{cyc}}$ to seconds, this can be expressed as

$$\Xi_{\mathrm{cyc}}(t, p_{\mathrm{cyc}}) = \sqrt{p_{\mathrm{cyc}} t \Delta\nu_{z,+}^2}\ . \tag{7.12}$$

The important takeaway information of this calculation is, that due to statistical averaging a linear increase of the originating physical effect $p_{\mathrm{cyc}}$ would lead to a scaling of the correlated

fluctuation with the square-root of the effect $\sqrt{p_{\mathrm{cyc}}}$. Combined with the calibration of the cyclotron energy $E_+$ described in section 7.4 the behavior of the fluctuation as a function of the cyclotron energy is investigated. To record the axial frequency fluctuation as a function

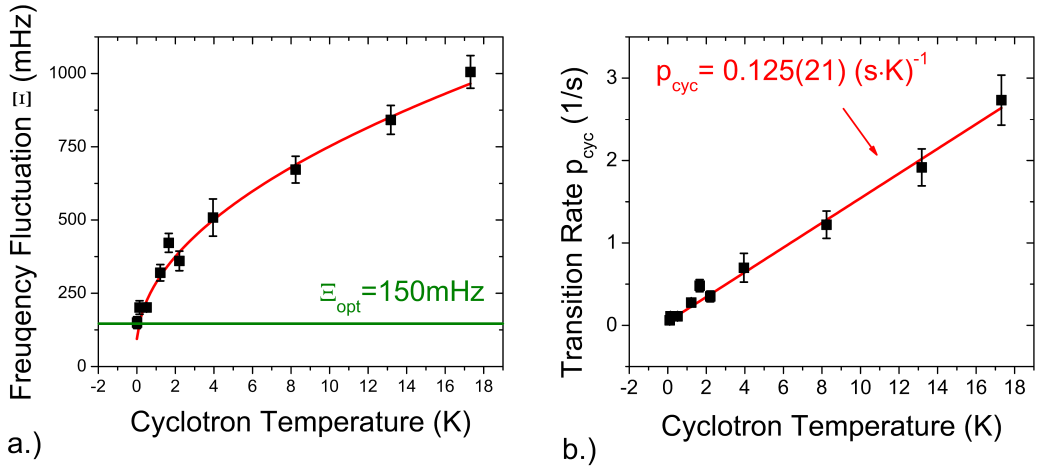


Figure 7.15: a.) Axial frequency fluctuation as a function of the cyclotron temperature. b.) Cyclotron transition rate $p_{\mathrm{cyc}}$ as a function of the cyclotron temperature.

of the cyclotron energy, $E_+$ of the proton is prepared to a certain value and frequency drift measurements $\nu_z(t)$ are recorded for 8 to 10 hours, which was found to be a time interval giving reproduceable information. The measurement was performed at an averaging time of 100 s. The results are shown in Fig. 7.15 a.). The filled squares represent the data, while the red solid line is due to a power-1/2-fit. The axial frequency fluctuation scales exactly with the square-root of the mode temperature, and thus, the cyclotron transition rate $p_{\mathrm{cyc}}$ linearly with $T_+$. From the fit, a transition rate of $p_{\mathrm{cyc}} = 0.125(21)\cdot(\mathrm{s}\cdot\mathrm{K})^{-1}$ is obtained. This linear scaling with temperature can be understood in the framework of quantum mechanics. The transition amplitude between two eigenstates $|n_+\rangle$ and $|n_+ \pm 1\rangle$ of a harmonic oscillator in presence of a driving field with amplitude $E_0$ is given by

$$\Gamma_{n_+ \to n_+ \pm 1} = \langle n_+ | q E_0 \rho_+ | n_+ \pm 1 \rangle \ . \tag{7.13}$$

This matrix element can be evaluated easily using the explicit Hermite-polynomial representation of the eigenstates giving the results

$$\Gamma_{n_+\to n_+ +1} = qE_0\sqrt{\frac{\hbar}{m\omega_+}}\sqrt{\frac{n+1}{2}} \tag{7.14}$$

$$\Gamma_{n_+\to n_+ -1} = qE_0\sqrt{\frac{\hbar}{m\omega_+}}\sqrt{\frac{n}{2}}\,. \tag{7.15}$$

The transition rate $p_{\mathrm{cyc}}$ scales $\propto \Gamma^2_{i\to f}$, and thus, the linear scaling of $p_{cyc}$ with temperature, which is shown in Fig. 7.15 b.), may be a direct picture of the quantum mechanical aspects of the cyclotron mode of the single trapped proton.

For a mathematically correct and detailed discussion of a noise-driven quantum mechanical oscillator, the quantum-Langevin equation has to be solved, which is beyond the scope of this thesis. To get more precise idea of the hypothetic drive amplitude, some simplifying assumptions are made:

- The energy levels of the cyclotron harmonic oscillator can be assumed to be a continuum;
- The drive is due to broadband noise;
- The effect of the drive is constant in a frequency window given by the linewidth parameter $\Delta_+ = \frac{1}{2\pi}\frac{e}{m}\frac{B_2}{B_0}\langle z^2\rangle \approx 17\,\mathrm{kHz}$ of the cyclotron resonance curve [49], where $\langle z^2\rangle$ is the expectation value of the axial amplitude-square for $T_z = 9.5\,\mathrm{K}$.

Under these assumptions it is possible to use Fermi's *golden rule*

$$p_{\mathrm{cyc}} = \Delta_+ \frac{2\pi}{\hbar}\rho_f(E_+)\Gamma^2_{i\to f} \tag{7.16}$$

for further discussion, where $\rho_f(E_+) = 1/\hbar\omega_+ = \text{const.}$ is the constant density of states of the one-dimensional harmonic oscillator. Combining the golden rule with Eq. (7.14) and Eq. (7.15), and the experimental result for the cyclotron transition rate $p_{\mathrm{cyc}}$, the amplitude of the broadband "noise-drive" can be evaluated and

$$E_0 = 210(10)\,\mathrm{pV}/(\mathrm{m}\cdot\sqrt{\mathrm{Hz}}) \tag{7.17}$$

is obtained. The thermal noise generated by a resistor of 200 Ω has an rms voltage-amplitude of 200 pV/$\sqrt{\text{Hz}}$ at a temperature of 4 K. This illustrates the incomparable sensitivity of our experiment and how challenging it is, in fact, to stabilize the axial frequency.

### *7.7 Axial Frequency Fluctuation as a Function of the Axial Temperature*

If the simple model-assumptions discussed in the previous section fit the experimental reality, the fluctuation should decrease with the square-root of the axial temperature $T_z$, since the linewidth of the cyclotron resonance decreases linearly with $T_z$. For the measurement of $\Xi(T_z)$, the proton was prepared to the lowest cyclotron-temperature bin and the fluctuation was measured for different axial temperatures. To avoid that the fluctuation which is due to analyzer averaging modifies the experimental results, a long averaging time $\Delta t_{\text{FFT}} = 300\,\text{s}$ was used. For such long times the fluctuation $\Xi_{\text{FFT}}$, which is due to averaging, has already converged below 50 mHz, and has not to be taken into account anymore. The results are

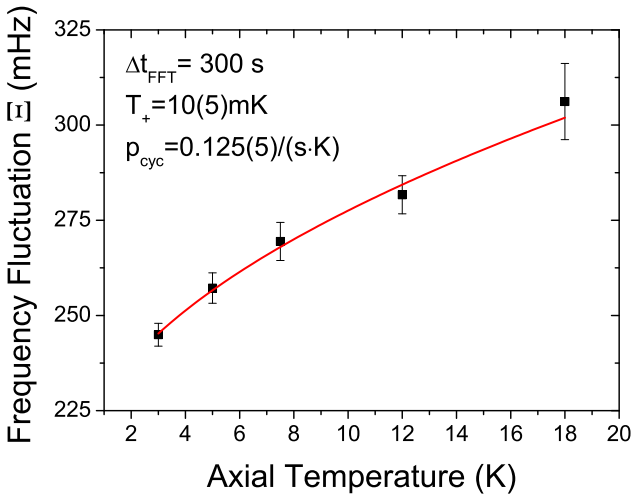


Figure 7.16: Axial frequency fluctuation as a function of the axial temperature. The cyclotron transition rate $p_{\text{cyc}}$ was extracted in section 7.6. For further discussion see text

shown in Fig. 7.16. The scaling of the axial frequency fluctuation behaves exactly as predicted. Decreasing the axial temperature leads to a reduction of the frequency fluctuation with the square-root of the axial temperature $T_z$. Unfortunately, reduction of the axial

temperature $T_z$ also leads to a decrease of the signal-to-noise ratio. To achieve the same frequency resolution in case of worse signal-to-noise ratio, the averaging time has to be increased. Both effects compensate almost exactly and, thus, by reduction of axial temperature the best achievable frequency fluctuation only decreases slightly. The results of two $\Xi(t)$ measurements are shown in Fig. 7.17[4]. The red filled squares correspond to an axial temperature of $T_z = 9.5\,\mathrm{K}$ while the blue filled circles are due to $T_z = 2.2\,\mathrm{K}$. In case of the lower temperature, the positive slope towards longer averaging times is decreased. The minimum fluctuation of both data sets is identical within the error bars.

Thus, a very important step for the experiment is the improvement of the axial detection systems, which is already in preparation [79]. With the new detection systems, the axial frequency can be measured at higher signal-to-noise ratio and lower temperature. Due to the

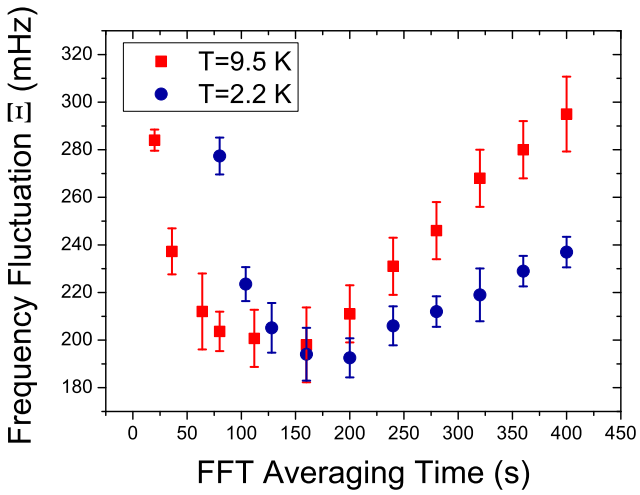


Figure 7.17: Axial frequency fluctuation as a function of time. The red filled squares correspond to $T_z = 9.5\,\mathrm{K}$, while the blue filled circles are recorded at $T_z = 2.2\,\mathrm{K}$. Decreasing the axial temperature reduces the cyclotron transition rate $p_{\mathrm{cyc}}$. Unfortunately the axial temperature reduction also reduces the signal-to-noise ratio. Thus, the fluctuation due to averaging is increased. Both effects compensate.

scaling of the fluctuation with the axial temperature, the phase-sensitive detection method

[4]The results are for slightly higher cyclotron temperature as in Fig. 7.14, thus, $\Xi_{\mathrm{min}} > 150\,\mathrm{mHz}$.

was up to now not applied in the analysis trap, and we concentrated on noise-dip detection.

### *7.8 Chapter-Conclusion*

In this chapter storage and detection of a single proton in a magnetic bottle of $B_2 = 3.030(75)\cdot 10^5\ \mathrm{T/m^2}$ was demonstrated. The axial frequency of the single proton stored in the magnetic bottle trap was stabilized to an axial frequency fluctuation of $\Xi = 150\,\mathrm{mHz}$. This is still not small enough to resolve a spin flip in the analysis trap in only one single experiment, but its is sufficiently stable to resolve spin flips in a series of statistical measurements, and thus, opens the way to a $g$-factor determination in the analysis trap, as will be shown in the next chapter.

# Chapter 8

# FIRST PROTON SPIN FLIPS EVER OBSERVED

In the previous chapter the optimization of the FFT averaging time $t_{\mathrm{FFT}}$ was described resulting in a minimum background fluctuation $\Xi_{\mathrm{back}} = 150\,\mathrm{mHz}$ at $t_{\mathrm{FFT}} \approx 80\,\mathrm{s}$. This value is not yet sufficiently stable to detect spin flips directly in one measurement sequence as described in chapter 2. However, averaging can be used to detect proton spin flips in a series of statistical measurements, which will be shown in this chapter. The data presented here are the crowning result of five years of dedicated lab-work. For the first time spin-flip transitions of a nuclear magnetic moment were detected. The content of the chapter is summarized in [33].

## *8.1 Driving Spin Flips*

Spin-flip transitions are driven using a disc coil mounted close to the electrode stack as shown in Fig. 8.1. The coil generates a transverse magnetic rf-field $\vec{b}_{\mathrm{rf}}$ with frequency $\nu_{\mathrm{rf}}$. To drive spin flips, the rf-drive is tuned near the Larmor frequency $\nu_{\mathrm{L}} = g_{\mathrm{p}}\nu_c/2$. This rf-field causes a precession of the proton spin around the $\vec{b}_{\mathrm{rf}}$-axis at the Rabi frequency $\Omega_R/2\pi = \nu_{\mathrm{L}} b_{\mathrm{rf}}/B_0$. In the presence of the strong magnetic bottle $B_2$ the spin-flip probability is given by [49]

$$P_{\mathrm{SF}} = \frac{1}{2}\left(1 - \exp\left(-\frac{1}{2}\Omega_R^2 t_0\ \chi(2\pi\nu_{\mathrm{rf}}, T_z)\right)\right)\ , \tag{8.1}$$

as explained in chapter 2. Since the trap is machined of copper, the magnetic field generated by the coil is shielded by the electrodes. In [60] comprehensive test experiments are described with the conclusion, that the amount of magnetic field strength which is guided to the trap center by means of the slits between the trap electrodes is large enough to drive spin transitions. An rf-power of 27 dBm causes an rf-amplitude of $b_{\mathrm{rf}} \approx 2.5\,\mu\mathrm{T}$ in the center of the trap.

This relatively high power is generated with an rf-synthesizer (Rohde und Schwarz SMY-02) and amplified with a power amplifier (Rohde und Schwarz HVV10). In first spin-flip

test experiments it was found, that the background noise of the power amplifier heats the cyclotron motion of the proton, leading to axial frequency shifts in the range of some Hz. Therefore, in the signal lines bandpass filters are used, which attenuate the signal at the cyclotron frequency $\nu_+$ about 100 dB, and at $2\nu_+$ still by 50 dB. Moreover, the signal line is connected to ground with an rf-relay whenever possible. After this optimization, the spurious effects of the rf-synthesizer noise on the axial frequency stability was not visible anymore.

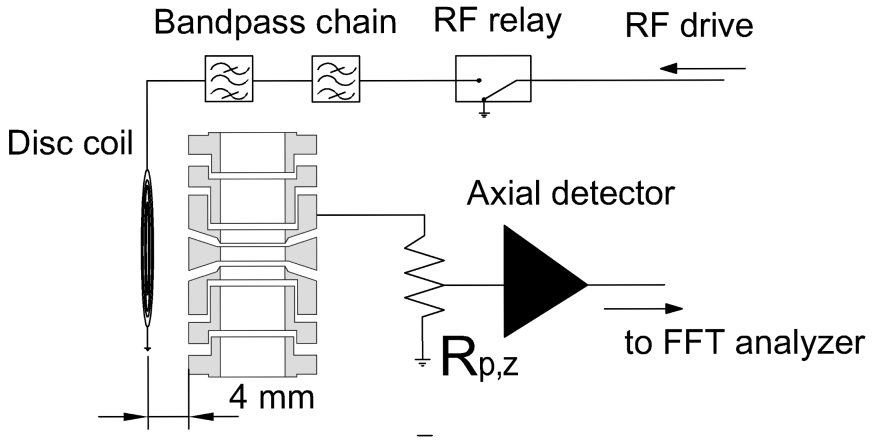


Figure 8.1: Schematic of the experimental setup to drive a spin flip. A disc coil is fixed near the trap, irradiating the magnetic rf-field with amplitude $b_{rf}$. The signal is guided through a chain of band pass filters attenuating the rf-field on the cyclotron frequency by $\approx 100$ dB. During the axial frequency measuring time, the line is connected to ground with a rf-relay.

### *8.2 Measuring Sequence*

For a statistical detection of spin flips the averaging time of the FFT analyzer is tuned to $\Delta t_{\rm opt}$. Then the axial frequency $\nu_z$ is determined in sequences of three measurements $\nu_{z,1}$, $\nu_{z,2}$, and $\nu_{z,3}$. as shown in Fig. 8.2 a.). Between the first and the second measurement, a spin-flip drive is turned on near the Larmor frequency Between the second and the third measurement, the rf-synthesizer is tuned to a reference frequency 100 kHz below $\nu_{\rm L}$, which is about one linewidth of the saturated proton Larmor resonance. Between the third and the first measurement of the following cycle $\nu_{z,1'}$, no rf-signal is applied to the trap. This

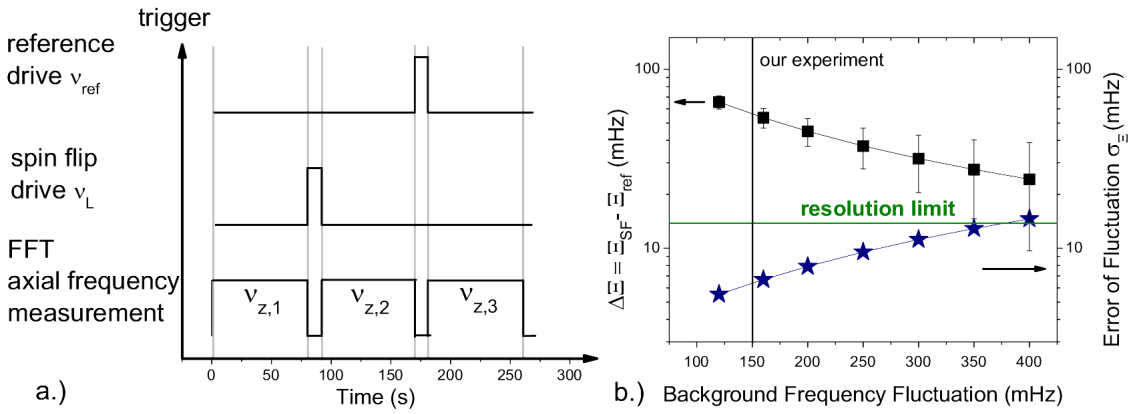


Figure 8.2: a.) Measuring sequence for spin flip detection. For details see text. b.) Result of example calculation for $N = 250$ measuring cycles: Shift of the fluctuation $\Delta\Xi = \Xi_{\rm SF} - \Xi_{\rm ref}$ (filled squares) as a function of the size of the background fluctuations $\Xi_{\rm back}$. The filled stars represent the errors $\sigma_{\Delta\Xi}$. A resolution limit is achieved, if the error is of the same size as the frequency shift. The conditions of our experiment are indicated by the black vertical line.

sequence is repeated for several hundred times and the fluctuations $\Xi_{\rm SF} = \nu_{z,2} - \nu_{z,1}$, $\Xi_{\rm ref} = \nu_{z,3} - \nu_{z,2}$ and $\Xi_{\rm back} = \nu_{z,1'} - \nu_{z,3}$ are evaluated. If spin flips are driven, the corresponding axial frequency shifts $\Delta\nu_{\rm z,SF}$ due to the continuous Stern-Gerlach effect add up in a statistical way. If the spin of the proton flips in $M$ cycles out of $N$, the total fluctuation is

$$\begin{aligned} \Xi_{\rm SF} &= \sqrt{\sum_i^M \frac{(\alpha_i \pm \Delta\nu_{z,SF} - \bar{\alpha})^2}{N-1} + \sum_{i=M}^N \frac{(\alpha_i - \bar{\alpha})^2}{N-1}} \\ &\approx \sqrt{\Xi_{back}^2 + P_{SF}\Delta\nu_{z,SF}^2}\ , \end{aligned} \tag{8.2}$$

where $P_{\rm SF}$ is given by Eq.(8.1). The comparison of $\Xi_{\rm ref}$ and $\Xi_{\rm back}$ is a means to test for spurious heating of the cyclotron motion due to rf-synthesizer noise. If both quantities are the same within error bars, this indicates, that the cyclotron motion is not affected and that an increase of $\Xi$ is due to proton spin flips. A resolution limit for the detection of spin flips by this method is reached if the error $\sigma_{\Delta\Xi} = ((\Xi_{\rm ref}/\sqrt{2N-2})^2 + (\Xi_{\rm SF}/\sqrt{2N-2})^2)^{0.5}$ [110] is of the same size as the frequency shift $\Delta\Xi = \Xi_{\rm SF} - \Xi_{\rm ref}$ which is shown in Fig. 8.2 b.) for an example calculation with $N = 250$. The conditions of our experiment are indicated

by the black solid line. For $P_{\mathrm{SF}} = 50\,\%$ $\Delta\Xi = 52\,\mathrm{mHz}$ are expected. This shows that it is possible to statistically detect spin flips with the proposed measuring sequence in a series of only fifty measurement cycles.

### *8.3 Results - First Proton Spin Flips Ever Observed*

In the experiment, the proposed sequence is repeated several hundred times. To drive spin flips, $\nu_{\mathrm{rf}} = 50.120\,\mathrm{MHz}$ is irradiated, and for the reference measurement, a frequency $\approx 100\,\mathrm{kHz}$ below. Then the frequency fluctuations $\Xi_{\mathrm{SF}}$ and $\Xi_{\mathrm{ref}}$ are determined. The evolution of both quantities as a function of measurement cycles is shown in Fig. 8.3 a.) along with a confidence band given by $\sigma_{\Delta\Xi}$. Obviously, both fluctuations converge for large measuring times to nearly constant values. A significant shift of $\Delta\Xi = 47\,\mathrm{mHz}$ between the reference measurement $\Xi_{\mathrm{ref}}$ and the resonant measurement $\Xi_{\mathrm{SF}}$ is observed. This clearly indicates, that spin flips are detected in the experiment. Using Eq. (8.2), we find that the average spin-flip probability is $P_{\mathrm{SF}} = 47 \pm 7\,\%$. The data set has also been analyzed

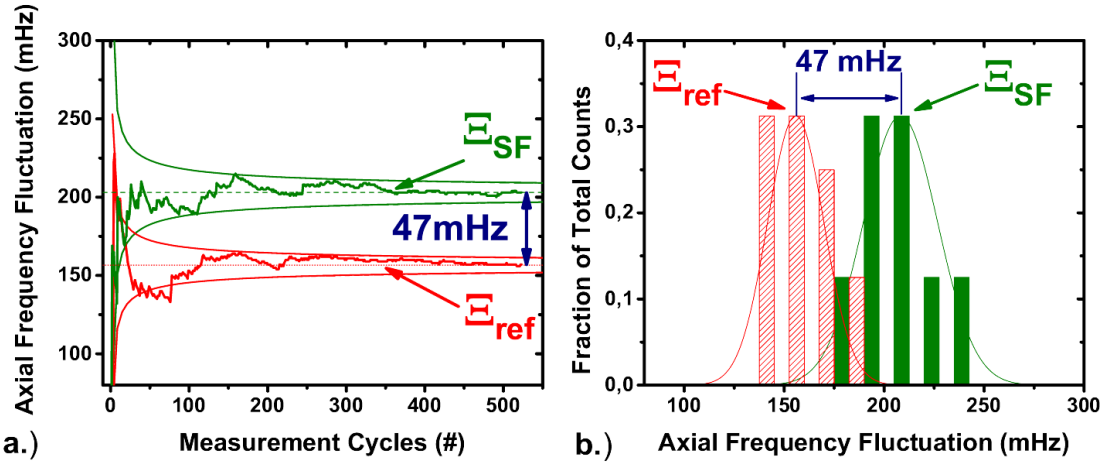


Figure 8.3: a.) Evolution of the mean values of the frequency fluctuations $\Xi_{SF}$ and $\Xi_{ref}$ as a function of measuring time. Both values converge with increasing measuring time leading to $\Delta\Xi = \Xi_{SF} - \Xi_{ref} = 47 \pm 4.5\,\mathrm{mHz}$ corresponding to a spin flip probability $p_{SF} = 47 \pm 7\,\%$. b.) The whole measurement sequence of 800 data points was separated in subsequences of 50 measurements and binned to two histograms. The hatched histogram shows the results for the reference measurement, the filled histogram represents the data points with spin flip drive.

in a different way. The whole sequence of 800 data points is split into subsequences of 50 measurements. For every subsequence $\Xi_{\mathrm{SF}}$ and $\Xi_{\mathrm{ref}}$ are determined and binned into histograms. Figure 8.3 b.) shows a distinct splitting between both distributions. This clearly shows, again, that proton spin flips are detected. This second evaluation resets the starting point of the sequence arbitrarily and assures, that the first result is not due to a statistical accident.

A spin flip resonance of the proton in the analysis trap has been measured by tuning $\nu_{\mathrm{rf}}$ in steps across the Larmor frequency $\nu_{\mathrm{L}}$. For every frequency point the measuring procedure described above is performed, the data are analyzed as above and the corresponding spin-flip probability $P_{\mathrm{SF}}$ is determined. Figure 8.4 presents the spin-flip resonance. Below the Larmor frequency, the spin-flip probability equals to zero. Then, the spin-flip probability increases "instantaneously" to $P_{\mathrm{SF}} = 50\,\%$, which is due to the Boltzmann distribution of the axial temperature $T_z$ (see section 2.6.1). The solid line is a best fit of Eq. (8.1) to the

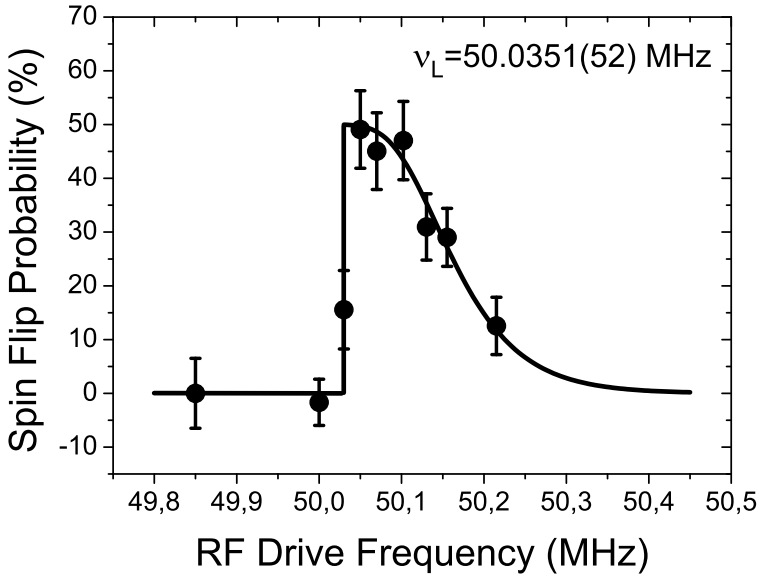


Figure 8.4: Proton spin flip resonance in the analysis trap with its inhomogeneous magnetic field.

data, where Eq. (2.54) was used for the lineshape $\chi(2\pi\nu_{\mathrm{rf}}, T_z)$. Fixed parameters are the

irradiation time $t_0 = 10\,\mathrm{s}$ and the axial temperature of $T_z = 9.5\,\mathrm{K}$, which has been measured independently (see section 7.4). Free fit parameters are the amplitude $b_{\mathrm{rf}}$ of the magnetic rf-field which comes out as $2.5\,\mu\mathrm{T}$, and the Larmor frequency $\nu_{\mathrm{L}}$. From the fit, the Larmor frequency $\nu_L = 50.0351(55)\,\mathrm{MHz}$ is yielded, corresponding to a relative precision of $1{\cdot}10^{-4}$, already. Figure 8.4 thus demonstrates, again, that proton spin flips were detected. For the determination of the $g$-factor, a high-resolution measurement of the free cyclotron frequency $\nu_c$ is required. The development of techniques to measure $\nu_c$ in the magnetic bottle with higher resolution as described in section 7.3 is in progress [47].

The data shown in Fig. 8.4 show a linewidth of about 120 kHz, which is due to saturation broadening. Based on the parameters obtained from the fit, new parameters can be derived to obtain optimum Larmor-frequency resolution (as explained in section 2.6.1). Currently an experiment with an irradiation time of one second at an axial temperature of about 2 K is running. A very promising first result obtained from that experiment shows a linewidth below 10 kHz, corresponding to a narrowing of the linewith by more than one order of magnitude. Compared to the data presented here, by that experiment the Larmor-frequency resolution should be increased to the ppm level. The results will be presented in [47].

### *8.4 Direct Observation of Spin Flips*

As shown in Fig. 8.4 b.), the axial frequency fluctuation $\Xi$ itself shows a Gaussian distribution. During the thesis writing period my colleagues Cricia Rodeqheri, Holger Kracke and Andreas Mooser decreased the average value of the axial frequency fluctuation by another 25 mHz. In their measuring sequences, time windows of about 1 h occur, where the background fluctuation is only about 100 mHz or better. Under such constraints, the direct observation of spin flips becomes possible. Figure 8.5 shows the axial frequency as a function of time. In this sequence, the axial temperature of the particle is feedback-cooled to $T_z \approx 2\,\mathrm{K}$, and the spin-flip drive is turned on for one second and with the settings described in the previous section. The resonance frequency is detuned from the Larmor frequency, such that the spin-flip probability is $p_{SF} = 10\,\%$. After every green filled-circle data point the spin-flip drive is turned on. At $t = 38\,\mathrm{min}$ the average axial frequency level shifts by 200 mHz, which may be due to a proton spin-flip.

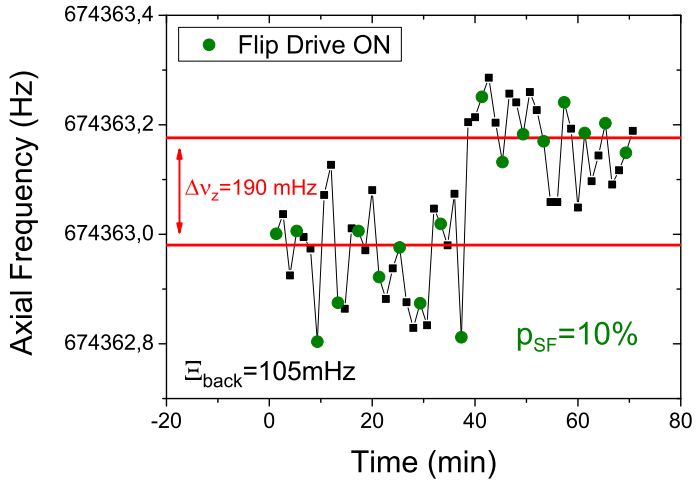


Figure 8.5: Axial frequency as a function of time. After the data points which are indicated by the green filled circles, a spin flip drive was turned on. After the drive at $t = 38\,\mathrm{min}$ the average axial frequency level changes by about 190 mHz, which may be due to a spin flip.

In the current status of the experiment, these regions can be observed once per day and only if the proton in the analysis trap is prepared in both radial modes to "zero temperature". This is still not sufficiently stable for a "traditional" $g$-factor measuring sequence, but it shows, that the apparatus is being developed continuously, and the required limit to achieve direct spin-flip resolution has already been reached in rare cases.

# Chapter 9

# CONCLUSION AND OUTLOOK

## *9.1 Achievements*

In this PhD-thesis, the very first observation of spin flips with a single trapped proton was presented. This is the most important milestone for the direct $g$-factor measurement of the free proton.

This experimental success is based on the setup and consequent improvement of a cryogenic double-Penning trap apparatus over years of experimental work. The fundament was built by developing highly-sensitive single-particle detection systems with outstanding quality. With these detection systems the resolution of one individual proton stored in a Penning trap with a superimposed magnetic bottle of $B_2 = 3.030(75) \cdot 10^5$ T/m$^2$ was achieved. Controlled charged particle storage under such extreme magnetic conditions has never been demonstrated before. Despite of the challenging experimental constraints arising from the large magnetic field inhomogeneity, experimental methods were developed to stabilize the axial eigenfrequency of the proton in the magnetic bottle trap. A new detection scheme allowing spin flip resolution in a series of statistical measurements was proposed and applied. The resulting data provide convincing evidence for the direct detection of single-proton spin flips. Based on these measurements a Larmor resonance curve was recorded, yielding the Larmor frequency of the free proton with a relative precision of $1 \cdot 10^{-4}$, already. Experimental methods were developed allowing further improvement to the ppm-level within the next months of experimental operation.

Besides this main objective, novel experimental methods were developed which may be applied routinely in future high-precision Penning trap experiments. The single trapped proton was used as an electro-mechanical probe to measure trap imperfections. Utilizing the remarkable understanding of the Penning trap potential, the axial, as well as the mag-

netron energy of the proton were calibrated, and the temperature $T_z$ of the axial detection system was measured as an array average. By means of the magnetic bottle, $T_z$ was measured as a time average. Both temperatures are identical within their errors, which can be understood as an experimental proof of the ergodic hypothesis, based on measurements with one single particle.

A novel technique was developed, allowing the simultaneous measurement of all eigenfrequencies of the trapped proton in one experimental run. The method is based on the simultaneous sideband-coupling of both radial oscillation modes to the axial mode by means of a "classical double-dressing", which has never been applied before. With that technique a cyclotron frequency measurement of the trapped proton at the level of 4 ppb was demonstrated.

These research achievements are crucially important steps towards a high-precision comparison of the $g$-factor of the proton and the antiproton. This will provide a new high-precision test of the $CPT$-symmetry in the baryon sector. All techniques developed in the framework of this thesis can be directly applied to the antiproton, and are important steps towards the improvement of the current precision by a factor of $10^6$.

## *9.2 Future Issues*

### *9.2.1 Cryo-Liquid Bath-Cryostat*

For the measurement of the $g$-factor with a relative precision of $\frac{\delta g_p}{g_p} = 10^{-9}$, the free cyclotron frequency $\nu_c$ of the trapped proton has to be determined at that level in the precision trap of the double-Penning trap stack. Currently, the precision is limited by magnetic field fluctuations, induced by the vibrations of the pulse tube cooler, which provides the cryogenic temperatures (see chapter 3). Therefore, the pulse tube cooler will be replaced by a cryo-liquid bath cryostat in the near future. This would increase the stability of the cyclotron frequency by orders of magnitude [26], which will lead to a very promising perspective - cyclotron noise-dip detection.

### *9.2.2 Cyclotron Noise-Dip Detection*

The effects limiting the performance of the cyclotron detection system were analyzed in detail in chapter 4. A further improvement of the detection system by about a factor of four is possible. This will lead to a cooling time constant of $\tau_+ = 3.75\,\mathrm{s}$. Increasing the temperature of the improved detections system by means of positively phased feedback, together with the increased stability of the magnetic field, cyclotron noise-dip detection becomes possible. If cyclotron noise-dip resolution is achieved, the axial frequency as well as the cyclotron frequency can be measured in thermal equilibrium simultaneously. The time required for a $g$-factor measuring sequence will decrease by a factor of 2 (see section 2.7), since frequency measurements do not have to be carried out sequentially anymore. Moreover, the frequency of the cyclotron noise-dip is defined by the field of the superconducting magnet. Naturally a frequency defined by a superconductor is much more stable as a frequency defined by a DC-voltage source [111]. Thus, achieving cyclotron noise-dip resolution with one single proton is one of the most desirable aims towards an ultra-high precision determination of the $g$-factor of the free proton. As soon as the axial frequency is stabilized to a level, where direct spin-flip resolution is possible, this will be a next experimental step of crucial importance. In [23, 24, 25] it is claimed, that the achieved $g$-factor resolution (about 0.5 ppb) is due to magnetic field and voltage drifts. A reduction of the measuring time by a factor of two, based on the simultaneous measurement of both eigenfrequencies, both in thermal equilibrium with the respective detection system, would increase the precision at least by a factor of $\sqrt{2}$. But, since the cyclotron frequency is observed directly, and the frequency is defined by the highly stable superconducting magnet, an even better improvement can be expected. A cyclotron noise-dip has never been observed, and thus, its detection is also of fundamental interest. To my personal opinion, this is one of the future "hot-topics" in Penning trap physics, especially if it would be resolved for the first time with a charge-one particle as the proton.

Historically, the design of the precision trap of the current setup is based on [23, 24, 25]. There, traps with an inner radius of 3.5 mm were used, and for the precision trap this geometry was adopted [53]. In the work presented here, single proton resolution in a Penning

trap with an inner radius of 1.8 mm was demonstrated. In a trap with such a small diameter, the effective electrode distance for cyclotron pick-up (see section 4.4) would be about 5 mm. Combined with the cyclotron detection system set up in this thesis, and with the improvements proposed in chapter 4, in such a small trap a cyclotron dip will have a linewidth of 250 mHz already and dip-detection becomes possible at 4 K. For an ultrahigh-precision $g$-factor measurement of the free proton, cyclotron noise-dip detection would be a crucially important development, and in the long-term, a smaller trap should be designed and the cyclotron detection system should be improved to achieve this aim.

### *9.2.3 Self-Shielding Coil*

If cyclotron noise-dip detection will be achieved, a next issue would be the stabilization of the superconducting magnet. An idea, being as brilliant as simple, was introduced by G. Gabrielse, the self shielding coil [113]. A shorted superconductor is introduced to the apparatus. A coil geometry can be found which exactly compensates the fluctuation of the external magnetic field (Lenz' law). This idea was taken up and adopted by S. Sturm and A. Wagner and applied at the highly charged ion experiment at Mainz [112]. It would improve the proton $g$-factor experiment also.

### *9.2.4 Axial Detection System*

As pointed out in chapter 7, the axial frequency fluctuation will decrease if detection systems with even higher quality will be used. In the framework of the PhD-thesis of Andreas Mooser [79] new axial frequency detectors were set up. These new detection systems are based on toroidal inductors, which have a smaller geometry at a higher performance. Currently only one axial frequency detection system is used in the experiment, which is connected to both traps. This limits the performance due to small inductances and parasitic losses (see chapter 4). With the smaller geometry, two axial frequency detection systems with higher inductance and higher quality factors can be used in future experimental runs. With these detection systems faster measuring cycles are possible and direct spin-flip resolution may be achieved.

### *9.2.5 Faraday-Cage*

A tiny background noise amplitude of only $200\,\mathrm{pV}/(\mathrm{m}\sqrt{\mathrm{Hz}})$ may be responsible for the drive of the cyclotron frequency. Therefore, the whole apparatus may be placed in a closed faraday-cage in the future. The ground should be filtered by cabin ground-filters. This would reduce the electrical interference liability of the whole apparatus. Especially with the perspective towards a high-precision $g$-factor measurement, where complex measuring sequences will be applied, and the apparatus has be connected to a multitude of rf-generators, switches, timing-units etc. (see f. e. section 6.12), this would be a crucially important improvement of the experimental setup.

### *9.2.6 Magnet-Tuning*

If the required axial frequency stability would not be achieved by these technical improvements, as a next step I would suggest to tune the superconducting magnet to a higher magnetic field $B_0$. Since the axial frequency shift $\Delta\nu_{\mathrm{z,SF}}$ caused by a proton spin flip is defined by $B_2$ and the magnetic moment of the proton $\mu_p$, an increase of the magnetic field would not affect the $\Delta\nu_{z,\mathrm{SF}}$. At the same time an increase of $B_0$ would decrease the cyclotron transition rate $p_{\mathrm{cyc}}$ since more energy is needed to drive cyclotron quantum jumps. An increase of the magnetic field to 6 T would decrease the axial frequency fluctuation at the given experimental constraints from currently 150 mHz down to 90 mHz.

## *9.3 Magnetic Bottle and the Quantum World*

Closing this thesis, I would like to focus on one aspect of our apparatus, which has not been studied so far to exhausting detail, since we fully concentrated on the resolution of spin flips: The transition from the quantum mechanical world to the classical world.
Textbooks propose different “formal” transitions. Most popular is the Wetzel-Kramers-Brillouin transition which formulates, that a transition between quantum- and classical-mechanics occurs, when the wavelength of a quantum mechanical particle becomes small compared to the typical length scale of the potential seen by the particle. Under these assumptions, Schrödinger’s equation can be transformed into the Hamilton-Jacobi-Equation,

being equivalent to the substitution of the commutator $[q_i, p_i]$ by the poisson bracket $\{q_i, p_i\}$, where $q_i$ and $p_i$ are canonically conjugated variables. These theoretical assumptions describe physical reality in a broad range of validity. On the other hand, it has been shown experimentally by means of interference of $^{70}$C fullerenes [114], that this criterion is only valid in presence of effects causing decoherence [115]. Decoherence occurs, if the time scale $\tau_m$ of a measuring process, which reduces an observed system to a quantum state is large compared to the typical time scale $\tau_p$ of a perturbation, which mixes the quantum states (as e. g. collisions [114]). If $\tau_m \ll \tau_p$, the measuring process "wins" and the system discloses its quantum aspects.

In the case where $\tau_m \gg \tau_p$, the system behaves classical and as discussed in [116], it can be described by a coherent state. A coherent state describes a non-dephasing wave packet (a classical particle) with a certain energy distribution. If $\hbar\omega n_0$ is the energy expectation value of the particle, the width of its energy distribution $\Delta E$ is $\hbar\omega\sqrt{n_0}$.

The Penning trap apparatus with its large magnetic bottle allows for the decision, whether the particle is in a coherent state or a quantum mechanical state, simply by measuring the linewidth of the axial noise-dip. The noise-dip has a linewidth which is defined by the properties of the axial detection system and the effective electrode distance (see chapter 4), and, as described above, by the coherent state linewidth defined by the energy distribution of the cyclotron oscillator $\Delta\nu_z = \sqrt{n_0} \cdot 68\,\mathrm{mHz}$. Expressing the cyclotron energy in units of temperature $T_+ = E_+/k_B$, the linewidth of the axial dip due to a coherent state distribution is about $\Delta\nu_{\mathrm{z,coh}} = 2.5\,\mathrm{Hz}/\sqrt{K} \cdot \sqrt{\mathrm{T_+}}$. The linewith of the axial dip due to particle detector interaction in the magnetic bottle trap is $\Delta\nu_{z,AT} \approx 3.5\,\mathrm{Hz}$. As discussed in section 7.4, the cyclotron energy of the particle can be measured absolutely. Measuring the linewidth as a function of the cyclotron energy $E_+$, and comparing the result to the coherent state linewidth, it can be decided whether the particle is in a coherent state, or its quantum mechanical state vector is reduced by the axial frequency measurement. Figure 9.1 are results of a measurement, where the axial linewidth was measured as a function of the cyclotron energy. The red filled circles represent the measured data, while the black squares are the calculated linewidths of the coherent state as a function of the cyclotron energy. This clearly indicates the reduction of the quantum mechanical state vector of the

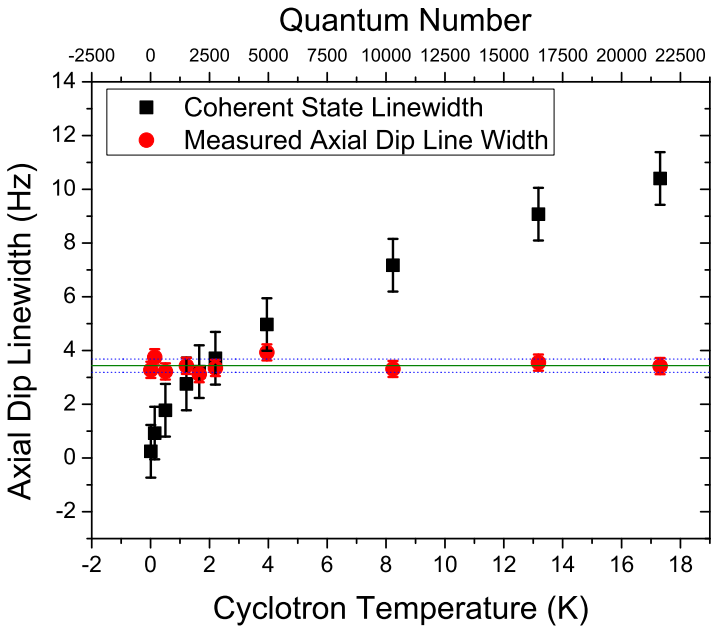


Figure 9.1: Linewidth of the axial dip as a function of the cyclotron energy $E_+$, which is expressed in terms of "temperature" $T_+ = E_+/k_B$. The red filled circles are experimental results, while the black filled squared are due to a calculation of the corresponding coherent state linewith [116]. On the upper axis, the corresponding quantum number is shown. This clearly indicates the reduction of the quantum mechanical state vector of the cyclotron harmonic oscillator at quantum numbers up to $n_+ = 22500$.

cyclotron harmonic oscillator due to the axial frequency measurement up to cyclotron quantum numbers of about $n_+ = 22500$!

This observation is possible, since our system is exceptionally clean. In the future the quantum behavior of the cyclotron mode will be investigated carefully, with special respect on the interaction of the axial frequency measuring process and the single trapped proton, as well as the transition from quantum mechanical behavior to classical physics.

With this highly exciting perspective, the thesis is closed.

# BIBLIOGRAPHY


[1] Th. Udem, A. Huber, B. Gross, J. Reichert, M. Prevedelli, M. Weitz, and T. W. Hänsch, Phys. Rev. Lett. **79**, 2646 (1997).

[2] S. J. Brodsky, C. E. Carlson, J. R. Hiller, and D. S. Hwang, Phys. Rev. Lett. **94**, 022001 (2005).

[3] R. Pohl *et al.*, Nature **466**, 213 (2010).

[4] R. Frisch and O. Stern, Z. Phys. A-Hadron Nulc. **85**, 4 (1933).

[5] P. A. M. Dirac, Proc. Roy. Soc. Lond. A. Mat. **117**, 610 (1928).

[6] I. I. Rabi, J. M. B. Kellogg, and J. R. Zacharias, Phys. Rev. **46**, 157 (1934).

[7] F. Bloch, W. W. Hansen, and M. Packard, Phys. Rev. **70**, 474 (1946).

[8] F. Bloch and C. Jeffries, Phys. Rev. **80**, 305 (1950).

[9] D. Collington, A. Dellis, J. Sanders, and K. Turberfield, Phys. Rev. **99**, 1622 (1955).

[10] P. F Winkler, D. Kleppner, T. Myint, and F. G. Walther, Phys. Rev. A **5**, 83 (1972).

[11] D. Hanneke, S. Fogwell, and G. Gabrielse, Phys. Rev. Lett. **100** 120801 (2008).

[12] T. Beier, H. Häffner, N. Hermanspahn, S. G. Karshenboim, H.-J. Kluge, W. Quint, S. Stahl, J. Verdù, and G. Werth, Phys. Rev. Lett. **88**, 011603 (2001).

[13] P. Mohr, B. Taylor, and D. Newell, Rev. Mod. Phys. **80**, 633 (2008).

[14] S. G. Karshenboim and V. G. Ivanov, Can. J. Phys. **80**, 1305 (2002).

[15] S. G. Karshenboim and V. G. Ivanov, Phys. Lett. B **566**, 27 (2003).

[16] L. Essen, R. Donaldson, M. Bangham, and E Hope, Nature **229**, 110 (1971).

[17] H. Häffner, T. Beier, S. Djekic, N. Hermanspahn, H.-J. Kluge, W. Quint, S. Stahl, J. Verdù, T. Valenzuela, and G. Werth, Eur. Phys. J. D - At. Mol. Opt. Plas. Phys. **22**, 163 (2003).

[18] A. Mooser, K. Blaum, H. Kracke, W. Quint, C. C. Rodegheri, S. Ulmer, and J. Walz, Can. J. Phys. **89**, 165 (2011).

[19] C. C. Rodegheri, K. Blaum, H. Kracke, S. Kreim, A. Mooser, C. Mrozik, W. Quint, S. Ulmer, and J. Walz, Hyperfine Interact. **194**, 93 (2009).

[20] K. Blaum, J. Phys. B: At. Mol. Opt. Phys. **42**, 154021 (2009).

[21] H. Dehmelt and P. Ekström, Bull. Am. Phys. Soc. **18**, 72 (1973).

[22] R. Van Dyck, Jr., P. B. Schwinberg and H. G. Dehmelt, Phy. Rev. Lett. **59**, 26 (1987).

[23] N. Hermanspahn, H. Häffner, H. Kluge, W. Quint, S. Stahl, J. Verdu, and G. Werth, Phys. Rev. Lett. **84**, 427 (2000).

[24] H. Häffner, T. Beier, N. Hermanspahn, H. Kluge, W. Quint, S. Stahl, J. Verdu, and G. Werth, Phys. Rev. Lett. **85**, 5308 (2000).

[25] J. Verdù, S. Djekic, S. Stahl, T. Valenzuela, M. Vogel, G. Werth, T. Beier, H. Kluge, and W. Quint, Phys. Rev. Lett. **92**, 093002 (2004).

[26] S. Sturm, K. Blaum, B. Schabinger, A. Wagner, W. Quint and G. Werth, J. Phys. B: At. Mol. Opt. Phys. **43**, 074016 (2010).

[27] T. Beier, Phys. Rep. **339**, 79 (2000).

[28] R. Bluhm, V. A. Kostellecky, and N. Russell, Phys. Rev. D **57**, 3932 (1998).

[29] G. Gabrielse, D. F. Phillips, W. Quint, H. Kalinowsky, G. Rouleau, and W. Jhe, Phys. Rev. Lett **74**, 3544 (1995).

[30] N. Guise, J. DiSciacca, and G. Gabrielse, Phys. Rev. Lett. **104**, 143001 (2010).

[31] T. Pask *et al.*, J. Phys. B **41**, 081008 (2008).

[32] W.Quint and G. Gabrielse, Hyperfine Interact. **76**, 379 (1993).

[33] S. Ulmer, C. C. Rodegheri, K. Blaum, H. Kracke, A. Mooser, W. Quint, and J. Walz, accepted by Phys. Rev. Lett. (2011).

[34] S. Earnshaw, Trans. Camb. Phil. Soc. **7**, 97 (1842).

[35] J. C. Maxwell, Roy. Soc. Trans. **155**, 459 (1865).

[36] J. R. Pierce, *in: Theory and Design of Electron Beams*, D. van Nostrand Co., NewYork (1949).

[37] L.S. Brown and G. Gabrielse, Rev. Mod. Phys. **58**, 233 (1986).

[38] L. S. Brown and G. Gabrielse, Phys. Rev. A **25**, 2423 (1982).

[39] M. Kretzschmar, Phys. Scr. **46**, 544 (1992).

[40] G. Gabrielse, L. Haarsma, and S. L. Rolston, Int. J. Mass Spec. **88**, 319 (1989).

[41] M. Abramowitz and I. A. Stegun, *Handbook of Mathematical Functions with Formulas, Graphs, and Mathematical Tables*, Dover, New York (1964).

[42] J. Verdù, PhD thesis, Johannes-Gutenberg Universität, Mainz (2003).

[43] F.C. Moon, *Chaotic vibrations*, Wiley and Sons Inc., New York (1987).

[44] L. D. Landau and E. M. Lifshitz, *Mechanics*, Pergamon Press Inc., Oxford (1965).

[45] J. Tan, PhD Thesis, Harvard University, Cambridge (1993).

[46] J. Tan, and G. Gabrielse, Phys. Rev. Lett. **67**, 3090 (1991).

[47] C. C. Rodegheri, PhD Thesis (to be submitted), Johannes-Gutenberg Universität, Mainz (2011).

[48] N. Hermanspahn, PhD Thesis, Johannes-Gutenberg Universität, Mainz (1999).

[49] L. S. Brown, Ann. Phys. **159**, 62 (1985).

[50] I. Rabi, J. Zacharias, S. Millman, and P. Kusch, Phys. Rev. **53**, 318 (1938).

[51] H. Häffner, PhD Thesis, Johannes-Gutenberg Universität, Mainz (2001).

[52] S. Ulmer, Diploma Thesis, Ruprecht-Karls Universität, Heidelberg (2006).

[53] S. Kreim, PhD Thesis, Johannes-Gutenberg Universität, Mainz (2009).

[54] cg-tec, *FRP- and CFRP-Shafts and -Tubes*, Datasheet (2011).

[55] DuPont, *Kevlar 49 Aramid Fiber*, Datasheet (2011).

[56] Oxford Insturments, *Cryospares - Cryolam Superinsulation*, Datasheet (2011).

[57] N. Kanani, *Galvanotechnik. Grundlagen, Verfahren und Praxis einer Schlsseltechnologie*, Hanser Fachbuch, Leipzig (2009).

[58] J. B. Camp, T.W. Darling, and R. E. Brown, J. Appl. Phys. **69**, 7126 (1991).

[59] H. Kracke, PhD Thesis (to be submitted), Johannes-Gutenberg Universität, Mainz (2012).

[60] A. Mooser, Diploma Thesis, Johannes-Gutenberg Universität, Mainz (2008).

[61] S. Ulmer, H. Kracke, K. Blaum, S. Kreim, A. Mooser, W. Quint, C. C. Rodegheri, and J. Walz, Rev. Sci. Inst. **80**, 123302 (2009).

[62] J. Ketelaer *et al.*, Eur. Phys. J. A **42**, 311 (2009).

[63] S. Ulmer, H. Kracke, K. Blaum, A. Mooser, W. Quint, C. C. Rodegheri, and J. Walz, *in preparation*, to be submitted to Rev. Sci. Inst. (2011).

[64] S. Stahl, PhD Thesis, Johannes-Gutenberg Universität, Mainz (1998).

[65] J. Johnson, Phys. Rev. **32**, 97 (1928).

[66] H. Nyquist, Phys. Rev. **32**, 110 (1928).

[67] D. J. Wineland and H. G. Dehmelt, J. Appl. Phys. **46**, 919 (1975).

[68] X. Feng, M. Charlton, M. Holzscheiter, R. Lewis, and Y. Yamazaki, J. App. Phys.**79**, 8 (2009).

[69] S. Ulmer and J. Verdù, in preparation, to be submitted to Int. Journ. Mass. Spec. (2011).

[70] J.D. Jackson, *Classical Electrodynamics* third Ed., Wiley and Sons Inc., New York (1998).

[71] H. Dehmelt, W. Nagourney, J. Sandberg, Proc. Nat. Acad. Sci. **83**, 5761 (1986).

[72] B. dUrso, B. Odom, and G. Gabrielse, Phys. Rev. Lett **90**, 43001 (2003).

[73] B. d'Urso, PhD thesis, Harvard University, Cambridge (2004).

[74] S.R. Jefferts, T. Heavner, P. Hayes, and G.H. Dunn, Rev. Sci. Instrum. **64**, 737 (1993).

[75] R. Kirschman, S. Lemoff, J. Lipa, and R. Experiment, Conf. Inf. Read. El. **1**, 21 (1992).

[76] A. Lee, Rev. Sci. Inst. **64**, 2373 (1993).

[77] A. Robinson, V. Talyanskii, Rev. Sci. Inst. **75**, 3169 (2004).

[78] W. W. Macalpine and O. Schildknecht, Proc. IRE **47**, 2099 (1959).

[79] A. Mooser, PhD Thesis (to be submitted), Johannes-Gutenberg Universität, Mainz (2013).

[80] R. Schetgen, *The ARRL handbook for radio amateurs*, The American radio relay league, Newington (1996).

[81] M. Tinkham, *Introduction to Superconductivity*, Dover Publications, Mineola (2004).

[82] W. Buckel and R. Kleiner, *Superconductivity*, Wiley-VCH, Weinheim (2004).

[83] M. N. Kunchur and S.J. Poon, Phys. Rev. B **43**, 2916 (1991).

[84] M. Bonura, A.A. Gallittoa, and M.L. Vigni, Eur. Phys. J. B **53**, 315 (2006).

[85] C. P. Bean, Phys. Rev. Lett. **8**, 250 (1962).

[86] M. W. Coffey and J. R. Clem, Phys. Rev. Lett. **67**, 386 (1991).

[87] P. Fabbricatore, G. Gemme, R. Musenich, R. Parodi, M. Viviani, B. Zhang, and R.J. Sinko, , IEEE Trans. Appl. SC **3**, 197 (1993).

[88] Y. Shapira and L.J. Neuringer, Phys. Rev. C **140**, 1638 (1965).

[89] L.S. Topchishvili and A.I. Naskidashvili, J. Nucl. Mat. **271**, 505 (1999).

[90] V.V. Schmidt, *The Physics of Superconductors*, Springer, Heidelberg (1997).

[91] D. F. Phillips, PhD thesis, Harvard University, Cambridge (1996).

[92] U. Tietze and C. Schenk, *Halbleiter-Schaltungstechnik*, Springer, Heidelberg (2002).

[93] Johanson Technologies, Multi-Layer High-Q Capacitors, Datasheet (2009).

[94] C. H. Suh, H. Rohdin and C. Stolte, Elec. Dev. Meet. **29**, 601 (1983).

[95] C. H. Suh, A. van der Ziel and R. P. Jindal, Sol. St. El. **24**, 717 (1981).

[96] S. Sturm, PhD Thesis (to be submitted), Johannes-Gutenberg Universität, Mainz (2011).

[97] E. Daw, B. Bradley, J. App. Phys. **82**, 1925 (1997).

[98] C. Roux, PhD Thesis (to be submitted), Ruprecht-Karls Universität, Heidelberg (2011).

[99] S. Guan and P. Jones, J. Chem. Phys. **91**, 775 (1989).

[100] C. Mrozik, Diploma Thesis, Johannes-Gutenberg Universität, Mainz (2008).

[101] J. Thompson, PhD thesis, Massachussetts Institute of Technology, Cambridge (2003).

[102] G. Gabrielse, A. Khabbaz, D.S. Hall, C. Heimann, H. Kalinowsky and W. Jhe, Phys. Rev. Lett. **82**, 3198 (1999).

[103] S. Rainville, PhD thesis, Massachussetts Institute of Technology, Cambridge (2003).

[104] E. A. Cornell, R. M.Weisskoff, K. R. Boyce, and D. E.Pritchard, Phys. Rev. A, **41**, 312 (1990).

[105] M. Kretzschmar, AIP Conf. Proc. **457**, 242 (1999).

[106] S. Stahl, J. Alonso, S. Djekic, H.J. Kluge, W. Quint, J. Verdù, M. Vogel, and G. Werth, J. Phys. B At. Mol. Opt. Phys. **38**, 297 (2005).

[107] F. DiFilippo, V. Natarajan, K. Boyce, and D. Pritchard, Phys. Rev. Lett. **68**, 2859 (1992).

[108] B. DUrso, R. Van Handel, B. Odom, D. Hanneke, and G. Gabrielse, G. Phys. Rev. Lett. **94**, 113002 (2005).

[109] J. Dalibard and C. Cohen-Tannoudji, J. Opt. Soc. Am. B **2**, 1707, (1985).

[110] G. L. Squires, *Messergebnisse und ihre Auswertung*, de Gruyter, Berlin (1971).

[111] K. Blaum, Phys. Rep **425**, 1 (2006).

[112] S. Sturm, K. Blaum, B. Schabinger, A. Wagner, W. Quint and G. Werth, submitted to Phys. Rev. Lett., (2011).

[113] G. Gabrielse and J. Tan, J. Appl. Phys. **63**, 5143 (2011).

[114] Klaus Hornberger, Stefan Uttenthaler, Björn Brezger, Lucia Hackermüller, Markus Arndt, and Anton Zeilinger, Phys. Rev. Lett. **90**, 160401 (2003).

[115] D. Giulini, E. Joos, C. Kiefer, J. Kupsch, I.O. Stamatescu, and H. D. Zeh, *Decoherence and the Appearance of a Classical World in Quantum Theorie* , Springer, Heidelberg (1993).

[116] R. J. Glauber, Phys. Rev. **131**, 2766 (1963).

# Danksagung

*Wolfgang Quint*, ich danke dir dafür, dass du mir jahrelang dein Vertrauen geschenkt hast, mir die bedingungslose Freiheit gelassen hast Ideen zu entwickeln und umzusetzen, und niemals müde wurdest, mich in den Vorhaben zu ermutigen. Danke für die vielen physikalischen Diskussionen und Reisen auf die du mich mit deinem subtilen Tiefsinn mitgenommen hast, in denen es eigentlich immer nur um eines ging - um die selbstlose Liebe zur Physik.

*Klaus Blaum*, vermutlich bist du als Säugling in einen Zaubertrank gefallen der dir hunderte simultane Leben beschert. Deine Produktivität, deine Hingabe und deine offensichtliche Freude an dem was du tust, sind beispiellos. Es ist ein unendlich wertvolles Geschenk in deinem Umfeld arbeiten zu dürfen, weil du mit deiner Tatkraft, deinem Optimismus und deinem Einsatz per se inspirierst. Ich bin bisher keinem Menschen begegnet, auf den die Umschreibung ,,larger than life" mehr zugetroffen hätte als auf dich! Deine Freude, dein Vertrauen, deine Ideen und deinen unumstößlichen Optimismus hast du uns über Jahre hinweg mit ins Labor gegeben, und dafür bin ich dir unsagbar dankbar. Klaus, dir gilt mein ganz besonderer Dank, weil du mich perönlich über all die Jahre in vielem aktiv gefördert und unterstützt hast, egal ob im Fachlichen oder Privaten, du warst mein Chef, aber auch ein guter Freund, auf den ich mich immer blind verlassen konnte!

*Jochen Walz*, deine Entschlossenheit, deine Geradlinikeit, dein Wille am Experiment ,,Nägel mit Köpfen" zu machen, und deine Fähigkeit eine abstrakte Idee in konkrete experimentelle Realität zu übersetzen sind im höchsten Maße inspirierend. Ich habe aus deiner anspruchsvollen experimentellen Schule und deinen klaren Ansätzen und Herangehensweisen sehr Vieles gelernt. Vielen Dank für all das! Ich wünsche dir, dass du deine Energie und Durchschlagskraft nie verlierst, und dass noch viele deiner Studenten in den kommenden Jahren davon lernen und zehren können.

*Wolfgang, Klaus* und *Jochen*, die Superposition eurer Charaktere schafft an diesem Experiment eine einzigartige Atmosphäre, der alle nur denkbaren Attribute inhärent sind. Ihr

seid professionell, höchst ambitioniert, kreativ, entschlossen, fordernd, und teilweise hart, aber gleichzeitig verständnisvoll, entgegenkommend, freundschaftlich und wohlwollend. Ihr schafft eine Atmosphäre des Vertrauens, ohne jemals die Zügel zu locker zu lassen, und gebt einem alle Freiheiten solange man ,,macht". Idealere und beflügelndere Randbedingungen sind nur schwer vorstellbar - VIELEN DANK!!!

Bei meinen Kollegen *Cricia C. Rodgheri*, *Holger Kracke* und *Andreas Mooser* möchte ich mich bedanken, für die gute und freundschaftliche Zusammenarbeit. Es ist unmöglich euch dreien in wenigen Worten gerecht zu werden.

*Cricia*, von spontanen Fahrten ins Ausland, über zahlreiche hitzige Diskussionen, bis hin zu vielen durchgemachten Nächten haben wir beide alles menschenmögliche getan um den Spinflip nachzuweisen, was am Ende gelang. Das macht uns auf ewig zu ,,Blutsbrüdern". Ich danke dir für ALLES und wünsche dir für die nahe Zukunft, dass du mit dieser Apparatur alles erreichen wirst, was du dir vorgenommen hast.

*Holger*, du hast mit deinem technischen Geschick und Verständnis vieles beigetragen, um die Apparatur auf den gegenwärtigen Stand zu bringen. Dir gehört die Zukunft dieses Experiments, und ich bin mir sicher, dass du mit der verbesserten Apparatur die erste ,,echte" $g$-Faktor Messung schaffen wirst, und du...

*Andi*, wirst diesen Wert weiter verbessern, weil du für ein Päzisionsexperiment wie geschaffen bist. Deine physikalische Intuition, dein Durchhaltevermögen, deine Hartnäckigkeit und deine höchst ausgeprägte Frustrationsschwelle werden dich dorthin führen.

Mit euch beiden ist dem Experiment eine erfolgreiche Zukunft gesichert!

Desweiteren möchte ich mich bei den Kollegen ,,der ersten Stunde" bedanken, insbesondere bei *Susanne Kreim*, *Stefan Stahl* und *J. Verdù*, die dieses Experiment mit ihren Studien

und Rechnungen auf den Weg gebracht haben.

Mein Dank gilt ebenfalls dem HCI-$g$-Faktor team, *Birgit Schabinger*, *Sven Sturm* und *Anke Wagner*, für den kreativen ,,workflow" zwischen beiden Experimenten. Mein besonderer Dank gilt dabei *Sven Sturm*, der uns mit seinen herausragenden technischen Fähigkeiten bereitwillig unterstützt hat.

Weiterhin bedanke ich mich bei allen Mitgliedern der *Arbeitsgruppe Walz* innerhalb der *QUANTUM*-Mainz, den Mitgliedern der *TRIGA-TRAP* Gruppe in Mainz, den Mitgliedern der *HITRAP*-Gruppe innerhalb der GSI-Darmstadt und allen Migliedern der *Arbeitsgruppe für gespeicherte und gekühlte Ionen* am MPI-K in Heidelberg, insbesondere *Christian Roux*, für die Durchsicht dieser Arbeit und seine Freundschaft!

Ebenfalls danken möchte ich dem ,,nicht-wissenschaftlichen" Personal am Institut für Physik an der Universität Mainz, besonders bei *Siegbert Felzer*, *Erwin Gries*, *Heiko Lott* und *Erich Wagner*, für ihre ausgezeichnete technische Arbeit.

Neben dem beruflichen Umfeld danke ich meinen Freunden *Carolin Strack*, *Christian Kurtz* und *Stefan Niedermeier* für ihre Freude am exzessiven Feiern und an der Musik. Ferner danke ich *Utz Täuber* und *Ira Schwaab*, für ,,Babysitting", unterhaltsame Kaffeekränzchen, gute Bewirtung und die schönen gemeinsamen Freizeitaktivitäten.

Meinen Eltern *Hedwig* und *Gerhard Ulmer* und meinen Geschwistern *Barbara, Dorothee, Christine* und *Hartmut* danke ich für die jahrelange Unterstützung und den Spaß und die Freude, den die Familie Ulmer macht. *Dorothee* danke ich insbesondere für das Durchlesen dieser Arbeit.
Meiner Oma *Friedel Ulmer* und meiner Großtante *Marta Ulmer* danke ich für den ,,Esprit" und die Lebensfreude, die sie sich bis ins hohe Alter erhalten haben.

Abschließend danke ich meiner allerliebsten, wunderbaren Frau *Eva Ulmer* und meinen Töchtern *Frida-Marie* und *Yara Luisa*. Ihr seid das Geschenk meines Lebens und das Glück das ich darüber empfinde, euch zu haben, ist nicht in Worte zu fassen. *Eva*, meine Dankbarkeit dir gegenüber kennt keine Grenzen. Deine Leichtigkeit, deine Lebensfreude, dein Esprit, den du mit jedem Blick, jedem Wort und jedem Atemzug ausstrahlst, sind für mich die grösste Freude und Inspiration, und bedeuten das pure Glück!